Structure and function of the epithelial sodium channel

by

Sigrid Noreng

A dissertation

Presented to the Biochemistry and Molecular Biology Graduate Program
and Oregon Health and Science University School of Medicine
in partial fulfillment of the requirements for the degree of:

Doctor of Philosophy

January, 2020

CERTIFICATE OF APPROVAL

This is to certify that the PhD Dissertation of

Sigrid Noreng

has been approved on January 23, 2020

_____

Advisor, Isabelle Baconguis, Ph.D.

_____

Member and Chair, Show-Ling Shyng, Ph.D.

_____

Member, Eric Gouaux, Ph.D.

_____

Member, Francis Valiyaveetil, Ph.D.

_____

Member, Steve Reichow, Ph.D.

_____

Member, David Ellison, M.D

TABLE OF CONTENTS

Acknowledgements

I want to thank my mentor, Isabelle Baconguis, for giving me the opportunity to join her lab. Although my background did not include expertise in biochemistry or structural biology, her trust in me and her encouragement in my abilities allowed me to reach the point where I am today. Although science is never easy, I've truly enjoyed my years as a graduate student, and Isabelle gave me the opportunity to prove myself and has been an inspiring mentor. I hope someday I can repay the kindness and support I received from her and encourage others to seek their passion in science.

I'm truly thankful for all the advice, insightful questions and support I've received from my dissertation committee. Having the opportunity to discuss my experimental results and be challenged by critical questions and helpful suggestions have contributed significantly to me becoming a better scientist.

I especially want to thank all members of the Baconguis lab. My day to day life in lab would not have been the same if it wasn't for Arpita Bharadwaj, who taught me a lot of the basic lab skills early on. She has been an excellent resource for help and a major source of support since I started. Rich Posert brought a new spirit to the lab when he joined, in addition to knowledge that was needed in order to continue studies on ENaC. Alex Houser, the most recent member has already made a great addition to our crew, and I'm looking forward to what new discoveries come from the Baconguis lab. I will miss being a part it.

In addition to the Baconguis lab, I want to thank all Gouaux and Whorton lab members, past and present. Thank you to Steve Mansoor and Nate Yoder who have been around since I started, and who not only helped contribute greatly to my scientific writing skills, but also gave support throughout these years. I also want to thank Natalie Sheldon, Wei Lü, Farzad Jalali-Yazdi, Johannes Elferich, Jonathan Coleman, Vikas Navratna, Prashant Rao and Shivani Ahuja who've all contributed in one way or another to expanding my set of lab skills and to my overall improvement as a scientist.

Thank you to Claudia Lopez, Craig Yoshioka and Drew Gingerich at the multiscale microscopy core who've provided excellent support not only when it comes to scheduling

sessions on high-demand electron microscopes, but also for always being available to help during cryo-EM data collection.

Life in Portland, Oregon would not have been the same if it wasn't for all the great people and friends I've met while I've been living here. There are so many inspiring people outside of my life in lab, which includes people who love to run, play soccer, climb, go skiing and go hiking. Having the opportunity to spend time outdoors has been crucial for my overall happiness, and I have been so fortunate to have friends to share all of my favorite activities with.

I want to thank Alex Bouneff who's been one of my best friends throughout the years here at OHSU. The GRIP domain of ENaC would not have had its name if it wasn't for him. Additionally, I want to thank his family who have been a major support and have made Portland feel like my home. His mom and stepdad, Kathy and Troy Doane. His sister, Lara Bouneff. His dad Tony Bouneff, and finally, his grandparents Christ and Barbara Bouneff.

Lastly, I want to thank my parents, Randi and Vidar Noreng. They deserve the biggest appreciation and thank you, because they have undoubtedly been my biggest support throughout my entire life. Even when I decided to move across the world. They have taught me what's most important in life, and working hard is solely a trait I got from them. Lastly, to both my sisters, Ida-Kristine Noreng and Anne-Silje Noreng who has been one of my closest friends growing up.

List of Tables

List of Figures

List of Abbreviations

ΔcASIC1a	chicken acid-sensing ion channel 1a, residues 26-463
$\Delta cASIC1_{mfc}$	chicken acid-sensing ion channel 1a, residues 2-466
ΔENaC	truncated epithelial sodium channel
$\Delta ENaC_{ASIC}$	truncated epithelial sodium channel with N-term
AQP2	aquaporin 2
ASDN	aldosterone-sensitive distal nephron
ASL	airway surface liquid
ASIC	acid-sensing ion channel
AT1	angiotensin II receptor type 1
ATP	adenosine triphosphate
AVP	arginine vasopressin
BASIC	bile acid sensing ion channel
BK	bradykinin
BPLE	brain polar lipid extract
CAP1	channel activating protein 1
CAP2	channel activating protein 2
CAP3	channel activating protein 3
cASIC1a	chicken acid-sensing ion channel 1a
CCD	cortical collecting duct
CCT	cortical collecting tubule
CD	collecting duct
CF	cystic fibrosis
CFTR	cystic fibrosis transmembrane regulator
CHS	cholesteryl hemisuccinate
Cryo-EM	cryo-electron microscopy
CT	connecting tubule
CTF	contrast transfer function
C.elegans	*Caenorhabditis elegans*
DCT	distal convoluted tubule
DCT1	distal convoluted tubule 1 (early part)
DCT2	distal convoluted tubule 2 (late part)
DDM	n-dodecyl-β-D-maltoside
DEG	degenerin
DHHC	aspartate-histidine-histidine-cysteine domain palmitoyltransferase
DTT	dithiothreitol
ECD	extracellular domain
EDTA	ethylenediaminetetraacetic acid
EGF	epidermal growth factor
EGFP	enhanced green fluorescent protein
EGTA	ethylene glycol tetraacetic acid
EMDB	electron microscopy data bank
ENaC	epithelial sodium channel
ER	endoplasmic reticulum

ERK2	extracellular signal-regulated kinase 2
ET-1	endothelin
Fab	fragment antibody
FaNaC	phe-met-arg-phe-amide sodium channels
Fc	fragment antibody constant domain
FL	full-length
FL-ASIC	full-length acid sensing ion channel
FL-ENaC	full-length epithelial sodium channel
FSC	fourier shell correlation
FSEC	fluorescence size exclusion chromatography
Fv	fragment antibody variable domain
GAS	glycine-alanine-serine
GPI	glycosylphosphatidyl-inositol
GRIP	Gating relief of inhibition by proteolysis
GRK2	G protein-coupled receptor kinase 2
HEK	human embryonic kidney cell
HG	histidine-glycine
HPLC	high performance liquid chromatography
MARCKS	myristoylated alanine-rich c-kinase substrate
MitTx	*Micrurus tener tener toxin*
MOI	multiplicity of infection
Msp	membrane scaffold protein
MR	mineralocorticoid receptor
NCC	electroneutral thiazide-sensitive Na^+:Cl^- cotransporter
Nedd4	Neural precursor cell-expressed developmentally downregulated 4
PBS	phosphate-buffered saline
PcTx1	*Psalmopoeus cambridgei toxin 1*
PDB	protein data bank
PHA1	pseudohypoaldosteronism type 1
PIP_2	phosphatidylinositol 4,5-biphosphate
PIP_3	phosphatidylinositol 3,4,5-biphosphate
PKA	protein kinase a
PKC	protein kinase c
P_o	open probability
PPK	pickpocket
PY	PPXY
RAAS	renin-angiotensine-aldosterone-system
ROMK	renal outer medullary potassium channel
SEC	size exclusion chromatography
SEM	standard error of the mean
sgk1	serum glucocorticoid regulated kinase 1
SMA	styrene-maleic acid
SCNN1	sodium channel non-voltage gated 1
TBS	tris-buffered saline
TEVC	two-electrode voltage clamp
TM	transmembrane

TM2	transmembrane 2
TMD	transmembrane domain
TRITC	tetramethylrhodamine
V	transepithelial voltage
V2R	vasopressin receptor type 2
V_i	inner membrane voltage
V_o	outer membrane voltage
WNK4	with-no-lysine kinase 4

Abstract

The epithelial sodium channel (ENaC) is expressed at the apical side of epithelial cells and is a key regulator of salt and water balance. By serving as the rate-limiting step of sodium reabsorption in the aldosterone sensitive distal nephron of the kidneys, ENaC regulates blood volume and thereby modulates blood pressure. ENaC is an obligate heterotrimeric ion channel comprised of three homologous subunits, α, β, γ, and belongs to the ENaC/degenerin superfamily, known to be voltage independent, sodium selective and sensitive to the small molecule amiloride. Members of this superfamily have short intracellular N- and C-termini, two membrane-spanning α-helical segments, and a large extracellular domain (ECD). The gating of ENaC is highly unusual for an ion channel, whereby the α and γ subunits are cleaved at distinct extracellular sites by proteases causing release of inhibitory peptides to activate the receptor and open the channel. Another unique property of the ENaC channel includes a high selectivity for sodium over potassium at 100:1 compared to 30-3:1 for acid sensing ion channels, another member in the same superfamily.

Up until the beginning of this work, no structure of ENaC was known, limiting the understanding of the molecular mechanisms underlining the physiological and pathophysiological roles of ENaC. The main challenges for structural studies of ENaC have included poor protein expression, significant sample heterogeneity, and inherent intramolecular pseudosymmetry, each hampering the use of structural methods such as x-ray crystallography and cryo-electron microscopy (cryo-EM). To overcome these challenges, our group took advantage of baculovirus-mediated infection as well as fluorescence size exclusion chromatography (FSEC) to identify ENaC constructs with increased expression and homogeneity. Using cryo-EM, I was able to determine the first structure of ENaC by generating

high-affinity monoclonal antibodies that targeted specific subunits of ENaC to form a receptor-antibody complex and break the inherent pseudosymmetry. The structure of ENaC provided the first view of the ENaC architecture and demonstrated how the three subunits, α-β-γ arrange in a counterclockwise direction (as seen from the luminal side of the membrane), and also revealed the location of the inhibitory peptides.

One drawback of the cryo-EM data, however, was the poorly resolved map in the region of the transmembrane domain (TMD), preventing visualization of the structural details necessary to explain the sodium-selective ion permeation pathway. Initially, the main concern was that the N- and C-terminal truncations made to generate a high expressing and homogeneous ΔENaC construct had potentially disrupted interactions important for the TMD stability. Thus, I started working towards determining the structure of wild type, full-length (FL) ENaC. However, after optimizing the expression and purification strategies to be able to study FL-ENaC by cryo-EM, analysis of FL-ENaC particles, once again revealed 2D class averages with a disordered micelle-TMD. This indicated that the N- and C-terminal truncations were not the primary reason the TMD was disordered, but emphasized the importance of the biochemical environment for TMD stability. Although multiple conditions were screened to find purification conditions of FL ENaC to improve the stability of the TMD, the optimal conditions to stabilize the TMD have not yet been identified and thus its molecular structure continues to remain ambiguous.

However, the cryo-EM map obtained from FL-ENaC was greatly improved and validated the first structure of ΔENaC, confirming that it was captured in an uncleaved state. As purified FL-ENaC is a mixture of uncleaved and cleaved states, I attempted to tease out structural differences by taking advantage of implemented cryo-EM data processing methods that perform focused classification to separate structural variabilities in small regions of the cryo-EM maps.

Using the focused classification methodology, I was able to separate cryo-EM maps based on whether density was present (uncleaved state) or absent (cleaved state) from the protease-sensitive domains of ENaC that harbor the inhibitory peptides. No large conformational changes were detected, aside from the area of missing density, and electrophysiology studies confirmed that the antibody 7B1 does not trap ENaC in a conformation that causes a change in the overall gating kinetics of ENaC. The cryo-EM data processing strategy thus presented demonstrates how we can use cryo-EM as a method to separate and study the structural differences between cleaved and uncleaved states of ENaC. The number of states ENaC can occupy as a result of proteolytic processing, and how these states differ structurally and functionally, is a topic within the ENaC field that has not been established.

Altogether, the work encompassed in my PhD dissertation has made two substantial contributions to the ENaC structure-function field: 1; the first structure of the ENaC channel elucidating the molecular architecture and important domains involved in gating, and 2; detailing a strategy towards separating cleaved and uncleaved states of ENaC, which creates a foundation for future structure determination of native ENaC.

Chapter 1

Introduction

The epithelial sodium channel/degenerin ion channel family

The epithelial sodium channel/degenerin (ENaC/DEG) gene family represents a group of ion channels that were discovered in the early 1990s[1-4]. There are six main subfamilies that make up the ENaC/DEG super family, three of which are only found in invertebrates: pickpocket (PPK) ion channels in Drosophila, the mechanosensitive DEGs found in *Caenorhabditis elegans* (*C.elegans*) and peptide-gated Phe-Met-Arg-Phe-amide Na^+ channels, (FaNaCs) expressed in snails (**Figure 1.1**). The remaining three subfamilies are mammalian: acid sensing ion channels (ASICs), the bile acid sensing ion channels (BASICs), and ENaCs (**Figure 1.1**). Characteristics that are conserved among all members of the ENaC/DEG family, include voltage independency, Na^+-selectivity, and sensitivity to amiloride, a small molecule pore-blocker. Another conserved characteristic is the presence of a small residue (such as serine or glycine) in the primary sequence, referred to as the DEG site that, when mutated to a larger residue, locks the ENaC/DEG family members in a constitutively open state. The DEG site was initially characterized in the founding member DEG when mutations were found to cause neurodegeneration of sensory neurons in *C. elegans*[5].

Receptors within the ENaC/DEG subfamilies assemble either as homo- or heterotrimers[4], and all subunits have a similar sequence homology and topology consisting of short N- and C-termini, two transmembrane helices and a large extracellular domain (ECD). Tissue distribution of these receptors in both invertebrates and vertebrates ranges from neuronal cells in the nervous system to epithelial cells in the kidney, lung and colon. Neurodegeneration, mechanotransduction, salt and water homeostasis, proprioception and nociception are all important physiological processes modulated by these ion channels[6], highlighting the broad functional heterogeneity of this ion channel superfamily.

ENaC in the ENaC/DEG superfamily

ENaCs were one of the first members of the ENaC/DEG family to be identified, and assemble into heterotrimers comprised of combinations from four subunits, α, β, γ and δ, that are each encoded by the genes SCNN1A, SCNN1B, SCNN1G, SCNN1D (Sodium Channel Non-voltage gated), respectively. The α subunit was cloned in 1993[2], followed by the β and γ subunits in 1994[3], and finally the δ-subunit in 1995[7]. All four subunits share minimal sequence identity ranging between 23-34%[8]. Functional assessment of α, β and γ subunits co-expressed in *Xenopus laevis* oocytes revealed that ENaC is an obligate heteromer that requires the presence of at least three subunits, α or δ, β and γ to form a fully functional channel. Both β and γ subunit (which are more similar to each other than to α) are required to form an active channel, while the δ-subunit shares a higher similarity to the α-subunit and one of these subunits is required to form a functional channel along with β and γ. The δ-subunit is mainly expressed in the brain, pancreas, testis and ovaries, and is the least studied subunit of the four[7]. As a result, little is known about the δ-subunit or about ENaC channels with a δ-β-γ subunit composition[9,10]. The majority of studies discussed in this dissertation, unless otherwise noted, will be studies that involve heterotrimeric ENaC composed of α-β-γ subunits.

ENaCs are expressed at the apical surface of epithelial cells and mediate reabsorption of Na^+ ions in the aldosterone-sensitive distal nephron (ASDN) of the kidney. This key role has been highlighted in gain-of-function mutations causing severe hypertension, such as Liddle syndrome, or in loss-of-function mutations causing the neonatal salt-wasting disorder Pseudohypoaldosteronism type 1 (PHA1). A distinguishable characteristic of ENaCs is the 100-fold (100:1) selectivity for Na^+ over K^+ compared to other members in the same superfamily, such as ASICs which are far less selective (30-3:1). Additionally, the gating mechanism of

ENaCs is remarkably distinct compared to other ion channels. Proteolytic cleavage of extracellular sites on the α and γ subunits induces the release of inhibitory peptides from these subunits, leading to increased open probability (P_o) of ENaC. As a result, once undergoing proteolysis, ENaCs remain constitutively active until recycled back into the cell and do not respond to voltage fluctuations or ligand binding, which typically are hallmarks of ion channel gating mechanisms.

Because of the constitutive activity of ENaCs, the regulation of receptor activity is extremely important and complex. As a result, a complete model of the multiple factors that have an effect on ENaC activity, and the channel's many functional states, has not yet been described. However, there are two main factors that determine ENaC activity: the number of ENaCs that are located at the plasma membrane, and the P_o of ENaC.

Brief history of studies that led to the identification of ENaC subunits

Two-membrane model by Koefoed-Johnsson and Ussing

In 1958, Koefoed-Johnsson and Ussing provided the first clear description of active Na^+ transport across an epithelium, and referred to it as the two-membrane model[11]. Ussing had, since the late 1940s, been isolating frog skin to measure active Na^+ transport, initially using radioisotopes of Na^+ and Cl^- to demonstrate that Na^+ can move across isolated frog skin against an electrochemical gradient[12,13]. In 1951, Ussing designed a short-circuit technique to control the voltage difference across the isolated frog skin layer, permitting measurement of the transepithelial current, effectively representing the net flux of Na^+ ions (influx and outflux)[14].

The implementation of the short-circuit technique on frog skin was a crucial step toward the understanding of transepithelial ion movement.

In the two-membrane model, Na^+ ions move across the outer membrane (apical side/lumen) into the cells via channels that are localized only on the apical membrane of the epithelial cell. To maintain the low cytosolic Na^+ concentration, Na^+ ions are pumped out via the inner membrane (basolateral side/blood). Thus, the basolateral membrane works as a "typical" cell, impermeable to Na^+ ion diffusion, while the apical membrane contains the unusual property of being permeable to Na^+ ion diffusion. The Na^+-K^+ ATPase pump, restricted to the basolateral membrane of epithelial cells, pumps Na^+ out of the cell and transports K^+ into the cell across the basolateral membrane, and K^+ ions are then recycled out of the cell via K^+ channels that also are restricted to the basolateral membrane (**Figure 1.2**)[11]. A transepithelial potential is generated as a result of the active Na^+ transport, and in isolated live frog skin, the potential difference is maintained for hours with the inside (basolateral side) being more than 100 mV positive relative to the outside (apical side)[14].

The contribution from anions accompanying Na^+ ions across the epithelial cells were minimized in the initial studies done by Koefoed-Johnsson and Ussing in order to focus on the major movements of K^+ and Na^+. However, under physiological conditions, the uptake of Cl^- and other anions (as well as the export of cations in certain epithelial cells) are important for Na^+ entry into the cell. In isolated frog skin, the transport of Cl^- was found to occur via mitochondria-rich cells that are arranged in parallel with the Na^+-transporting cells [15]. The movement of Cl^- ions across tight epithelia can also occur via tight junctions. Claudins are a family of proteins located in tight junctions of epithelial cells that facilitate paracellular ion movements, including Cl^- ions[16]. In epithelial kidney cells, Na^+ influx is partially driven by the outflux of K^+ ions

across the apical membrane, resulting in K^+ secretion into the urine [17]. The renal outer medullary potassium channel (ROMK) is one of the potassium channels located at the apical membrane that facilitate K^+ secretion in response to Na^+ ions entering the cell (**Figure 1.2**).

Discovery of amiloride, a new tool to use in studies of Na^+ transport

The two-membrane model explained the distinct properties of the apical and basolateral membrane that cause the two membrane voltages (V_o and V_i) to make up the transepithelial voltage (**Figure 1.2**). However, the underlying molecular mechanism behind the Na^+ permeable membrane (apical) and K^+ permeable membrane (basolateral) creating this asymmetric voltage difference was not yet determined. The discovery of the potassium-sparing diuretic amiloride in the late 1960s provided a vital tool for the study of transepithelial Na^+ transport[18-20]. In the 1950s and 1960s, the urinary bladder extracted from toads became another popular epithelium used in studies of Na^+ transport. In fact, the urinary bladder was the first tissue where aldosterone, a key hormone involved in regulation of salt and water homeostasis in the kidney and the colon, was shown to stimulate transport of Na^+ ions[21]. Studies revealed that a small molecule, named amiloride, was a potent inhibitor of Na^+ transport across the toad bladder epithelium [22]. Multiple investigations were then carried out in frog skin and toad urinary bladder to provide the evidence that amiloride only affected the transepithelial Na^+ transport from the apical side of the epithelium, without affecting ion transport on the basolateral side[23-25]. The model that amiloride specifically targets a Na^+-selective receptor was proposed by Lindeman and Van Driessche through voltage-clamp current noise analysis[26]. In the same study, the Na^+ receptor inhibited by amiloride, was shown to be a pore whose Na^+ influx could be saturated upon increased Na^+ concentration. Additional studies on amiloride concluded that only the

monovalent cationic form of amiloride was active[27,28]. Two analogs of amiloride, phenamil and benzamil, were found to be more potent, and were used in several future studies (**Figure 1.3**)[20].

Radioligand binding assays of the amiloride-binding protein

Beginning in the 1980s, different groups utilized radioactive and photoreactive amiloride analogs (mainly tritiated phenamil, benzamil and 6-bromomethylamiloride) in attempts to identify and extract the so-called amiloride-binding protein that had been identified in epithelial cell tissue[29-40]. Short-circuit current studies and patch clamp physiology of native epithelial cells had identified a Na^+-selective ion channel that was referred to as the epithelial Na^+ channel, believed to be the amiloride-binding protein. All studies reported high affinity binding when using an amiloride analog as a marker, which mirrored the results from electrophysiology patch clamp experiments. However, attempts to identify the molecular composition of the amiloride-binding protein were inconclusive. As noted in a review by Garty and Palmer [41], an amiloride-binding protein was purified from bovine kidney papilla and A6 cells by amiloride affinity purification[37-40]. The purified protein could be reconstituted in a lipid bilayer and was blocked by amiloride, suggesting this protein was a functional receptor[42-44]. However, the measured conductance and ion selectivity of the reconstituted amiloride-binding protein did not agree with patch clamp experiments of native amiloride-sensitive Na^+ channels in rat cortical collecting tubule (CCT) or A6 cells from amphibian kidney[45,46].

In a handful of other studies, the use of radiolabeled phenamil revealed the difficulty of isolating ENaCs and identifying the amiloride-binding protein as the Na^+ selective protein in kidneys. A phenamil-binding receptor (which was assumed to be the same as the amiloride-binding protein) was purified from pig kidney membranes[32-35]. The same purification strategy was applied to human kidneys to extract the putative amiloride-binding protein and isolate the

cDNA[36]. However, the resulting protein from this purification strategy was found to be a cytoplasmic enzyme, deamine oxidase, that binds phenamil at a similar affinity as ENaCs[47].

First cloning of ENaC genes

Although determination of Na^+ flux through a Na^+-selective channel across vesicular membranes, together with evidence of selective inhibition by amiloride and analogs indicated the presence of ENaC at the apical membrane, attempts to isolate and identify this channel proved challenging[32,37]. Incomplete optimization of the purification strategies, discussed above, along with uncertainty pertaining to the molecular composition of ENaC, likely contributed to misleading conclusions and interpretation of these results. Nevertheless, a decade later the three subunits needed to form a functional ENaC were identified, which changed the field of Na^+ transport. The α, β and γ subunits were first isolated and cloned from rat colon, by Canessa and colleagues, who demonstrated large amiloride-sensitive Na^+ currents when all three subunits were co-expressed in *Xenopus laevis* oocytes[2,3]. The biophysical properties of these currents were in close agreement with previous studies of ENaC from native tissue[46]. Following the elucidation of the molecular composition of ENaC, the field of Na^+ transport focused on identifying expression patterns of ENaC in different tissues, as well as attempting to define the receptor's molecular architecture to help identify physiological and cellular roles.

Biophysical and pharmacological properties of ENaC

ENaCs are pore-forming channels that are selectively permeable to small cations like Na^+, Li^+, and H^+[48]. Larger cations such as K^+, Cs^+ and Rb^+ are impermeable, which suggest that ENaCs distinguish ions based off of size, such that only a completely dehydrated ion can pass through the receptor's open pore. The total rate of Na^+ diffusion through ENaC channels depends

on both the open probability (P_o) of ENaC and the surface density of ENaC channels. Separating the effects of ENaC's complex regulatory pathway from its intrinsic properties as a channel have complicated studies of the channel's biophysical properties. For instance, ENaC's gating mechanism and its effect on P_o are unknown, and multiple different receptor structural states, each with its own unique P_o, may coexist at the surface membrane at one time.

Ion selectivity, conductance and gating kinetics

One of the unique characteristics of ENaC is the unusually high selectivity for Na^+ ions over K^+ ions. It has been demonstrated that ENaC's selectivity for Na^+ is 100:1 (Na^+:K^+), and has been speculated to reach as high as 1000:1[48,49]. The selectivity for Li^+ over K^+ is even higher than for Na^+, being in the range of 1.2 – 2 times that of Na^+ (depending on the ortholog of ENaC)[48,50-52]. Functional studies pertaining to ENaC selectivity were derived from electrophysiological studies in frog skin and rat cortical collecting ducts (CCDs), and recombinantly expressed rat ENaC channels confirmed these selectivities[3].

Palmer and Frindt identified ENaC as a low-conductance channel by patch-clamp experiments from epithelial cells in rat CCD[45]. Conductance can range between as low as 2 pS for some ion channels[53], and as high as 80 pS for others[54]. Palmer and Frindt reported that under physiological Na^+ concentrations, the single-channel conductance for ENaC is around 5 pS[45]. For Li^+ ions, the measured single-channel conductance is around 8 pS, which further emphasized the selectivity for Li^+ ions[45]. Similar conductance values were found for the recombinantly expressed rat ENaC[3].

Following the identification of ENaC in rat CCD, Palmer and Frindt explored whether ENaCs are dependent on ion concentration or voltage, as earlier studies indicated that Na^+ transport can saturate when luminal Na^+ concentration is increased[55]. They observed that altering

Na^+ and Li^+ concentration modulated conductance properties with half-saturation values of 20 mM and 50 mM for Na^+ and Li^+, respectively, suggesting that Na^+ binds to specific sites within the channel pore, and at high Na^+ concentrations, the transport through the pore is dependent upon the dissociation of the Na^+ ion. Altering membrane voltage did not affect ion channel conductance, but only affected the P_o of ENaC.

ENaCs expressed at the plasma membrane spontaneously transition between open and closed conformations with an overall P_o of ~ 0.5[56]. Gating movements have been reported to be slow, with open and closed times that ranges between 0.5 - 5s from ENaCs expressed in native tissue and in heterologous cells[3,45,57]. Patch clamp studies have demonstrated that the gating kinetics of ENaC can vary dramatically from patch to patch, suggesting that even patches from the same type of tissue can have significant variation. Although the number of distinct gating modes of ENaC have been difficult to determine, based on single-channel recordings there is clear evidence that ENaCs have at least two distinct states with different P_o values[46,56]. In a study with an average P_o of 0.5, the distribution of spontaneous P_o values was reported to be either > 0.7 or < 0.3, with very few individual values having a P_o value of 0.5, suggesting that ENaCs occupies either a low or a high P_o state. The molecular mechanism governing the different P_o states is currently not known.

ENaCs are known to be voltage independent. The studies detailing current-voltage relationships reveal these channels comply with the constant-field equation, demonstrating only a mild dependence of P_o on voltage[55,56]. In response to hyperpolarization, Palmer and Frindt observed that the P_o of ENaC increased in an all or none effect. This is an opposite effect to that of other excitable Na^+ channels, where upon hyperpolarization the P_o is close to 0. The reason for this is not known.

Amiloride and analogs and their effect on ENaC

Inhibition of channel activity by amiloride, a potassium-sparing diuretic that was developed in the 1960s, is one of the defining characteristics of the ENaC/DEG family of ion channels. Amiloride is a small-molecule that has a pyrazine ring attached to a carbonyl guanidinium at position 2 (**Figure 1.3**). Additionally, two amino groups are attached at position 3 and 5, and a chloride group at position 6[20].

Sub-micromolar concentrations of amiloride are required for ENaC channel inhibition (IC50 of 0.1 – 1 μM). The affinity of amiloride is dependent upon the transmembrane voltage, extracellular pH and extracellular Na^+ concentration[20], and is increased both under hyperpolarizing conditions and when amiloride is protonated (guanidinium pKa 8.7), suggesting that the binding site is located within the pore. Negative membrane voltage partially drives positively charged amiloride within the pore, inhibiting Na^+ flux. Schild and colleagues identified amino acids in mouse ENaC that are important for binding of amiloride, and these amino acids are all located within the pore (αSer556, βGly527, and γGly536 in human ENaC)[58]. However, other groups have suggested that amiloride may also have a secondary binding site in the extracellular domain (ECD) of ENaC[59-61]. For example, Baconguis and colleagues, solved a high-resolution structure of amiloride bound in the ECD of the acid-sensing ion channel (ASIC)[62]. In this crystal structure of ASIC, amiloride interacted at sites within fenestrations near the pore, and also in areas of ASIC ECD that are involved in proton sensing and gating.

Multiple studies have reported that the on and off binding rates of amiloride is ~10–30 $\mu M^{-1}\ s^{-1}$ and ~2–5 s^{-1}, respectively. All kinetic studies are in fairly good agreement, as discussed in a review by Garty and Palmer[41]. These binding rates, however, can easily be altered by slight modifications of the structural elements in amiloride. Benzamil and phenamil are two analogs of

amiloride that contains an addition of a benzyl and phenyl group to the guanidium group of amiloride, respectively (**Figure 1.3**). The addition of a hydrophobic functional group stabilizes the bound state of both phenamil and benzamil, resulting in higher affinities than amiloride with slower off rates[63].

Factors that regulate ENaC activity

The regulation of ENaC activity can be divided into two distinct groups. The first group involves factors that regulate ENaC either directly via interactions, like ions and lipids, or indirectly, like hormones, which regulate ENaC by up- or down-regulation of ENaC-interacting proteins. The second group involves post-translational modifications that are crucial for the P_o and density of ENaCs at the plasma membrane. These post-translational modifications include phosphorylation, palmitoylation, glycosylation, proteolytic cleavage and ubiquitination.

Regulation by Na^+ ions – Na^+ self-inhibition and Na^+ feedback inhibition

ENaC activity is regulated by Na^+ via two distinct mechanisms, Na^+ self-inhibition and Na^+ feedback-inhibition. Na^+ self-inhibition happens acutely and refers to a rapid decrease in ENaC current after extracellular Na^+ concentration increases. Na^+ feedback-inhibition, on the other hand, results from increased intracellular Na^+, and happens over a slower time course (minutes to hours). While Na^+ self-inhibition is believed to be caused by Na^+ ions binding in the ENaC ECD to reduce P_o[64-66], Na^+ feedback-inhibition activates a signaling pathway to reduce the number of ENaC localized at the membrane[67,68].

ENaC Na^+ self-inhibition was first described in 1977, and led to numerous studies detailing a variation in the P_o as a result of Na^+ ions[69]. Na^+ self-inhibition occurs when the extracellular Na^+ concentration changes from low (~ 1 mM) to high (> 100 mM), causing a rapid initial peak current that reduces to a steady state current within seconds. This observation is

explained by ENaC receptors initially occupying a high P_o state that upon Na^+ binding, subsequently undergoes a conformational change that shifts its pore to a lower P_o state[66]. The effect of Na^+ self-inhibition is blunted when ENaC is cleaved by proteases, suggesting that proteolytic cleavage relieves the regulatory effect of Na^+ ions[66]. Amino acid mutagenesis of ENaC have identified regions in the ECD that are important in Na^+ self-inhibition[70]. One challenge is to distinguish whether these sites directly participate in Na^+ binding or through allosteric interactions. Reports of single amino acid mutations have also been described in which the P_o of ENaC is increased and Na^+ self-inhibition is then abolished[71]. However, a complete understanding of Na^+ self-inhibition remains unsolved, particularly when assessing the contribution of each ENaC subunit to the modulation of ENaC P_o.

Na^+ feedback-inhibition is an effect that was explained by MacRobbie and Ussing as early as 1961 through studies on frog skin epithelia[72]. They discovered that the epithelial cells did not swell when blocking the Na^+/K^+-ATPase (thereby preventing Na^+ from being transported out of the cell). This phenomenon was later named Na^+ feedback-inhibition, and shown to result in a decrease in both the number of ENaCs at the plasma membrane and of their P_o[67,68,73,74]. The reduction of ENaCs at the cell surface is due to internalization of ENaCs, mediated via Nedd4 (Nedd4-2, also known as Nedd4L, in human, mouse, and rat), and is the primary mechanism to reduce ENaC activity in response to increased intracellular Na^+ [75]. Reduction of ENaC P_o is due to reduced proteolytic activation as a result of increased intracellular Na^+ [76].

Regulation by other ions

Multiple other ions regulate ENaC activity. Although most studies have focused on Na^+ ions and sites within ENaC that are affected by Na^+ modulation, other studies have shown that divalent cations including Ni^{2+} and Zn^{2+} also have an impact on ENaC activity[77,78]. Monovalent

cations like Li^+ do not exhibit as strong of a self-inhibition effect as Na^+ does. However, H^+ ions have been shown to reduce ENaC Na^+ self-inhibition with a pH_{50} of 7.2, meaning that acidic pH augments ENaC currents[79]. A potential explanation for this increase in current is that H^+ ions contribute to the overall current by passing through the pore. This explanation seems unlikely though, since the modulatory effect of H^+ is abolished when the ENaC P_o is increased either via the common DEG mutation or due to proteolytic processing. It is therefore more likely that H^+ ions alter channel gating properties in a yet to be defined mechanism. Work done by the same group also showed that Cl^- has an inhibitory effect on ENaC[80]. Similar to H^+ regulation, the effect was abolished when the ENaC P_o was increased by the other mechanisms mentioned above.

Regulation by lipids

Phosphatidylinositols are a family of lipids which participate in different signaling pathways within cells. Phosphatidylinositol 4,5-biphosphate (PIP_2) and phosphatidylinositol 3,4,5-triphosphate (PIP_3) have both been shown to activate ENaC[81,82]. Putative PIP_2 and PIP_3 binding sites are found on the intracellular N-terminus of ENaC β and γ subunits, which contain multiple charged residues[83,84]. The β and γ subunits have also been shown to bind strongly to phosphatidic acid, which is a degradation product of phosphatidylinositol lipids. A recent study showed that this degradation product inhibited ENaC activity[85], suggesting that the anionic nature of PIP2 and PIP3 are important for binding and activation of ENaC.

Modulation by PIP_2 and PIP_3 molecules requires sequestration in order to increase local concentrations of lipid to levels that can affect channel activity, as PIP_2 constitutes less than 1 in 1,000 membrane lipid molecules[86]. One protein that associates with PIP_2 (and other anionic lipids) is Myristoylated Alanine-rich C-Kinase Substrate (MARCKS), which is expressed in

sodium-transporting epithelium[87]. Additionally, studies have co-immunoprecipitated ENaC β subunit with MARCKS antibody. It has been suggested that MARCKS is part of a regulatory mechanism which delivers PIP_2 to ENaC for activation[82]. This theory proposes that phosphorylation of MARCKS by protein kinase C (PKC) reduces membrane association of MARCKS, disrupting PIP_2 association with ENaC, and thereby reducing ENaC activity. This theory was supported in a recent study where PKC-α knockout mice had increased ENaC P_o and increased blood pressure in comparison to wild type[88].

Regulation by hormones

The hormonal regulation of ENaC activity is important, especially as it relates to blood volume regulation where ENaC plays a crucial role. Although the vast majority of studies on ENaC regulation by hormones are done in the context of the kidney or colon, the mechanisms underlying modulation of ENaC activity within these pathways is not fully understood. A more thorough discussion regarding the important hormones that regulate ENaC in the kidney will be discussed in the subsection of "The role of ENaC in humans".

Post-translational modifications

Post-translational modification is important not only in cell signaling, but also for protein maturation. ENaCs undergo multiple post-translational modifications, resulting in increased or decreased activity by altering P_o or surface density or both. The next section will give an overview of the multiple post-translational modifications affecting ENaCs.

Proteases: Proteolytic processing is one of the defining characteristics of ENaC gating. Multiple studies, mostly in vitro, have discussed how this unique mechanism increases the P_o of ENaCs and relieves Na^+ self-inhibition. Only the α and γ subunits are cleaved at distinct

extracellular sites to releases embedded inhibitory peptides[89,90], the release of which shifts ENaC from a low to a high P_o state, without affecting single-channel conductance or ion-selectivity[91,92].

The first hint of ENaC being regulated by proteases was presented as early as 1980 when the application of a protease inhibitor (aprotinin) reduced short-circuit current in isolated urinary toad bladder[93]. In 1997, Vallet and colleagues provided the first evidence of ENaC being activated by a serine protease, which they named channel-activating protease 1 (CAP1)[94]. CAP1 was discovered by screening the DNA library of a *Xenopus* kidney epithelial cell line (A6) for a functional complementation assay. Co-expression of CAP1 with rat ENaC in *Xenopus laevis* oocytes increased amiloride-sensitive currents by threefold, and CAP1 was found to be expressed in kidney, gut, lung and skin. The human ortholog of CAP1 is prostasin, and both proteases contain a glycosylphosphatidyl-inositol (GPI) domain that anchors it to the membrane, likely facilitating association with membrane-embedded ENaCs. Shortly after the identification of CAP1, the mouse ortholog was cloned, and two additional membrane-bound serine proteases, named CAP2 and CAP3 were identified and also shown to amplify ENaC-mediated currents.

Since then, a number of proteases have been shown to cleave ENaC, including furin, a trans-Golgi resident member of the proprotein convertase family of serine proteases[70,95]. Protease sites identified in the α and γ subunits (human α[175]RSRR, α[201]RRAR, γ[135]RKRR) were found to be specific to furin[95,96], and mutations introduced at the defined furin sites prevented proteolytic processing and channel activation. Additionally, one site downstream of the proposed cleavage site of furin in the γ subunit was identified as a CAP1 and prostasin site (γ[178]RKRK). Mutation of this site abolished activation of ENaC by CAP1[90,97]. Cleavage at both furin sites in the α subunit causes a release of a 26-residue peptide that has been shown to increase ENaC P_o. A short 8-mer peptide (α [184]LPHPLQRL) within this 26-residue peptide was identified to

inhibit ENaC channels[98]. Similarly, in the γ subunit, if the putative furin and prostasin sites are cleaved, a 43-residue peptide is released. Studies have identified an 11-mer peptide (γ[153]RFSHRIPLLIF) within this 43-residue tract that retains inhibitory effects of ENaCs[99]. Release of both inhibitory peptides causes an increase in ENaC P_o. Interestingly, the release of the γ subunit inhibitory peptide is dominant in channel activation, shifting the P_o of ENaC close to 1, independent of cleavage α subunit inhibitory peptide[97].

Although multiple studies have identified proteases that cleave and activate ENaC, the mechanism by which these proteases activate the channel is still largely debated. Most studies have utilized heterologous expression systems, whereas the role of the same protease regulation *in vivo* has not been investigated. CAP1 is one of few proteases that have been shown to be a physiological regulator of ENaC[100,101]; however, its action on ENaC has not been established. Catalytically-incompetent CAP1 (with a mutated catalytic triad) can still activate ENaC as well as its wild type counterpart[102,103]. Altogether, serine proteases are undoubtedly important regulators for ENaC function, however, the exact mechanism and signaling pathway of protease regulation of ENaC remains to be determined.

Ubiquitination: Ubiquitination is one of the most important post-translational modifications for ENaC cell surface stability. All three ENaC subunits, α, β, and γ harbor a PY motif (PPXY) at the C-terminus, which is the recognition motif of ENaC's main E3 ubiquitin ligase, Nedd4-2[104]. Nedd4-2 is a member of the Nedd4 (Neural precursor cell-expressed developmentally downregulated 4) family of HECT ligases. The Nedd4 family of ligases is important in the regulation of many membrane proteins, and ubiquitination of ENaC by Nedd4-2 is known to greatly reduce surface density of ENaC channels[105,106]. Nedd4-2 comprises a C2 domain, four WW domains and a ubiquitin ligase HECT domain. The C2 domain is responsible

for calcium-dependent membrane binding and subcellular localization, the WW domains binds to the PY motifs of ENaC subunits, and the HECT domain is the catalytic domain. Nedd4-2 ubiquitinates ENaC on N-terminal lysine residues of the α and γ subunits.

Liddle syndrome is a clear demonstration of the importance of ubiquitination in regulating ENaC activity. The vast majority of mutations reported in Liddle syndrome are due to missense, nonsense, and frame shift mutations that cause loss or disruption of the PY motifs in the β or γ subunits, thereby removing the ability of Nedd4-2 to bind and ubiquitinate ENaC[107,108]. Disruption of ENaC-Nedd4-2 binding causes more ENaCs to remain at the cell surface and reabsorb more Na^+ ions, which is one of the main regulatory mechanisms in response to low blood volume[109]. Specifically, phosphorylation of Nedd4-2 disrupts the ENaC-Nedd4-2 interaction, preventing internalization of ENaCs. As a result, ENaCs remain at the luminal membrane in the kidney and more Na^+ ions are reabsorbed, increasing blood volume and pressure increase.

Glycosylation: N-glycans are important for proper folding of proteins by permitting interaction of ER folding chaperones like Calnexin and Calreticulin, as well as facilitating membrane proteins to exit the endoplasmic reticulum (ER). Most membrane proteins, including ENaC, undergo N-linked glycosylation and maturation from a high mannose to a complex glycan during transit through the Golgi network [3,110-112]. Human ENaC has multiple predicted N-linked glycosylated sites, five in the α subunit (N232, N293, N312, N397, N511), eleven in the β subunit (N135, N141, N146, N199, N207, N260, N364, N378, N449, N484), and five in the γ subunit (N209, N248, N271, N291, N497). The exact role for all of these glycosylation sites is not known, although some are likely to participate in proper folding, maturation and trafficking. Some studies have suggested that there appears to be two distinct pools of ENaC receptors at the

plasma membrane. One pool is ENaCs that contain immature N-glycans (high mannose) with uncleaved α and γ subunits, while the second pool contains ENaCs with complex N-glycans and cleaved α and γ subunits[96,113], suggesting that perhaps glycosylation plays an important role for recognition of proteolytic processing. However, a clear link between ENaC glycosylation state and proteolytical processing has not been established.

Palmitoylation: Cys-palmitoylation is a reversible event where palmitate is attached to a cytoplasmic cysteine (cys) residue. Palmitoylation sites have been found in mouse ENaC: two in the β subunit (C43, C557)[114], and two in the γ subunit (C33, C41)[115]. Both studies concluded that knockout of one or both palmitoylation sites within each subunit caused a reduction in ENaC P_o and enhanced Na^+ self-inhibition. This effect is more dominant in the γ subunit than the β subunit, when compared to wild type[115]. Five of a total 23 palmitoyltransferases (DHHCs) increased ENaC activity when co-expressed in *Xenopus laevis* oocytes[116]. However, the physiological role the DHHCs have on modulating ENaC function *in vivo* is not known, as it has not been determined whether DHHCs regulate ENaC channel function by directly palmitoylating ENaC itself, or through palmitoylation of other ENaC-interacting proteins.

Phosphorylation: There are multiple kinases that are known to regulate ENaC either directly or indirectly. Many of the kinases that regulate ENaC directly primarily target the C-terminus of the ENaC β and γ subunits, two of which include ERK2 (extracellular signal-regulated kinase 2) and casein kinase 2. Both phosphorylation events directly lead to internalization of ENaCs mediated by Nedd4-2[117,118]. Another kinase that has been shown to phosphorylate the ENaC β subunit is GRK2 (G protein-coupled receptor kinase 2)[119,120]. Phosphorylation of the β subunit disrupts the ENaC-Nedd4-2 interaction, preventing ENaC

recycling and internalization[120]. Sgk1, a kinase that is upregulated by the hormone aldosterone phosphorylates Nedd4-2, also preventing the internalization of ENaCs by disrupting the interaction between Nedd4-2 and ENaCs. However, Sgk1 can also directly phosphorylate the α subunit of ENaCs to stimulate ENaC activity[121]. Phosphorylation by PKC has been shown to downregulate ENaC activity[122,123]. This regulation is indirect, as PKC phosphorylates MARCKS proteins to prevent membrane localization and activation of ENaC by phosphatidylinositol.

Although there is a lot of data confirming ENaC phosphorylation by kinases, the exact mechanism and physiological contexts of these events are poorly understood.

The role of ENaC in humans

ENaCs role in the kidney

ENaCs are primarily known for their role in the kidneys, where they serve as the rate-limiting step for Na^+ reabsorption. On average, a single human kidney filters 180 L of blood through the glomerulus per day (**Figure 1.4**). The glomerulus is a crucial component of the nephron, which removes waste products from the body. Each human kidney has approximately 1,000,000 nephrons, with 11-12 nephrons connecting via one collecting duct (CD) leading fluid to a centralized area called the renal pelvis. Fluid then exits the renal pelvis, and flows through tubes called the ureter into the urinary bladder (**Figure 1.4**)[124]. Approximately 90% of the filtrate is reabsorbed in the proximal convoluted tubule and in the loop of Henle. Of the remaining fluid that exits the loop of Henle, 9% is reabsorbed in the distal nephron, made up of the distal convoluted tubule (DCT), connecting tubule (CT) and CD[125]. For example, a healthy adult that

intakes on average of 2 L/day will release a final urine volume, and after filtration and reabsorption, between 0.8 – 2 L.

In the kidneys, ENaCs are expressed in the aldosterone-sensitive distal nephron (ASDN). Thus, ENaCs reabsorb Na^+ ions from the final 9% of fluid remaining after the proximal convoluted tubule (**Figure 1.4**, purple region illustrates the ASDN in the nephron). Aldosterone is the main mineralocorticoid hormone that binds to the mineralocorticoid receptor (MR), and is the key hormone responsible for maintaining salt and water balance[126]. There are two main pathways of Na^+ reabsorption that occur in the ASDN. One is via the electroneutral thiazide-sensitive Na^+:Cl^- cotransporter (NCC) that reabsorbs Na^+ and Cl^- ions, and is expressed in the DCT only. The second is via ENaCs which, in synergy with the renal outer medullary potassium channel (ROMK), reabsorb Na^+ ions and secrete K^+ ions, respectively. ENaCs are expressed in the late section of the DCT (referred to as DCT2), CT and CD (**Figure 1.4**)[125,127]. Both the NCCs and ENaCs are important for regulating blood volume; however, comparing gain-of-function and loss-of-function mutations distinguishes the respective roles of each receptor in the distal nephron. For example, loss-of-function of NCCs results in hypotension (low blood pressure) and hypokalemia (low levels of K^+ in the blood). In response to this form of NCC dysregulation, in the early DCT (where ENaC expression is low), more Na^+ ions are delivered to the DCT2 (where ENaC expression is high). ENaC reabsorbs more Na^+, leading to more K^+ secretion by the ROMK channel. Loss-of-function mutations in ENaC causes hypotension and hyperkalemia (high levels of K^+ in the blood) due to diminished reabsorption of Na^+ ions and diminished secretion of K^+ ions by ROMK. NCC gain-of-function mutations results in hypertension (high blood pressure), and hyperkalemia. Hyperkalemia occurs because overactive NCC causes a reduction in Na^+ delivered to the DCT2, resulting in less Na^+ reabsorption by ENaC, followed by

a reduction in K^+ secretion by ROMK. Gain-of-function mutations of ENaCs result in hypertension and hypokalemia from increased Na^+ reabsorption, and thereby increased K^+ secretion.

The aldosterone paradox emphasizes how aldosterone can respond to two different physiological conditions, hypovolemia (low blood volume) and hyperkalemia[128]. The physiological response to aldosterone under conditions of hyperkalemia causes increased K^+ secretion without changing the rate of Na^+ reabsorption, while the response to aldosterone under conditions of hypovolemia causes increased Na^+ reabsorption with minimal K^+ secretion. This paradox clearly indicates that regulation of salt and water homeostasis in relation to blood volume is more complex than aldosterone solely mediating ENaC functionality. This is in part because aldosterone is activated by the renin-angiontensin-aldosterone system (RAAS) signaling pathway that only responds to hypovolemia, where angiotensin II is the hormone that stimulates the release of aldosterone[128]. Additionally, aldosterone is activated in response to hyperkalemia, while the RAAS pathway is not, suggesting that aldosterone in the presence with angiotensin II responds to hypovolemia, while aldosterone alone (or in combination with other signals) responds to hyperkalemia. Although a significant amount is known, the understanding of the aldosterone signaling pathway and its regulation of ENaC activity is incomplete.

The unique functions of NCC and ENaC in addition to their locations in the distal nephron offer an explanation as to how hormonal regulation in response to either hyperkalemia or hypovolemia can be separated such that one physiological event can be corrected while the other remains unaffected. The next few paragraphs will discuss some of the hormones that have been shown to regulate ENaC activity, either on a transcriptional level or by upregulating proteins that interact with ENaC.

Aldosterone: Aldosterone is the major regulator of ENaC in the kidneys, and studies have shown that aldosterone upregulates the synthesis of the α subunit in the kidney, but not the β and γ subunits[129]. The increased synthesis of the ENaC α subunit correlates with an increase in cleaved α and γ subunits at the plasma membrane[130]. However, the aldosterone-induced increase of the α subunit does not fully contribute to the increase in net Na^+ reabsorption, suggesting that other processes are needed for upregulation of ENaC[131]. Aldosterone also upregulates serum glucocorticoid regulated kinase 1 (sgk1), which phosphorylates Nedd4-2, thereby preventing the interaction between ENaC and Nedd4-2. This reduces ubiquitination of ENaC and increases ENaC density at the plasma membrane, which in turn, causes more Na^+ ions to be reabsorbed in order to increase blood volume and blood pressure[109,132]. Additionally, it has become clear in the last decade that the effect of aldosterone on ENaC activity depends on where ENaC is expressed. Even though all segments of the distal nephron where ENaC is expressed also co-express the mineralocorticoid receptor, recent studies have shown that constitutively active ENaC is found in DCT2 and early CT regardless of aldosterone levels[133]. ENaC activity in the late CT and cortical collecting duct (CCD), on the other hand, is dependent on aldosterone (**Figure 1.4**). This finding suggests that other hormones are involved in regulation of ENaC activity in the DCT2 and CT, segments which are more important for maintaining K^+ and Na^+ homeostasis[133].

Angiotensin II: Angiotensin II is a hormone that is commonly known to activate aldosterone; however, the role of Angiotensin II in the regulation of ENaC activity is not well understood. Two studies in 2012 determined that angiotensin II acutely augments ENaCs P_o[134,135]. The stimulatory effect on ENaC was abolished in the presence of losartan, an inhibitor of the angiotensin II receptor type 1 (AT1 receptor), which suggests that ENaC activity is increased via the AT1 receptor pathway. The with-no-lysine (K) kinase 4 (WNK4) is currently

believed to be the kinase responsible for the acute increase in ENaC activity upon angiotensin II stimulation[125], but the mechanism behind the increased ENaC activity is not understood. The current hypothesis is that WNK4 inhibits ENaC activity independent of its kinase activity and independent of Nedd4-2 mediated ubiquitination[136,137].

Vasopressin: Vasopressin (arginine vasopressin, AVP) is a hormone that controls plasma osmolality by modulating aquaporin 2 channel (AQP2) expression. AVP also upregulates ENaC via the vasopressin receptor type 2 (V2R) signaling pathway[138]. This pathway is mediated via cAMP to activate protein kinase A (PKA), that similarly to Sgk1, phosphorylates Nedd4-2 to prevent its interaction with and ubiquitination of ENaC[139]. Aldosterone and vasopressin have a synergistic relationship, where aldosterone protects Na^+ balance and vasopressin promotes reabsorption of water, both of which are dependent on Na^+ reabsorption[140]. A study by Mironova and colleagues demonstrated that ENaC activity is robust in adrenalectomized mice (the adrenal gland which excretes aldosterone has been removed), and observed that levels of vasopressin were increased due to the absence of aldosterone to maintain ENaC activity[138]. This clearly demonstrates that vasopressin regulates ENaC activity through a mechanism independent of aldosterone regulation, and the mechanism of ENaC activity contributes to water conservation, rather than Na^+ balance.

Lastly, a number of other hormones have been shown to regulate ENaC activity. Studies have demonstrated that ENaC is upregulated in response to insulin, suggesting a potential role in regulation of blood pressure through ENaCs[141-143]. ENaC upregulation by insulin does not appear to be acute[144], but the mechanism detailing the exact role of insulin remains unknown. Finally, hormones that reduce ENaC activity include bradykinin (BK), endothelin 1 (ET-1), and the epidermal growth factor (EGF), all summarized in the recent review by Rossier[125].

Region-specific expression patterns of ENaCs

ENaC is expressed in a wide array of different tissues throughout the body, and ENaC expression in the kidney, the colon and the lung are examples where a clear functional role has been established. Other tissues expressing ENaC, including the salivary gland, lingual epithelium, the skin, endothelia, heart, eye, brain and vascular smooth muscle are understudied[8]. In the following sections, the well-established role of ENaC in the lungs and colons will be discussed.

Lung: ENaCs are important for regulating airway surface liquid (ASL) level and mucociliary clearance in the lungs. Movement of Na^+ ions across the airway epithelium via ENaCs is coupled to the secretion of Cl^- ions via the cystic fibrosis transmembrane regulator (CFTR). This balance between Na^+ and Cl^- transport is important in maintaining a proper thickness and viscosity of the ASL. The importance of ENaCs in the lung was established through knockout studies in mice done by Hummler and colleagues where knockout of the ENaC α-subunit led to the failure of liquid clearance in the lungs, and mediated death within 40 hours after birth[145]. Similarly, overexpression of ENaCs has been shown to cause a phenotype that is similar to cystic fibrosis (CF)[146]. ENaC and its role in CF-like symptoms will be discussed in the section "ENaC and human diseases".

Colon: ENaC is mainly expressed in the distal part of the colon where it serves a role in regulating the reabsorption of Na^+ ions. The majority of Na^+ reabsorption happens earlier in the gut by electroneutral transporters, while the final reabsorption happens in the distal colon. Similarly to its regulation in the kidney, ENaC is controlled by aldosterone and dexamethasone (another hormone that regulates transcription of ENaC subunits). However, in the kidney, aldosterone and dexamethasone upregulate the synthesis of the α subunit, while in the colon,

both hormones upregulate the synthesis of β and γ subunits. Studies on mice with ENaC α knockout in the colon resulted in a phenotype predicated on Na^+ loss and resistance to aldosterone, although this specific phenotype can be compensated by the RAAS system in the kidney[147]. The Na^+ reabsorption in the colon is therefore not as essential as Na^+ reabsorption in the kidney.

ENaC and human diseases

ENaC's greatest impact on human health is through its large effects on blood pressure and clearance of liquid in the lungs. Severe phenotypes are observed in both gain-of-function mutations, as seen in Liddle syndrome, and loss-of-function mutations, as seen in the neonatal salt waste disorder, Pseudohypoaldosteronism type 1 (PHA1). Although dysfunction of ENaC affects Na^+ and water balance in multiple tissues where ENaC is expressed, the main phenotypes are seen in the kidney and the lungs. The next section will describe Liddle syndrome and PHA1 that are disorders related to chronic high and low blood pressure, respectively. Finally, the relation of ENaC to cystic fibrosis will be discussed.

Liddle syndrome

Liddle syndrome is an autosomal dominant disorder that was described in 1963 by Liddle et al[148]. It is characterized by chronic hypertension with severe hypokalemia and metabolic alkalosis. The disorder resembles primary hyperaldosteronism (excessive release of aldosterone due to activation via the RAAS pathway), however, low levels of plasma aldosterone is a key characteristic indicating that the increased Na^+ reabsorption is not mediated by aldosterone, but rather by increased ENaC activity.

The molecular mechanism behind Liddle syndrome is well-established, where mutations in ENaC cause increased cell surface density and increased channel activity. Due to increased ENaC activity, more Na^+ is reabsorbed, leading to increased plasma volume, hypertension and hypokalemia. To date, less than 40 causative mutations have been reported and the vast majority of the reported mutations are due to mutations within the PPXY (PY) motif found in the C-termini of the β and γ subunits[149]. Mutation or deletion of the PY motif disrupts binding of Nedd4-2, blocking the Nedd4-2 mediated internalization of ENaC such that more ENaCs remain at the plasma membrane.

Pseudohypoaldosteronism type 1 (PHA1)

PHA1 was described for the first time in 1958 as a syndrome that caused salt wasting and unresponsiveness to aldosterone[150]. Patients with PHA1 experience salt loss from all tissues that are controlled by aldosterone, which includes the kidney, colon, sweat glands, and lungs[151].

Mutations that cause PHA1 have been found in all three ENaC subunits, leading to loss of function and decreased reabsorption of Na^+ ions[152-160]. One of the best-characterized mutations is the highly conserved His-Gly (HG) motif located on the intracellular N-terminus of all ENaC subunits (also found in all ENaC/DEG members). Mutation of this motif significantly reduces the P_o of ENaC[157], and the molecular mechanism for this is not known.

Cystic fibrosis (CF)

CF is a genetic disorder that is caused by mutations of the CFTR chloride channel, leading to reduction or complete loss of function of the CFTR, resulting in devastating phenotypes. As a result of these mutations in CFTR, the pulmonary mucus viscosity is increased, dramatically increasing the risk of bacterial infections in the lungs are therefore very high. Gradual lung failure is the major life limitation in patients with CF.

The CFTR, as mentioned, secretes Cl^- ions, and as a balance, ENaC reabsorbs Na^+ in airway epithelium to maintain a healthy airway surface liquid (ASL). The importance of ENaC as a regulator of ASL has been emphasized in ENaC α subunit knockout mice, which have increased early mortality due to failure to clear liquid from the lungs[145]. Although the exact role of ENaC in CF pathogenesis is not settled[161,162], it is known that CFTR negatively regulates ENaC. Dysfunction of the CFTR leads to increased ENaC activity, suggesting that ENaC hyperactivity contributes to the CF phenotype[163]. In addition, there are ENaC gain-of-function mutations associated with atypical CF[164,165].

Structural aspects of ENaC

The initial cloning of DEG and ENaC subunits, followed by the identification of other ENaC/DEG members boosted the research of these ion channels in the 1990s. This allowed groups to investigate the molecular aspects of ENaC/DEG channels to understand their unique functional and cellular roles. Early on, stoichiometry was a controversial topic. Although the components of ENaC were agreed upon (minimum one subunit each of α or δ, β, and γ), the proposed number of subunits composing a functional ENaC ion channel ranged from a total of three subunits up to nine subunits. As reflected in the early literature, most groups seemed to accept a stoichiometry of four subunits to form the fully functional channel: two α subunits and one each of β, and γ subunits. When the first structure of an ENaC/DEG member revealed a trimeric assembly in 2007, the field largely accepted the hypothesis that ENaC also is composed of three subunits[4]. However, other groups continued to question the stoichiometry and, as recently as 2016, still suggested ENaC forms a tetrameric assembly[166].

Molecular structures of ASIC

ASIC is the only member of the ENaG/DEG superfamily that has well-characterized structure-function relationships[4,62,167-171]. While the molecular mechanism behind the physiological role of ASIC in pain sensation and synaptic plasticity still remains ambiguous, the gating mechanism of ASIC is well understood. The channel is thought to cycle through three major functional states: ASICs remain in a closed state at high pH, and is activated by protons within milliseconds to change conformation to an ion-conducting state (the open state), and then rapidly undergo desensitization to a non-conducting state within tens to hundreds of milliseconds (the desensitized state).

The first structure of chicken ASIC1a (cASIC1a) was determined by x-ray crystallography at a resolution of 1.9Å in 2007[4]. This structure revealed that ASIC assembles as a homotrimer, and provided the first view of the molecular architecture of an ENaC/DEG ion channel. When folded, an ASIC protomer resembles a forearm with a hand clenching a ball. In this metaphor, the transmembrane domain (TMD) makes up the forearm, while the large extracellular domain (ECD) makes up the hand that is holding the ball. The ECD is further divided into six distinct domains that are named the palm, wrist, finger, thumb, knuckle and β-ball (**Figure 1.5a**). Surface analysis of the first ASIC structure revealed the pH sensor, which was named the "acidic pocket", and it was found to be located between the finger and the thumb domain (**Figure 1.5a**).

Although the first structure of ASIC was of a non-functional construct due to truncations of the N- and C-termini (ΔcASIC1a, residues 26-463 of cASIC), a structure of a fully functional receptor construct, called the minimal functional ASIC (ΔcASIC1$_{mfc}$, residues 2-466 of cASIC1a) published two years later, revealed the same architecture of a homotrimer[167]. Both

published structures had nearly identical models of the ECD and were presumed to be in a desensitized state, as both were crystallized in a low pH environment. Additionally, inspection of the structure revealed that within the “acidic pocket”, the acidic side chain pairs were closer to each other than expected at neutral pH, suggesting that they were protonated.

In the following years, multiple structures of cASIC were published in different functional states. Toxins that modify the gating of ASIC were used to capture an open “gating modified” state and an open state (PcTx1 and MitTx, respectively)[62,168,169]. The crystal structures revealed that both toxins bind in the acidic pocket to modulate the gating of ASICs. Following the crystal structures of ASIC-toxin complexes, the crystal structure of ΔcASIC and the cryo-EM structure of full-length (FL) cASIC in a resting, closed state at high pH, were determined[170]. The structures of ΔcASIC and FL-cASIC were nearly identical, confirming that truncation of ASIC did not cause artifacts within the TMD. The structure of ASIC in a closed, resting state provided the final piece of the structural framework to describe the complete gating cycle of the three distinct functional states cASIC1a occupies. Additionally, the structural results validated by functional studies in which cross-linking of engineered cysteine residues (chosen based on positions from the high-resolution structures) trapped ASIC in a closed or less-desensitized state[170].

The TMD of all published ASIC structures have revealed different TMD conformations, illustrating the sensitivity of this domain to conformational changes. However, the reasons for the apparent differences in TMD structure can easily be explained and are understood. What appears to be the correct conformation of ASIC TMD is a break in transmembrane helix 2 (TM2) midway through the membrane. The break in the TM2 α helix causes a domain swap, where a GAS belt (Gly-Ala-Ser) forms a horizontal extended structure that places the lower part of TM2

α helix (named TM2b) in continuation with the upper TM2 α helix (named TM2a) of the neighboring subunit (**Figure 1.5b**). Thus, each membrane-spanning transmembrane α-helix is comprised of residues from two different subunits. The GAS belt forms a constriction point with a pore radius of 3.6 Å in the ion permeation pathway, and this contributes to ion selectivity of a hydrated Na^+ ion (radius of hydrated Na^+ ion is 3.8 Å)[62].

The initial structures of the two desensitized states had significant differences within the TMD when compared to each other[4,167]. This is not surprising, however, given that one of the constructs is non-functional. The toxin-bound state of ASIC-PcTx1[168] also revealed a TMD conformation that differed in comparison to other ASIC TMDs (cASIC desensitized state[167], cASIC-MitTx open state[62], and cASIC closed state[170] all featured the break of TM2 and domain swap). Finally, the extraction of FL-ASIC from membranes using styrene-maleic acid (SMA) revealed a new motif within the TMD, an N-terminal re-entrant loop preceding transmembrane helix 1[172]. The cryo-EM structure of FL-ASIC extracted directly from membranes by SMA (and thus solved in a native lipid environment) confirmed the break of TM2 α helix and the domain swap. The re-entrant loop harbors the His-Gly (HG) motif that is highly conserved among ENaC/DEG family members, and is known to cause PHA1 when mutated in ENaC subunits[157], indicating its central importance in ASIC (and likely ENaC/DEG) ion permeation and selectivity. Altogether, structures of ASIC TMD underline the importance of the biochemical environment for ENaC/DEG TMD stability.

Differences and similarities between ENaC and ASICs

The overall sequence identity between ENaC and ASIC subunits ranges between 11-16%[8]. The palm domain and β-ball of ASICs and ENaCs share the highest sequence similarity, and represent a β strand-rich scaffold that forms the core of the ECD. The more peripheral

domains consist of the thumb, knuckle and finger domain, comprised mainly of α-helices and loops. The finger domain is the most divergent area by sequence comparison between ENaC and ASIC subunits. In ENaC subunits, a large sequence insertion is found in the finger domain that is absent from the ASIC sequence. This insertion contains the inhibitory tracts of the α and γ subunits, which are released by proteolytic processing[89,90]. The sequence differences in this region suggest that ENaC might have a unique domain fold contributing to its gating mechanism that is different from ASICs.

TM2 of both ENaC and ASICs shares a high sequence identity. Given the unique fold of cASIC TM2 that results in the break and domain swap of TM2, it is likely that ENaC TM2 folds in a similar manner. However, while the sequence identity is high, there are some interesting and likely important differences. Within the TM2 sequences, the amino acid identity at the selectivity filter differs significantly between ENaCs and ASIC. In ASIC, the GAS belt contributes to ion selectivity, while in ENaC the selectivity filter differs in each subunit from the common G/S-X-S (αGSS, βGGS, γSCS). The unique sequence differences in ENaC subunits is likely to give rise to structural differences that causes its high selectivity for Na^+ in ENaC.

The HG motif is highly conserved within the ENaC/DEG family, and when mutated in ENaCs, causes a reduced P_o (as observed in PHA1). The recent discovery of the ASIC N-terminal re-entrant loop that harbors the highly conserved HG motif suggests that ENaC might have a similar architecture in this region.

Significance and approach

Hypertension is arguably the single most important risk factor for the development of cardiovascular disease and stroke, and it has been shown that treatment of hypertension can reduce that risk[173,174]. ENaC is a key protein that regulates blood pressure and its direct role has been illustrated in gain-of-function mutations that result in hypertension (Liddle syndrome) as well as loss-of-function mutations that result in severe hypotension and salt wasting (PHA1). Statistics reported from the American Heart Association show that 33% of US adults >20 years of age have hypertension, and African American adults have among the highest prevalence in the world at 44%[175,176]. Polymorphisms have been identified in ENaCs, and these variants are more common in black individuals, suggesting an explanation for the higher prevalence of low-renin hypertension seen in this cohort[177].

Thiazide diuretics are among the most prescribed anti-hypertensive drugs, and are often combined with other antihypertensive drugs[178]. While amiloride is the preferred treatment for individuals of Liddle syndrome, it is not widely used clinically due to fear of hyperkalemia. The K^+ secretion coupled to ENaC-mediated Na^+ reabsorption is the main secretory pathway for K^+ secretion in the kidney. Thus, under a standard K^+ diet, blocking Na^+ reabsorption with amiloride to reduce blood pressure might contribute to increased concentrations of plasma K^+. Due to the fear of the amiloride-induced hyperkalemia, clinical studies that have tested the efficacy of amiloride for the treatment of hypertension have only used the drug at low concentrations, which in turn have not shown any significance in lowering blood pressure[179].

The development of novel diuretics would ideally have a synergistic effect to block both ENaC and the thiazide NCC receptor. Such an ideal drug would bind to ENaCs at high affinity to lower its activity without completely blocking the Na^+ reabsorption, while simultaneously

lowering the activity of NCC to promote more K^+ secretion. Understanding the structure of ENaC to help explain its function at a molecular levels is the first step toward the rational design of such a drug.

Until the work presented in this dissertation, the structure of ENaC was unknown, presenting a significant barrier to a complete understanding of ENaC function. Multiple structures of the ENaC/DEG member, ASIC, have contributed to the understanding of ENaCs; however, there are important characteristics of ENaCs that can't be modeled from ASIC structures, as some of the key gating domains and sequences differ significantly. These areas in ENaC include the regions involved in its proteolytic cleavage and its high Na^+-selectivity. A high-resolution structure of ENaC would allow us to visualize domains that are crucial in regulation of ENaC P_o and areas that would be of interest as targets for antihypertensive drugs to reduce overall P_o. Additionally, elucidating the ion permeation pathway and the amiloride binding site would significantly increase our understanding of ENaC function.

In my dissertation I have taken advantage of biochemical approaches such as cryo-EM and the use of high-affinity monoclonal antibodies to solve the first structure of ENaC and elucidate key gating domains to increase our understanding of ENaC stoichiometry, molecular architecture and function. The work presented here will be important for development of the next generation of diuretics in the treatment of hypertension.

Prelude to this dissertation

Chapter two in this dissertation focuses on the biochemical approaches that were utilized to express and purify microgram quantities of homogeneous ENaC channels for structural studies

using single particle cryo-electron microscopy (cryo-EM). By facilitating fluorescence size-exclusion chromatography (FSEC) and a baculovirus-mediated expression system, we identified a promising construct for structural studies. This construct (ΔENaC) was truncated at the N- and C-termini and had mutations in the putative protease sites to capture ENaC in an uncleaved state. The results explain how we overcame the pseudosymmetry of ΔENaC that initially hampered particle alignment during cryo-EM data analysis. Our group used monoclonal, high-affinity antibodies that bound two distinct subunits of ENaC. These antibodies broke the pseudosymmetry, allowing for proper particle alignment and generation of the first structure of ENaC (ΔENaC-DiFab). Fitting subunit-specific glycosylation sites and aromatic residues into map protrusions allowed us to correctly identify ENaC subunits in our map. The first structure of ENaC confirms its stoichiometry as a heterotrimeric receptor and demonstrates how the three subunits arrange in a counterclockwise direction (α-β-γ) as seen from the luminal side of the membrane. The result also revealed the location of the inhibitory peptides, offering the first view of the molecular architecture of a defining domain in this receptor class. One drawback of the first structure of ENaC, however, was the poorly resolved map in the transmembrane domain region, preventing structural analysis that might explain the Na^+ permeation pathway and high Na^+ selectivity.

Chapter three details the first structure of full-length (FL) ENaC-DiFab, which confirms and validates the first structure of ΔENaC-DiFab. The result shows that the transmembrane domain of ENaC continues to remain ambiguous, which suggest that the disordered TMD of ENaC is not caused by disruption of interactions due truncations of the N- and C- termini in the ΔENaC construct, but rather due to inherent sensitivity of this domain to its external environment. Additionally, this chapter outlines cryo-EM data processing strategies to separate

ENaC into cleaved and uncleaved states. The purified FL-ENaC protein sample contains both cleaved and uncleaved states, as assessed by SDS PAGE prior to preparing samples for data collection. The cryo-EM strategies performed shows that structural variabilities within the protease sensitive regions of ENaC can be separated, revealing maps of ENaC with missing densities in these regions. Surprisingly, no large conformational changes are seen when comparing the extracellular domain between ENaC cleaved and uncleaved maps, except for within the region of missing density. To test if one of the monoclonal antibodies (mAb) that is located near one of the protease sensitive sites traps ENaC in a conformational state, preventing any conformational changes from occurring, electrophysiology patch clamp experiments were performed. The result shows that the mAb does not alter ENaC gating kinetics, suggesting that the lack of large conformational changes between cleaved and uncleaved maps of FL-ENaC is not due to binding of the mAb.

In short, these chapters explain the work underlying the biochemical and functional approaches utilized towards gaining the first direct understanding of the structure and function of ENaC. The studies outlined reveal how, using protein engineering strategies paired with biochemical techniques, we developed ΔENaC. The development of ΔENaC provided two key advancements towards gaining a better structural understanding of this unique ion channel. First, capturing ENaC in a homogeneous, uncleaved state provided the first glimpse of the receptor's structure, giving us enough knowledge to develop future strategies towards resolving cleaved or unmodified states of ENaC. Second, a purified homogenous sample of uncleaved ENaC allowed us to raise high-affinity monoclonal antibodies to use as tools in our structural studies. Although the question has been studied, the ENaC field has still not definitively demonstrated exactly how many cleaved and uncleaved states exist, nor have we shown what fraction of these states exist

as channels at the plasma membrane. The structure of recombinantly expressed FL-ENaC at a high resolution provides a foundation upon which we could develop a computational data-processing strategy to separate cleaved and uncleaved states in ENaC.

Taken together, the results presented in this dissertation have provided tremendous insight into ENaC stoichiometry, molecular architecture and function and set the stage for implementing new strategies to purify ENaC from native tissue, where we can start exploring these looming, unanswered questions about ENaC in a physiological context.

Acknowledgements: Thank you to L. Vaskalis for assistance with figures presented in this introduction.

Figures and legends

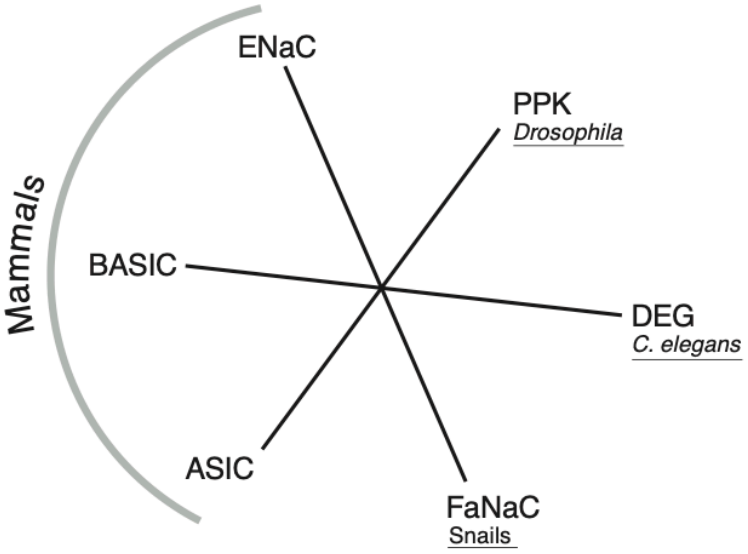

Figure 1.1. The Epithelial sodium channel/degenerin (ENaC/DEG) superfamily.

Phylogenetic tree of the ENaC/DEG family adapted from Boscardin et al[180]. The subfamilies consist of three members found only in invertebrates: the pickpocket (PPK) found in drosophila, the mechanosensitive DEG found in *C. elegans*, and FaNaC found in snails. The remaining three submembers are only found in mammals and include the acid-sensing ion channel (ASIC), the bile acid sensing ion channel (BASIC) and ENaC.

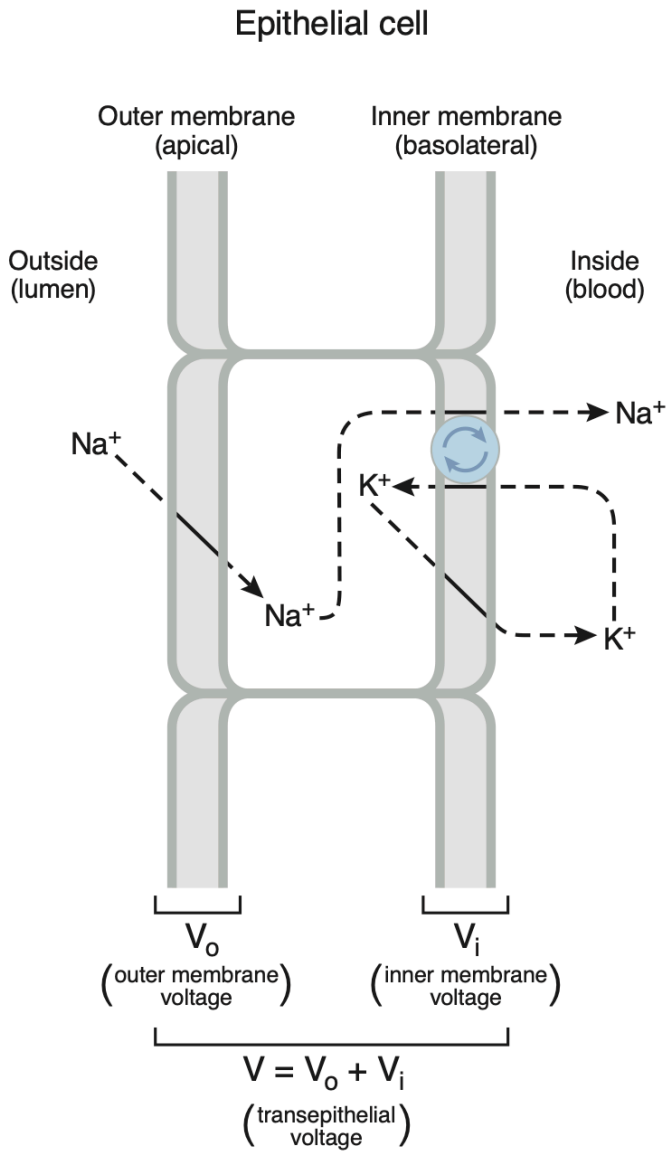

Figure 1.2. The Koefoed-Johnsson and Ussing Two-membrane model of transepithelial Na^+ transport. Figure is adapted from the Palmer et al[17]. The movement of Na^+ ions diffuses across the apical membrane down an electrochemical gradient. The Na^+-K^+ ATPase, restricted to the basolateral membrane, pumps Na^+ out of the cell and transport K^+ into the cell. K^+ are recycled out of the cell via K+ channels located at the basolateral membrane. The transepithelial voltage (V) is made up of the voltage across the apical membrane (V_o) and the voltage across the basolateral membrane (V_i).

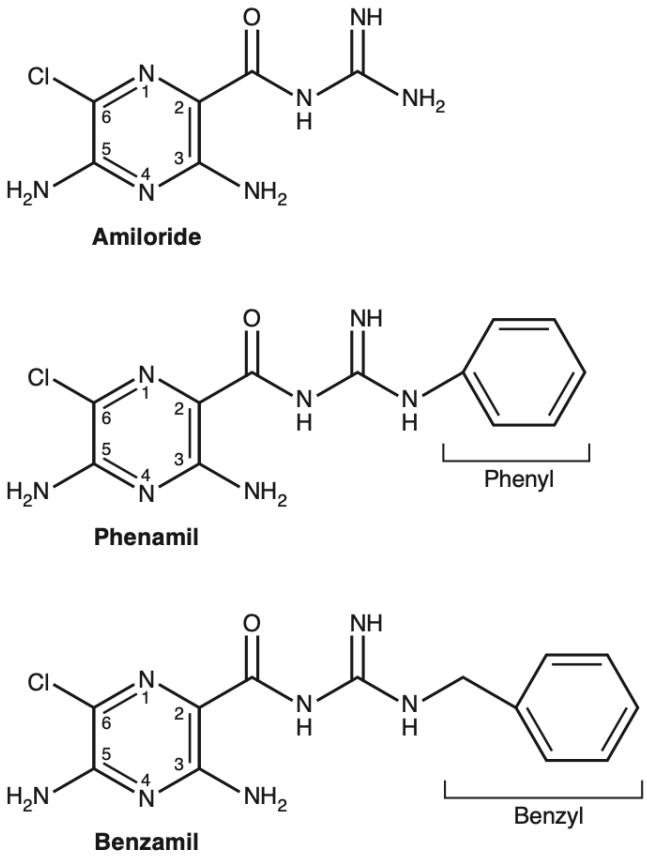

Figure 1.3. The structure of amiloride and analogs. Amiloride consist of a pyrazine ring that is attached to a carbonyl guanidium group at position 2. Additionally, two amino groups are attached at position 3 and 5, and a chloride group at position 6. The analogs, phenamil and benzamil have a similar structure as amiloride with an addition of a phenyl and benzyl group to the carbonyl guanidium group at position 2.

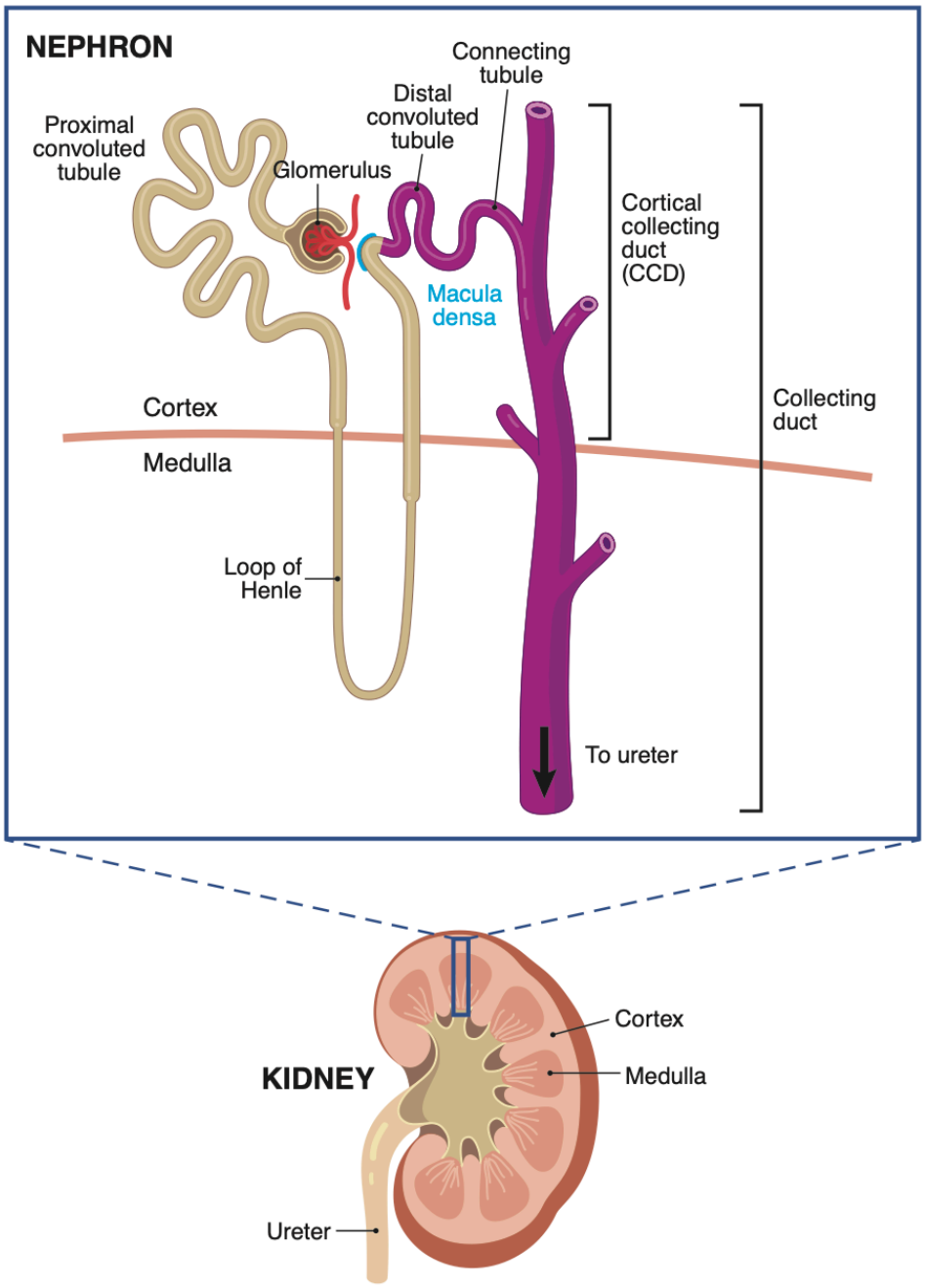

Figure 1.4. The functional unit of the kidney, the nephron. Figure is adapted from Rossier et al[125]. The nephron is composed of the Glomerulus (filtering apparatus), the Proximal Convoluted Tubule, the loop of Henle, the Macula Densa (thickening where the distal tubule touches the glomerulus), the Distal Convoluted Tubule (DCT), the Connecting Tubule (CT) and the

Collecting Duct (CD) where portion of CD located in the cortex region is named the Cortical Collecting Duct (CCD). The glomerulus is the filtering apparatus that removes waste products from the body. 60% of the fluid is absorbed in the proximal tubule section, 30% in the loop of Henle, and the remaining 9% in the DCT, CT and CD before it enters the renal pelvis that is connected to the ureter where it flows to the urinary bladder. Colored in purple represents the aldosterone-sensitive distal nephron (ASDN). The ASDN consists of the DCT, CT and CD, and ENaC is expressed in all the second part of the DCT (named DCT2) in addition to in the CT and CD regions. The electroneutral thiazide-sensitive Na^+:Cl^- cotransporter (NCC) is expressed in the DCT.

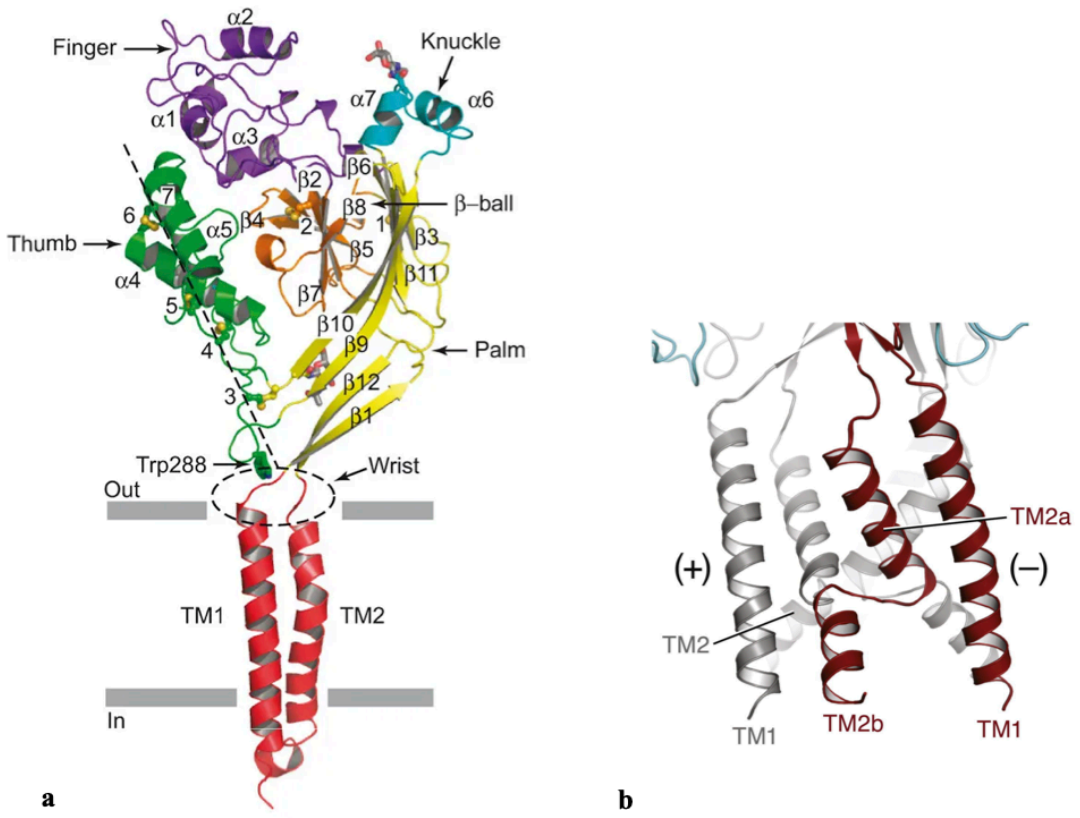

Figure 1.5. Domain organization and architecture of the transmembrane domain of chicken ASIC. a. The domain organization of one ASIC subunit, panel is reproduced from Jasti et al[4]. ASIC subunit resembles a hand clenching a ball. The transmembrane domain (red) make up the forearm, while the extracellular domain makes up the hand holding the ball, and is divided in to six domains: wrist, palm (yellow), thumb (green), finger (purple), knuckle (cyan) and β-ball (orange). **b,** The architecture of ASIC transmembrane (TM) domain, panel is reproduced from Baconguis et al[62]. The break in TM2 α helix causes a domain swap, where a GAS belt (Gly-Ala-Ser) forms a horizontal extended structure that places the lower part of TM2 α helix (named TM2b) in continuation of the upper TM2 α helix (named TM2a) of the neighboring subunit

Chapter 2

Structure of the human epithelial sodium channel by cryo-electron microscopy

The contents of chapter two are published in modified form:

Noreng, S., Bharadwaj, A., Posert, R., Yoshioka, C. and Baconguis, I. Structure of the human epithelial sodium channel by cryo-electron microscopy, eLife 2018;7:e39340

Author contributions

S.N., A.B., and I.B. designed the project. I.B. carried out preliminary characterization and purification. R.P designed ENaC constructs. S.N. and A.B. performed sample preparation. S.N., A.B., and C.Y. collected cryo-EM data and S.N. and C.Y. analyzed and processed cryo-EM data. I.B. carried out model building and refinement. S.N and I.B. performed electrophysiology, and S.N. carried out confocal microscopy experiments. S.N., A.B., R.P., C.Y., and I.B. wrote the manuscript.

Abstract

The epithelial sodium channel (ENaC), a member of the ENaC/DEG superfamily, regulates Na^+ and water homeostasis. ENaCs assemble as heterotrimeric channels that harbor protease-sensitive domains critical for gating the channel. Here we present the structure of human ENaC in the uncleaved state determined by single-particle cryo-electron microscopy. The ion channel is composed of a large extracellular domain and a narrow transmembrane domain. The structure reveals that ENaC assembles with a 1:1:1 stoichiometry of α:β:γ subunits arranged in a counter-clockwise manner. The shape of each subunit is reminiscent of a hand with key gating domains of a 'finger' and a 'thumb'. Wedged between these domains is the elusive protease-sensitive inhibitory domain poised to regulate conformational changes of the 'finger' and 'thumb'; thus, the structure provides the first view of the architecture of inhibition of ENaC.

Introduction

The fine-tuning of Na^+ homeostasis is largely mediated by epithelial sodium channels (ENaC) that are related in amino acid sequence to acid-sensing ion channels (ASIC) found in eukaryotes, degenerin channels (DEG) of *Caenorhabditis elegans*, and the FMRF-amide peptide-gated channels (FaNaCh) of mollusk[1,41,181-188]. These ion channels belong to the voltage-independent, Na^+-selective, and amiloride-sensitive ENaC/DEG superfamily which together perform diverse cellular functions in different organisms. In humans, ENaCs are expressed at the apical surface of epithelial tissues throughout the body, and play critical roles that range from regulation of total-body salt, water, and blood volume, to modulating airway surface liquid clearance in epithelial cells in the lungs[189-192]. The importance of ENaC in Na^+ homeostasis is highlighted by gain of function mutations causing severe hypertension, as in Liddle syndrome, or loss of function mutations causing the neonatal salt-wasting disorder pseudohypoaldosteronism type 1 (PHA1)[107,156-158,193,194]. More subtle ENaC dysfunction contributes to diseases as diverse as essential hypertension, heart failure, and nephrotic syndrome[195-197]. ENaCs require three different subunits to form a functional channel, α, β, and γ[3]. Despite decades of study, the number of subunits in an active channel remains unclear[166].

Unique among the ENaC/DEG channels, ENaCs are activated by proteolysis of peptidyl tracts embedded in the extracellular domain (ECD), which releases inhibitory peptides. The cleavage event increases channel opening probability (P_o)[92-96,99,198-200]. Amino acid sequence alignments and biochemical analyses in the ECD have so far revealed that only the β subunit lacks the characteristic motifs for protease recognition. ENaCs are widely known as substrates of serine proteases like furin, and a growing list of proteases that recognize sites in ENaC suggests a multifaceted regulation of channel function[201]. Indeed, the complexities of ENaC function

involving the requisite heteromeric subunit assembly and asymmetric subunit modification via differential proteolytic processing are critical to ion channel gating. Thus, to define subunit arrangement and stoichiometry, and elucidate the molecular architecture of ENaC inhibition, we determined the structure of ENaC in the uncleaved state by single-particle cryo-electron microscopy (cryo-EM).

Materials and Methods

***Construct Design*:** The cDNA encoding the full length α, β and γ subunits of human ENaC were cloned into pEG BacMam expression vector harboring an N-terminal eGFP[202]. The Δα was generated by removing both N- and C-terminal segments and modifying the furin sites obtaining a mutant variant of the α subunit lacking 42 and 89 residues at N- and C- termini, respectively. While the Δβ was designed to possess truncations of 30 and 79 residues at the N- and C-terminal regions, $\Delta\beta_{ASIC}$ has the same truncated regions as Δβ but contains an additional N-terminal 2-22 residues of cASIC upstream of Δβ. Lastly, Δγ lacks 20 and 79 residues at the N- and C-terminal domains, has modified furin and prostasin sites, and includes a Strep-tag II, an octa-histidine tag, eGFP, and Thrombin cleavage site at the N-terminus.

***Generation and isolation of Fabs*:** Mouse monoclonal antibodies 7B1 and 10D4 were generated using standard procedure by Dan Cawley at the Vaccine and Gene Therapy Institute (OHSU). Liposomes containing asolectin:cholesterol:lipidA:brain polar lipid extract (BPLE) (16:4.6:1:5.3) were prepared in 20 mM Tris, 150 mM NaCl at pH 8.0 at a concentration of 40 mg/mL. The mixture was subjected to repeated freeze-thaw cycles followed by extrusion through a 200-nm filter. Purified $\Delta ENaC_{ASIC}$ (Δα, $\Delta\beta_{ASIC}$, Δγ) protein was added to the liposome mixture in the presence of 400 mM NaCl and 0.8% Na-cholate and passed through a PD-10 desalting column to

remove excess salt and detergent. Mice were immunized with approximately 30 μg of the reconstituted $\Delta ENaC_{ASIC}$ for generation of hybdridoma cell lines (**Figure 2.4a,b**). Monoclonal antibodies were screened by FSEC and BioDot blot to identify clones that recognize tertiary or primary epitopes. The 7B1 and 10D4 mAbs were selected because they recognize tertiary epitopes of ENaC. The mAbs were purified, and their Fabs were generated by papain cleavage. Fab 7B1 was isolated by anion exchange using HiTrap Q HP column while Fab 10D4 was eluted using Protein A column to remove Fc. After isolation, both Fabs were dialyzed in 200 mM NaCl and 20 mM Tris at pH 8.0.

***Expression and purification of ΔENaC-Fab complexes*:** Human embryonic kidney cells lacking N-acetylglucosaminyltransferase I (HEK293S GnTI$^-$ cells) were grown in suspension at a density of 2 – 4 x 10^6 cells/mL in Freestyle medium with 2% FBS and transduced with the virus (Δα, Δβ and Δγ) at a multiplicity of infection (MOI) of 1 and incubated at 37°C. Eight hours post-transduction, sodium butyrate and phenamil mesylate were added to 10 mM and 500 nM, respectively, and cells were incubated at 30°C. After 36 hours, the cells were collected by centrifugation at 4790 xg for 15 min. The pellet was washed with 20 mM Tris, 200 mM NaCl and followed by a second round of centrifugation at 4790 xg for 15 min. Cells were homogenized with a dounce homogenizer and sonicated in 20 mM Tris, 200 mM NaCl, 5 mM $MgCl_2$, 25 μg/mL DNase I and protease inhibitors. Lysed cells were centrifuged at 9715 xg for 20 min; the resulting supernatant containing the membrane fraction was further centrifuged at 100,000 xg for 1 hr. Membrane pellets were resuspended and solubilized in 20mM TRIS pH 8, 200 mM NaCl, 20 mM n-dodecyl-β-D-maltopyranoside (DDM, Anatrace), 3 mM cholesteryl hemisuccinate (CHS), 2 mM ATP, 2 mM $MgSO_4$, protease inhibitor and 25 U/mL nuclease for 1 hr at 4°C. The solubilized fraction was isolated by ultracentrifugation 100,000 xg for 1 hr, and

ΔENaC was bound to streptactin resin packed into an XK-16 column. The column was washed with 20 mM TRIS, 200 mM NaCl, 0.5 mM DDM, 75μM CHS and 25 U/mL nuclease, followed by an additional wash of the same buffer containing 2 mM ATP, and eluted with 2.5 mM desthiobiotin. The eluted fractions were concentrated and then incubated with either one Fab 10D4 (monoFab complex) or two Fabs 7B1 and 10D4 (diFab complex) in a 1:3 molar ratio of ENaC:Fab for 10 min, and clarified by ultracentrifugation 100,000 xg for 1 hr. The supernatant was injected onto a Superose 6 Increase 10/300 GL column equilibrated in 20 mM TRIS pH 8.0, 200 mM NaCl, 0.5 mM DDM, 75 μM CHS and 1 mM TCEP to isolate the protein complex by size-exclusion chromatography. Monodispersed fractions were pooled and concentrated to 2.2 mg/mL.

For FSEC experiments analyzing peak shifts of the ΔENaC and FL-ENaC with 7B1 and 10D4, ΔENaC was expressed in HEK 293S GnTI$^-$, as described above, while FL-ENaC was expressed in HEK 293T/17. The HEK 293T/17 cells were grown in suspension at a density of 2 - 4 x 10^6 cells/mL in Freestyle medium with 2% FBS and transduced with the virus (FL-α, FL-β and FL-γ) at a multiplicity of infection (MOI) of 1 and incubated at 37°C. Eight hours post-transduction, 500 nM phenamil mesylate was added, and cells were incubated at 30°C. After 36 hr post-transduction, the cells were collected by centrifugation at 4790 xg for 15 min. The pellet was washed with 20 mM Tris, 200 mM NaCl and followed by a second round of centrifugation at 4790 xg for 15 min. Cell pellets were resuspended and solubilized in 20 mM TRIS pH 8, 200 mM NaCl, 20 mM n-dodecyl-β-D-maltopyranoside (DDM, Anatrace), 3 mM cholesteryl hemisuccinate (CHS), protease inhibitor and 25 U/mL nuclease for 1 hr at 4ºC. The solubilized fraction was isolated by ultracentrifugation 100,000 xg for 1 hr, then incubated with either one Fab (7B1 or 10D4) or two Fabs (7B1/10D4) in a 1:3 molar ratio of ENaC:Fab for 10 min, and

clarified by ultracentrifugation 100,000 xg for 1 hr. The supernatant was injected onto a Superose 6 Increase 10/300 GL column for FSEC analysis.

***Immunoblotting*:** Aliquots of 7 µg purified ENaC were incubated with 2.5 µg/mL trypsin for 10 min at room temperature. These samples were then run through 4 – 20% Criterion SDS-PAGE gels and blotted onto nitrocellulose membranes according to manufacturer's instructions (Bio-Rad). After blocking overnight in 5% non-fat milk in TBS, membranes were incubated in primary antibody (ENaC α subunit, 6 µg/blot SC-21012; ENaC β subunit, 6 µg/blot SC-21013; ENaC γ subunit, 10 µg/blot abcam ab133430) for 2 hr. The membranes were then incubated in 1 µg/blot IR Dye 800CW goat anti-rabbit IgG (Licor) for 1 hr.

***Image acquisition and processing*:** Purified ΔENaC-Fab complexes were applied to glow-discharged Quantifoil holey carbon grids (Au 1.2 µm/1.3 µm hole space/hole separation, 300mesh), blotted using a Vitrobot Mark III (FEI) with the following conditions, 7 s wait time, and 5 s blot time at 100% humidity, and then plunge-frozen in liquid ethane cooled by liquid nitrogen. All images were collected on a Titan Krios electron microscope operating at 300 kV at the Multiscale Microscopy Core (OHSU). Images were recorded by a Gatan K2 Summit direct electron detector operating in super-resolution mode, and the images were collected using the automated acquisition program SerialEM[203]. Magnification of the recorded images corresponded to a pixel size of 1.33 Å in counting mode (0.665 Å in super-resolution mode). For the ΔENaC-10D4 complex, two data sets were acquired and were initially processed separately, and subsequently combined for 3D reconstruction. Each image in the first dataset was dose-fractionated to 30 frames with 0.5 s per frame and a total exposure time and dose of 15 s and 54 $e^-/Å^2$, respectively. The second dataset was collected in counting mode, and was therefore not binned when combined with the first where each image was dose-fractionated to 60 frames with

0.25 s per frame and a total exposure time and dose of 15 s and 50 $e^-/Å^2$, respectively. Similarly, two separate datasets were obtained for ΔENaC-7B1/10D4 complex in super-resolution mode. Like in the monoFab complex, each data set was processed separately and later combined for further analysis and 3D reconstruction. The images of the first dataset of the diFab complex were dose-fractionated to 40 frames with 0.25 s per frame and a total exposure time and dose of 10 s and 62 $e^-/Å^2$, respectively, while the images of the second dataset were dose-fractionated to 48 frames with 0.25 s per frame and a total exposure time and dose of 12 s and 71 $e^-/Å^2$, respectively.

The ΔENaC-10D4 data set collected in super-resolution mode was binned 2 x 2 while the ΔENaC-10D4 data set collected in counting mode was left unbinned. Both data sets were motion corrected using MotionCor2[204], and automated particle selection was performed using DoGPicker[205]. Defocus values for individual particles were estimated using Gctf[206], and particles belonging to low-abundance classes were removed via 2D classification and 3D classification in RELION[207]. The final set of particles was further analyzed in cryoSPARC and refined to a nominal resolution of 5.4 Å[208].

For the ΔENaC-7B1/10D4 data sets, super-resolution counting images were 2 x 2 binned, and motion corrected using MotionCor2. Manual and automated particle selections were performed where DoGPicker was utilized for the latter resulting in a total of 667,984 particles. Defocus values for individual particles were estimated using Gctf, and particles of low-abundance classes via 2D classification in RELION were removed. For 3D classification in RELION, a reference model of a low-resolution map of ENaC-7B1/10D4 obtained from a data set (14.4 Å) was low-pass filtered to 50 Å, and particles were classified into 2 classes where the major class contained 385,997 particles. Duplicates (as a result of RELION2.0 re-centering

particles after 2D classification) and particles close to micrograph edges were removed, resulting in 329,180 particles that were subjected to *ab initio* 3D classification in cryoSPARC[208], and 3D classification and refinement in cisTEM[209]. Particles belonging to the low abundance class in cryoSPARC and cisTEM were discarded yielding 244,223 and 290,007 particles, respectively. Using default settings in cryoSPARC, particles with class probability of > 0.9 were used for refinement; thus, final reconstruction and refinement used 244,223 particles. For cisTEM, initial 3D classification and refinement was done using a refinement threshold of 8 Å and applying a mask during the last few iterations that excluded the constant domain (Fc) of the Fabs. During this process, we noticed that extraneous features, such as the micelle, were having a strong influence on alignment and classification, so the cisTEM particles were then re-processed using a mask that excluded both the micelle and the Fc of the Fabs, and aligned with a 5.4 Å limit. This dataset consisted of 302,263 particles and improved the resolution, as determined by the FSC = 0.143 criterion (~3.9 Å). More importantly, the electrostatic potential map was notably improved in the regions of interest. The resolutions reported in **Table 2.1** are based on the FSC = 0.143 criterion (gold-standard in the case of RELION and cryoSPARC). Final resolution reported in **Figure 2.13c** and **Table 2.1** are solvent adjusted FSC = 0.143 criterion. No symmetry was applied during data processing.

***Model building*:** Homology models of the human α, β, and γ subunits were generated with the crystal structure of cASIC[4] (PDB code: 2QTS, chain A) as a template using SWISS-MODEL server and homology models for the Fabs were also generated by SWISS-MODEL[210]. All models were docked into the EM potential in UCSF Chimera then rigid-body fitted into the EM potential using Coot[211,212]. We incorporated models generated from Rosetta[213] into manual fitting and adjustments during model-building in Coot to build the palm, knuckle, TM, thumb, β-ball,

and finger domains. To build the GRIP domains, we integrated analysis from Jpred4, PSIPRED v3.3, and QUARK online *ab initio* protein structure prediction to support our analysis of the cryo-EM map[214-216]. The final model was subjected to refinement using the module phenix.real_space_refine in PHENIX[217].

The cryo-EM map in all three subunits preceding the N-terminal side of the α2 helices was unambiguous and showed features consisting of two β-strands connected by a loop, the P3 and P4 segments of the GRIP domains (**Figure 2.20**). Secondary structure prediction analysis by online servers Jpred4, PSIPRED v3.3, and QUARK supported this observation[214-216]. We found that the potential map in the β subunit had the best-defined feature demonstrating four β strands (**Figure 2.20**). Based on the cryo-EM map, the P1 segments in α and γ adopt β strand-like conformations, like in the β subunit, which is also supported by the secondary structure prediction servers (**Figure 2.15 and Figure 2.20**). The regions between P1 and P3 in the α and γ subunits, however, are disordered in the cryo-EM map. We built stretches of residues into the P1 potential maps in the α- and γ-GRIP domains using sequence alignment with the β-GRIP domain and cryo-EM potential map features as guides.

For validation, FSC curves were calculated between the final model and the EM map as well as the two half maps generated by cisTEM. We implemented MolProbity to analyze geometries of the atomic model[218]. All figures of map and atomic model were prepared using UCSF Chimera and Pymol[211,219].

***Two-electrode voltage clamp electrophysiology*:** All constructs used for two-electrode voltage clamp electrophysiology (TEVC) experiments were cloned into pGEM vector, linearized and transcribed to mRNA using mMESSAGE mMACHINE T7 Ultra Kit (Ambion) procedure. *Xenopus laevis* oocytes purchased from Ecocyte were injected with a volume of 50 nL

containing either 0.5 – 1.0 ng of each FL-ENaC subunit mRNA or 5 ng of each ΔENaC and Δ*ENaC subunit mRNA. For experiments containing combinations of FL-ENaC and ΔENaC, 5 ng of each subunit mRNA was injected. Oocytes were incubated at 16^{o}C for 12 - 48 hr in the presence of 100 μM amiloride and 250 μg/mL amikacin. The recordings were performed using two different ionic solutions with or without 100 μM amiloride (110 mM KCl and 110 mM NaCl) where all buffers additionally contained 1.8 mM $CaCl_2$ and 10 mM HEPES (pH 7.4). Macroscopic ENaC currents are defined as the difference between inwards currents obtained in the absence and in the presence of 100 μM amiloride. To test full activation of ΔENaC constructs, 2.5 μg/mL Trypsin was perfused for 5 min in the presence of 100 μM amiloride. Amiloride-sensitive currents were recorded prior to Trypsin treatment as well as after in order to determine the increase in current amplitude. All recording experiments were carried out at a holding potential of -60 mV and repeated independently at least three times.

***Whole-cell patch clamp electrophysiology*:** HEK293S GnTI^{-} cells were grown in suspension at a density of 2 – 4 x 10^6 cells/mL in Freestyle medium with 2% FBS and transduced with the virus (Δα, Δβ, and Δγ; or FL-α, FL-β, and FL-γ) at a multiplicity of infection (MOI) of 1 and incubated in the presence of 500 nM phenamil mesylate at 37°C for 12 hr. Five hours before recording, cells were transferred to wells containing glass coverslips at a density of 0.3 - 0.5 x 10^6 cells/mL and in Dulbecco's Modified Eagle Medium supplemented with 5% FBS and 500 nM phenamil mesylate. Whole-cell recordings were carried out 17 - 24 hr after transduction. Pipettes were pulled and polished to 2 – 2.5 MΩ resistance and filled with internal solution containing (in mM): 150 KCl, 2 $MgCl_2$, 5 EGTA and 10 HEPES (pH 7.35). External solution contained (in mM): 150 NaCl, 2 $MgCl_2$, 2 $CaCl_2$, 10 HEPES (pH 7.4), and 0.1 amiloride. Test external solution did not contain 0.1 mM amiloride. As in TEVC experiments, macroscopic

ENaC currents are defined as the difference between inwards currents obtained in the absence and in the presence of 100 μM amiloride. Holding potential was at -60 mV.

***Confocal Microscopy*:** Six mg of mAb 10D4 was dialyzed into 0.2 M carbonate-bicarbonate (Na_2CO_3/$NaHCO_3$) solution buffered at pH 9.0. The dialyzed mAb was concentrated to 6 mg/mL. Tetramethylrhodamine (TRITC, ThermoFisher 46112) was dissolved in DMSO at a final concentration of 1 mg/mL. To the 10D4 solution, 35 μg of TRITC was slowly added and mixed thoroughly. The 10D4-TRITC mix was incubated at room temperature in the dark for 2 hr followed by gel filtration to remove excess TRITC. The carbonate-bicarbonate buffer was exchanged with Tris-buffered saline buffer (200 mM NaCl, 20 mM TRIS, pH 8.0) using PD-10 desalting column. The dye:protein molar ratio of the final TRITC-labeled mAb 10D4 in TBS buffer was approximately 2.8.

HEK293S GnTI$^-$ cells were resuspended from DMEM into 2 mL HBSS media, stained with 10 μg (5 μg/μL stock) of WGA Alexa Fluor 647 conjugate (ThermoFisher W32466) and 170 μg (4.9 μg/μL stock) of 10D4-TRITC and subsequently incubated at 37^{o}C for 10 min. The cells were then washed with PBS two times before resuspended in 1 mL HBSS. Live cell imaging was performed on a Yokogawa CSU-W1 spinning disk confocal microscope using a 60 x 1.4 Plan Apo VC objective. Images were acquired at a pixel size of 0.108 μm for three different wavelengths, starting at 640 nm, 561 nm and then 488 nm. Exposure time varied depending on sample intensity, but remained the same for each wavelength between the two samples of infected cells (FL-ENaC and ΔENaC), 400 ms for 640 nm, 2 s for 561 nm and 600 ms for 488 nm. Images were imported into Fiji for image analysis.

Results

Design and expression of ΔENaC

We first assessed the expression of full-length (FL) ENaC by small-scale expression in adherent HEK293S GnTI$^-$ cells and fluorescence-detection size-exclusion chromatography (FSEC)[220]. We found a low, wide peak, indicating a poorly-expressing polydisperse population unsuitable for cryo-EM (**Figure 2.1a**). We thus screened a number of deletions and mutations in each ENaC subunit, harnessing information derived from previous biochemical and functional experiments gauging the propensity for heterotrimeric formation of ENaC and its susceptibility to proteolytic processing[3,92-96,99,198,199], before arriving at the construct referred to here as ΔENaC (**Figure 2.1a-c, Figure 2.2 and Figure 2.3**).

ΔENaC is composed of α, β, and γ subunits truncated at the N- and C-termini (**Figure 2.1b,c**). Additionally, the Δα and Δγ subunits possess mutations in the identified furin and prostasin sites which prevent subunit cleavage and channel activation[90,96]. For protein purification, neither Δα nor Δβ were modified with affinity tags because there is strong evidence that the α subunit can readily form functional homomeric channels, and the termini of Δβ are sensitive to perturbations[2]. As a result, Δγ contains both GFP and a Strep-II tag at the N-terminus (**Figure 2.1c**), minimizing contamination by homomeric Δα channels during purification. This construct provided a homogeneous and highly-expressing population. However, the inherent pseudosymmetry from common secondary and tertiary structures between the α, β, and γ subunits of human ENaC hindered particle alignment (**Figure 2.1d**).

To evaluate biochemical integrity and to facilitate cryo-EM three-dimensional reconstruction of ΔENaC, we generated subunit-specific monoclonal antibodies (mAbs) that bind to three-dimensional epitopes in ΔENaC and FL-ENaC. For immunization, we exploited the

high-expressing chicken ASIC (cASIC) by adding the first 22 N-terminal amino acids of cASIC to Δβ, which tolerated the fusion. This construct is referred to hereafter as $\Delta\beta_{ASIC}$. Together, Δα, $\Delta\beta_{ASIC}$, and Δγ comprise $\Delta ENaC_{ASIC}$ (**Figure 2.4a, b**)[4]. Two fragment-antigen binding domains (Fabs) were isolated that recognize different epitopes (7B1 and 10D4). While these antibodies were raised against $\Delta ENaC_{ASIC}$ (**Figure 2.4a, b**), both Fabs bind to both ΔENaC expressed in HEK 293S GnTI$^-$ and FL-ENaC expressed in HEK293T/17, and indicates that ΔENaC is properly folded and that the Fabs do not bind to the ASIC segment (**Figure 2.4c, d and Figure 2.5a, b**). Inclusion of 7B1 and 10D4 allowed for proper alignment of the particles (**Figure 2.1e**). Moreover, maps of the particles with only 10D4 (monofab) compared to those with both 10D4 and 7B1 (difab) show that each Fab recognizes only one subunit (**Figure 2.5c-f**). We monitored and compared grid conditions and the resulting data quality (including ice thickness, sample quality, particle distribution, and orientation) between the monoFab and the diFab complexes of ENaC and discovered that the diFab complex was a more promising complex for cryo-EM analysis.

Functional characterization of ΔENaC

We investigated ΔENaC function by two-electrode voltage-clamp electrophysiology (TEVC) and whole-cell patch clamp electrophysiology in oocytes and GnTI$^-$ HEK cells, respectively (**Figure 2.6**, **Figure 2.7 and Figure 2.8a,b**). Unlike FL-ENaC (**Figure 2.6a, Figure 2.8a**), ΔENaC does not exhibit amiloride-sensitive currents in oocytes and HEK cells, and the only Na^+-specific currents resemble those from uninjected oocytes (**Figure 2.7a,b**). Similarly, oocytes expressing ENaC channels with restored protease sites in the Δ subunits (Δα* and Δγ*) to form Δ*ENaC did not present amiloride-sensitive currents (**Figure 2.7c**). Because HEK cells

are better suited to defining whether ΔENaC traffics to the plasma membrane, we examined surface expression of ΔENaC and FL-ENaC expressed in GnTI$^-$ HEK cells using confocal microscopy. To ensure robust expression, we transduced the HEK cells with baculovirus encoding the ΔENaC and FL-ENaC proteins, taking advantage of the N-terminal eGFP in the Δγ subunit and the N-terminal eGFP in all three FL subunits to visualize expression, respectively. Based on eGFP fluorescence, we observed robust expression of both ΔENaC and FL-ENaC (**Figure 2.8c,d**). We employed tetramethylrhodamine (TRITC)-labeled 10D4 mAb, an antibody that binds to the extracellular domain of ENaC, to probe the plasma membrane localization of ENaC channels. Indeed, we observed overlapping signals from both eGFP and TRITC-10D4 mAb in cells expressing FL-ENaC but not in cells expressing ΔENaC. Based on the confocal imaging results, ΔENaC is not trafficked to the plasma membrane, in agreement with the electrophysiology results in HEK 293S GnTI$^-$ cells and oocytes (**Figure 2.8**).

We further examined whether disruption of the channel by mutagenesis also caused the absence of ΔENaC current. We tested channels comprising a single Δ or Δ* subunit in complex with the two complementary FL-ENaC subunits. Channels comprising Δα-FLβ-FLγ conduct amiloride-sensitive Na^+ currents which increase approximately 5-fold upon trypsin treatment (compared with 2.2-fold for FL-ENaC, **Figure 2.6b and Figure 2.9**). Since this trypsin response could be a result of cleavage of FLγ, we also tested channels of Δα*-FLβ-FLγ (**Figure 2.6c**). These channels show an increase in total current compared to Δα-FLβ-FLγ, and demonstrate a more archetypal ENaC current trace (**Figure 2.6a and Figure 2.9**). These results, in addition to the cleavage pattern of an anti-α immunoblot (**Figure 2.10**) indicate that Δα adopts a biologically relevant fold, capable of forming active channels with other full-length subunits, and that it is likely cleaved once at its N-terminal furin site (RSRA in Δα) but not the C-terminal furin site

(AAAA in Δα, **Figure 2.2**). By restoring the protease sites, as in Δα*, the inhibitory peptide was effectively removed.

The FLα-Δβ-FLγ channels conducted amiloride-sensitive Na^+ currents with a post-trypsin/pre-trypsin ratio of 1.5 (**Figure 2.6d and Figure 2.9**), similar to that of FL-ENaC. Moreover, an anti-β immunoblot shows no cleavage of Δβ, as expected (**Figure 2.11**).The FLα-FLβ-Δγ channel also conduct an amiloride-sensitive Na^+ current with approximately 9.5-fold increase upon trypsin treatment (**Figure 2.6e and Figure 2.9**). Although the Δγ subunit has the canonical furin and prostasin sites mutated (AAAA and QQQQ respectively, **Figure 2.2**), there are other basic residues near the furin and prostasin sites that could be cleaved by trypsin. This hypothesis is further supported by the immunoblot showing significant trypsin digestion in Δγ (**Figure 2.12**) as well as the even higher trypsin activation of FLα-FLβ-Δγ* (approximately 13.3-fold, **Figure 2.6f and Figure 2.9**). Nevertheless, the results are a promising direction for future studies. Importantly, the combination of TEVC traces of each Δ subunit and the α and γ Δ* counterparts supports ΔENaC representing a biologically relevant channel.

Cryo-EM analysis of ΔENaC

We solved the structure of ΔENaC difab complex in n-Dodecyl β-D-maltoside (DDM) by cryoEM (**Figure 2.13 and Table 2.1**). We first carried out cycles of 2D and 3D classifications to remove ice contamination, micelles, and denatured complexes. The remaining particles were subjected to unsupervised *ab initio* 3D classification and refinement in cryoSPARC[208] as well as 3D classification and refinement in cisTEM[209] to arrive at the cryo-EM potential map with a nominal resolution of 4.2 Å from both programs, based on the gold standard FSC = 0.143 and solvent adjusted FSC = 0.143 criteria, respectively (**Figure 2.14**). Additionally, we conducted a

masked refinement excluding the flexible Fc domains of the Fabs and micelle in cisTEM (**Figure 2.13a**), and obtained a map at 3.9 Å, as determined by the solvent adjusted FSC = 0.143 criterion (**Figure 2.13b,c**), with local resolution estimates generated by BSoft[221] indicating regions of the map with a resolution of 3.7 Å (**Figure 2.13d**).

Discussion

ENaC Structural Overview

The cryo-EM potential map has three major regions into which the two Fabs and homology models of ΔENaC were manually fitted (**Figure 2.15**). Alignment of predicted glycosylation sites and aromatic residues to distinct features in the map allowed for the correct assignment of the homology models of the ENaC ECD, generated from the desensitized state of ASIC (PDB: 2QTS, **Figure 2.16-2.20**). The β subunit is predicted to have eleven glycosylation sites by primary sequence, considerably more than α or γ. Six prominent glycosylation sites were used to assign β (as opposed to the 3 each in α and γ) whereas a glycosylation on the β9-α4 loop distinguished α from γ (**Figure 2.2, Figure 2.3 and Figure 2.16a-c**). Guided by these features and the 10D4 monoFab ΔENaC map, we assigned the identity of 7B1 and 10D4 as binding α and β subunits, respectively (**Figure 2.5 and Figure 2.15**).

Forming a trimeric ensemble, the α-β-γ subunits arrange in a counterclockwise manner, as reported by previous studies[222-224] (**Figure 2.15b, d**). The overall domain organization within each subunit of ΔENaC concurs with that of ASIC, which was first illustrated in the crystal structure of chicken ASIC (cASIC)[4] (chicken ASIC shares 18 – 20% sequence identity with human ENaC; **Figure 2.21 and Figure 2.22**). Each subunit of ΔENaC harbors a cysteine-rich ECD resembling a hand with the palm, knuckle, finger, and thumb domains clenching a “ball” of

β strands. This compact organization is stabilized by eight disulfide bridges in the ECDs of α and γ and nine in β. Seven of the disulfide bonds are conserved throughout the ENaC/DEG family (**Figure 2.2, Figure 2.3 and Figure 2.21a-c**). The eighth is unique to the three ENaC subunits. For the purpose of consistency in the following discussion, domain and secondary structure assignment in ENaC follow those of ASIC (**Figure 2.21d**).

At the center of the trimeric architecture of the ECD are β-sheets formed by β1, β3, β6, and β9-β12 that constitute the palm domain, which are divided into two sections, the upper and lower palm domains. The upper palm domain cradles the β-ball, which is composed of β2, β4, β5, β7, and β8 in all three subunits, contrary to previous findings which suggested that the α subunit lacked the β4 and β5 strands[225]. Completing the 'clench' around the β-ball are the α1-3 of the finger, α4-5 of the thumb, and α6 of the knuckle domains. The lower palm is directly linked to the transmembrane domain (TMD) via β1 and β12 and to the α4 and α5 of the thumb through β9 and β10. The thumb and the lower palm converge to forge interactions with the TMD at a juncture called the "wrist" (**Figure 2.22a, b**). Underscoring the importance of the wrist region and the critical roles that disulfide bridges play in maintaining the structural and functional integrity of ENaC, alterations of a conserved cysteine, α-Cys479 to an Arg, causes Liddle syndrome due to a missense mutation that not only eliminates a disulfide bridge located at the juncture of the thumb and palm domains but also introduces a bulky, positively charged residue[226] (**Figure 2.21a**).

ENaC differs significantly from ASIC in both structure and primary sequence at the knuckle and finger domains (**Figure 2.2, Figure 2.3 and Figure 2.22**). Each knuckle domain in ENaC makes extensive interactions with the α1 and α2 helices of the finger domain in the adjacent subunit (**Figure 2.23**). Together, the knuckle and finger domains of all three subunits

form a ‘collar’ at the top of the ECD. Sequence alignment of the three subunits demonstrate divergence in amino acid sequence at the C-terminal end of both α1 and α6 in all three subunits, which results in distinct types of molecular interactions at each subunit interface that are, perhaps, associated with assembly and stability of the ENaC. The contact between the finger and thumb domains is mediated by long antiparallel helices α1 and α2, which form a barrier between the thumb domain and the β6-β7 loop with α2 making the primary contacts with the thumb domain (**Figure 2.22 and Figure 2.23**). The domain arrangement observed in the ΔENaC structure agrees with the functional study probing Na^+ binding sites in the α subunit of ENaC[71]. The α2 helix makes an almost 90° turn towards the palm domain breaking the helix. This architecture marks another departure from ASIC, in which contacts between the finger and thumb domains are largely mediated by α1, α3, α5, and the α4-α5 loop (**Figure 2.22**).

The TMD is not well ordered, hampering our ability to model the entire TMD region and assign a functional state of the channel. Nevertheless, the EM map offers a glimpse of the positions of TM1 and TM2 on the extracellular side from each subunit (**Figure 2.24**). The overall configuration of the TMD shows that TM2 of all three subunits are positioned near the central axis, poised to mediate ion conduction in agreement with the crystal structures of ASIC and previous elegant functional studies probing ion selectivity and channel block[182]. Strikingly, the potential map for γ-TM1 on the extracellular side illustrates clear map for the main chain preceding the β1 strand validating a sequence disparity between the γ subunit and the other ENaC and ASIC subunits (**Figure 2.24**). The γ subunit lacks two residues preceding the palm domain (**Figure 2.24f**). Consequently, interactions within the wrist region in the γ subunit may differ from that of α and β subunits.

The GRIP domain

Previous studies of ENaC have probed stretches of amino acids and their roles in ENaC function by perturbing known protease sites, observing changes in molecular weight, recording channel activity, and conducting cross-linking studies[89,90]. The structure of ΔENaC indicates that these stretches of 20-40 amino acids are pieces of larger domains located in the periphery of the ECD near subunit interfaces (**Figure 2.25**). These stretches of amino acids, located between α1 and α2 are unique to ENaC and are responsible for channel **G**ating **R**elief of **I**nhibition by **P**roteolysis and will hereafter be referred to as the GRIP domain. Each GRIP domain is composed of a core of β strands that forge interactions with the finger and thumb domains forming a β-sheet "blanket" that conceals the α2 helix of the finger (**Figure 2.26**). Surprisingly, although the β subunit is not known to gate the channel via proteolysis, it also possesses a GRIP domain with similar organization to those of the α and γ subunits.

In all three subunits, the GRIP domains comprise two antiparallel β strands stapled together by a disulfide bond located in the loop that rests against the thumb domain (**Figure 2.25b-d and Figure 2.26b-d**). Furthermore, an additional disulfide bond in the loop near the β-γ interface stabilizes the GRIP domain of the β subunit. We suspect that this additional disulfide bond contributes to the well-ordered behavior of the β GRIP domain, allowing the resolution of nearly the whole segment between α1 and α2 in the β subunit. Moreover, the 10D4 Fab binds the β GRIP domain, allowing us to resolve two additional antiparallel β strands. In the α and γ subunits, we can only identify one stretch of residues that adopt an extended conformation. Based on the shared features observed in all three subunits, it is plausible that the α and γ subunits also contain a fourth β strand. With four possible β strands in the GRIP domains, each strand or stretch of peptides is referred to here as P1-4 (**Figure 2.25**).

Structural insight gleaned from the β GRIP domain reveals the possible positions of the functionally well-characterized but structurally elusive inhibitory tracts and furin and other protease sites in the α and γ GRIP domains. Studies by the Kleyman group have identified 8- and 11-mer peptide tracts within the α and γ GRIP domains, respectively, which are implicated in channel gating[98,99,227]. Sequence comparison between the three subunits suggests that the inhibitory tracts contain the P1 strand (**Figure 2.2, Figure 2.25b-d and Figure 2.26b-d**). Based on this configuration, the first furin site lies at the N-terminal side of P1 whereas the second protease site (furin for α and other protease sites for γ) is likely located at the C-terminal side of P2. The anti-parallel organization of P1 and P2 strands places the two protease sites in close proximity to each other. We speculate that this arrangement allows for efficient proteolysis, especially for the cleavage of the α subunit by furin.

Aromatic pocket

The first crystal structure of ASIC identified the finger and the thumb domains as major players in ion channel gating. Rearrangements of these domains are coupled to the TMD via the wrist. Additionally, the crystal structure provided insight into the domain essential for fine-tuning ASIC pH-response, deemed the acidic pocket, formed by the β-ball, finger, and thumb domains of one subunit, and the palm domain of the adjacent subunit[228]. While the acidic pockets in ASIC are lined with negatively charged residues, the equivalent crevices in ENaC are replete with aromatic residues. In fact, aside from Ser428 of Δβ (Asp346 in ASIC), the equivalent sites in the thumb domain that are acidic in ASIC are occupied by tyrosines in all three subunits (**Figure 2.2, Figure 2.3 and Figure 2.27**)[4]. Accordingly, the pocket that is largely occupied by α2 in ΔENaC is referred to here as the aromatic pocket.

Tucked in the aromatic pocket, α2 makes contacts with all critical elements of the gating machinery in ENaC. This observation is consistent with studies finding that site-directed mutagenesis perturbing residues in the α2 results in changes in Na^+ self-inhibition and binding of the P1 segment of the GRIP domain[227]. In all three ENaC subunits, the α2 forms contacts with the thumb, α1 helix, the β6-β7 loop and the GRIP domain, and with the knuckle and the upper palm domains in the adjacent subunit (**Figure 2.27**). Moreover, studies using synthesized 8-mer (LPHPLQRL)[98] and 11-mer peptides (RFLNLIPLLVF)[99], the inhibitory peptides of α and γ subunits, respectively, have identified residues in α2 to be critical to the binding of the inhibitory peptides. These peptides pack against α2 and form a wedge between the thumb domain and α1 in the ΔENaC structure (**Figure 2.25b-d and Figure 2.26b-d**). These inhibitory peptides contain prolines that introduce a kink within the tract that may serve as a point that divides P1 into two segments: the N-terminal side, which interacts with the finger and thumb; and the C-terminal side, which interacts primarily with α2 and P3. The observed orientation of the P1 segment is consistent with the cross-linking experiments by Kashlan et al., which provided two major findings: 1) the inhibitory tracts adopt an extended conformation and 2) the N-terminal side of the peptide binds near the thumb/finger interface[227,229].

The potential map for α-P1 suggests that the N-terminal side mirrors that of β-P1 forging contacts with the α1 helix (**Figure 2.26b, c**). In contrast, the potential map for the γ-P1 suggests that the peptide interacts with the thumb and α1/α2 more extensively and extends towards α3 (**Figure 2.26d**). These distinct points of contact with the finger and thumb domains between the α- and γ-P1 segments may influence the extent to which the subunits influence channel P_o. While removal of the inhibitory tract in α transitions the channel to an intermediate P_o state, excision of the γ-P1 segment places the channel in the high P_o state; this high P_o state can be accomplished

without the removal of the α-P1[97]. The visual evidence of direct interactions between P1 and the finger and thumb domains demonstrated in the ΔENaC structure sheds light into how these inhibitory tracts can modulate channel function in ENaC.

Mechanism

ΔENaC follows a common organization that was first observed in ASICs: a scaffolding structure in the upper palm, the flexible lower palm which is tethered to the TM and thumb, and the β-ball (**Figure 2.22a, b**)[4]. However, the specialized finger domains deviate from what is observed in ASIC and such deviations accommodate the distinct functions between the proton sensors of ASIC and the protease-sensitive regulators of ENaC.

Key gating structures are preserved, albeit with specific structural configurations in both ASIC and ENaC supporting the idea that the superfamily of ENaC/DEG channels conform to a gating scheme that involves conformational changes of the finger and thumb domains, rearrangements that are propagated to the ion channel via the wrist[4]. In the case for ENaC, a speculative model for gating involves proteolysis and the subsequent removal of the P1 segment, which serves as a wedge, inducing rearrangements of the finger and thumb domains (**Figure 2.28**).

The structural work presented here provides new insight into ENaC assembly and gating. The structure unveils the positions of the GRIP domains, specifically the key peptidyl tracts that inhibit ENaC activity, and the distinct interactions that they mediate with the finger and thumb domains. Furthermore, it reveals that there are different interactions between the finger and knuckle domains at each subunit interface, and between the base of the thumb and the TMD in

the wrist region suggesting that each subunit differentially contributes towards gating the channel, supporting electrophysiological findings. Importantly, the structure provides the first molecular model for protease-dependent regulation of ENaC opening and Na^+ and water homeostasis.

Acknowledgements

We thank the Multiscale Microscopy Core (OHSU) and the Advanced Light Microscopy Core (OHSU) for support with microscopy and the Advanced Computing Center (OHSU) for computational support. We are grateful to L. Vaskalis for assistance with figures, to D. Cawley for monoclonal antibody production, to D. Ellison, M. Mayer and R. Goodman for advice, and to A. Bouneff for naming the GRIP domain. We also want to thank the members of the Gouaux and Whorton labs for helpful discussions. This work was supported by the NIH (I.B., DP5OD017871).

Tables

Table 1: Statistics of data collection, three-dimensional reconstruction, and model refinement.

Statistic	ΔENaC 10D4		ΔENaC 7B1-10D4	
	1	2	1	2
FAb	10D4		7B1 & 10D4	
Microscope	FEI Krios		FEI Krios	
Voltage (kV)	300		300	
Detector	Gatan K2 Summit		Gatan K2 Summit	
Detector Mode	Super resolution	Counting	Super resolution	Super resolution
Defocus range (μm)	-1.5 – -3.5	-1.5 – -3.0	-1.0 – -2.5	-0.8 – -1.75
Exposure time (s)	15	15	10	12
Dose rate ($e^-/Å^2$/frame)	3.7	3.3	6.2	6
Frames per movie	30	60	40	48
Pixel size (Å)	1.33	1.33	1.33	1.33
Total dose ($e^-/Å^2$)	54	50	62	71
Motion correction	UCSF MotionCor2		UCSF MotionCor2	
CTF estimation	GCTF		GCTF	
Particle picking	DoG Picker		DoG Picker & Manual	
2D/3D classification	Relion 2.0		Relion 2.0	
3D classification and refinement	Relion 2.0 cryoSPARC 1	Relion 2.0 cryoSPARC 1	cryoSPARC 1 Frealign	cryoSPARC 1 Frealign
Initial reconstruction	cryoSPARC		cryoSPARC	Frealign
Symmetry	C1		C1	C1
Particles processed	41 459		329 180	329 180
Particles refined	41 459		244 223	290 007
Resolution masked (Å)	5.4		4.2	4.2
Map Sharpening B-factor ($Å^2$)			-200	-200
Final map reconstruction			Frealign	
Symmetry			C1	
Particles refined			302 263	
Resolution masked (Å)			3.9	
Protein residues			1 813	
Resolution(FSC= 0.143, Å)			4.0	
Molprobity score			5	
C_β deviations			0	
Ramachandran outliers			0	
Ramachandran allowed			4%	
Ramachandran favored			96%	
Bond length rmsd			0.003	
Bond angle rmsd			0.656	

Table 2.1. Cryo-EM data collection and processing statistics.

Figures and legends

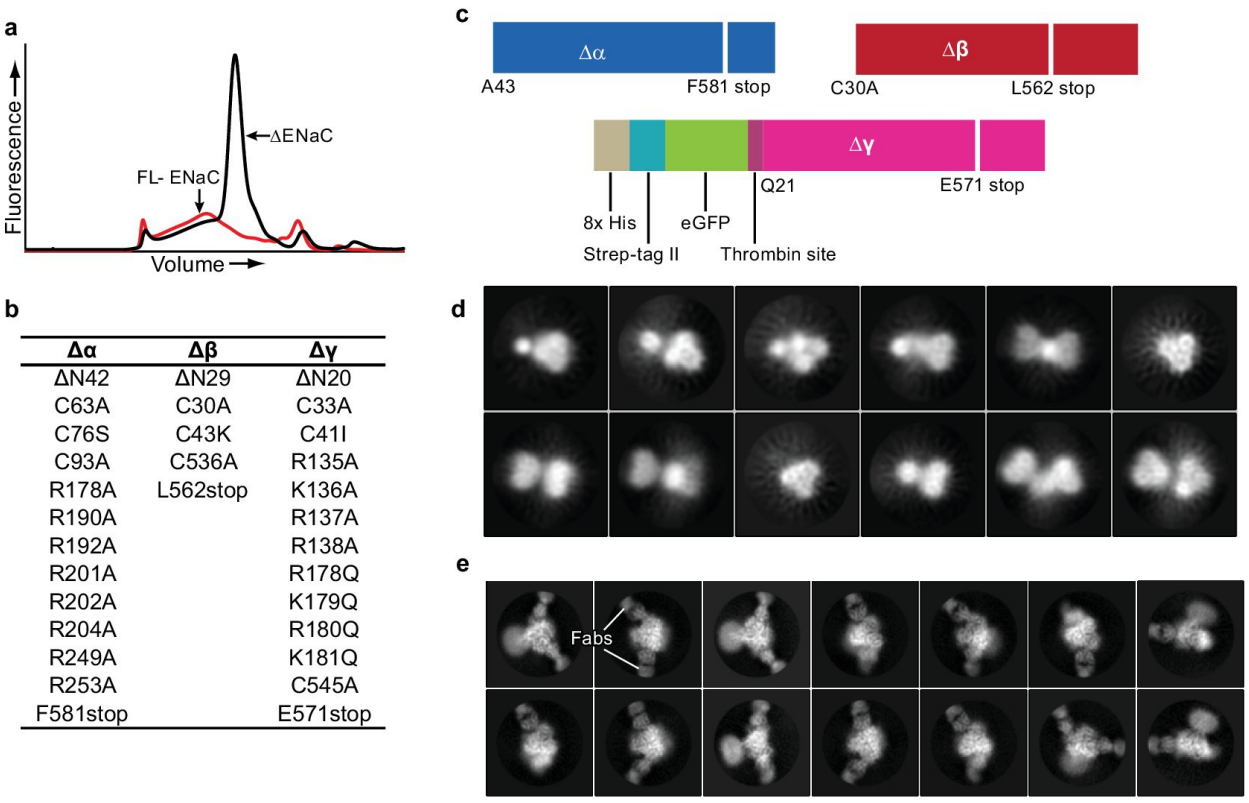

Δα	Δβ	Δγ
ΔN42	ΔN29	ΔN20
C63A	C30A	C33A
C76S	C43K	C41I
C93A	C536A	R135A
R178A	L562stop	K136A
R190A		R137A
R192A		R138A
R201A		R178Q
R202A		K179Q
R204A		R180Q
R249A		K181Q
R253A		C545A
F581stop		E571stop

Figure 2.1. Creation and analysis of ΔENaC. a, Representative FSEC traces of full-length ENaC (FL-ENaC, red) and ΔENaC (black). **b,** Summary of mutations in ΔENaC. **c,** Summary of ΔENaC constructs. **d,** Representative 2D class averages of ΔENaC show that pseudosymmetry inherent in ENaC hampers particle alignment. **e,** Representative 2D class averages of ΔENaC-7B1/10D4 complex showing increased detail due to alignment aid from Fabs.

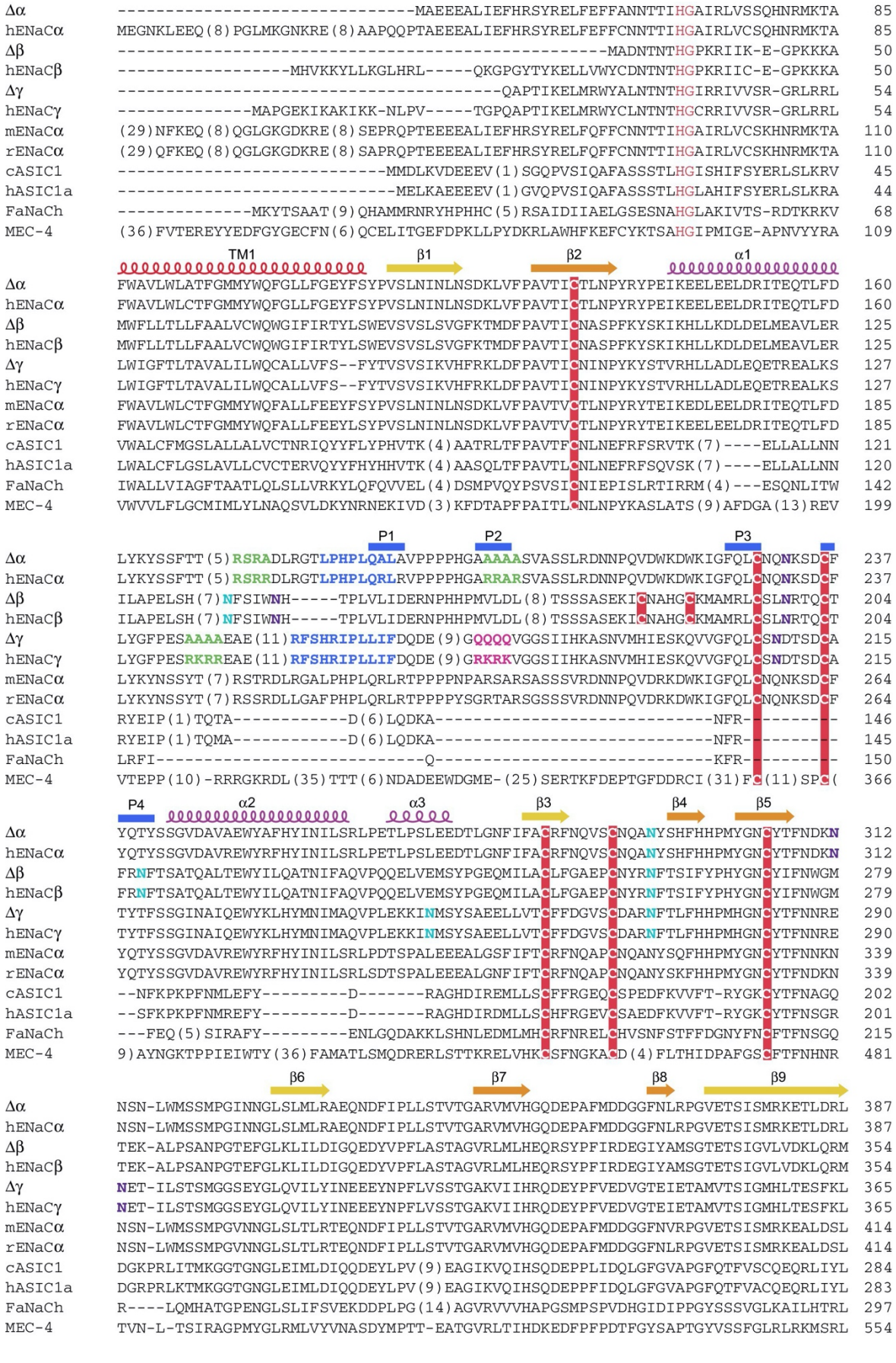
Δα
hENaCα
Δβ
hENaCβ
Δγ
hENaCγ
mENaCα
rENaCα
cASIC1
hASIC1a
FaNaCh
MEC-4
TM1
β1
β2
α1
P1
P2
P3
P4
α2
α3
β3
β4
β5
β6
β7
β8
β9

Figure 2.2. Sequence alignment of ENaC with other members of the ENaC/DEG superfamily (human ENaC α residues 1-387). Sequence alignment of ΔENaC with full-length ENaC from human (hENaCα, GenBank ID: 4506815; hENaCβ, 124301096; hENaCγ, 42476333), chicken acid sensing ion channel (cASIC1a, 94957761), human (hASIC1a, 21536351), FMRF-amide activated sodium channel (FaNach, 1149511) and degenerin (MEC-4, 1297371). The sequences were aligned with Clustal Omega and manually adjusted. The secondary structure allocation is based on Δβ. Coloring or shading is as follows: HG motif and selectivity filter are in red, cysteine participating in disulfide bonds are in red boxes, glycosylation sites present in cryo-EM map in cyan, while predicted sites not observed in cryo-EM map are in purple, furin sites are in green, prostasin sites are in magenta, and the 8-mer and 11-mer peptide discussed in the main text are in blue.

Figure 2.3. Sequence alignment of ENaC with other members of the ENaC/DEG superfamily (human ENaC α residues 388-669).

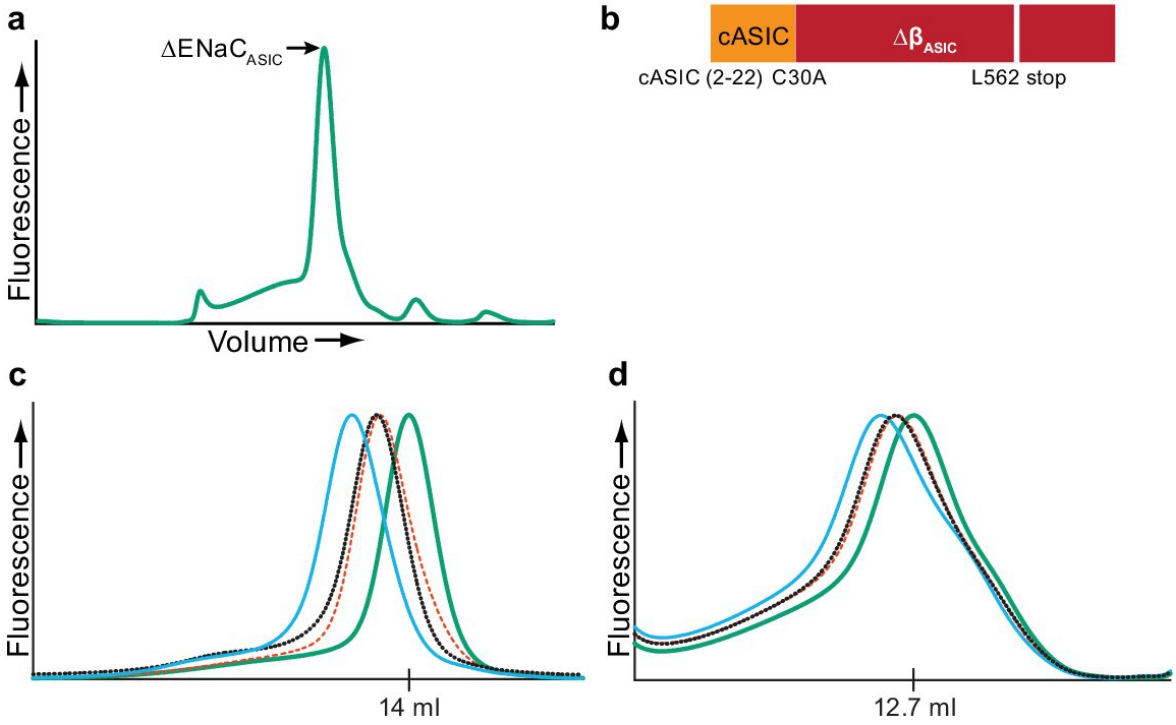

Figure 2.4. Fab generation. a, Representative FSEC trace of ΔENaC$_{ASIC}$ **(b)**, which was used to generate Fabs. **c and d,** Representative FSEC traces of ΔENaC **(c)** and FL-ENaC **(d)** in complex with Fabs. The ΔENaC and FL-ENaC (solid green trace) were expressed in suspension-adapted HEK293S GnTI$^-$ and HEK 293T/17, respectively, using baculovirus. The binding of one (red and black dotted traces) or both (solid blue trace) Fabs incrementally shifts the elution volume to a larger molecular weight, indicating recognition of independent moieties.

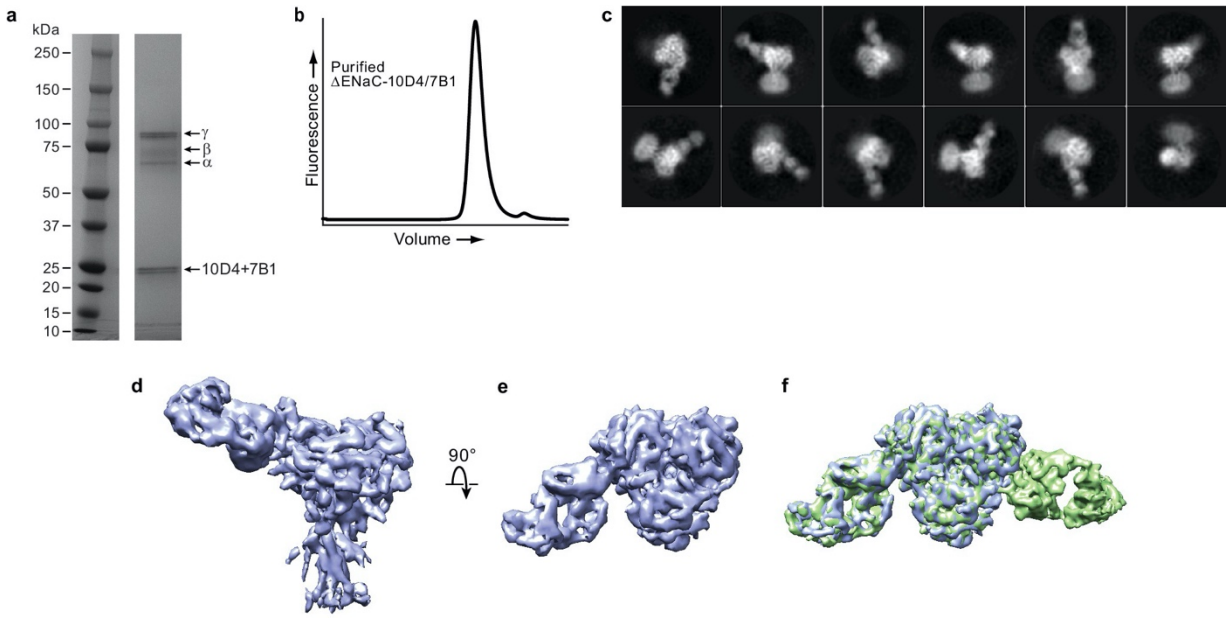

Figure 2.5. Fab binding properties. a, Coommassie-stained SDS-PAGE gel of purified ΔENaC-7B1/10D4 complex. **b,** Representative FSEC trace of purified ΔENaC-7B1/10D4. **c,** Representative 2D class averages of ΔENaC-10D4 complex show that 10D4 Fab facilitates particle alignment. **d and e,** Cryo-EM density of ΔENaC-10D4 viewed parallel **(d)** and perpendicular **(e)** to the membrane. **f,** Superposition of the ΔENaC-10D4 and ΔENaC-7B1/10D4 maps show subunit-specific binding of the Fabs.

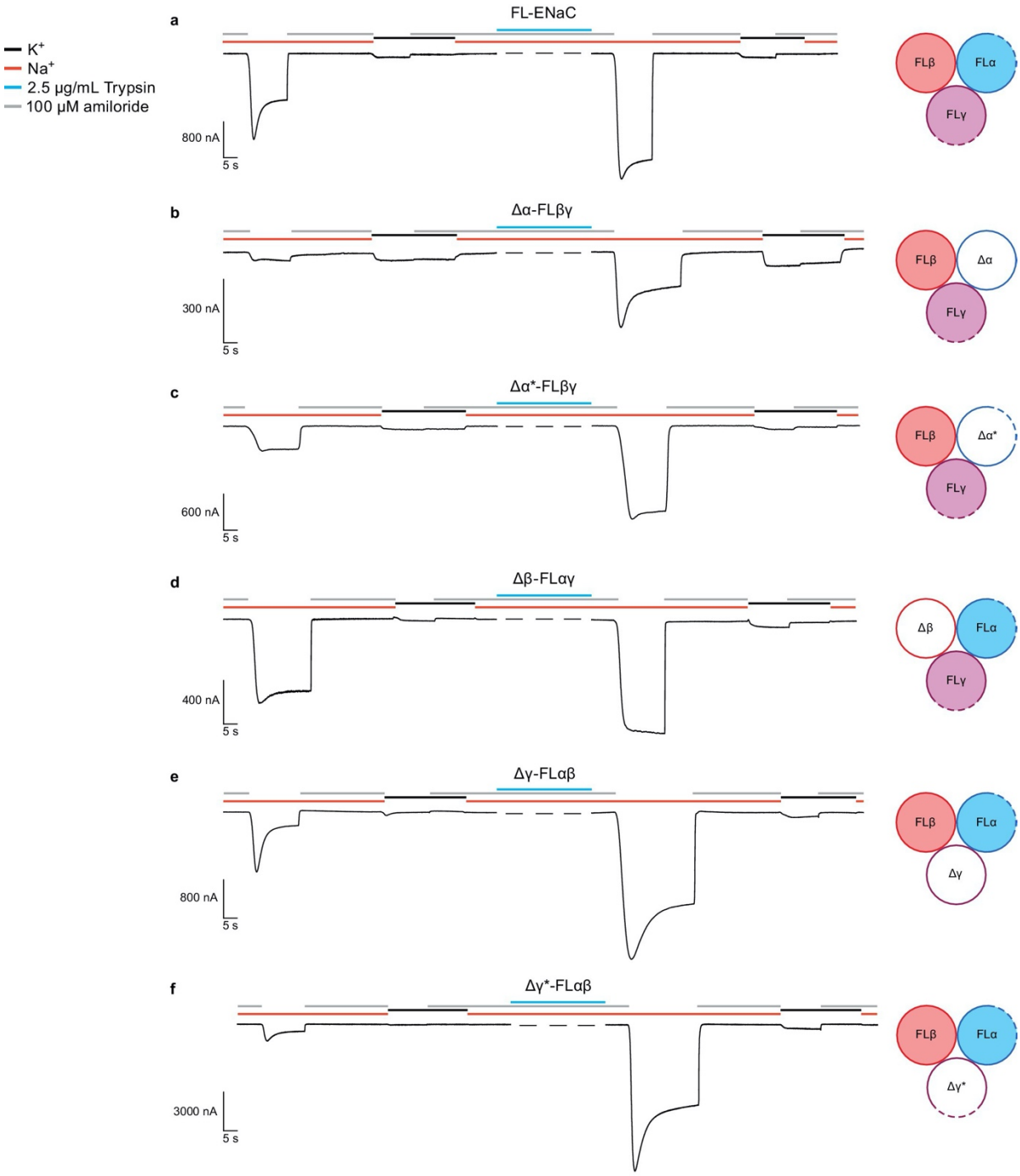

Figure 2.6. Functional characterization of ΔENaC by TEVC. a, Representative current trace of FL-ENaC shows selectivity of Na^+ over K^+, block by amiloride and sensitivity to trypsin treatment (2.5 µg/mL for 5 min) by a 2.22 ± 0.49 fold increase in steady state currents post-trypsin treatment (n = 3). The cartoon located on the right side of each current trace represents

the combination of subunits injected in the oocytes. Filled circles represent FL-ENaC subunits while open represent the ΔENaC subunits. Dotted lines represent ENaC subunits that contain the intact protease sites. **b-f,** Representative current traces of Δα-FLβγ **(b)**, Δα*-FLβγ **(c)**, Δβ-FLαγ **(d)**, Δγ-FLαβ **(e)**, Δγ*-FLαβ **(f)** demonstrate that the ΔENaC subunits can form a functional channel with two FL-ENaC subunits that are selective for Na^+ over K^+ and sensitive to amiloride and trypsin treatment. Currents after trypsin treatment increased by 5.15 ± 1.13 **(b)**, 4.42 ± 0.61 **(c)**, 1.46 ± 0.1 **(d)**, 9.52 ± 2.88 **(e)** and 13.26 ± 5.67 **(f)** fold (n = 3 for all combinations).

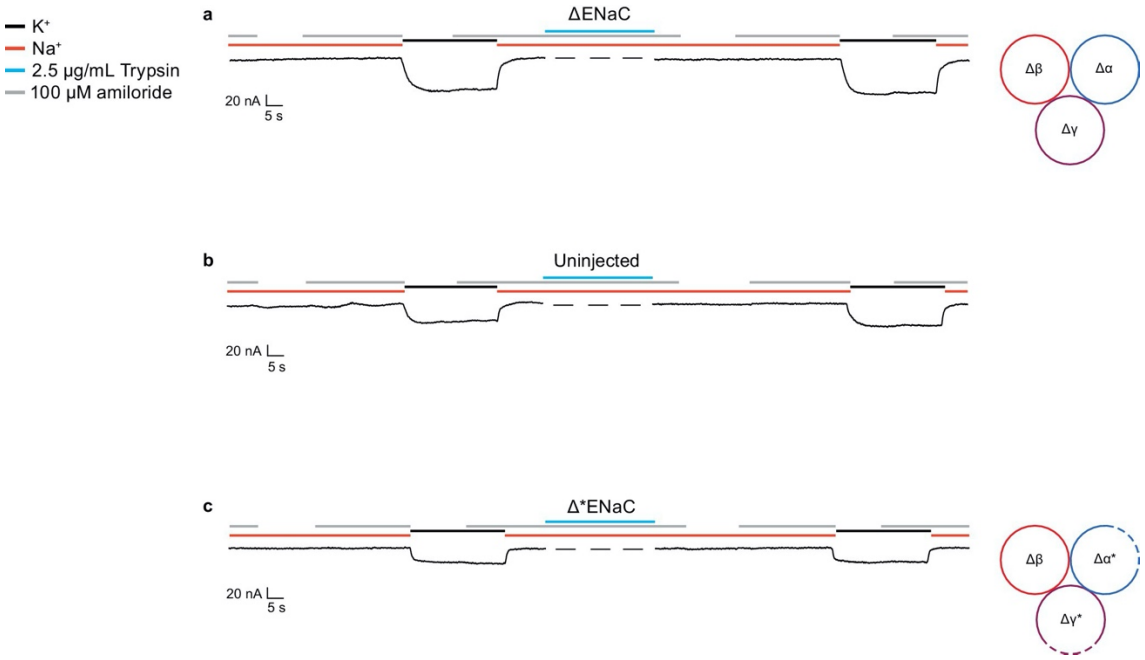

Figure 2.7. Current measured in oocytes injected with ΔENaC resembles currents observed in uninjected oocytes. a-c, Representative current traces of ΔENaC (Δα-Δβ-Δγ) **(a)**, uninjected oocytes **(b)**, and Δ*ENaC (Δα*-Δβ-Δγ*) **(c)**.

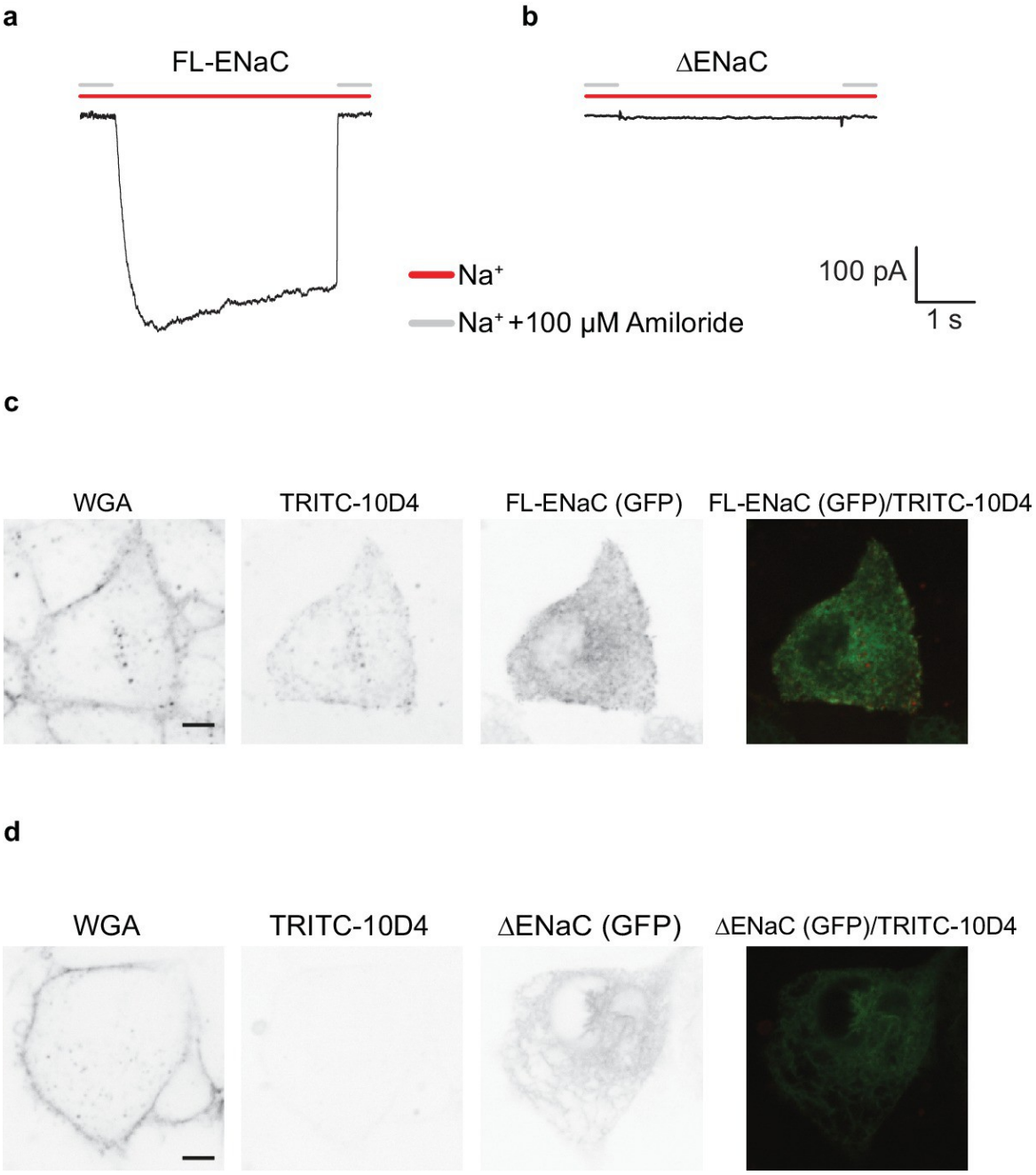

Figure 2.8. FL-ENaC and ΔENaC trafficking in HEK 293S GnTI$^-$ cells. Representative current traces of FL-ENaC **(a)** and ΔENaC **(b)** expressed in GnTI$^-$ cells. Cells expressing FL-ENaC demonstrated inward Na^+ currents that were blocked by 100 μM amiloride. Na^+ currents

were not detected in cells expressing ΔENaC. Live confocal microscopy analysis of cells expressing FL-ENaC **(c)** and ΔENaC **(d)** with eGFP fusion (third column) stained with WGA (first column) and TRITC-labeled 10D4 (second column) show that FL-ENaC is expressed on the cell surface while ΔENaC is not. Overlay of the eGFP and TRITC channels are shown in the fourth column.

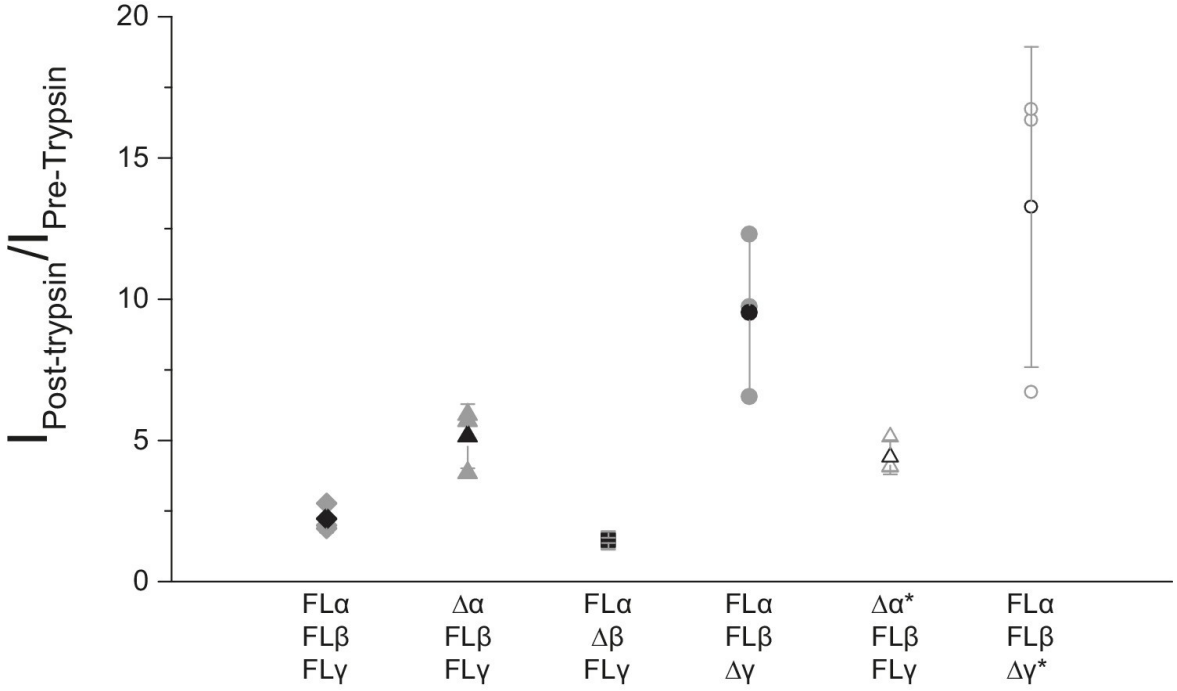

Figure 2.9. Functional characterization of ΔENaC by TEVC. Oocytes treated with trypsin demonstrated increased current amplitude that were 2.22 ± 0.49, 5.15 ± 1.13, 4.42 ± 0.61, 1.46 ± 0.10, 9.52 ± 2.88 and 13.26 ± 5.67 fold larger than before trypsin application in FL-ENaC, Δα-FLβγ, Δα*-FLβγ, Δβ-FLαγ, Δγ-FLαβ, Δγ*-FLαβ, respectively (n = 3 for per subunit combinations).

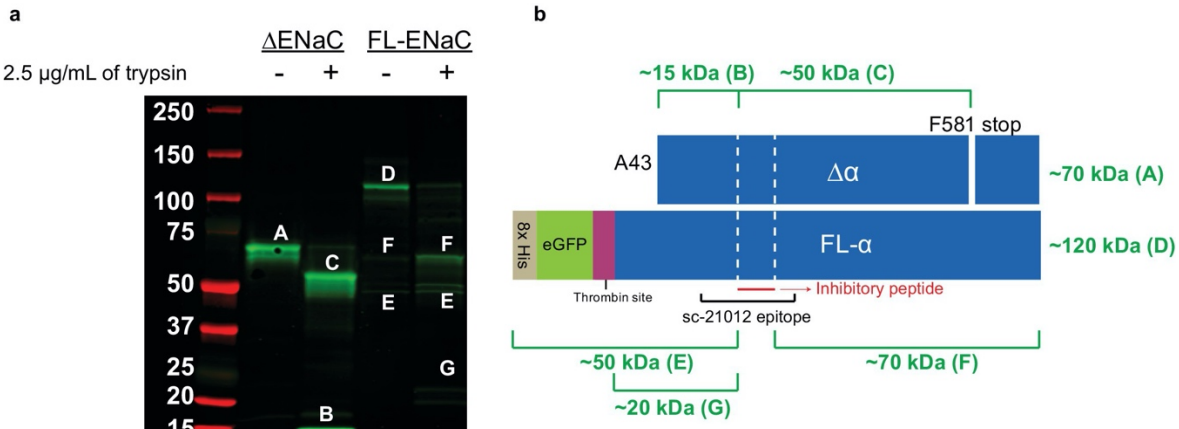

Figure 2.10. Cleavage of ENaC Δα and FL-α by trypsin shows expected banding. a, Western blot (IB: ENaC α subunit, SC-21012) of purified ENaC Δα and FL-α subunits treated with trypsin (7 µg ENaC/well; 2.5 µg trypsin/mL; incubated at room temperature for 10 min). The uncut Δα band (band A) is cut into the fragment N-terminal of the inhibitory peptide (band B) and C-terminal of the inhibitory peptide (band C). The uncut FL-α lane already has some cut ENaC (bands F and E) in addition to uncut (band D). This is expected due to the unperturbed cleavage sites in FL-α. Upon trypsin treatment, we observe stronger intensity for the two fragments, as well as the N-terminal fragment with liberated eGFP (band G). **b,** Schematic of ENaC band progenitors. White dotted lines, furin sites.

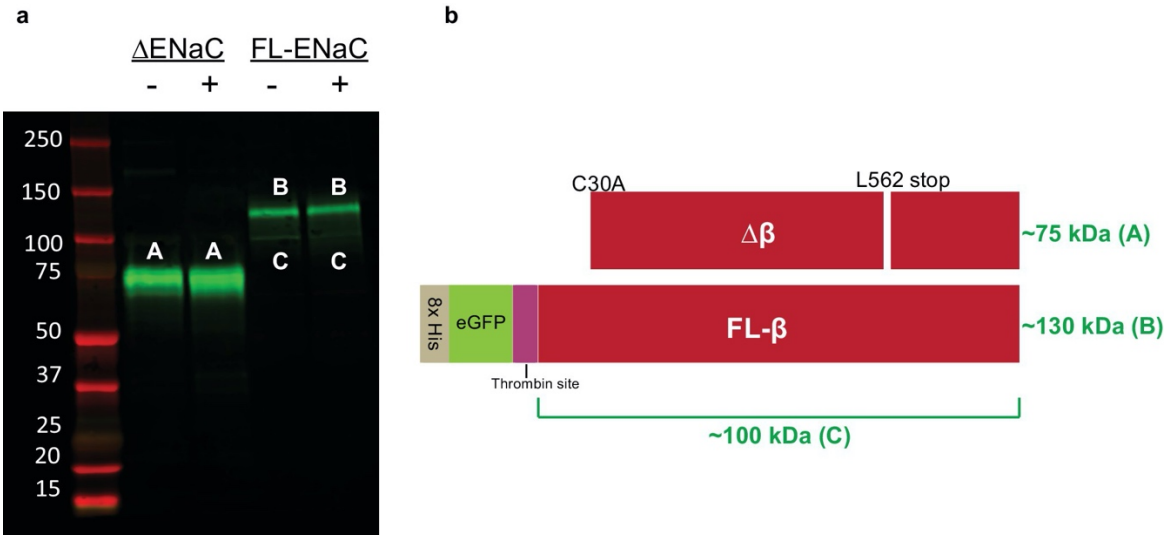

Figure 2.11. Cleavage of ENaC Δβ and FL-β by trypsin shows expected banding. a, Western blot (IB: ENaC β subunit, SC-21013) of purified ENaC Δβ and FL-β subunits treated with trypsin as in **Figure 2.10**. As expected, neither Δβ (band A) nor FL-β (band B) is cleaved by trypsin treatment. Some eGFP is liberated from FL-β at the trypsin site, giving rise to a faint band (band C). **b,** Schematic of ENaC band progenitors.

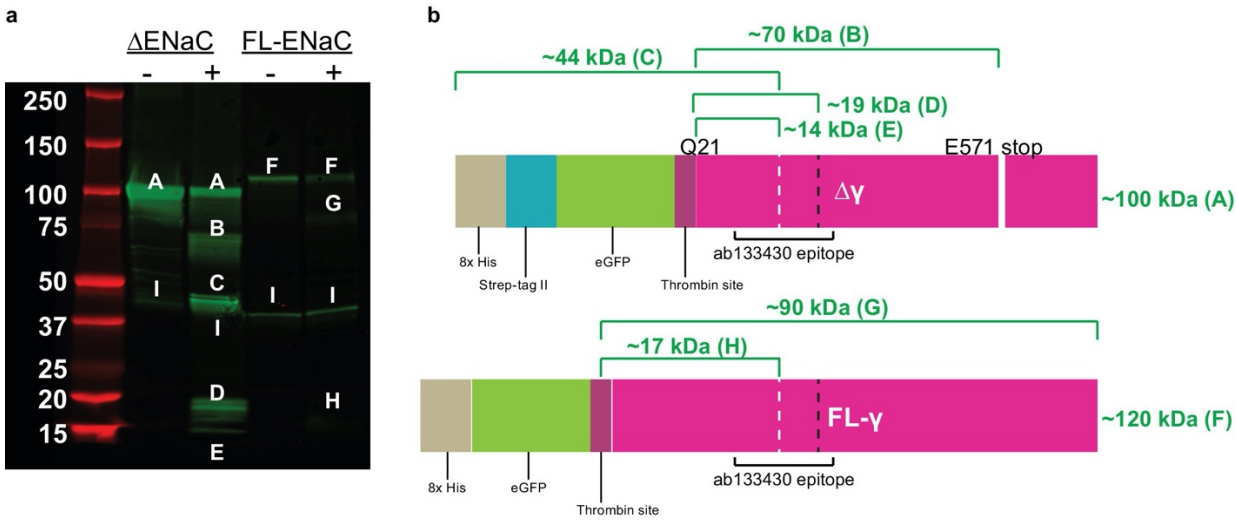

Figure 2.12. Cleavage of ENaC Δγ and FL-γ by trypsin shows expected banding. a, Western blot (IB: γ subunit, abcam ab133430) of purified ENaC Δγ and FL-γ subunits treated with trypsin as in **Figure 2.10**. When treated with trypsin, the uncut Δγ band (band A) loses eGFP (band B), is cleaved at or near the N-terminal furin site (band C), at or near the thrombin and prostasin sites (band D), at or near the thrombin and furin sites (band E). FL-γ (band F) is cut at the thrombin site (band G) and at or near the thrombin and furin sites (band H). A non-specific band is present in all lanes (band I). **b,** Schematic of trypsin treated ENaC Δγ and FL-γ. White dashed lines, furin site. Black dashed line, prostasin site.

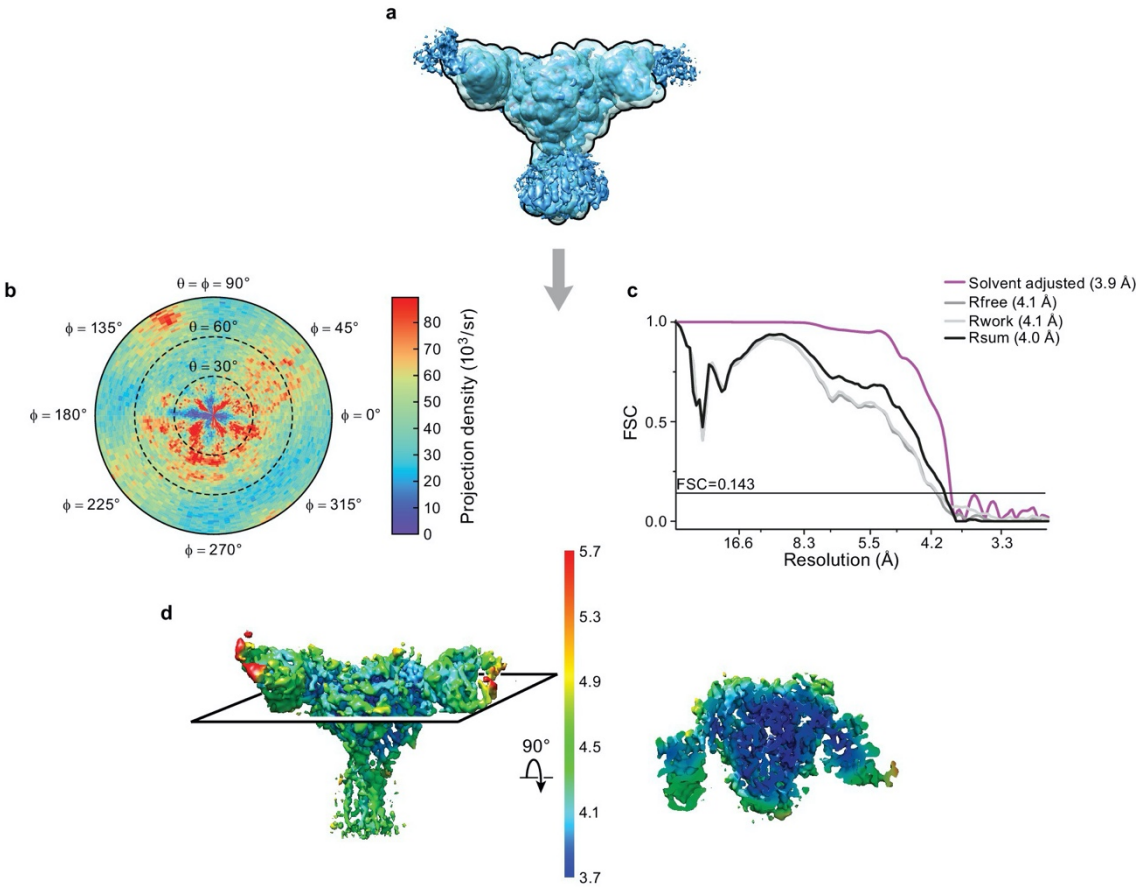

Figure 2.13. Cryo-EM analysis of final 3D reconstruction map. a, Outline of mask used in the final 3D refinement of ΔENaC-7B1/10D4 complex. **b,** Angular distribution of particle projections of the ΔENaC-7B1/10D4 complex. **c,** Solvent adjusted FSC curve (purple) by cisTEM along with FSC curve between the atomic model of ΔENaC-7B1/10D4 complex and half map 1 (R_{free} – dark grey), half map 2 (R_{work} – light grey) and final reconstruction map (R_{sum} – black). The solid line indicates FSC = 0.143. **d,** 3D map colored according to local resolution estimation using Bsoft. Blue indicates regions where local resolution is estimated to be ~ 3.7 Å.

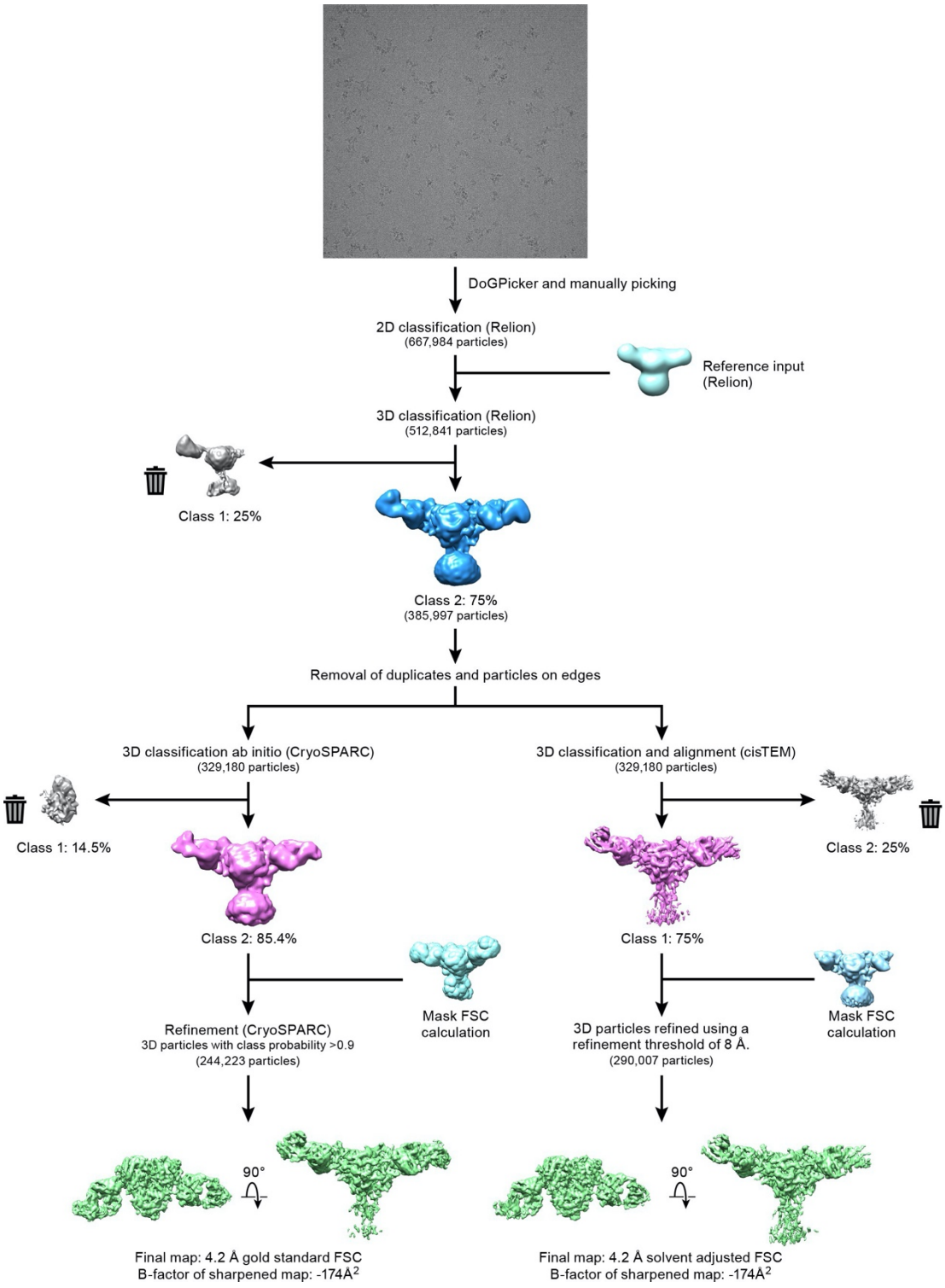

Figure 2.14. Cryo-EM data processing. Workflow of the three-dimensional reconstruction of ΔENaC-7B1/10D4 complex using cryoSPARC and cisTEM programs.

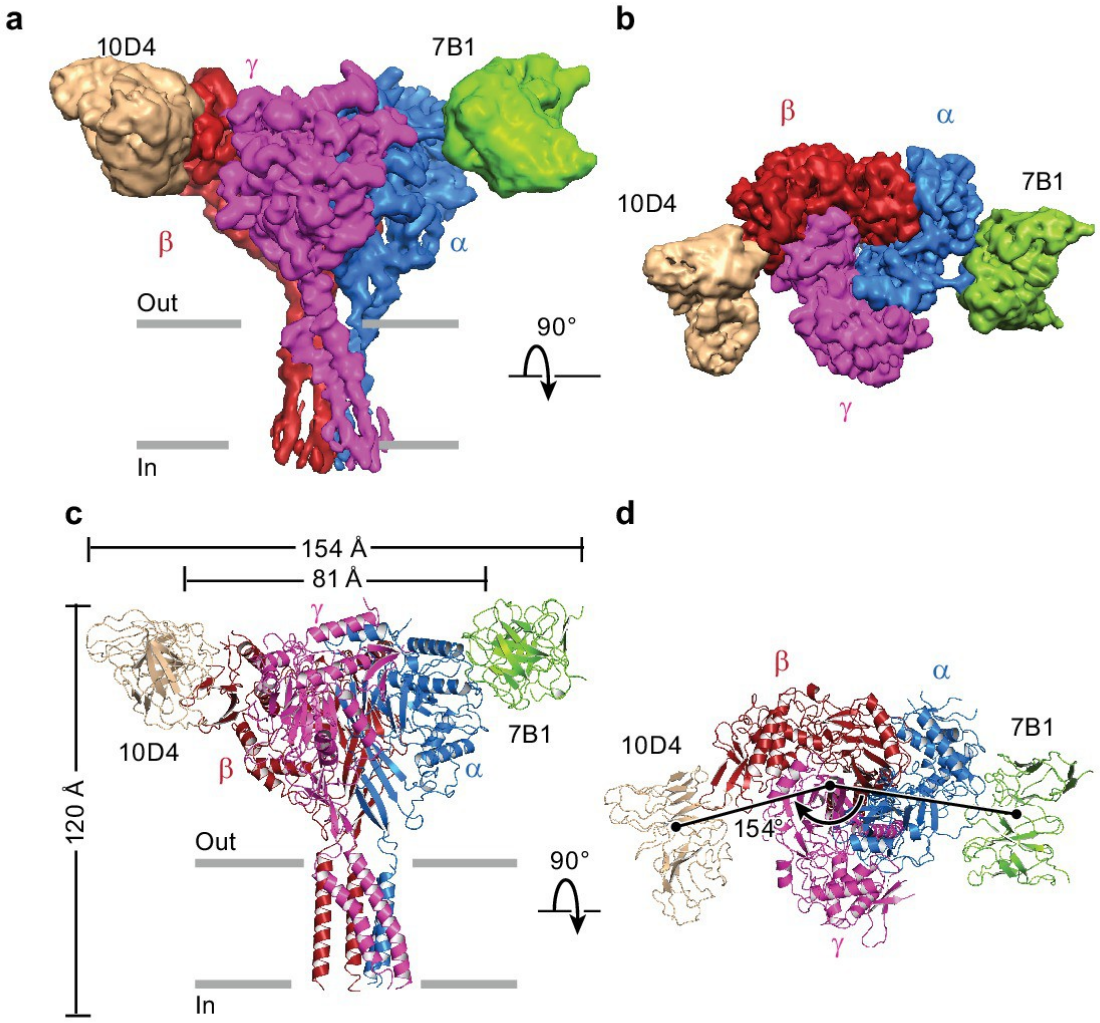

Figure 2.15. Architecture of the human epithelial sodium channel. a and b, Cryo-EM map of the ΔENaC-7B1/10D4 complex viewed parallel **(a)** and perpendicular **(b)** to the membrane. The α, β and γ subunits are colored blue, red and magenta, respectively. The 7B1 and 10D4 Fv densities are colored green and wheat, respectively. **c and d,** Cartoon representation of the ΔENaC-7B1/10D4 complex viewed and colored as in **(a)** and **(b)**. The dimensions of the complex and ΔENaC alone are indicated. The centers of mass of the Fv's make 154º angle.

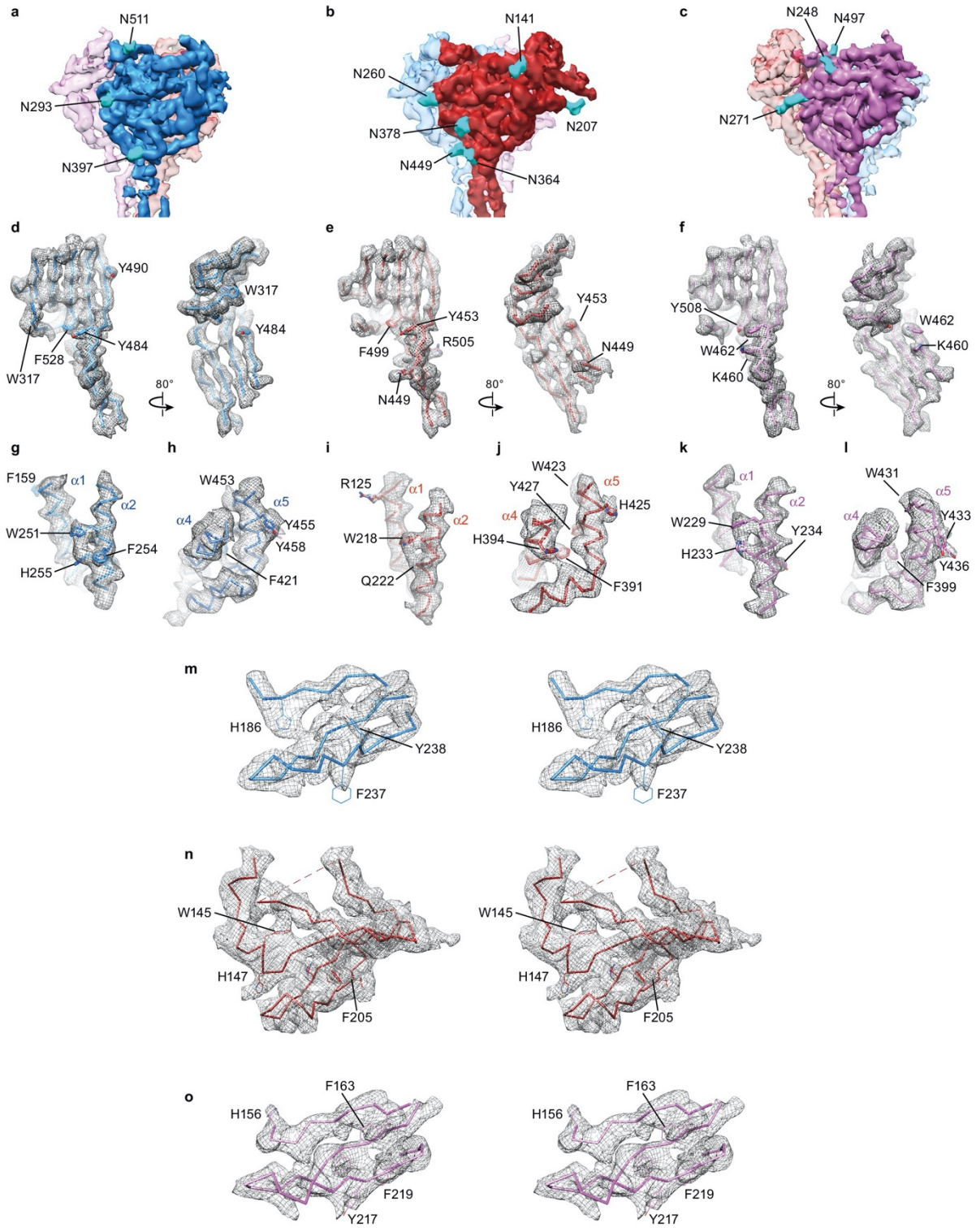
a
N511
N293
N397
b
N141
N260
N207
N378
N449
N364
c
N248
N497
N271
d
Y490
W317
Y484
F528
W317
80°
e
Y453
F499
R505
N449
Y453
N449
80°
f
Y508
W462
K460
W462
K460
80°
g
F159
α1
α2
W251
F254
H255
h
W453
α5
α4
Y455
Y458
F421
i
R125
α1
α2
W218
Q222
j
W423
Y427
α5
H425
α4
H394
F391
k
α1
α2
W229
Y234
H233
l
W431
α5
α4
Y433
Y436
F399
m
H186
Y238
F237
H186
Y238
F237
n
W145
H147
F205
W145
H147
F205
o
F163
H156
F219
Y217
F163
H156
F219
Y217

Figure 2.16. Unique map features facilitated subunit identification and model building. a-c, Potential map of ΔENaC highlighting features of glycosylation which are colored cyan. There are three glycosylation sites in α **(a)**, six in β **(b)**, and three in γ **(c)**. The map is sharpened with a lower B-factor (-100 $Å^2$) for better visualization of glycosylation site features. **d-l,** Well-ordered aromatic and basic residues found in the palm domain **(d-f)**, finger domain **(g, i, k)** and thumb domain **(h,j,l)** provided further validation of subunit identity. The β strands that comprise the palm domain (β1, β3, β6, β9-12) are well ordered in all three subunits α **(d)**, β **(e)** and γ **(f)**. The α2-helices in the finger domain display potential map features of several aromatic residues including a highly conserved Trp residue, W251 in α **(g)**, W218 in β **(i)** and W229 in γ **(k)**. The α4 and α5 helices in the thumb domains display potential map features for aromatic residues that are shared, but also distinct between α **(h)**, β **(j)** and γ **(l)**. Stereo view showing potential map of the GRIP-domains of α **(m)**, β **(n)** and γ **(o)**.

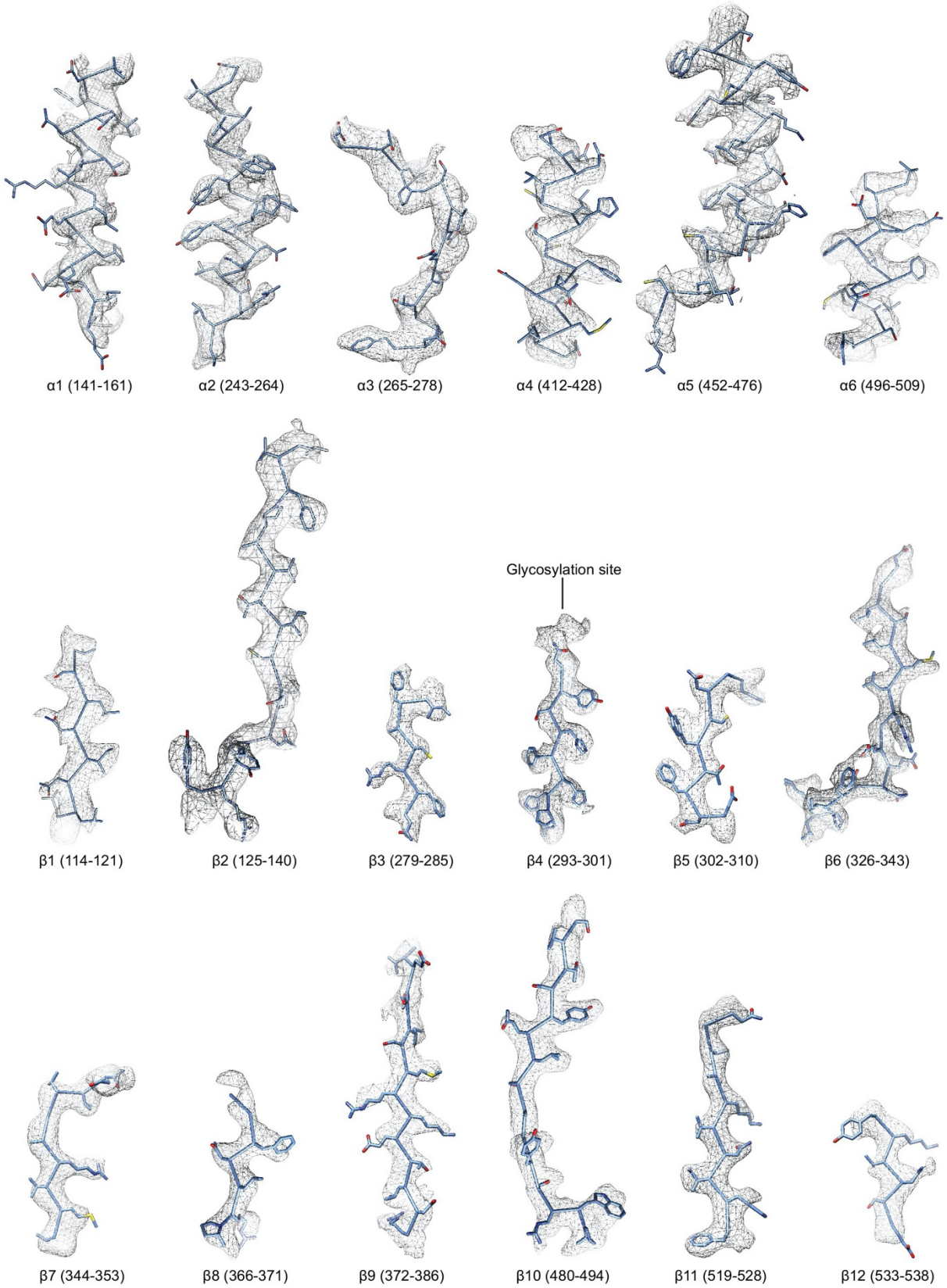
α1 (141-161)
α2 (243-264)
α3 (265-278)
α4 (412-428)
α5 (452-476)
α6 (496-509)
Glycosylation site
β1 (114-121)
β2 (125-140)
β3 (279-285)
β4 (293-301)
β5 (302-310)
β6 (326-343)
β7 (344-353)
β8 (366-371)
β9 (372-386)
β10 (480-494)
β11 (519-528)
β12 (533-538)

Figure 2.17. Cryo-EM map of Δα secondary structures. Regions of the Δα ENaC subunit model shown in stick representation superimposed with the potential map in light grey mesh, contoured between 7.5 and 8.0 sigma. The model is colored as in **Figure 2.15**.

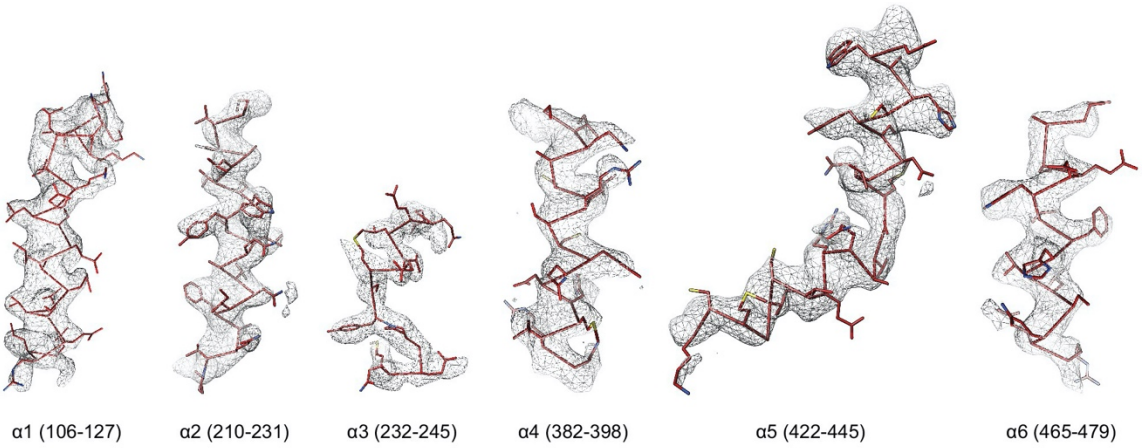
α1 (106-127)
α2 (210-231)
α3 (232-245)
α4 (382-398)
α5 (422-445)
α6 (465-479)

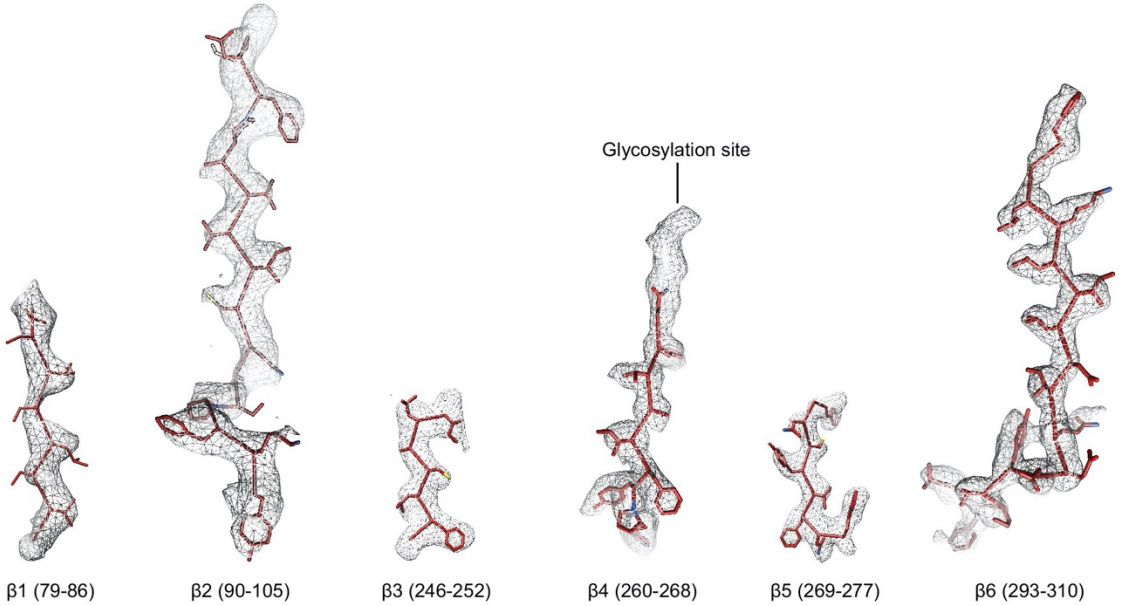
Glycosylation site
β1 (79-86)
β2 (90-105)
β3 (246-252)
β4 (260-268)
β5 (269-277)
β6 (293-310)

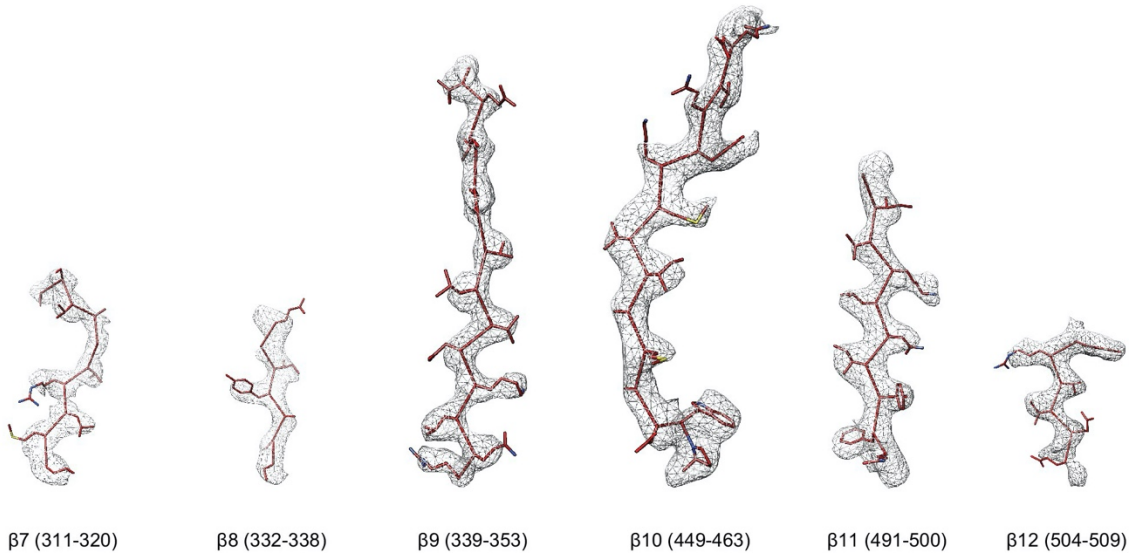
β7 (311-320)
β8 (332-338)
β9 (339-353)
β10 (449-463)
β11 (491-500)
β12 (504-509)

Figure 2.18. Cryo-EM map of Δβ secondary structures. Regions of the Δβ ENaC subunit model shown in stick representation superimposed with the potential map in light grey mesh, contoured between 7.5 and 8.0 sigma. The model is colored as in **Figure 2.15**.

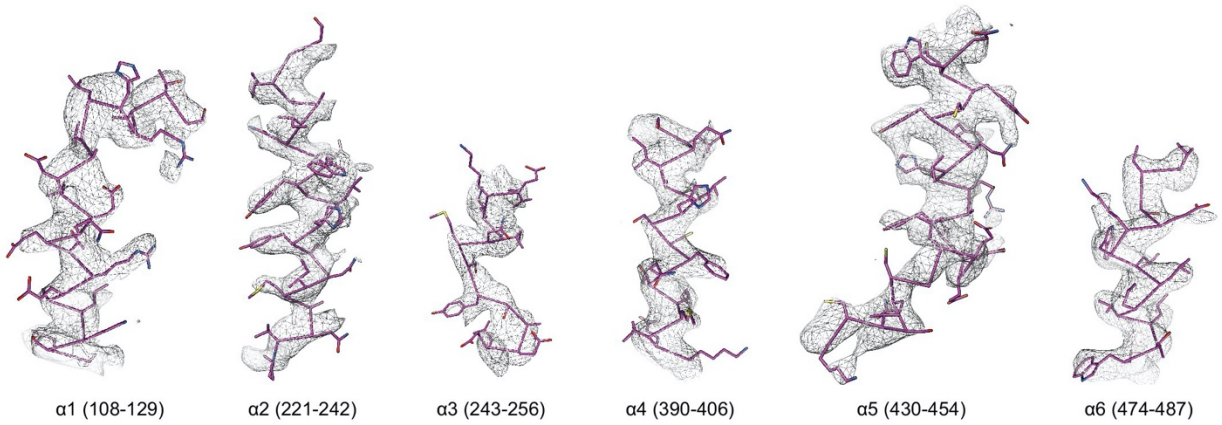

α1 (108-129) α2 (221-242) α3 (243-256) α4 (390-406) α5 (430-454) α6 (474-487)

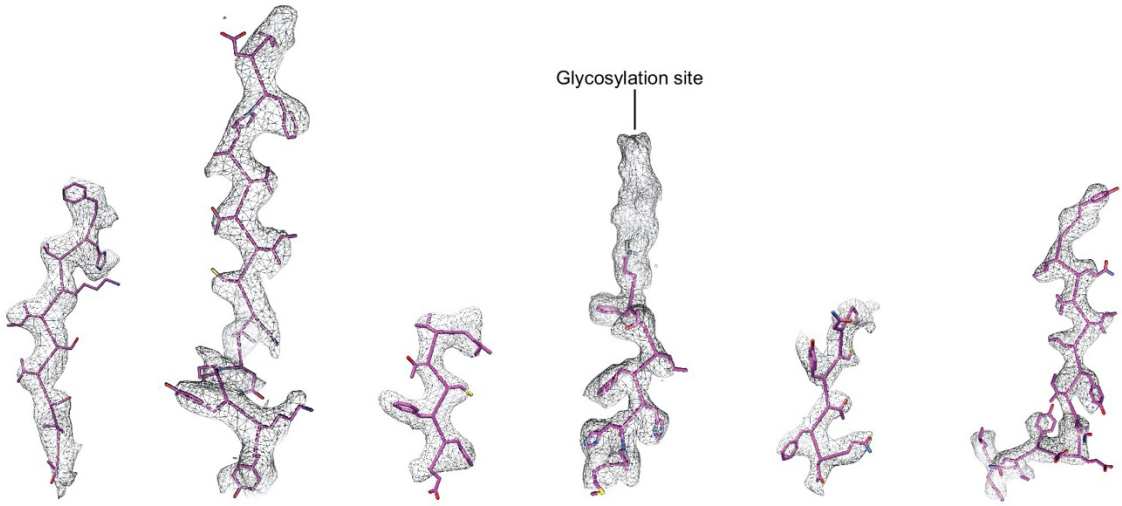

β1 (80-89) β2 (92-107) β3 (257-263) β4 (271-279) β5 (280-288) β6 (304-321)

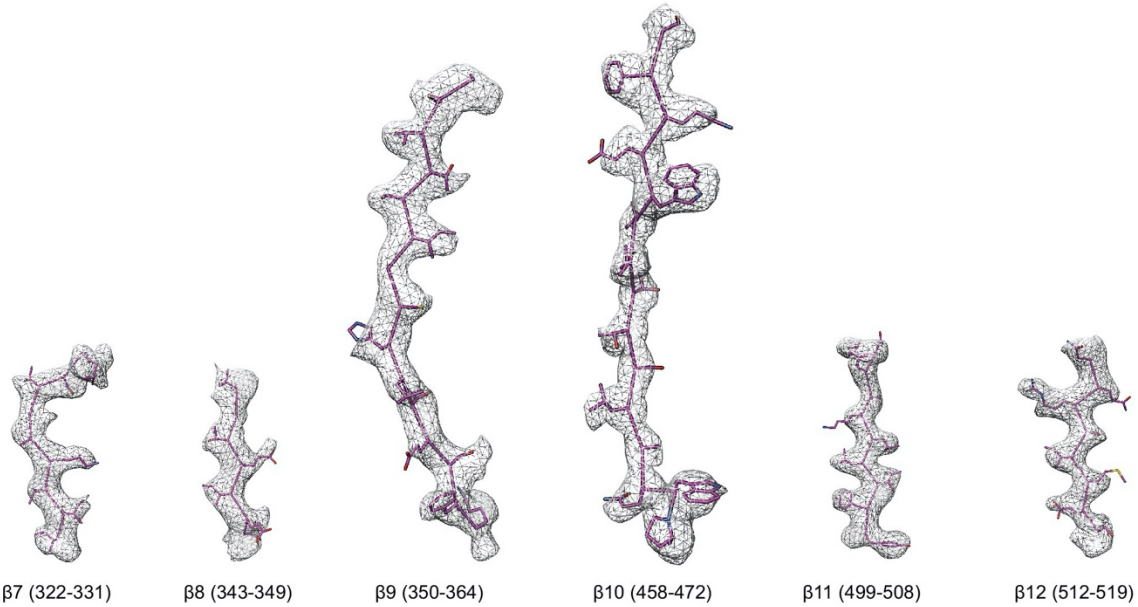

β7 (322-331) β8 (343-349) β9 (350-364) β10 (458-472) β11 (499-508) β12 (512-519)

Figure 2.19. Cryo-EM map of Δγ secondary structures. Regions of the Δγ ENaC subunit model shown in stick representation superimposed with the potential map in light grey mesh, contoured between 7.5 and 8.0 sigma. The model is colored as in **Figure 2.15**.

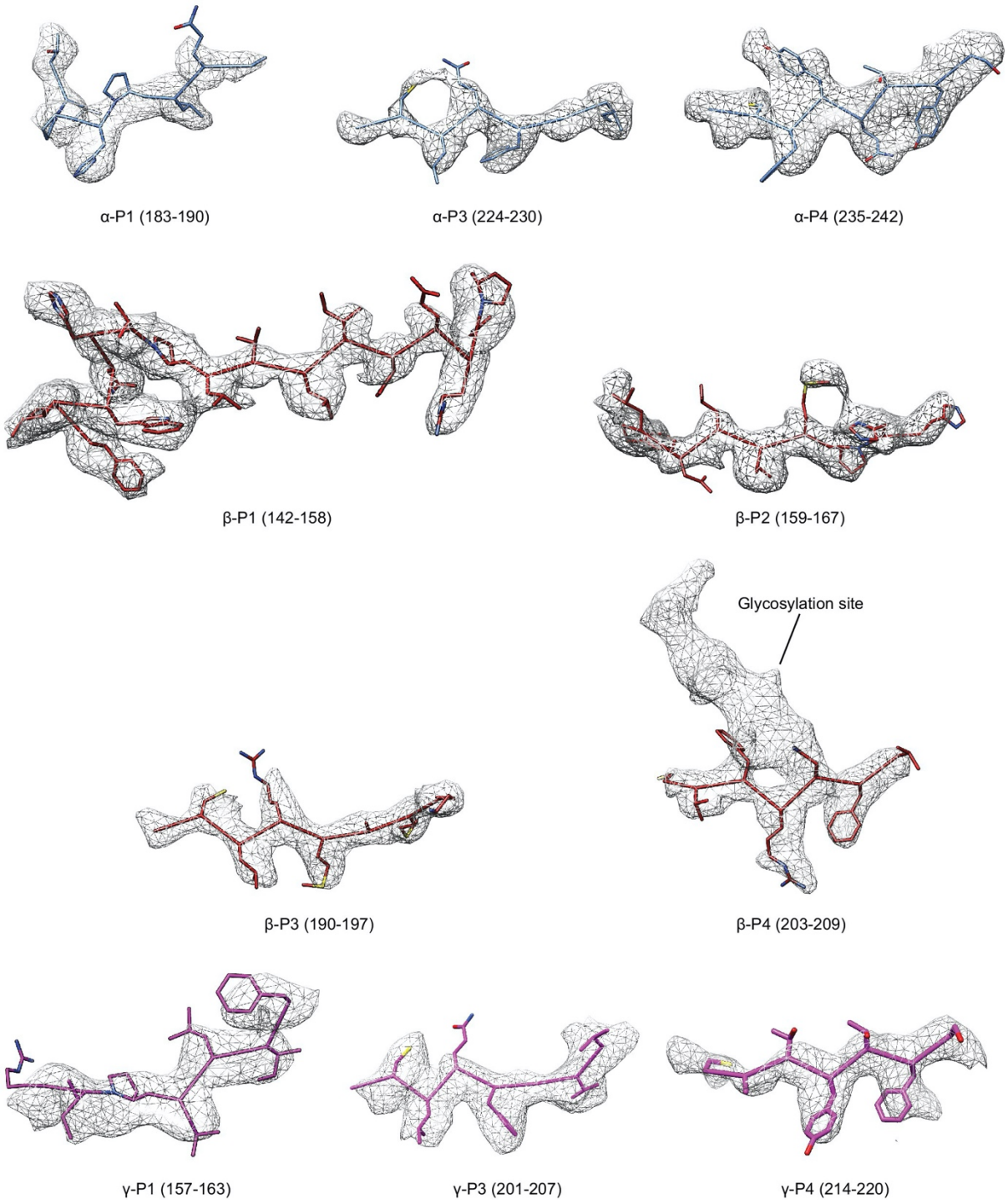

Figure 2.20. Select regions of the GRIP domain in all three subunits. Model is colored as in **Figure 2.15**, potential map is light grey mesh and contoured at 6.5 sigma.

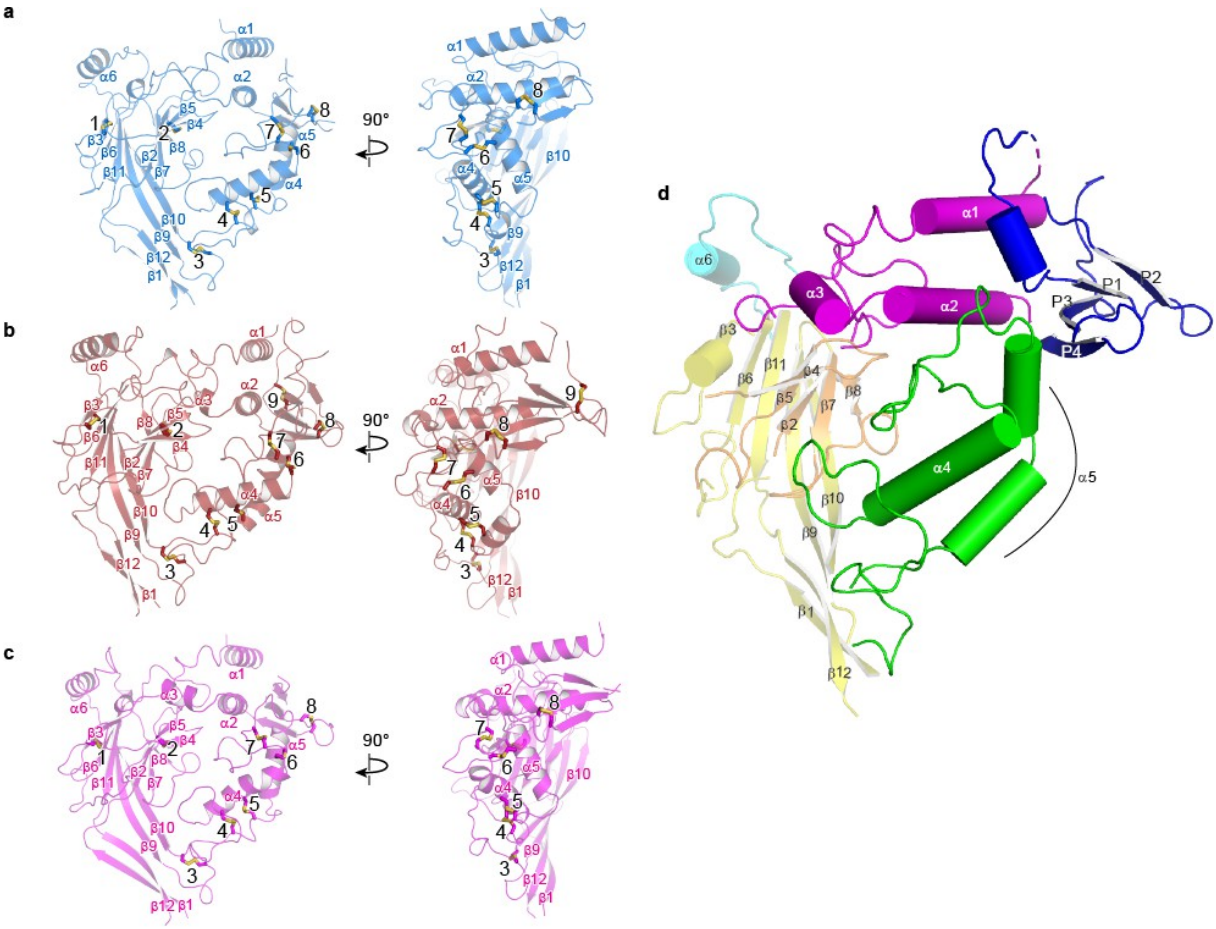

Figure 2.21. Domain organization in each subunit of ΔENaC resembles a hand clenching a ball. a-c, Domain organization of each ENaC subunit and locations of disulfide bridges. Disulfide bridges 1-7 are conserved across ENaC/DEG family while the eight disulfide bridge is shared by α **(a)**, β **(b)**, and γ **(c)** and located in the GRIP domain (P1 – P4). The β subunit contains a ninth disulfide bridge that is also located in the GRIP domain. All subunits are in cartoon representation and colored as in **Figure 2.15** and the disulfide bridges are in sticks representation. **d,** Schematic diagram of secondary structure elements of ENaC subunits colored as follows: knuckle, cyan; palm, yellow; finger, purple; GRIP, blue; β-ball, orange; thumb, green.

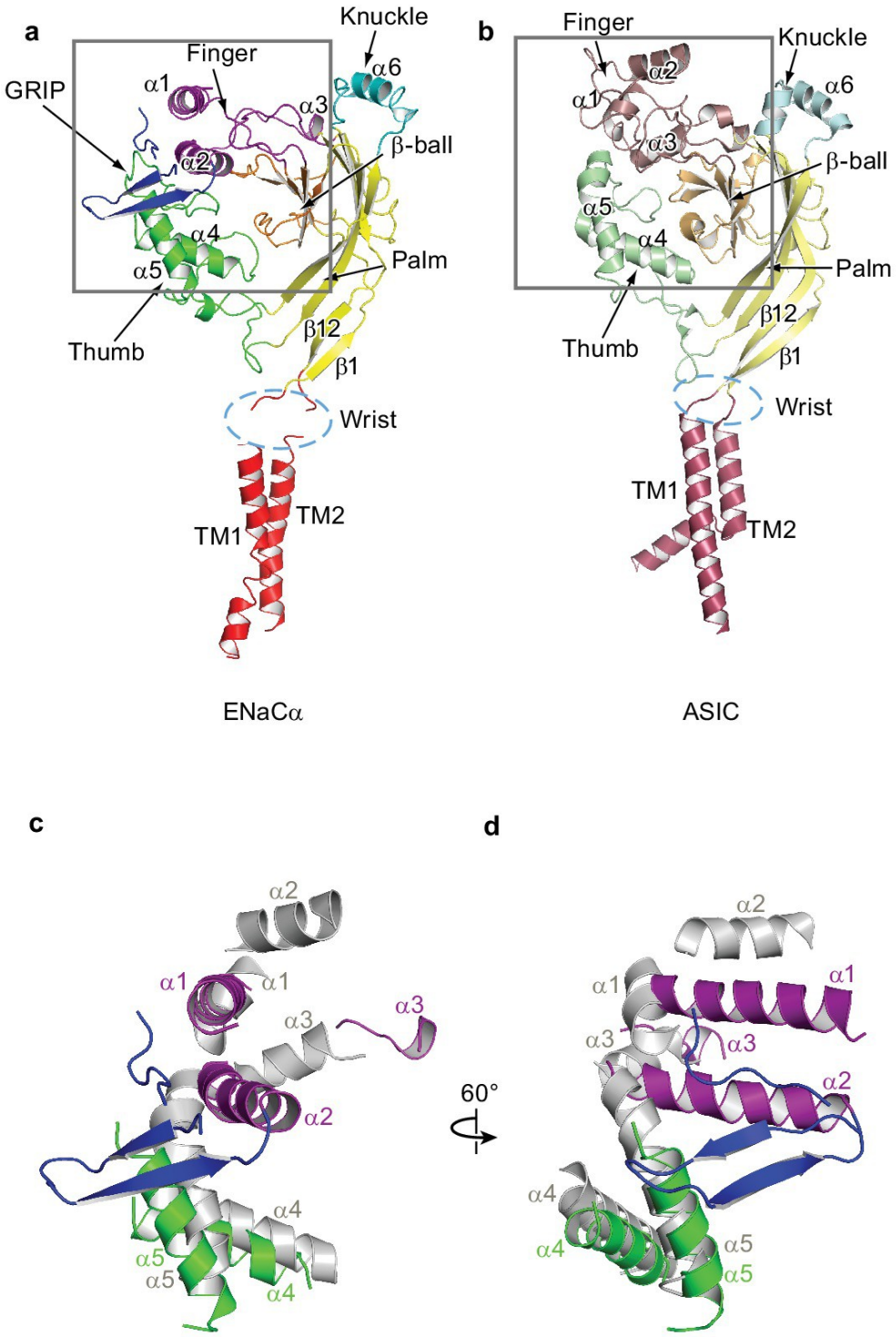
a
Knuckle
Finger
GRIP
α1
α6
α3
β-ball
α2
α4
α5
Palm
Thumb
β12
β1
Wrist
TM2
TM1
ENaCα
b
Finger
Knuckle
α2
α1
α6
α3
β-ball
α5
α4
Palm
β12
Thumb
β1
Wrist
TM1
TM2
ASIC
c
α2
α1
α1
α3
α3
α2
α4
α5
α5
α4
60°
d
α2
α1
α1
α3
α3
α2
α4
α4
α5
α5

Figure 2.22. Comparison between ENaC and ASIC subunit structure. a, Overall architecture of the ENaC subunit is similar to the subunit architecture of **(b)** chicken ASIC (PDB: 5WKV). Domains of high sequence similarity between the two ion channels like the palm (yellow – ENaC, pale yellow – ASIC) and β-ball (orange – ENaC, light orange – ASIC) domains are structurally conserved. Structural differences are observed in the knuckle (cyan – ENaC, pale cyan – ASIC) and finger (purple – ENaC, raspberry – ASIC) domains. **c and d,** Superposition of the ENaC (colored) and ASIC (grey) subunits in the upper palm domain illustrates deviations in domain structures. View of boxed region in **(a)** and **(b)**. For clarity, loops, β-ball, palm, and knuckle domains are omitted.

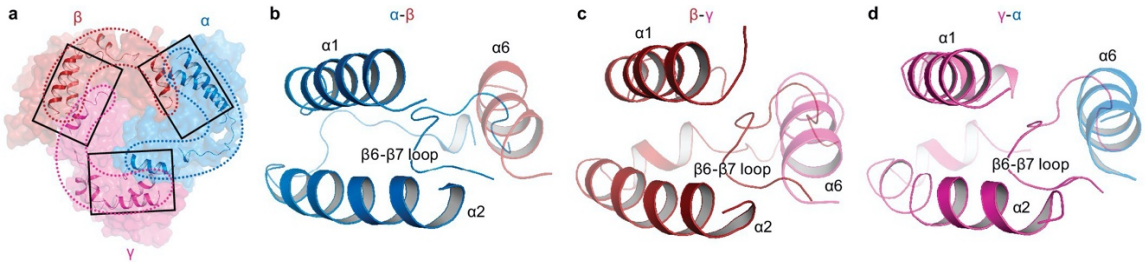

Figure 2.23. Intersubunit interactions in ΔENaC in the finger and knuckle domains. a, The finger and knuckle domains forge intersubunit interactions forming a 'collar' at the top of the ECD. Surface representation of ΔENaC viewed perpendicular to the membrane. Subunits are colored as in **Figure 2.15**. The finger (α1-3) and knuckle domains (α6) are shown in cartoon representation. **b-d,** Detailed view of the interfaces boxed in **(a)**. The views are parallel to the membrane and show how the helices from the finger and knuckle domains constitute an enclosure around the β6-β7 loop.

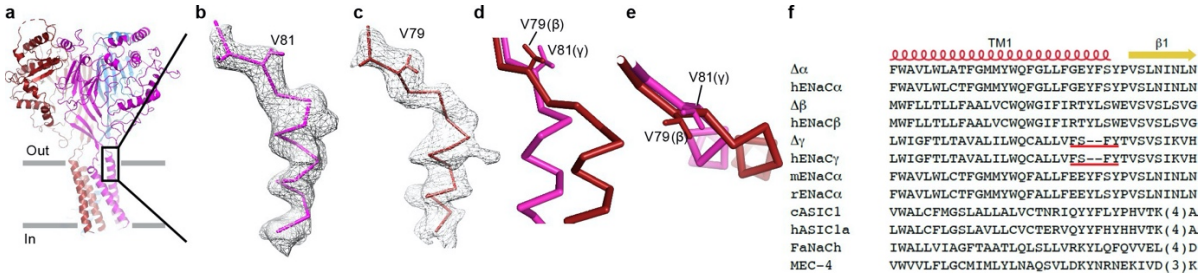

Figure 2.24. The ΔENaC structure demonstrates asymmetric interactions at the wrist region. a, Overall view of ΔENaC as colored in **Figure 2.15** in cartoon representation. **b,** View of the boxed region in **(a).** EM map of TM1 of the γ subunit near the wrist region. The γ subunit is shown in ribbon representation and γ-Val81 in sticks. **c**, EM map of TM1 of the β subunit near the wrist region. The β subunit is shown in ribbon representation and β-Val81 in sticks representation. **d and e,** Superposition of the β1 strands of β and γ subunits viewed parallel **(d)** and perpendicular **(e)** to the membrane show that the additional two residues in β extends the linker region between the β1 and TM1 segments. **f,** Sequence alignment analysis show that the subunit lacks two residues at the TM1/β1 strand interface.

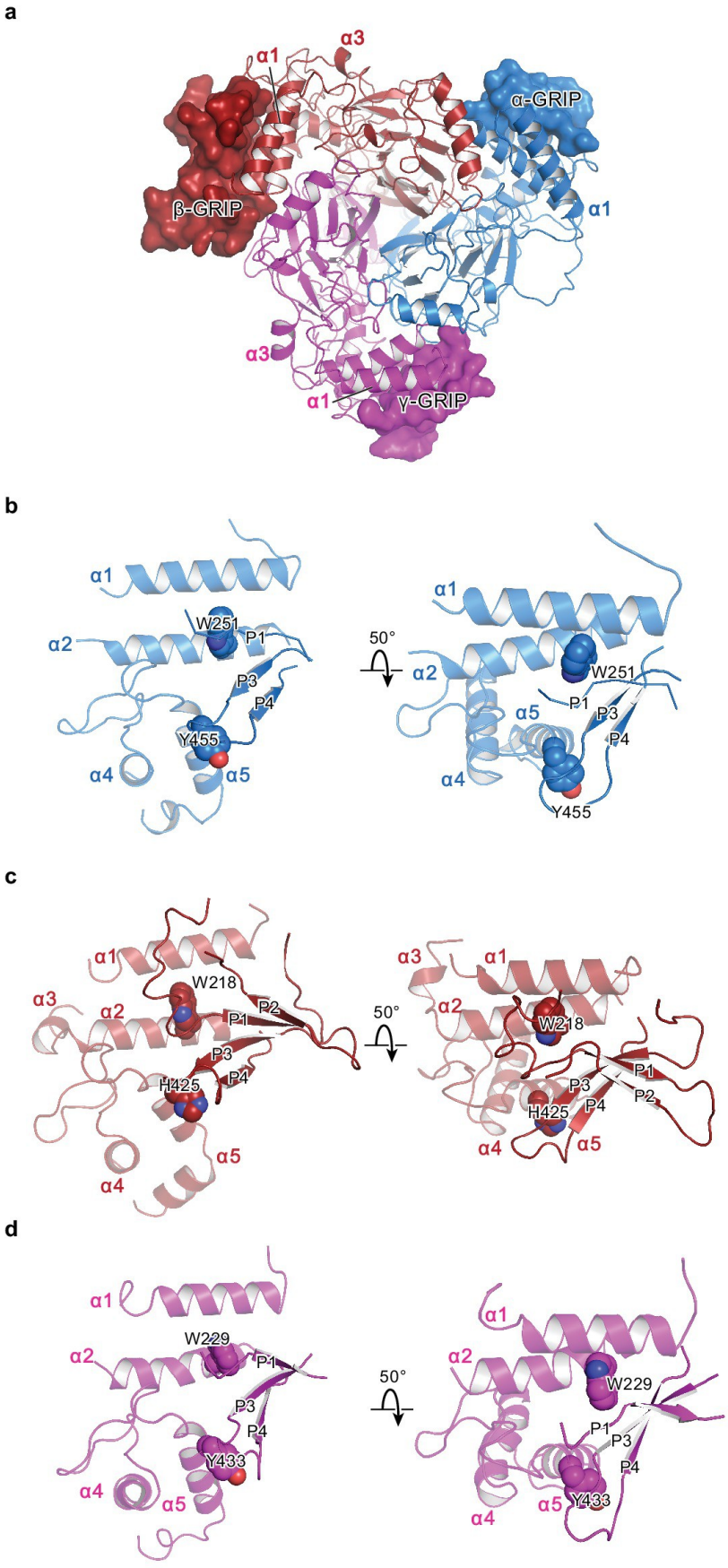
a
α1
α3
α-GRIP
β-GRIP
α1
α3
α1
γ-GRIP
b
α1
W251
α2
P1
P3
P4
Y455
α4
α5
50°
α1
α2
W251
P1
α5
P3
P4
α4
Y455
c
α1
W218
α3
α2
P1
P2
P3
H425
P4
α5
α4
50°
α3
α1
α2
W218
P1
P3
P2
P4
H425
α4
α5
d
α1
W229
α2
P1
P3
P4
Y433
α4
α5
50°
α1
α2
W229
P1
P3
P4
α4
α5
Y433

Figure 2.25. The protease-sensitive domain in ENaC is part of the GRIP domain. a, ΔENaC is shown in cartoon representation and colored as in **Figure 2.15**. The GRIP domain is shown in surface representation. Close-up view of the cleft formed by the finger and thumb domains and the P3-P4 segments in α **(b)**, β **(c)**, and γ **(d)**. The cleft is occupied by the P1 segment of the GRIP domain. All three subunits contain conserved tryptophans in α2 (αTrp251, βTrp218, and γTrp229), which interacts with the P1 segment. The P3 and P4 strands are stabilized by the α5 of the thumb domain by docking on top of aromatic residues (αTyr455, βHis425, and γTyr433).

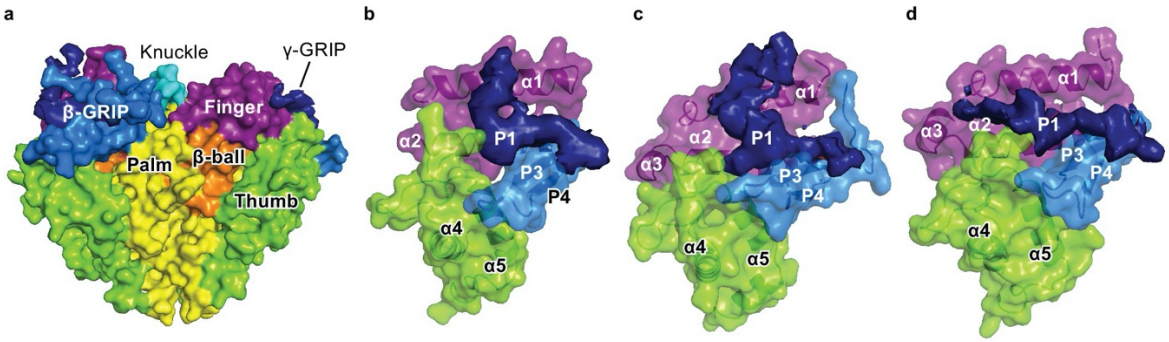

Figure 2.26. Cryo-EM map of the P1 segments in α, β, and γ demonstrates critical interactions with the finger and thumb domains. a, All the domains in ENaC are represented as the surface derived from the ΔENaC model, except the P1 segments, which are directly reproduced from the potential map. The domains of all three subunits are colored as in **Figure 2.21d**. The P3-P4 segments are colored light blue while the potential map of P1 is shown and colored dark blue. **b-d,** Close-up view of the finger, thumb and GRIP domains of each subunit. The finger and thumb domains and P3 and P4 strands of α **(b)**, β **(c)**, and γ **(d)** are shown in cartoon and surface representations derived from the model of ΔENaC. The potential map of the less-ordered P1 strand of α resembles that of β. The P1 potential map of γ, however, extends toward α3 helix.

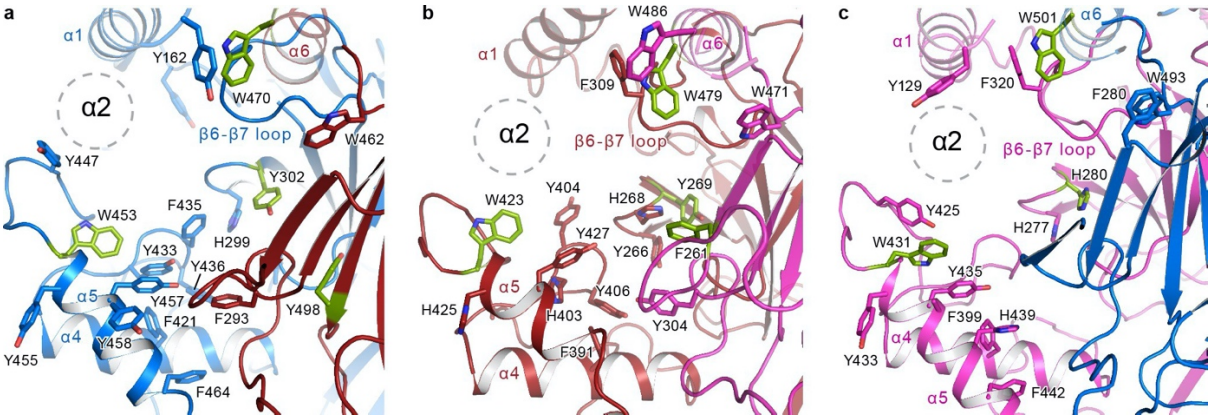

Figure 2.27. The α2 helix is buried in the aromatic pocket formed by key gating domains in ENaC. The aromatic pockets at the α-β **(a)**, β-γ **(b)** and γ-α **(c)** interfaces are shown in cartoon representation. The aromatic residues are shown in sticks representation. Residues conserved in ASIC are colored green. The α2 helices and the GRIP domains are omitted for clarity. The positions of the α2 is shown as dotted circles.

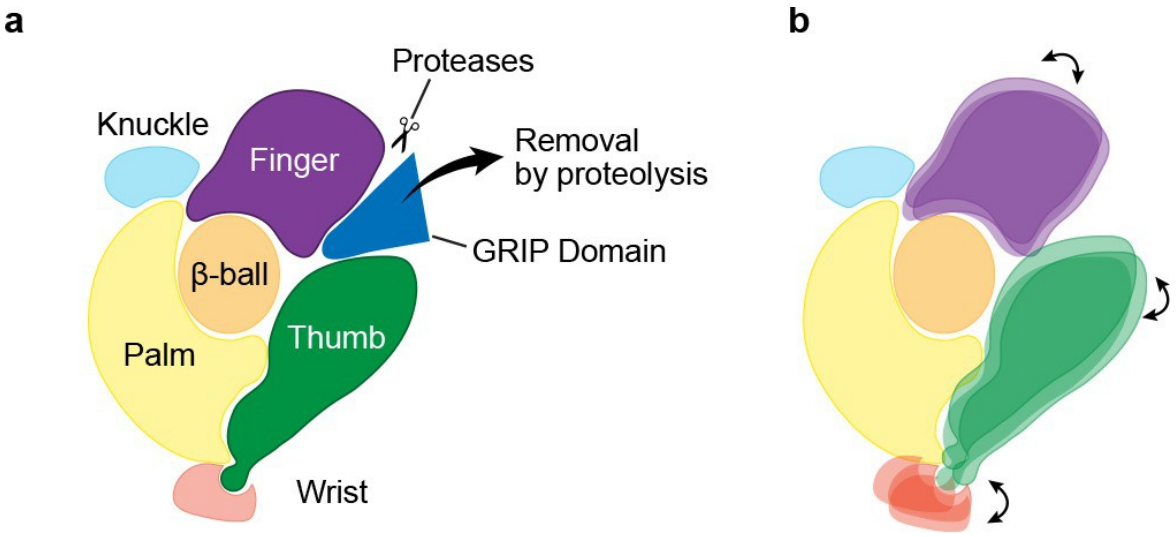

Figure 2.28. Mechanism of protease-dependent gating in a single ENaC subunit. Removal of the protease sensitive segments of the GRIP domain **(a)** induces conformational changes in the finger and thumb domains **(b)**, which is perhaps coupled to ion channel gating through the wrist.

Chapter 3

Structure of the full-length epithelial sodium channel reveal heterogeneity in the protease-sensitive domains

The contents of chapter three are the first draft of a manuscript in preparation for submission:

Noreng, S., Posert, R., Bharadwaj, A., and Baconguis, I. Structure of the full-length epithelial sodium channel reveal heterogeneity in the protease-sensitive domains

Author contributions

S.N and I.B. designed the project. S.N., A.B., and I.B. expressed and purified ENaC. S.N. and R.P. prepared ENaC grids for cryo-EM data collection. S.N. and R.P collected and processed data of ENaC. I.B. built the model of ENaC. S.N. and I.B. performed electrophysiology experiments. S.N. performed radioligand binding assay. S.N and I.B. wrote the manuscript and all authors edited the manuscript.

Abstract

The epithelial sodium channel (ENaC) is a member of the ENaC/degenerin superfamily, and is important for regulation of salt and water homeostasis. ENaC assembles as a heterotrimer with subunits α-β-γ arranged, counterclockwise from the extracellular surface and is known to be activated by proteases where two of the three subunits: α and γ, harbor proteases-sensitive sites that releases inhibitory peptides upon proteolytic processing. Here we present the structure of full-length (FL) ENaC solved by single particle cryo-electron microscopy (cryo-EM). The purified FL-ENaC sample contains a mix of cleaved and uncleaved particles, and we show that cryo-EM data processing strategies can separate these states from each other. Thus, the strategy outlined creates a foundation for future studies that involves structural determination of ENaC in native tissue.

Introduction

The epithelial sodium channel (ENaC) is expressed at the apical side of epithelial cells and is a key regulator of salt and water balance, playing a critical role in blood volume regulation, and thereby blood pressure[177,230,231]. The important role of ENaC in blood pressure regulation is best illustrated by ENaC gain of function mutations, as seen in Liddle syndrome[57,107,108,232], and by ENaC loss of function mutations as seen in pseudohypoaldosteronism type 1 (PHA1)[157,158,233]. ENaC belongs to the ENaC/degenerin family, characterized by their Na^+-selectivity, voltage independence and sensitivity to the pore blocker amiloride. Members of this superfamily have short intracellular N- and C-termini, two membrane-spanning helices, and a large extracellular domain (ECD) that can form either homotrimeric or heterotrimeric ion channels[4,234]. ENaC consists of three homologous subunits, α, β, and γ, which assemble as a heterotrimer. The subunits are arranged α-β-γ counterclockwise as seen from the extracellular space[234], and all three subunits need to be present for ENaC to form a fully functional channel[3].

The regulation of ENaC is complex with multiple posttranslational modifications playing important roles modulating ENaC open probability (P_o). However, one unusual mechanism for regulation involves proteolytic processing, in which two of the three subunits, α and γ, are cleaved at distinct extracellular sites, causing the release of inhibitory peptides, resulting in an increase in the P_o of ENaC[89,90,98,99], without changing either single-channel conductance or ion-selectivity[91,92]. The first hint of ENaC being regulated by proteases was presented as early as 1980[93], and after the initial cloning of all ENaC genes in 1994[2,3], studies directly showed that maturation of ENaC involved proteolytic processing[94,96]. In addition to multiple proteases, furin regulates ENaC[95,235]. The exact number of different cleavage states of ENaC, and where all putative protease-sensitive sites are located, remains elusive.

The first structure of ENaC was determined by our group using a construct (ΔENaC) in which all subunits (α, β and γ) were truncated at the N- and C-termini and putative protease sites in α and γ were mutated, in order to capture ENaC in a homogeneous uncleaved state[234]. The structure provided the first view of the protease sensitive domains in ENaC, which was named the **G**ating **R**elief of **I**nhibition by **P**roteolysis (GRIP) domain. Interestingly, our structure clearly shows the presence of a β-GRIP domain, even though the β subunit has not been shown to be sensitive to proteases. Unfortunately, the transmembrane domain (TMD) in the cryo-EM map of ENaC was poorly resolved, preventing detailed structural analysis that might reveal the Na^+ permeation pathway and explain the high Na^+ selectivity, both of which are important characteristics of ENaC function.

In this study we present the structure of the human full-length (FL) ENaC-DiFab complex, solved by single-particle cryo-electron microscopy (cryo-EM) at 3.1 Å. Although the ENaC TMD potential map remains ambiguous, the improved cryo-EM map of FL-ENaC validates the structure of ΔENaC. Additionally, the improved resolution allows us to make detailed analysis of the molecular interactions that favor a triheteromeric assembly of ENaC as well as interpretation of the important areas of contact where the inhibitory peptides of α and γ bind. Furthermore, we demonstrate that structural heterogeneity within the α- and γ-subunit GRIP domains can be separated by focused classification of the cryo-EM data, giving a potential window into an understanding of ENaC cleaved states.

Materials and Methods

***Construct design*:** The cDNA encoding the full-length (FL) α, β, and γ subunits of human ENaC were cloned into the pEG BacMam expression vector, with each FL subunit harboring an N-terminal 8x His tag, eGFP and thrombin cleavage site (LVPRGGR)[202]. The untagged full-length (UTFL) α and β subunits were generated to reduce the number of eGFP fluorophores per ENaC to improve binding and elution efficiency when using an eGFP nanobody for affinity purification. UTα and UTβ were wild type α- and β-subunit with no tags. FL-ENaC refers to the combination of FLα, FLβ and FLγ, and also to the combination of UTα, UTβ and FLγ as no functional or structural difference have been detected between channels composed from any of these constructs.

***Generation and isolation of Fabs*:** Generation and isolation of Fabs was the same as described in Noreng et al[234]. Mouse monoclonal antibodies 7B1 and 10D4 were generated using standard procedure by Dan Cawley at the Vaccine and Gene Therapy Institute (OHSU). The 7B1 and 10D4 mAbs were previously selected because they recognize tertiary epitopes of ENaC. The mAbs were purified, and their Fabs were generated by papain cleavage. Fab 7B1 was isolated by anion exchange using HiTrap Q HP column while Fab 10D4 was eluted using Protein A column to remove Fc.

***Expression and purification of ENaC-Fab complexes*:** Human embryonic kidney cells (HEK293T/17) were grown in suspension at a density of 2 - 4 x 10^6 cell / mL in Freestyle medium with 2% FBS and transduced with the virus (Flα, FLβ, FLγ or UTFLα, UTFLβ, FLγ) at a multiplicity of infection (MOI) of 1 and incubated at 37°C. Five to eight hours post transduction, amiloride was added to a final concentration of 1 μM, and cells were incubated at 30°C. After 24-48 hr, the cells were collected by centrifugation at 4,790xg for 20 min. The pellet

was washed with 20 mM Tris, 200 mM NaCl and followed by a second round of centrifugation at 4,790xg for 15 min.

There were two approaches to purification of ENaC that the cryo-EM data set arrived from. In both purifications, GFP-cleaved ENaC-DiFab at pH 7.4 was the final purified complex used for cryo-EM sample preparation and will be referred to as FL-ENaC. In one purification, membranes were prepared and ENaC was purified from the prepared membranes, while in the second purification ENaC was purified from the cell pellet.

In the first purification, cells expressing FL-ENaC were homogenized with a dounce homogenizer and sonicated in 20 mM Tris pH 7.4, 200 mM NaCl, 5 mM $MgCl_2$, 25 μg/mL DNase I and protease inhibitors. Lysed cells were centrifuged at 9,715 xg for 20 min and the resulting supernatant containing the membrane fractions were further centrifuged at 100,000 xg for 1 hr. Membrane pellets were resuspended and solubilized in 20mM Tris pH 7.4, 200 mM NaCl, 1% digitonin (high purity, Millipore Sigma), 25 U/mL nuclease and protease inhibitor for 1 hr at 4°C. The solubilized fraction was isolated by ultracentrifugation 100,000 xg for 1 hr at 4°C.

In the second purification, cells expressing FL-ENaC were homogenized with a dounce homogenizer in 20 mM HEPES pH 7.4, 150 mM NaCl, 2 mM $MgCl_2$, 25 U/mL nuclease and protease inhibitor. Homogenized cells were solubilized by adding the same buffer containing 2% digitonin (high purity, Millipore Sigma) and 4 mM ATP at 1 x initial volume (final volume 2x) for 2 hr at 4°C. The solubilized fraction was isolated by ultracentrifugation 100,000xg for 1 hr at 4°C and supernatant was filtered through 0.45 μm filters.

Solubilized ENaC (from both purifications) was bound to GFP nanobody resin by batch binding for 2 hr at 4ºC. ENaC bound to GFP nanobody resin was packed into an XK-16 column, and the column was washed with 20 mM Tris pH 7.4, 200 mM NaCl, 0.1% digitonin and 25 U/mL nuclease (second purification: 20 mM HEPES pH 7.4, 150 mM NaCl, 0.1 % digitonin and 25 U/mL nuclease) followed by an additional wash of the same buffer containing 2 mM ATP. For elution, thrombin at 30 μg/mL and 5 mM $CaCl_2$ in the same buffer was applied to the column and incubated for 30min. GFP-cleaved ENaC was eluted off with the same wash buffer and the eluted fractions were concentrated and then incubated with the Fabs 10D4 and 7B1 (DiFab complex) in a 1:2 molar ratio of ENaC:Fab for 10 min, and clarified by ultracentrifugation 100,000 xg for 1 hr at 4ºC. The supernatant was injected onto a Superose 6 Increase 10/300 GL column equilibrated in 20 mM Tris pH 7.4, 200 mM NaCl, 0.1 % digitonin (second purification: 20 mM HEPES pH 7.4, 150 mM NaCl, 0.1 % digitonin) to isolate the protein complex by size-exclusion chromatography. Monodispersed peaks were pooled and concentrated to 2 - 3 mg/mL. Both purified ENaC samples that was used for structural determination will be referred to as FL-ENaC.

***Image acquisition and data processing*:** Purified GFP-cleaved ENaC-DiFab complexes at a concentration of 2 - 3 mg/mL was applied on holey-carbon cryo-EM grids which were prior glow discharged at 15mA for 60sec (Quantifoil Au 1.2/1.3 μm 300 mesh). Grids were prepared using a Vitrobot Mark III (FEI) at 100% humidity and 12 ºC, where 3.5 μL of purified ENaC-DiFab complexes were applied followed by a manual blot on the side of the grid. Then another 3.5 μL of purified ENaC-DiFab complexes were applied before a wait time of 10 s, 3.5 s blot time at blot force 1, and then plunge frozen in liquid ethane cooled by liquid nitrogen. Three large data sets were collected on the same microscope, a Titan Krios at the Multiscale

Microscopy Core at OHSU, equipped with a Gatan K3 detector. One of the large data sets were collected from the purification of ENaC solubilized from membranes with a total of 9,435 movies, while the other two large data sets were collected from ENaC purified directly from cells (see section "expression and purification" for more details), one of the data sets containing 9,605 movies and the other containing 6,153 movies. For all three data sets, movies were collected in super resolution mode with a pixel size of 0.415Å. Total acquisition time was 3 s, and all three data sets were dose-fractionated to 60 frames with a dose rate of 1 $e^-/Å^2$/frame and total dose of 60 $e^-/Å^2$. Multishot with image shift between four holes was performed to speed up data collection. All data sets were binned 2 x 2 and motion corrected using motioncor2 with patch of 5 x 5[204]. Each data set was processed individually using the software cryoSPARCv2[208] to determine the overall quality of final FL-ENaC-DiFab cryo-EM map before all three data sets were combined for final data processing. Defocus values were estimated using CTFFIND4[236], and cryoSPARCv2 blob picker was used for automated particle picking, initially resulting in 1,787,887 particles (**Table 3.1**). Multiple rounds of 2D classification in cryoSPARCv2 were performed where positive 2D classes of ENaC were saved, and particles belonging to false - positive classes were combined and re-classified by 2D classification to further reveal and include true ENaC-Fab classes (**Figure 3.7**). After multiple rounds of 2D classification, a set of 453,875 particles was classified by cryoSPARCv2 ab initio and three rounds of 3D classification by heterogeneous refinement in cryoSPARCv2 (**Figure 3.8**). To include as many true positive ENaC-Fab particles as possible, 3D classes of false – positive particles went through additional 2D classification and positive ENaC-Fab 2D classes were re-added for heterogeneous 3D classification (**Figure 3.8**). The final data set containing 252,071 particles, was processed using non-uniform refinement in cryoSPARCv2 with default settings and C1 symmetry for a final 3D

reconstruction with a Gold standard Fourier Shell Correlation (GS FSC) resolution of 3.06Å (**Figure 3.4e,f**). In addition, the same particles were exported from cryoSPARCv2 by using the pyem conversion script (csparc2star.py)[237], and then imported to cisTEM 1.0.0[209]. In cisTEM particles were sorted by 2D classification, and 248,079 particles were refined with a mask that contained the ECD only to a solvent adjusted FSC of 3.11 Å (**Figure 3.8**). The final 3D map from 252,071 particles created in cryoSPARC v2 was used for model building and refinement.

To separate cleaved states of ENaC, focused classification (only refining the translational x and y parameters in cisTEM1.0.0) was performed in the GRIP domain of the α and γ subunits (**Figure 3.13**). Subsequent classes obtained from focused classification were imported to cryoSPARC and *ab initio* was performed refined to confirm the missing densities (**Figure 3.14 and Figure 3.15**).

***Model building*:** The extracellular coordinates of the ΔENaC structure and the antigen-binding domains of 7B1 and 10D4 (PDB code: 6BQN[234]) were docked into the cryo-EM map of FL-ENaC using Chimera[211]. The coordinates were then manually inspected and adjusted using the computer program COOT[212]. The overall improved map quality for the ENaC ECD, as observed in the α- and γ-GRIP domains and glycosylation sites, allowed for more residues to be built at the N-terminal end of the P1 strands and sugars, respectively. It is important to note that N-acetylglucosamines (GlcNac) were added into glycosylation sites with well-defined features contoured at 8 σ (0.43 e/A^3). In total, seven glycosylation sites were modeled: 2 in α, 4 in β, and 1 in γ. Iterative rounds of manual building and real-space refinement were conducted using COOT[212] and PHENIX[217], respectively[238]. Structure validation was performed using Molprobity[218].

***Radioligand binding assay*:** Filter binding assay was carried out to determine the half-saturation concentration of ^{3}[H] labeled benzamil. Membranes were prepared by homogenizing thawed HEK293T/17 cells expressed with UTFL-ENaC, or dissected kidneys from rat, in 50 mM potassium phosphate buffer (pH 7.4). Homogenized cells were cleared by centrifugation at 800 xg for 10 min, and supernatant was centrifuged at 8,000 xg for 10 min. Final supernatant was centrifuged at 100,000 xg for 1 hr where the membrane pellets were homogenized in 50 mM potassium phosphate buffer (pH 7.4). The final binding reaction volume was 500 µL and contained 4 nM of recombinant expressed ENaC, while for rat kidney the concentration was unknown. In both cases, the binding reaction was carried out with varying concentrations of labeled ^{3}[H] Benzamil. The specific binding was the difference curve of binding reaction in presence and absence of 100 µM phenamil mesylate. All conditions were performed in triplicate to determine an average. Binding reactions were incubated at room temperature for 90 - 180 min before being stopped by rapid filtration through Whatman GF/B glass fiber filters that had been pretreated with 0.3% polyethyleneimine (PEI, 25000 MW linear) in 50 mM potassium phosphate buffer (pH 7.4). Additionally, two washes of 5 mL of 50 mM potassium phosphate buffer (pH 7.4) reduced the non-specific binding to the GF/B glass fiber filters, and then filters were transferred to scintillation vials containing 5 mL of liquid scintillation cocktail before counting.

***Whole cell patch clamp experiments*:** HEK293T/17 cells were grown in suspension at a density of 2 - 4 x 10^{6} cells/mL in Freestyle medium with 2% FBS and transduced with the virus (FLα,FLβ, FLγ) at a multiplicity of infection (MOI) of 1 and incubated at 37 ^{o}C. After ~5hrs the transduced suspension cells were incubated in the presence of 500 nM phenamil mesylate at 30^{o}C for 12 – 14 hr. About 2 - 3 hours before recording, cells were transferred to wells containing glass coverslips at a density 0.3 - 0.5 x 10^{6} cells/mL and in Dulbecco's Modified

Eagle Medium supplemented with 2% FBS and 500 nM phenamil mesylate. Whole cells recordings were carried out 17 - 24 hr after transduction. Pipettes were pulled and polished to 2.5 - 3.5 MΩ resistance and filled with internal solution containing (in mM): 150 KCl, 2 $MgCl_2$ 5 EGTA and 10 HEPES (pH 7.4). For IC50 experiments, external solutions that were used contained (in mM): 150 NMDGCl or NaCl, 2 $MgCl_2$ $CaCl_2$ and 10 HEPES (pH 7.4). Increasing concentrations of amiloride, phenamil mesylate or benzamil was added to the solution containing 150 NaCl (1 nM, 3 nM, 10 nM, 30 nM, 100 nM, 300 nM, 1 μM, 100 μM). The macroscopic ENaC current was determined as the blocker-sensitive Na^+ - current that was blocked by 100 μM amiloride, phenamil mesylate or benzamil. To determine the voltage-sensitivity of each blocker, steps of +20 mV, from a starting holding potential at -60 mV up to 0mV was performed for each experiment and the IC50 was determined for each voltage step (-60 mV, -40 mV, -20 mV and 0 mV). All recording experiments were repeated independently 5 times.

For whole cell patch clamp experiments to determine the effect of the monoclonal antibody (mAb) 7B1, cells were treated with trypsin (5 μg/mL) for 5 min to increase amiloride-sensitive Na^+-currents. Post treatment with trypsin cells were incubated with mAb 7B1 at a final concentration of 100 nM for 3 min. Then the amiloride-sensitive Na^+-current was recorded before and after incubation with mAb. The final Na^+-currents were normalized to compare whether there was a difference in ENaC Na^+ self-inhibition as a result of mAb binding.

Results

Functional characterization

We assessed the functional properties of human FL-ENaC by performing whole cell patch clamp of the same cells used to express and purify FL-ENaC for structural determination.

Robust amiloride-sensitive currents at -60 mV and 0 mV can be detected from cells expressing FL-ENaC (**Figure 3.1a, b**). In addition, well-characterized high-affinity pore blockers of ENaC (amiloride, phenamil and benzamil) block ENaC currents at -60 mV with the following IC50 values: 86.34 ± 27.04 nM, 51.01 ± 14.12 nM and 32.90 ± 12.66 nM, respectively. At 0 mV the IC50 values of amiloride, phenamil and benzamil are 97.14 ± 21.62 nM, 51.37 ± 10.42 nM and 36.74 ± 13.25 nM, respectively (**Figure 3.1c**), which are all IC50 values that agrees with what has been measured[20,239]. We compared IC50s for each blocker at -60, -40, -20 and 0 mV to determine the voltage dependency, and saw that there was no strong voltage dependency for any of the blockers (**Figure 3.1c, d and Figure 3.2a-d**). Additionally, treatment of cells expressing FL-ENaC with 5 μg/mL trypsin for 5 min reveals an increase in amiloride-sensitive steady state current, in keeping with reported values (**Figure 3.2e**)[94,240].

Altogether, electrophysiology whole cell patch clamp of ENaCs expressed in the same cell line that is used for expression and purification of ENaC, shows that ENaCs, at the plasma membrane, are functional and exhibits all the typical ENaC current characteristics that previously have been described[3].

To assess the integrity of the transmembrane domain of FL-ENaC we performed radioligand binding assays using [^{3}H] labeled benzamil, reasoning that since amiloride binds in the pore, binding curves are a suitable proxy for TMD stability. Binding assays were carried out using membranes prepared from the same cells used for structural studies. The specific binding of [^{3}H] benzamil was considered to be the difference curve in absence and presence of 100 μM phenamil. As a positive control we prepared membranes from rat kidney cortex and medulla[29].

The half-saturation concentration for the membranes prepared from rat kidney cortex and medulla was 23.4 nM, which is in close agreement with previous findings[29]. However, the membranes prepared from HEK293 cells expressing recombinant ENaC never reach saturation under the conditions tested (**Figure 3.2f**). The half-saturation calculated from a fitted curve was significantly lower at 286 nM. One explanation for this result is that the majority of recombinantly-expressed ENaCs are not transported to the plasma membrane, resulting in a large population remaining within the ER and Golgi[234]. The fraction of ENaCs that do not reach the plasma membrane are largely uncleaved, resulting in immature ENaCs which have a lower binding affinity to amiloride and analogs[90].

Nevertheless, whole cell patch clamp recordings of ENaCs expressed in the same cell line that is used for purification of ENaC, exhibit all the typical ENaC current characteristics[3].

Structure determination

The structure of FL-ENaC-DiFab complex was purified in digitonin and determined from three large data sets that were individually processed and then merged (**Table 3.1, Figure 3.3 - 3.6**). The final data set consisted of 252,071 particles that had been extensively sorted through multiple rounds of both 2D and 3D classification (**Figure 3.7 and Figure 3.8**). The final cryo-EM map was determined at a resolution of 3.1 Å (gold standard FSC), and validates the first structure of ΔENaC in an uncleaved state[234]. The map features were significantly improved in the α-GRIP and γ-GRIP regions, where the protease-sensitive sites and inhibitory P1 peptides are found. This allowed us to build more residues of the inhibitory P1 peptides and confirm the proper register of residues located in this region, since the first map of ΔENaC was less resolved in the GRIP domain (**Figure 3.3c, d and Figure 3.6**). Additionally, two arginine residues

(αR249, αR253) originally mutated to alanine residues in the ΔENaC construct (potential protease-sensitive sites) were revealed in our new map (**Figure 3.3e,f**). The improved structure of FL-ENaC shows protrusions of density in the α2 helix where the arginine residues are located, confirming the proper register (**Figure 3.3e,f**).

Unfortunately, the map region of the ENaC TMD was not improved in our FL-ENaC map, and currently remains unresolved (**Figure 3.3b**). We have made multiple attempts to resolve the TMD of ENaC, including reconstitution of ENaC into nanodiscs for a more native, lipid-like environment as well as trying multiple detergents and detergent/lipid combinations. One explanation for the poorly resolved ENaC TMD is the likely sensitivity of this domain to its external environment, as similarly seen for a region of the TMD of cASIC[172] (See Appendix 1 for a discussion regarding ENaC TMD and biochemical approaches towards trying stabilize this domain). Although more work is required to elucidate the molecular architecture of ENaC TMD, the results so far are exciting, especially given the recent discovery revealing the importance of the external environment.

Determinants of subunit arrangement and stoichiometry

The α, β and γ subunits share ~30% sequence identity, and all three subunits adopt a similar subunit fold that contains a palm, finger, thumb and knuckle domain that encapsulate the β-ball domain (**Figure 1.5 and Figure 2.22a**). As observed in ASIC and in ΔENaC structures, the upper palm domains forge extensive molecular contacts at the threefold and pseudo threefold axis, respectively, and forms two separate vestibules, the upper vestibule and the central vestibule. Additionally, ENaC subunits harbor the GRIP domain that is located between the

finger and thumb domains and two of the subunits, α and γ are sensitive to proteolytic processing within this domain[89,90,94-96,98,99,234]. FL-ENaC forms a trimeric ensemble of α-β-γ, arranged in a counterclockwise fashion when viewed from the extracellular side of the membrane, which is in agreement with the first structure of ΔENaC and previous studies that have interrogated the Cu^{2+} and Cl^- binding sites[222,224]. While the α-β-γ combination of subunits has been shown to demonstrate robust Na^+ currents, studies using heterologous expression have shown that ENaCs can also form homotrimeric and diheterotrimeric channels that consists of either α subunits only, or combinations of α subunit with either β or γ subunits[2,3]. Amiloride-sensitive currents are detected from these channels, although at a much lower activity than for ENaC channels that consists of all three subunits, and the physiological relevance of these channels have not been determined. In our cryo-EM analysis, based upon inspection of 2D class averages and 3D reconstructions, we have only seen the combination of a heterotrimeric assembly of α-β-γ in a counterclockwise manner. ENaC channels that possibly comprise other subunit combinations have also not been seen as we would expect to observe 2D class averages where one fab (α-γ-γ), two fabs (α-α-γ) or three fabs (α-β-β, α-α-β, α-α-α) were bound. It appears that in our expression system the preferred stoichiometry is α-β-γ.

Using the coordinates of the FL-ENaC ECD structure, we generated models of ENaC containing homomeric α, β, and γ to gain insight into the stoichiometry and assembly of functional ENaC. We implemented two methods for generating these models. First, the simplest form is to generate the trimer using the symmetry-related molecules around the threefold axis of symmetry. Second, the two subunits are superposed with the coordinates corresponding to the other subunits which generates a homomeric trimer with an asymmetric arrangement. Using the first method, we observe striking differences between the three different homomeric forms. The

homomeric α can easily be accommodated. Conversely, the homomeric β and γ trimers contain numerous regions where domain interactions are disfavored due to steric clashes. These clashes occur at the top of the ECD both proximal and distal to the threefold axis. At the core, both homomeric β and γ contain steric clashes mediated by the N-terminal end of the knuckle domain (α6 helix), β6-β7 loop, and β10. At the periphery, we observe steric clashes between the C-terminal end of the knuckle domain and α2 helix of the finger domain **(Figure 3.9a-d)**.

Implementing the second method, the models demonstrate asymmetric arrangement of the subunits as expected. While there appears to be no major steric clashes compared to the models generated in the first method, in this method, there are molecular interactions that demonstrably favor the heteromeric forms over the homomers. Within the ECD of ENaC, there are two main areas of contact between the subunits, where the sequence differs for each subunit. One of the areas is found in the upper vestibule where all three subunits come together, mainly forming interaction via three short loops (connecting two β-strands: β8-β9) and a β-strand that together forms a pore-like structure. The β10 strand (palm domain) of one subunit and the β8 strand (β-ball) of the neighboring subunit forms contact **(Figure 3.10a,e)**, where a short loop at the top connects to the β9 strand (palm domain), and the β9 strand make intra-subunit interaction with the β10 strand **(Figure 3.10e)**. All amino acids in these regions are vastly different in each subunit where at the top of β8 strand α-subunit has an arginine (R370), β-subunit has a methionine (M337) and γ-subunit has a glutamate (E348) that all are pointing into the three fold axis **(Figure 3.10e)**. The arginines in the α model are exposed likely interacting with water molecules and ions in the upper vestibule region, and perhaps, forming cation-π interactions with the αY490 from the β10 strand. In the homomeric β model, the pore axis is lined with two layers of hydrophobic plug lined by βM337 from β8 and βM459 from β10, in the β-ball and upper palm

domains, respectively. The two-layer hydrophobic plug separates the upper and central vestibules. Lastly, unlike homomeric α and β in which the αR370 and βM377 side chains form molecular plugs at the pore axis, the γE348 side chain sits adjacent to γM351 in the β8-β9 loop, and above γL486 from the adjacent β10 strand. In this arrangement, γE348 is buried within a hydrophobic environment which likely perturbs its pKa. In the heteromeric form, γE348 is forging ionic interactions with αR370, which illustrate an energetically favorable salt bridge formed between these two residues.

Another area of contact and sequence deviation is found at the C-terminal end of each knuckle domain (α6 helix of each subunit) that forms contact mainly with C-terminal and N-terminal ends of α1 and α2 helices of the neighboring subunit, respectively **(Figure 3.10a-d)**. The molecular interactions at the subunit interface vary in character, although they do harbor a common theme positioned at the interface between α2 and α6 **(Figure 3.10b-d)**. Capped by serines that are conserved in all three subunits, the two first helical turns of each α2 in ENaC largely make van der Waals interactions with α6 of the next subunit. In contrast, the characteristics of the interactions formed between α1 and α6 of the adjacent subunit vary at all three interfaces. In the α-subunit, Tyr162 forms polar interactions with Gln477 and Glu478 and interactions with Val474 of β-subunit **(Figure 3.10b)**. Hydrophobic residues Ile126 and Leu127 in β-subunit forge interactions around Trp486 **(Figure 3.10c)**, and finally, the segment bordered by Tyr129 and Phe131 of the γ-subunit make polar interactions with Arg508 and Gln509 of α-subunit where Tyr129 interacts with Met505 **(Figure 3.10d)**. In the homomeric models, these matching molecular interactions are not obeyed. For example, the hydrophobic sidechain of β-Leu127 clashes with the polar side chain of β-His473 **(Figure 3.9c)**. The divergence in amino acid sequence at the C-terminal end of both α1 and α6 in all three subunits undeniably results in

distinct forms of molecular interactions at each subunit interface that favor assembly of the triheteromeric channel.

Considering how the triheteromeric and homomeric α channels form, we speculate that the interactions within the upper palm, knuckle, and finger domains favor the arrangement of the α-β-γ in a counterclockwise fashion. Superposition of the individual subunits at the upper palm domain reveal the marked difference of the positions of the finger and thumb domains of the α subunit from β and γ. The rigid-body shift observed in the α subunit can readily accommodate the knuckle domain of the adjacent subunit, in the case of the triheteromer, the β knuckle domain **(Figure 3.9e-g)**. This α-mediated favored interaction likely gives rise to the functionally competent homomeric α, diheteromeric α/β and α/γ channels in heterologous expression systems. The steric clashes we observed in the finger and knuckle domains in homomeric β and γ disfavors assembly of these channels. Equally important to note is that as our cryo-EM map of ENaC TMD is disordered, we currently cannot visualize specific interactions that may contribute to the preferred heterotrimeric channel formation.

Identification of a putative Na^+ ion binding site

One of the unique characteristics of ENaC is not only the fact that it is highly selective for Na^+ ions, but also that Na^+ can act as an allosteric modulator of ENaC. This is known as the Na^+ self-inhibition where at high Na^+ concentrations ENaC is inhibited which causes a reduction in overall open probability(P_o)[64-66,71,227]. Studies have found conserved acidic residues that when mutated, reduces the inhibitory response of Na^+ self-inhibition[71]. However, these residues haven't been confirmed as Na^+ binding sites due to challenging nature of distinguishing these as actual Na^+ binding sites or allosteric interactions. What is known is that the presence of the

inhibitory peptides increases the affinity for Na^+ ions, thereby causing a stronger Na^+ self-inhibition as opposed to when the inhibitory peptides are cleaved where the affinity for Na^+ ions are reduced and Na^+ self-inhibition is blunted[66].

Our cryo-EM map indicates that the majority of ENaC particles that make up the map are in an uncleaved state, and when we inspected the map to locate the putative Na^+ binding sites we found in particular one residue that appeared to have a strong map density feature potentially caused by a Na^+ ion binding in this region. The residue Asp338 in the α-subunit, equivalent to Asp365 in mouse αENaC[71], have been shown to strongly correlate with Na^+ inhibition and is located in the β6-β7 loop of the α-subunit **(Figure 3.11a)**. It is not unusual that cryo-EM map features of acidic residues are less prominent due to the negative charge, however, in our cryo-EM map the map feature of Asp338 is very clear with an extra feature at the end that appear to interact with a backbone carbonyl group of Glu335. Other carbonyl groups of Val346 and Leu135 are also pointing towards the putative Na^+ bound, and are potentially part of coordinating the binding of the Na^+ ion **(Figure 3.11a)**. Coordinating distances at this putative Na^+ site range between 2.5 – 3.1 Å, certainly longer than the measured distances observed in crystal structures of proteins with highly selective Na^+ sites[241]. Studies have shown that other monovalent cations like Li^+ and K^+ can exert varying degrees of inhibition albeit to lesser extent than Na^+ [64].

Interestingly, the β-subunit as well as the γ-subunit have negatively charged residues that are homologous to the Asp338 found in the α-subunit. However, in the cryo-EM map these residues appear to not bind Na^+ ions, and the chain in this region is flipped where the acidic residues in both β and γ subunits are facing out. Instead, at the same location when superposing

the β6-β7 loop of β-subunit to α **(Figure 3.11b)**, or γ-subunit to α **(Figure 3.11c)** the tyrosine residues (Tyr306 in β, Tyr317 in γ) are flipped and occupying the same pocket as Asp338, which in α-subunit is different with Phe339 being flipped the opposite direction of the tyrosines **(Figure 3.11)**. Interestingly, the hydroxyl group of the tyrosines is in the equivalent position as the Na^+ forming a network of hydrogen bonds with the equivalent carbonyl groups. No studies have alluded to β and γ having Na^+ sensitive sites despite the sequence homology seen in this region, and the current structure of FL-ENaC offer an explanation as to why these sites potentially can not bind Na^+ ions.

The improved map regions of the inhibitory P1 peptides of α and γ subunits

A major improvement of the new map, as mentioned, is the map features in the region where the inhibitory P1 peptides of α and γ are located. These are the peptides that have been shown to inhibit ENaC at micromolar concentrations in both heterologous and native systems, and when released by proteases, shift ENaC from a low P_o to a high P_o[89,90,98,99]. In our first structure the density in these regions were less resolved, which prevented any detailed analysis of the molecular interactions between these peptides and the receptor interfaces[234]. However, in our structure of FL-ENaC, the side chains of the peptides can be placed with high accuracy allowing for more detailed analysis of important areas of interaction. The inhibitory peptide of α consists of 8 residues, LPHPLQRL (184-191 in human α), while in γ, the peptide consists of 11 residues, RFSHRIPLLIF (153-163 in human γ). The inhibitory effect of the α-P1 is highly dependent of both Leu184 and Leu191 at each end of the peptide being present[98], while in γ-P1

the presence of Arg153 at the N-terminal end (basic residues) and Phe163 at the C-terminal end are crucial for full inhibition[99].

Superposition of the α and γ subunit reveal that the C-terminal end of γ-P1 and α-P1 adopt a similar fold (highlighted in bold: αLPH**PLQRL**, γRFSHRI**PLLIF**), where the sites of interactions are similar for both α-P1 and γ-P1 **(Figure 3.12a)**. The conserved αPro187/γPro159 and αLeu188/γLeu160 in both inhibitory peptides (highlighted in bold: αLPH**PL**QRL, γRFSHRI**PL**LIF) allows for close interactions with the α2 helix where αLeu188 and γLeu160 make hydrophobic interactions with a conserved αTrp251 and γTrp229 on the α2 helix, respectively **(Figure 3.12b,c)**. Sequence comparison of P3-P4 β-sheet reveal that the identity between α and γ in this region is close to 50%, while less than 30% when comparing α/γ P3-P4 β-sheet to the same region of the β subunit. A glycine residue (Gly225) on the P3 β-strand of the α subunit has been shown to be important for the binding of the C-terminal end of the α-P1 peptide[227]. Similarly, the γ subunit harbors a glycine (Gly203) at this location, while the β subunit does not. In the same study, additional residues on the P3-P4 of the α subunit was identified to be important for α-P1 binding and inhibition[227]. In our structure, the C-terminal end of the P1 peptide for both α and γ lies on top of the P3-P4 β-sheet where αLeu191 and γPhe163 pack into a pocket formed by residues from P3-P4 β-sheet, explaining why the residues in this region are so important **(Figure 3.12b,c)**.

The N-terminal end of α-P1 and γ-P1 differ significantly, which perhaps underlies the reason for the main functional differences related to peptide inhibition in α and γ (highlighted in bold: α**LPH**PLQRL, γ**RFSHRI**PLLIF). In α-P1, Leu184 at the N-terminal end form an interaction with Ile153 in the α1 helix **(Figure 3.12b)**. Additionally, His186 has been shown to

be an important residue involved in α-P1 binding, and when mutated to a charged residue (basic or acidic), the inhibitory effect of α-P1 is reduced[65,79]. Substitution of a tyrosine at this position, however, regains the α-P1 inhibition. Within our structure the His186 is facing down towards the top of the thumb domain and does not appear to interact closely with the α2 helix **(Figure 3.12b)**. Inspection of the map in this region reveals an extra density connected to His186, which potentially suggest that the histidine forms a hydrogen bond with a water molecule **(Figure 3.6 and Figure 3.12d)**. Residues at the interface of the thumb domain and C-terminal end of α2 helix (D446 and R262) are important for α-P1 binding, especially related to His186[227], which suggest that these residues are involved in maintaining an important interface that His186 interacts with. As mentioned, the inhibition of α-P1 is reduced when His186 is mutated to a positively charged residue, and this might offer a partial explanation as to how protons regulate ENaC activity. Protons have been shown to increase the activity of ENaC[79], but the site that is regulated by protons has not been located. A putative candidate, His255 on α2 helix, when mutated to an arginine revealed an increased activation by protons[65,79]. The His255 is part of the interface where the α-P1 peptide binds **(Figure 3.12b)**. If His186 on α-P1 peptide is the site that is regulated by H^+, protonation of His186 would reduce the binding of the α-P1 peptide, and perhaps even more so when His255 is mutated to an arginine due to the proximity of two positively charged residues (protonated His186 and His255Arg) **(Figure 3.12b)**.

In γ-P1, the N-terminal side of the inhibitory peptide contains more residues, and is stretched towards the interface of the thumb domain and the C-terminal end of α2 helix (highlighted in bold: γ**RFSHRI**PLLIF). Within the peptide the SHR amino acids have been shown to not be sensitive to changes in terms of peptide inhibition, and our structure agrees with

this notion as the residues are mainly facing the extracellular space **(Figure 3.12c)**. The isoleucine (Ile158) along with PL (Pro159, Leu160 that binds to Trp229 as explained) are the most crucial residues for γ-P1 binding and are highly conserved[8,99]. Inspection of Ile158 reveals close interactions in a hydrophobic pocket created by multiple hydrophobic residues in this region, and His233 on α2 helix is in close proximity of Ile158. His233 is located at the same α2 helix position as αHis255, and was similarly as His255 suggested to be a putative proton sensing site. However, when mutated to an arginine, ENaC activity increases with no sensitivity to protons[65,79]. Mutation of His233 to arginine most likely breaks the interaction with the γ-P1 peptide as Ile158 is closely interacting with this histidine, and this explains why these channels are largely activated as a result of mutation at this site. The release of γ-P1 has been shown to increase ENaC P_o to ~1 [90]. Lastly, Arg153 at the N-terminal end makes polar interactions with Gln426 which is the final site that contributes to the binding of γ-P1 **(Figure 3.12c)**. At the same position as Gln426, there is an arginine (R448) in the α-subunit, and interestingly, there is an arginine (R181) located as the third residue upstream of Leu184 in α-P1 **(Figure 3.12b,e)**. αArg181 aligns with γArg153, and the substitution of Arg448 in the α-subunit (compared to Gln426 in γ) is perhaps the reason why the N-terminal side of α-P1 does not extend as far as γ-P1. Overall, the similarities between the C-terminal ends of the P1 peptides as well as the high sequence identity between α and γ P3-P4 β-sheets suggest a similar mechanism of binding in this region. The N-terminal ends of the α and γ P1 peptides, including the areas of interactions, are vastly different, perhaps explaining why these peptides have such large differences in their inhibitory effect of ENaC. γ-P1, once removed, dominates the P_o of ENaC, while the removal of α-P1 appear to have less pronounced effect on ENaC P_o.

Detection of missing densities in α-GRIP and γ-GRIP by focused classification

The purified sample of ENaC reveal multiple bands on an SDS PAGE gel (**Figure 3.4b**). The two bands at 15 kDa and 20 kDa are derived from γ and α subunits, respectively, determined by mass-spectrometry (data not shown). Their masses correspond with the predicted molecular weight of an N-terminal sequence (α and γ cleaved at the furin site in the extracellular domain), suggesting that the final purified FL-ENaC sample is a mix of cleaved and uncleaved ENaC channels.

As the final cryo-EM map of FL-ENaC includes well-resolved density features of the P1 inhibitory peptide in both the α-GRIP and γ-GRIP, which suggests that majority of the particles that contributes to the final cryo-EM map of FL-ENaC are uncleaved ENaCs. However, based upon results from mass-spectrometry and from SDS PAGE, the purified FL-ENaC sample presumably contains cleaved N-terminal sequences of α and γ subunits, and we wondered whether cleaved particles also contributed to the final cryo-EM map. Based off our experience with the first structure of ENaC, we suspected that structural heterogeneity would occur in the α- and γ-GRIP domains as a result of proteolytic removal of the P1 inhibitory peptides[234]. To tease apart these potential particle classes, we performed focused classification, using cisTEM[209], to separate structural variabilities within a masked region of interest in a cryo-EM map. A circular "3D mask" of the region of interest is specified in relation to the cryo-EM map where the cryo-EM map serves as a reference projection. The circular "3D mask" is then converted to individual 2D masks for each particle as a function of the particle orientation, which classifies variabilities of the signal within the masked region.

We provided a circular "3D mask" for both the α-GRIP and the γ-GRIP domains (**Figure 3.13a,b**), and separately performed focused classification of the final particles based on these regions (**Figure 3.13**). Five classes were requested for focused classification of the α-GRIP domain. Two of the five resulting classes were combined, as the two maps looked similar to each other (**Figure 3.13a,c,e and Figure 3.14**). Five classes were requested for focused classification of the γ-GRIP (**Figure 3.13b,d,f and Figure 3.15**). To verify all the classes from focused classification, we imported each class in to another cryo-EM software package, cryoSPARC[208]. Each class was reconstructed from *ab initio* method in cryoSPARC before final 3D reconstruction refinement (**Figure 3.14 and Figure 3.15**), and the resulting classes were compared to each other based upon differences within the GRIP domain regions. In both the α-GRIP and the γ-GRIP there was one class that was a clear outlier compared to other classes, revealing missing map density features in the region where the inhibitory P1-peptide is located (**Figure 3.13-3.17**). The most abundant class for both α-GRIP and γ-GRIP resembled the cryo-EM map of FL-ENaC as well as ΔENaC where the inhibitory P1-peptide remained intact, suggesting that the most prevalent classes are uncleaved α-GRIP and γ-GRIP.

The map with the missing P1-peptide density, for both the α-GRIP and the γ-GRIP regions, is the least abundant class, comprising ~ 10% of the total set of particles, and is referred to as "α-GRIP cleaved" or "γ-GRIP cleaved". Additionally, α/γ-GRIP cleaved classes are lower abundance classes and therefore featuring an overall lower resolution preventing detailed structural analyses that normally is only possible with high-resolution cryo-EM maps. However, the cryo-EM maps of α/γ-GRIP cleaved classes can be analyzed to evaluate structural changes of larger domains like secondary structural elements, as the overall resolution is better than 5 Å for both maps.

In addition to the α/γ-GRIP cleaved classes, the most abundant classes (containing ~ 50% of the total set of particles) resembled uncleaved states and are referred to as "α-GRIP uncleaved" and "γ-GRIP uncleaved". The remaining classes of either α-GRIP and γ-GRIP are referred to as "undefined" because these classes contain partial map density features or map features that deviate from the uncleaved maps of the α/γ-GRIP domain. The undefined classes are suspected to be partially cleaved ENaCs that presumably are cleaved at one furin site in α-GRIP or γ-GRIP domain. Additionally, γ-GRIP contains other protease sites (not recognized by furin), and one or multiple of these sites might be cleaved. The undefined maps have not yet been further evaluated due to the fact that little is known about the different proteolytic states of ENaC and therefore more work is required in order to elucidate structures of ENaC found in a distinct cleaved state. In any case, focused classification clearly shows that we can detect heterogeneity in the ENaC α-GRIP and γ-GRIP domains, which allows us to separate the structural variabilities that are due to different cleaved states of ENaC.

Comparison of α/γ-GRIP cleaved, uncleaved and undefined maps

Surprisingly, when comparing the different classes of α/γ-GRIP (cleaved, uncleaved and undefined), we see no large conformational changes in the ENaC ECD. In fact, most of the maps are similar to each other, although at different resolutions depending on the number of particles. We generated difference maps of both α-GRIP and γ-GRIP uncleaved and cleaved (subtracting the cleaved map from the uncleaved map) to look more carefully at the differences of these maps (**Figure 3.16 and Figure 3.17**). As the uncleaved map for both α-GRIP and γ-GRIP were at a higher resolution, we lowpass-filtered the uncleaved maps to a similar resolution as the cleaved

maps before subtracting the cleaved maps. The difference map between cleaved and uncleaved reveals that the largest difference in density is seen in the region of the GRIP domains of both α and γ subunit as was suspected based upon initial comparison between cleaved and uncleaved maps (**Figure 3.16 and Figure 3.17**). The difference map for the α-GRIP shows a much more distinct difference in the region of the GRIP domain in comparison to γ-GRIP, where the difference map is significantly noisier and the density in the GRIP domain region of the γ-subunit is not as well-defined. During focused classification of the α-GRIP classes, the population of each class converges earlier than for the γ-GRIP classes (**Figure 3.13c,d**). We speculated that perhaps γ-GRIP was more heterogeneous, and so we increased the number of classes to eight for focused classification. However, the resulting classes converged at a rate similar to that of classification using fewer classes. When assessing the classes at earlier iterations the γ-GRIP cleaved class has less density in the GRIP domain region. However, as classification progresses the γ-GRIP cleaved class becomes more populated and density in the γ-GRIP domain region where the inhibitory P1 peptide is located, starts reappearing. The approaches of focused classification for both α-GRIP and γ-GRIP are the same, and therefore the different results from classification suggests that there are some significant differences in cleaved α-GRIP vs γ-GRIP that can't be explained as of now. Regardless, the γ-GRIP class reveals missing density where the inhibitory P1 peptide is located (**Figure 3.17e**), and is the class that best resembles a "fully cleaved γ-GRIP".

A fraction of α-GRIP cleaved particles are also γ-GRIP cleaved particles

We next asked was whether a fraction of the particles that belonged to "α-GRIP cleaved" class also simultaneously belonged to the "γ-GRIP cleaved" class. Because focused classification can only detect structural variabilities within one region of the map at a time, the cleaved states of α-GRIP contained a mixture of cleaved, uncleaved and undefined γ-GRIP particles, and vice versa.

In fact, as expected, a very small fraction (less than 2%) of the total particles that are classified to α-GRIP cleaved class, are also classified to γ-GRIP cleaved class, and when combining these particles, we get a "fully cleaved" class of ENaC (**Figure 3.18a**). We did the same for "α-GRIP uncleaved", and "γ-GRIP uncleaved" class to distinguish a "fully uncleaved" class. Additionally, we analyzed all combinations of α-GRIP cleaved/uncleaved/undefined with γ-GRIP cleaved/uncleaved/undefined in order to assess all possible combinations of ENaC states based upon the different classes (**Figure 3.18a**). We cannot state that this truly reveals all the different states of ENaC, as we do not know how many different cleaved and uncleaved states of ENaCs actually exist. However, the strategy emphasizes that we can separate differences in two different regions, and further distinguish multiple combinations of states that perhaps make up all relevant ENaC states.

The fully cleaved and fully uncleaved ENaC particles that we separated by this analysis were extracted and processed in cryoSPARC before final 3D refinement and reconstruction to validate the final cryo-EM map from these particles. The fully uncleaved map of ENaC had an overall higher resolution than the map of the fully cleaved ENaC, as expected, due to the small number of fully-cleaved particles. To compare the maps of ENaC fully uncleaved and fully

cleaved, we created a difference map using the same method as above. Although the maps are at a low resolution, the difference map clearly illustrates missing density in both α-GRIP and γ-GRIP domains (**Figure 3.18b**).

Although these structures are low-resolution, our strategy of classification and group analysis points to a potential pathway for native tissue structural biology. Additionally, collecting more data will increase number of particles which subsequently will lead to a higher resolution for structural analysis.

The monoclonal antibody 7B1 does not trap ENaC in a single conformational state

There are multiple explanations as to why there are no obvious large conformational changes of the different cleaved and uncleaved classes of α-GRIP and γ-GRIP. One explanation is our use of antibodies to break the inherent pseudosymmetry of ENaC. One or both antibodies could trap ENaC in a conformational state that is independent of the cleavage state, and therefore a dominant, physiologically-irrelevant class.

We inspected the map of ENaC and the interactions with each of the antibody fragments (Fab), and determined that the 7B1 Fab, which binds near the α-GRIP domain in the α subunit seemed like a possible candidate that could trap ENaC in a conformational state. The other Fab 10D4 binds in the β-subunit GRIP domain, which is not sensitive to proteolysis, and therefore seems like a less likely candidate that could alter ENaC open probability.

The Fab 7B1 binds in the finger domain of the α-subunit next to the GRIP domain and mainly interacts with the chain of amino acids located on the C-terminal side of the α2 helix of the α-subunit. Unlike the β and γ subunits which feature short (two-turn) α3 helices, the same

stretch of amino acids in the alpha subunit are pulled away from the channel core, and the cryo-EM map contains no features of an α3 helix (**Figure 3.19a,b**). Instead the "α3-helix" of the α subunit is packed within a groove in 7B1, and two prolines within this stretch of amino acids contributes to the main area of contact between α-subunit and 7B1 (**Figure 3.19a,c,d**). Interactions with 7B1 are also seen in the loop region preceding α1 helix of the α subunit (**Figure 3.19e**). The domains in the α-subunit that are involved in forming these interactions with 7B1 are regions that likely play a role in ENaC gating, and perturbations within these regions might alter ENaC function.

To test this hypothesis, we performed electrophysiology patch clamp experiments of ENaCs expressed in HEK293 cells. Amiloride-sensitive Na^+-currents can be close to undetectable with ENaCs expressed in HEK293 cells, so to increase the activity of ENaC, we treated the cells with trypsin (5 μg/mL) for 5 min before comparing the amiloride-sensitive Na^+ current of ENaCs pre- and post-incubation of 7B1 (**Figure 3.20a**). As 7B1 has been found to have a slow off rate, and binds at a very high affinity as measured by bio-layer interferometry (data not shown), the amiloride-sensitive Na^+ current post addition of 7B1 is the Na^+ current of ENaCs bound to 7B1. The normalized current traces of ENaC Na^+ currents pre and post addition of 7B1 are identical, indicating that 7B1 binding does not alter the gating kinetics of ENaC (**Figure 3.20b**).

Discussion

Here we present the structure of FL-ENaC-DiFab complex that validates the structure of $\Delta ENaC^{234}$. The improved cryo-EM map of FL-ENaC reveals significantly more details about the

extracellular domain of ENaC, including a putative Na^+ ion binding site and inter-subunit contact areas, providing an explanation as to why ENaC favors a triheteromeric assembly over a homomeric assembly. The regions of the protease-sensitive GRIP domains are significantly improved, revealing similarities and differences in the area of interactions where the inhibitory peptides of α and γ binds. Although the TMD of ENaC remains elusive as the map features in the region of the micelle are poorly resolved, recent discoveries of ASIC TMD, revealing sensitivity to the external environment[172], suggest that ENaC TMD might harbor a similar characteristic and perhaps is even more sensitive than ASICs.

Additionally, the improved structure of FL-ENaC has allowed us to investigate whether we can tease apart structural differences within the GRIP domain region of α and γ subunits. Our purified FL-ENaC sample contains a mix of cleaved and uncleaved ENaC channels, and being able to separate these states by cryo-EM data processing methods will contribute to future structural strategies of ENaC in native tissue. The results are promising and reveal that cryo-EM is a viable method where, by using focused classification, we can separate structural variabilities within the α-GRIP and γ-GRIP domains, revealing ENaC maps with missing density in these regions. Subsequently we show that a fraction of the particles with missing density in α-GRIP also have missing density in the γ-GRIP, and 3D reconstruction of this small subset of particles reveal a "fully cleaved" ENaC map at low resolution.

We see no large conformational changes when comparing the different cleaved and uncleaved maps of ENaC and a potential explanation is that the antibody 7B1 traps ENaC in a single conformational state. However, electrophysiology studies reveal that 7B1 does not alter ENaC gating mechanism. The maps of ENaC in different cleaved states are lower resolution maps as they contain less particles, and so it is quite possible that any small conformational

changes that might be present cannot be detected at the current resolution. Future studies aimed to capture ENaC in cleaved states will answer this question.

Acknowledgements

We thank the Multiscale Microscopy Core (OHSU) and the Pacific Northwest Cryo-EM Center (PNCC) for support with microscopy and the Advanced Computing Center (OHSU) for computational support. We are grateful to L. Vaskalis for assistance with figures. We also want to thank the members of the Gouaux and Whorton labs for helpful discussions. This work was supported by the NIH (I.B., DP5OD017871) and AHA (S.N., 18PRE33990205). Additional support was provided by Tartar Trust Fellowship.

Tables

Table 1: Statistics of data collection, three-dimensional reconstruction, and model refinement.

Statistic	$ENaC_{EM}$		
	1	2	3
Material Source	Membrane	Whole cell	Whole cell
Detergent	Digitonin	Digitonin	Digitonin
FAb	7B1 & 10D4	7B1 & 10D4	7B1 & 10D4
Microscope	FEI Krios	FEI Krios	FEI Krios
Voltage (kV)	300	300	300
Detector	Gatan K2 Summit	Gatan K2 Summit	Gatan K2 Summit
Defocus range (μm)	-0.8 – -2.2	-0.8 – -2.2	-0.8 – -2.2
Exposure time (s)	3	3	3
Dose rate ($e^-/Å^2$/frame)	1.0	1.0	1.0
Frames per movie	60	60	60
Pixel size (Å)	0.415	0.415	0.415
Total dose ($e^-/Å^2$)	60	60	60
Motion correction	UCSF MotionCor2	UCSF MotionCor2	UCSF MotionCor2
CTF estimation	CTFFIND 4	CTFFIND 4	CTFFIND 4
Particle picking	cryoSPARC blob	cryoSPARC blob	cryoSPARC blob
2D/3D classification	cryoSPARC 2.11	cryoSPARC 2.11	cryoSPARC 2.11
3D classification and refinement	Relion 3.0, cryoSPARC 2.11, cisTEM 1.0	Relion 3.0, cryoSPARC 2.11, cisTEM 1.0	Relion 3.0, cryoSPARC 2.11, cisTEM 1.0
Symmetry	C1	C1	C1
Particles processed	172 954	218 428	71 549
Resolution masked (Å)	3.57	3.05	3.96
Map Sharpening B-factor ($Å^2$)	91.8	87.3	97.9
		cryoSPARC 2.11 merged map	
Merged Symmetry		C1	
Merged particle count		252 071	
Merged resolution masked (Å)		3.06	
		cisTEM 1.0.0 merged map	
Merged Symmetry		C1	
Merged particle count		248 079	
Merged resolution masked (Å)		3.11	
Protein residues		1 594	
Resolution (FSC= 0.143, Å)		3.11	
Molprobity score		1.41	
C_β deviations		0	
Ramachandran outliers		0	
Ramachandran allowed		2.33%	
Ramachandran favored		97.67%	
Bond length rmsd (Å)		0.001	
Bond angle rmsd (°)		0.370	

Table 3.1. Cryo-EM data collection, refinement and validation statistics.

Figures and legends

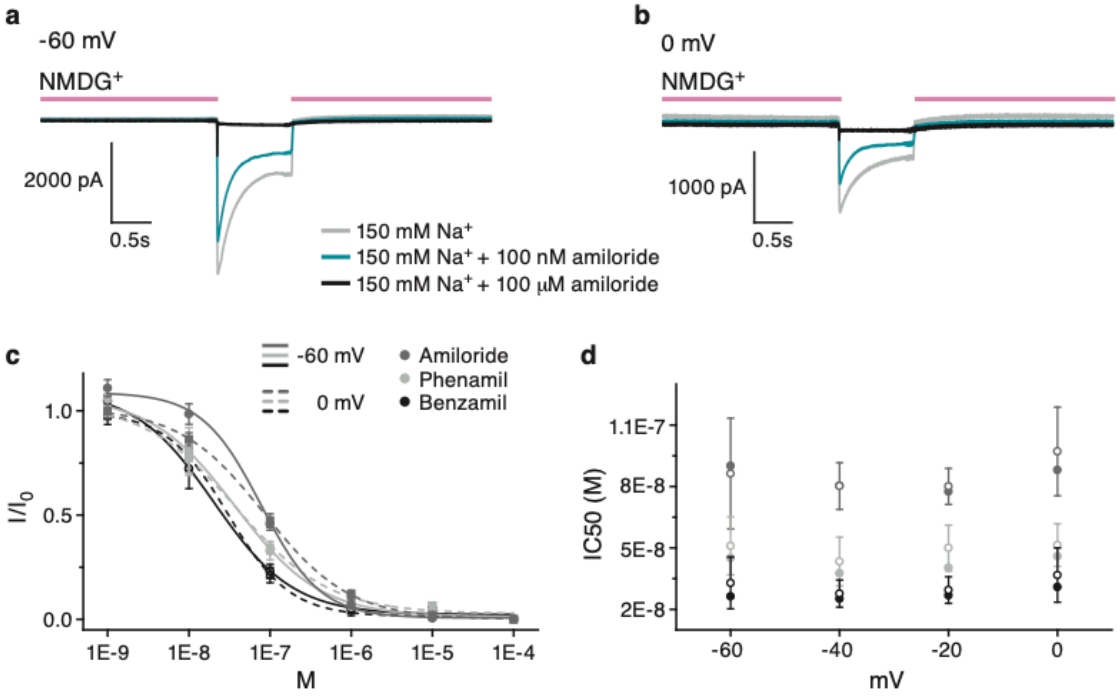

Figure 3.1. Functional characterization of ENaC. a,b, Representative whole cell patch clamp recording of FL ENaC expressed in HEK293 cells at -60mV **(a)** and 0mV **(b)**. Light grey trace represents Na^+-current with no blocker, dark green represents Na^+-current with 100 nM amiloride, and dark grey represent Na^+-current in presence of 100 µM amiloride. Light pink bar illustrates where $NMDG^+$ was the main ionic solution. **c,** Dose response curves of FL ENaC at -60 mV and 0 mV for the three different pore blockers amiloride (grey), phenamil (light grey) and benzamil (dark grey). The dose response was determined using the following concentrations of each blocker, 1 nM, 10 nM, 100 nM, 1 µM, 10 µM and 100 µM. The amiloride-sensitive current response (Na^+-current subtracted from Na^+-current in presence of 100 µM blocker) was normalized to the amiloride-sensitive Na^+-current with no blocker. Each dose response was

repeated 5 times for each blocker, and a curve was fitted to mean ± S.E.M . **d,** Plot of IC50 vs voltage shows that there is no voltage dependency. The IC50 was determined for each dose response and represent 5 independent experiments for each blocker (mean ± S.E.M). Closed circles represent the IC50 determined from a curve fitted to the average normalized current, open circles represents the mean value after fitting a dose response curve to each individual experiment and determining the IC50.

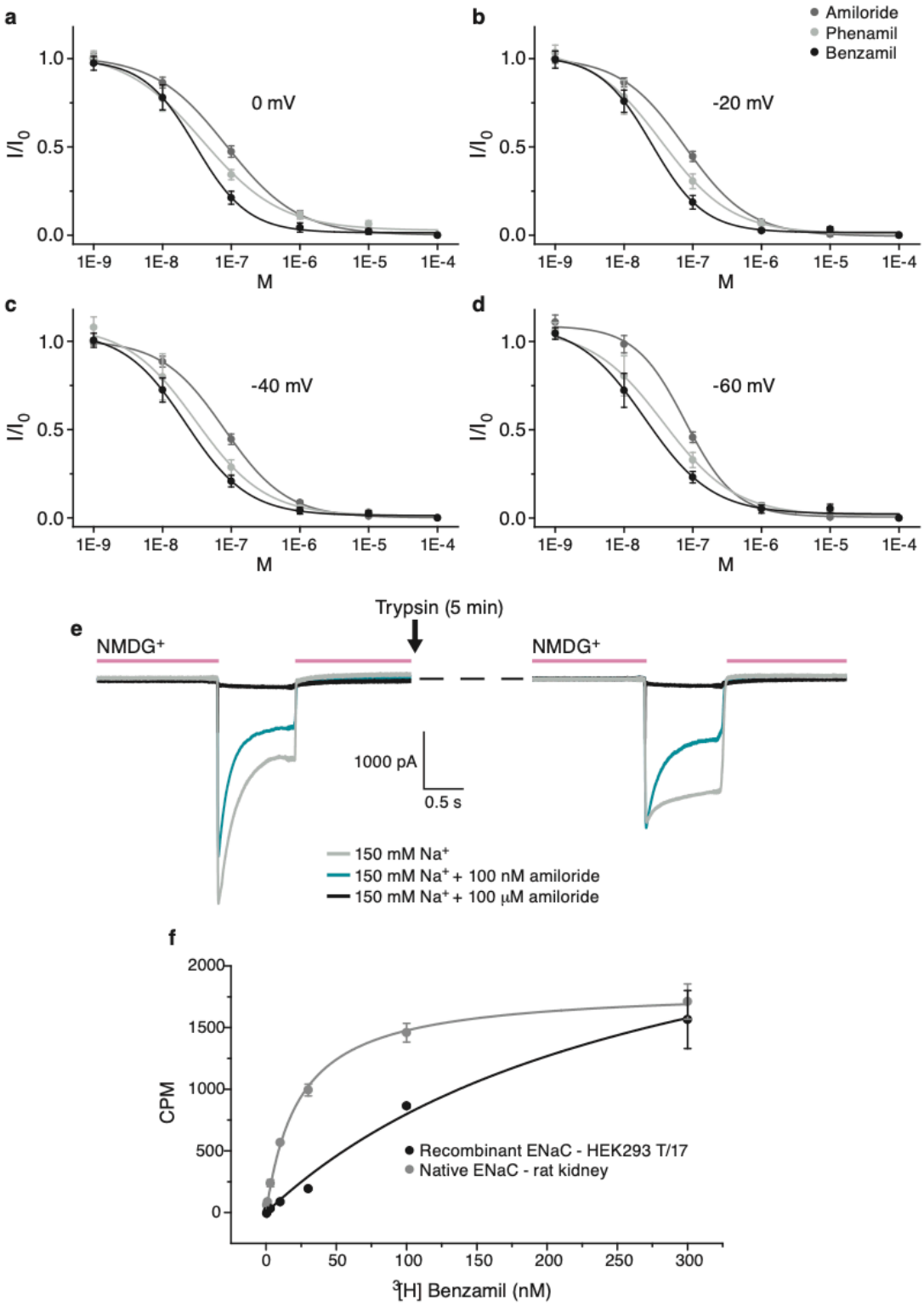
a
b
c
d
e
f
Amiloride
Phenamil
Benzamil
0 mV
-20 mV
-40 mV
-60 mV
I/I0
M
1E-9
1E-8
1E-7
1E-6
1E-5
1E-4
Trypsin (5 min)
NMDG+
1000 pA
0.5 s
150 mM Na+
150 mM Na+ + 100 nM amiloride
150 mM Na+ + 100 μM amiloride
CPM
Recombinant ENaC - HEK293 T/17
Native ENaC - rat kidney
[3H] Benzamil (nM)

Figure 3.2. Functional characterization of ENaC. a-d, Dose response curves of FL ENaC at 0 mV **(a)**, -20 mV **(b)**, -40 mV **(c)** and -60 mV **(d)** for the three different pore blockers amiloride (grey), phenamil (light grey) and benzamil (dark grey). The IC50 was determined for each experiment and each blocker and was for **0 mV**; 97.14 ± 21.62 nM, 51.37 ± 10.42 nM and 36.74 ± 13.25 nM , **-20 mV**; 80.05 ± 8.78 nM, 49.97 ± 11.18 nM and 29.41 ± 6.47 nM, **-40 mV**; 80.25 ± 11.37 nM, 43.37 ± 11.86 nM and 27.72 ± 6.65 nM and for **-60 mV;** 86.34 ± 27.04 nM, 51.01 ± 14.12 nM and 32.90 ± 12.66 nM for amiloride, phenamil and benzamil, respectively at all the voltages (mean ± S.E.M.). Fitted dose response curves in **a-d** represent the average normalized amiloride-sensitive Na^+-current with S.E.M. **e,** Representative whole cell patch clamp recording of FL ENaC expressed in HEK293 cells at -60mV pre **(e)** and post trypsin treatment (5 μg/mL for 5min) showing an increase in steady state amiloride-sensitive Na^+-current upon treatment with trypsin. Experiments have been repeated individually more than 3 times. **f,** Radio ligand binding saturation curve of ^{3}[H] benzamil to native ENaC in rat kidney cortex and medulla membrane (light grey) and membranes prepared from recombinant ENaC in HEK293 cells (dark grey). The fitted curve represents the specific binding of ^{3}[H] benzamil, which is considered to be the difference curve of ^{3}[H] benzamil binding in presence and absence of 100 μM unlabeled phenamil. Error bars represent the S.E.M of the total signal in absence of 100 μM unlabeled phenamil.

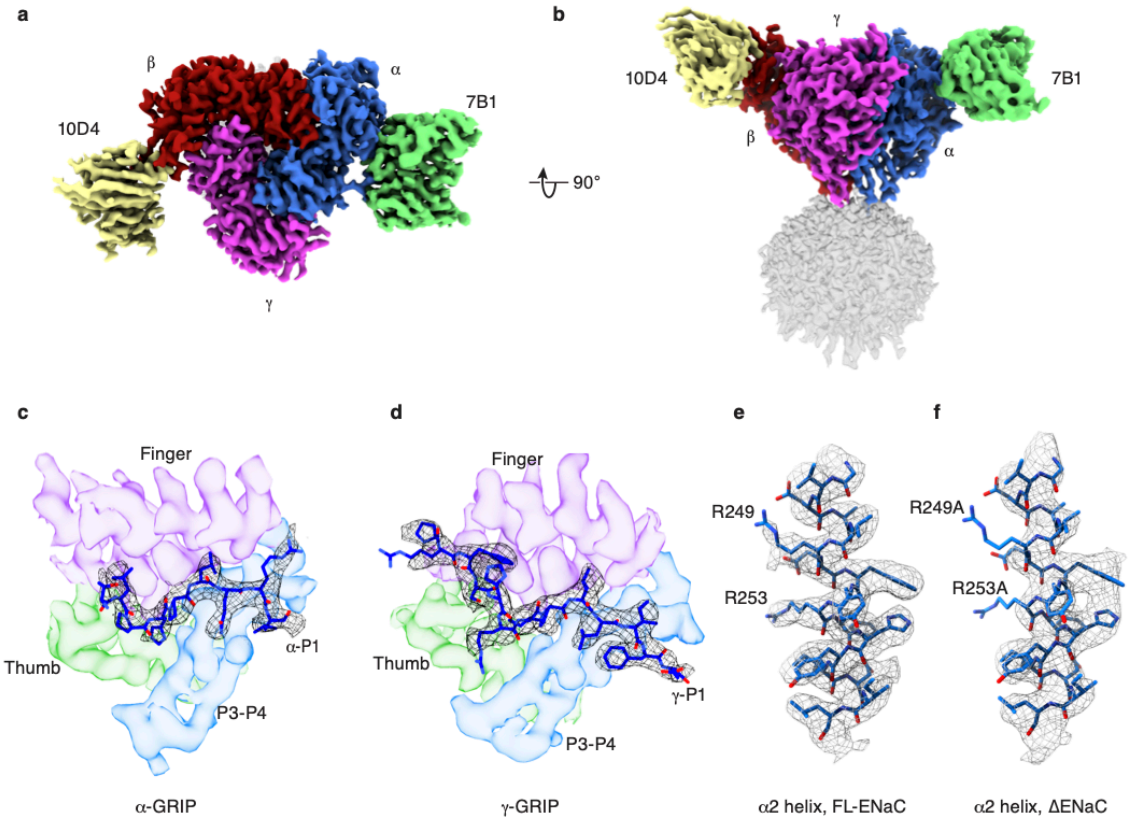

Figure 3.3. Cryo-EM map of ENaC-DiFab. Cryo-EM map of GFP-cleaved full-length ENaC-DiFab complex in digitonin viewed parallel **(a)** and perpendicular **(b)** to the membrane. α, β and γ subunits are colored blue, red and magenta, respectively. The Fabs, 10D4 and 7B1 Fv maps are colored wheat and green, respectively. **c,d,** The cryo-EM potential density map of ENaC α-GRIP (**G**ating **R**elief of **I**nhibition by **P**roteolysis) **(c)** and ENaC γ-GRIP **(d)** shows improved density of P1 inhibitory peptide (black mesh with blue stick representation of the peptide). The finger domain containing α1 and α2 helix is colored in light purple, the thumb domain in light green and GRIP domain featuring the P3-P4 β-sheet is colored light blue. **e,f,** Cryo-EM potential map of the α2 helix in the finger domain of the α-subunit of FL-ENaC-DiFab map **(e)** and ΔENaC-

DiFab map[234] **(f)** showing the improved resolution, and the appearance of two arginines (αR249, αR253) **(e)** that were mutated to an alinine residues in the ΔENaC-DiFab structure **(f)**. Both maps are colored in grey mesh, and the amino acid sequence is represented in blue sticks, and is from the registry of FL-α subunit with wild type arginines.

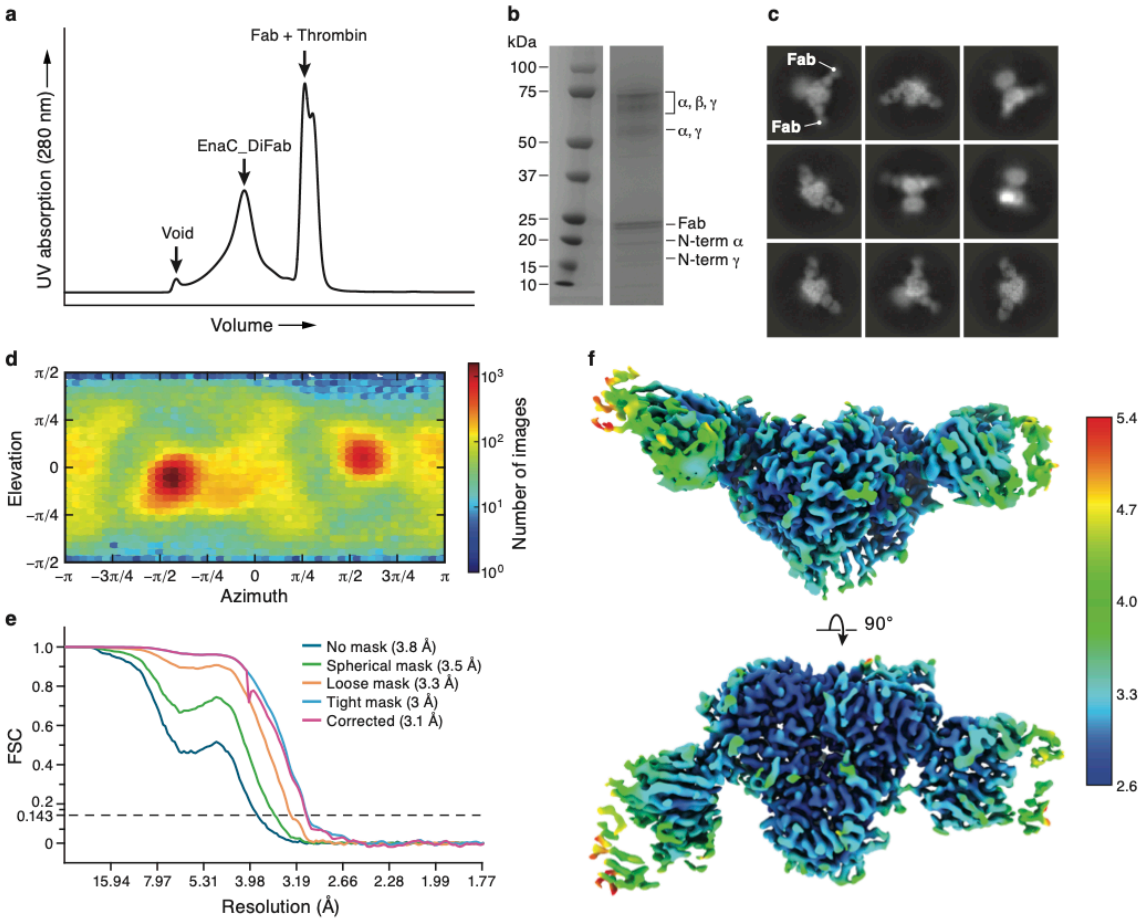

Figure 3.4. Cryo-EM of FL ENaC-DiFab. a,b, FSEC **(a)** and SDS PAGE **(b)** analysis of ENaC-DiFab complex in digitonin after size-exclusion chromatography. **c-f,** cryo-EM 2D classes **(c)**, angular particle distribution **(d)**, gold standard fourier shell correlation (GS-FSC) **(e)** and local resolution estimate **(f)** of FL-ENaC-DiFab complex.

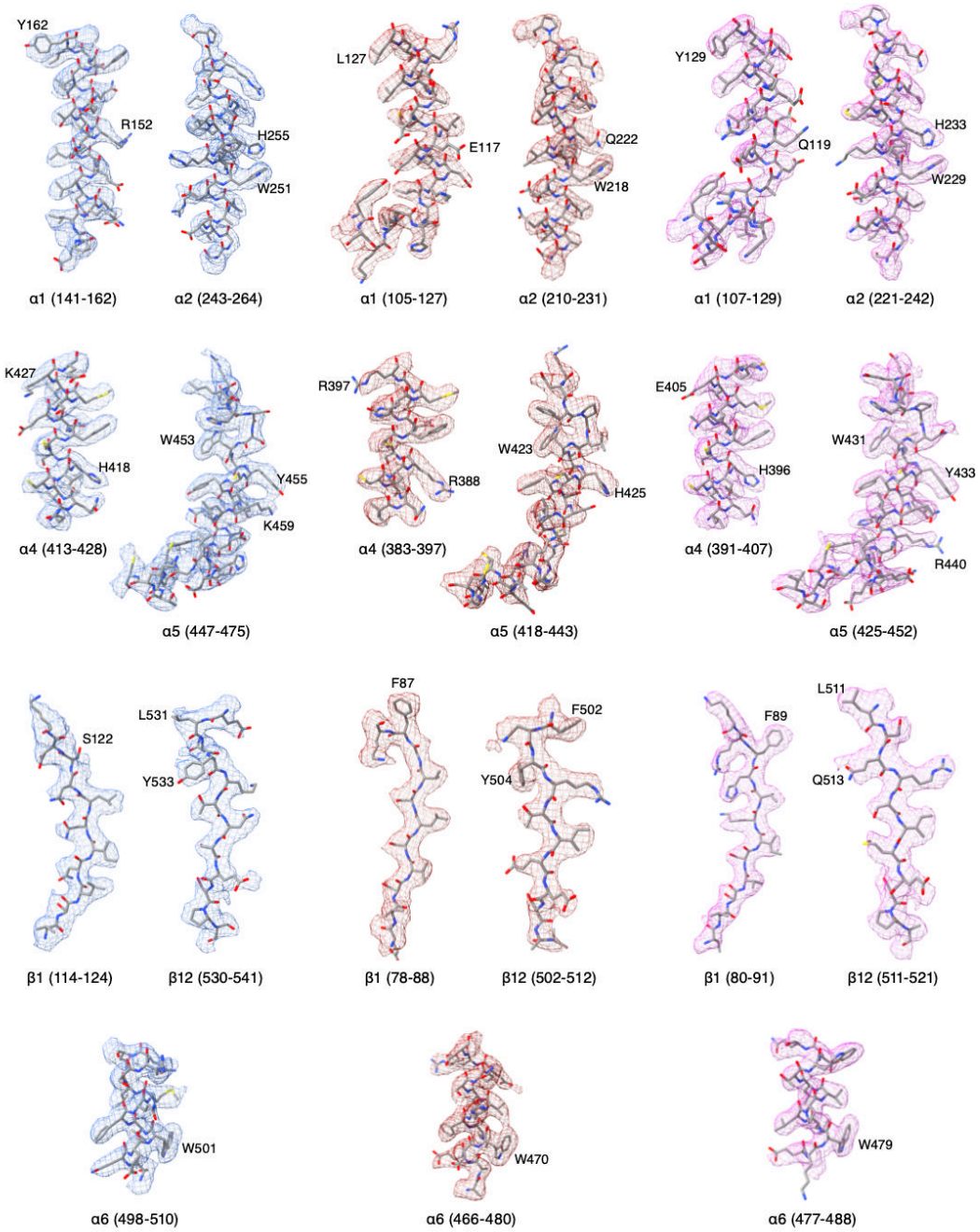

Figure 3.5. Cryo-EM potential maps of different regions in ENaC-DiFab map. α, β, and γ subunit maps are represented in blue, red and magenta colored mesh, respectively. FL-ENaC model is represented in grey stick superposed with the colored mesh maps.

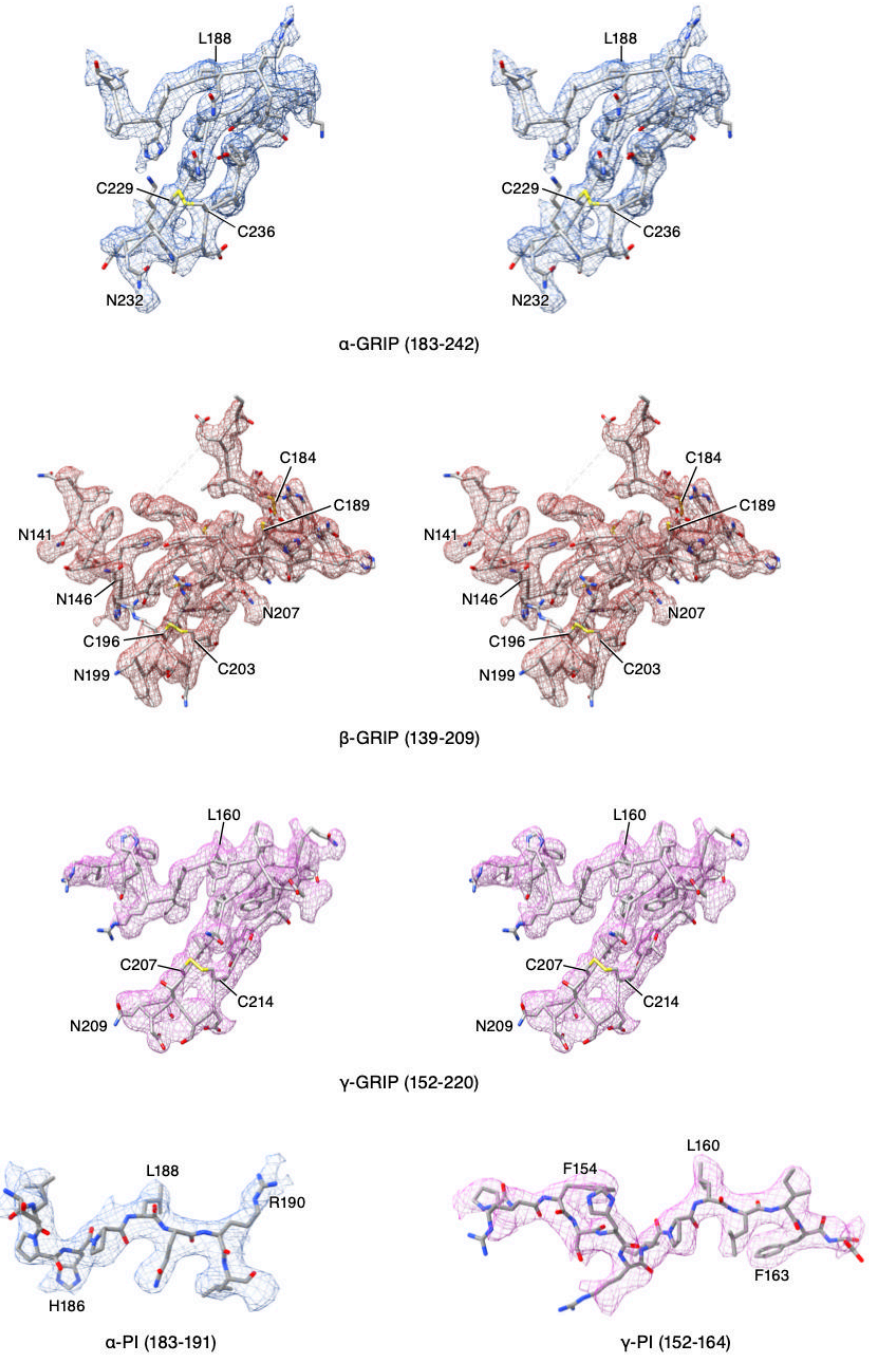

Figure 3.6. Stereoview of cryo-EM potential maps of the GRIP domain in ENaC-DiFab map. α, β, and γ subunit maps are colored in blue, red and magenta colored mesh, respectively. FL ENaC model is represented in grey stick superposed with the colored mesh maps.

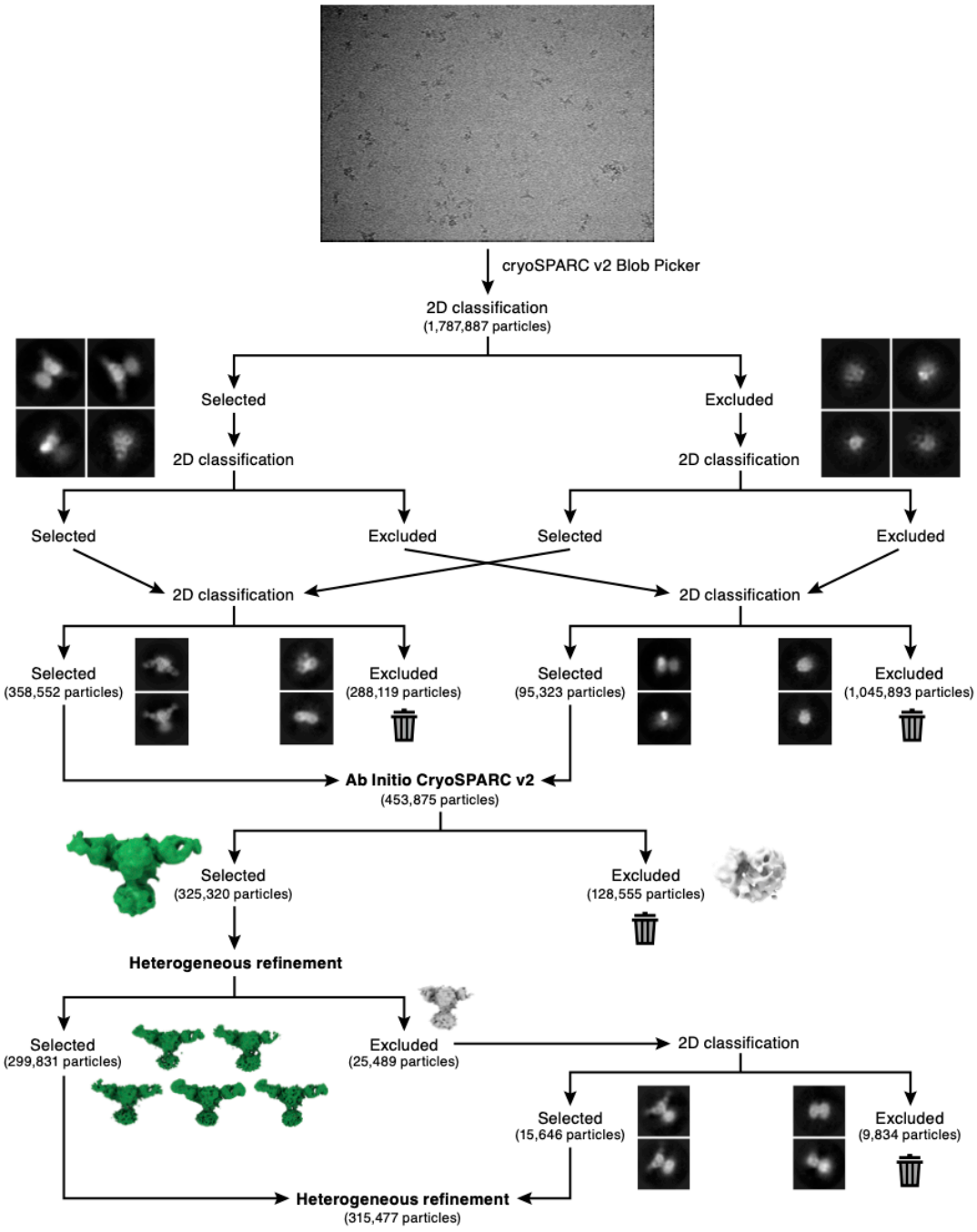

Figure 3.7. Cryo-EM initial data processing. Workflow of the initial data processing to remove particles belonging to false positive classes.

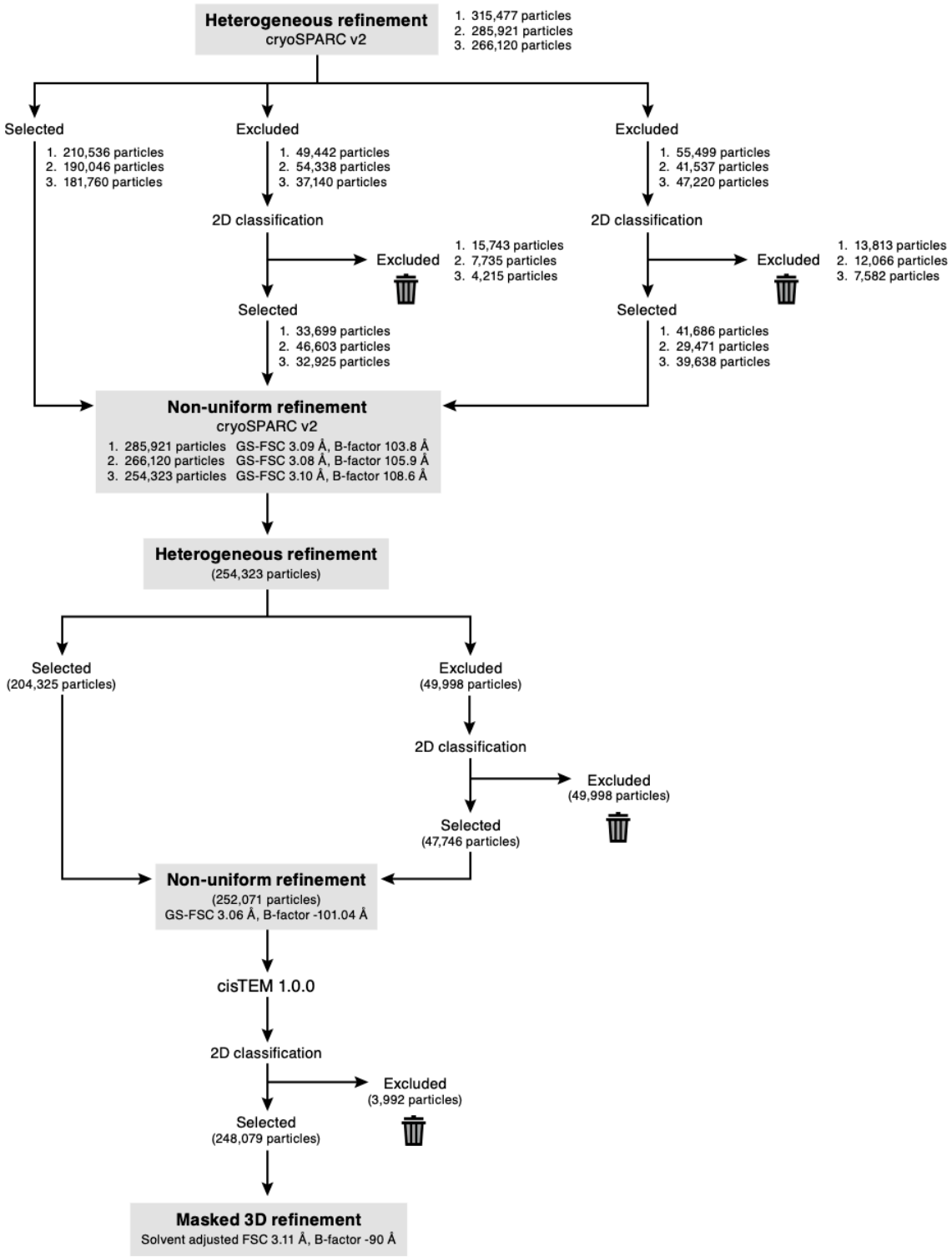
Heterogeneous refinement
cryoSPARC v2
1. 315,477 particles
2. 285,921 particles
3. 266,120 particles
Selected
1. 210,536 particles
2. 190,046 particles
3. 181,760 particles
Excluded
1. 49,442 particles
2. 54,338 particles
3. 37,140 particles
2D classification
Excluded
1. 15,743 particles
2. 7,735 particles
3. 4,215 particles
Selected
1. 33,699 particles
2. 46,603 particles
3. 32,925 particles
Excluded
1. 55,499 particles
2. 41,537 particles
3. 47,220 particles
2D classification
Excluded
1. 13,813 particles
2. 12,066 particles
3. 7,582 particles
Selected
1. 41,686 particles
2. 29,471 particles
3. 39,638 particles
Non-uniform refinement
cryoSPARC v2
1. 285,921 particles GS-FSC 3.09 Å, B-factor 103.8 Å
2. 266,120 particles GS-FSC 3.08 Å, B-factor 105.9 Å
3. 254,323 particles GS-FSC 3.10 Å, B-factor 108.6 Å
Heterogeneous refinement
(254,323 particles)
Selected
(204,325 particles)
Excluded
(49,998 particles)
2D classification
Excluded
(49,998 particles)
Selected
(47,746 particles)
Non-uniform refinement
(252,071 particles)
GS-FSC 3.06 Å, B-factor -101.04 Å
cisTEM 1.0.0
2D classification
Excluded
(3,992 particles)
Selected
(248,079 particles)
Masked 3D refinement
Solvent adjusted FSC 3.11 Å, B-factor -90 Å

Figure 3.8. Cryo-EM data processing – final map. Workflow of data processing to further clean up particles for 3D reconstruction of the final map.

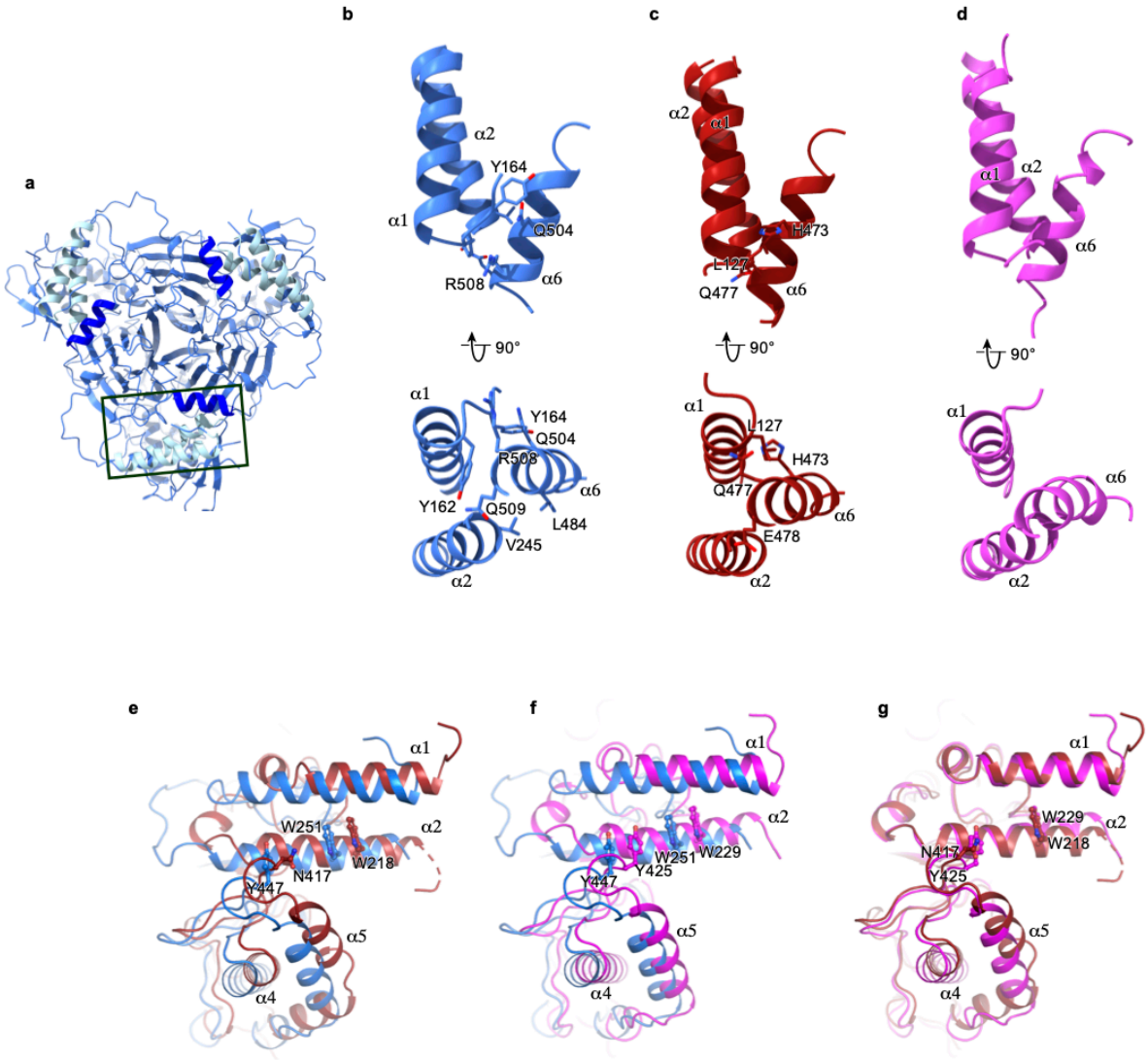

Figure 3.9. Generation of homomeric channels reveal areas with steric clashes. a-d, Generation of homomeric trimers using symmetry-related molecules around the threefold axis of symmetry reveal that homomeric α are accommodated unlike homomeric β and γ where domain interactions are disfavored due to steric clashes. **a,** Homotrimeric α viewed perpendicular to the membrane. Boxed region shows that the inter-subunit area of α1/α2 and α6 of homomeric α does not contain any major clashes, favoring a trimeric assembly **(b)**, while for homomeric β **(c)** and γ **(d)** trimers there are steric clashes in this region. Hydrophobic side chains of βLeu127

clashes with the polar side chain of βHis473 **(c)**, while the relative angle of α1/α2 clashes with α6 in homomeric γ **(d)**. **e-g,** Generation of asymmetric homotrimeric channels by superposition of subunits at the upper domain reveal a rigid body shift for the α-subunit relative to β and γ. α compared to β **(e)**, α compared to γ **(f)** and β compared to γ **(g)** reveal a shift of one helical turn only for α relative to β and γ, as seen by comparing highly conserved Trp residues on α2 helix (αTrp251, βTrp218, γTrp229), as well as a Tyr (αTyr447, βN417 and γTyr425 in thumb domain) conserved in α and γ.

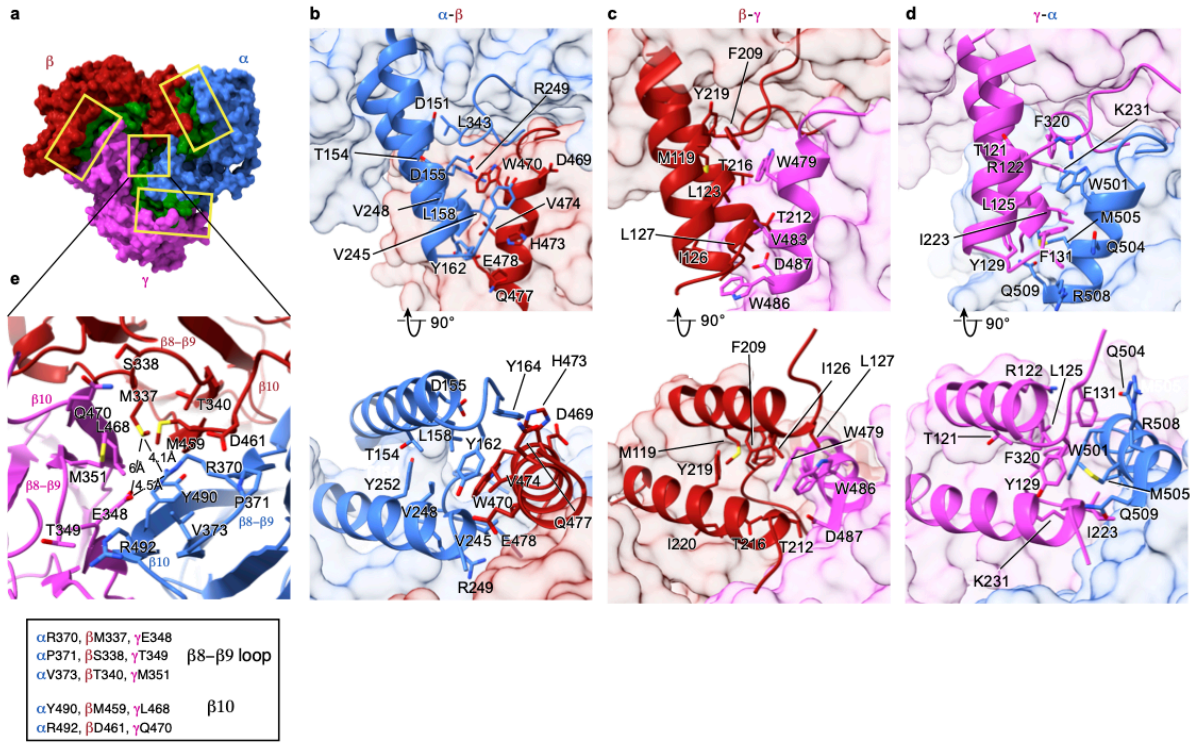

Figure 3.10. Inter-subunit interactions in FL-ENaC. a, Surface representation of FL-ENaC viewed perpendicular to the membrane. Subunits are colored as in **Figure 3.3**. Residues mediating inter-subunit interactions are colored in green. The box at the pseudo symmetric axis is viewed in panel **e**, while the three rectangles are viewed in **b**,**c** and **d**. **b-d,** Residues mediating inter-subunit interactions are viewed in stick representation. **(b)** Interactions between α and β subunits forge both van der Waals and polar interactions. **(c)** Interactions between β and γ subunits largely involve van der Waals interactions, distinct from intersubunit interactions at the equivalent sites in α-β and γ-α interfaces. **(d)** Molecular contacts at the γ-α interface, while similar to that of the α-β interface in properties, involves strong interactions between Y129 and M505. **(e)** The difference of the residues at the pseudo symmetric axis creates a unique area of contact between the β-strands of palm and β-ball domain.

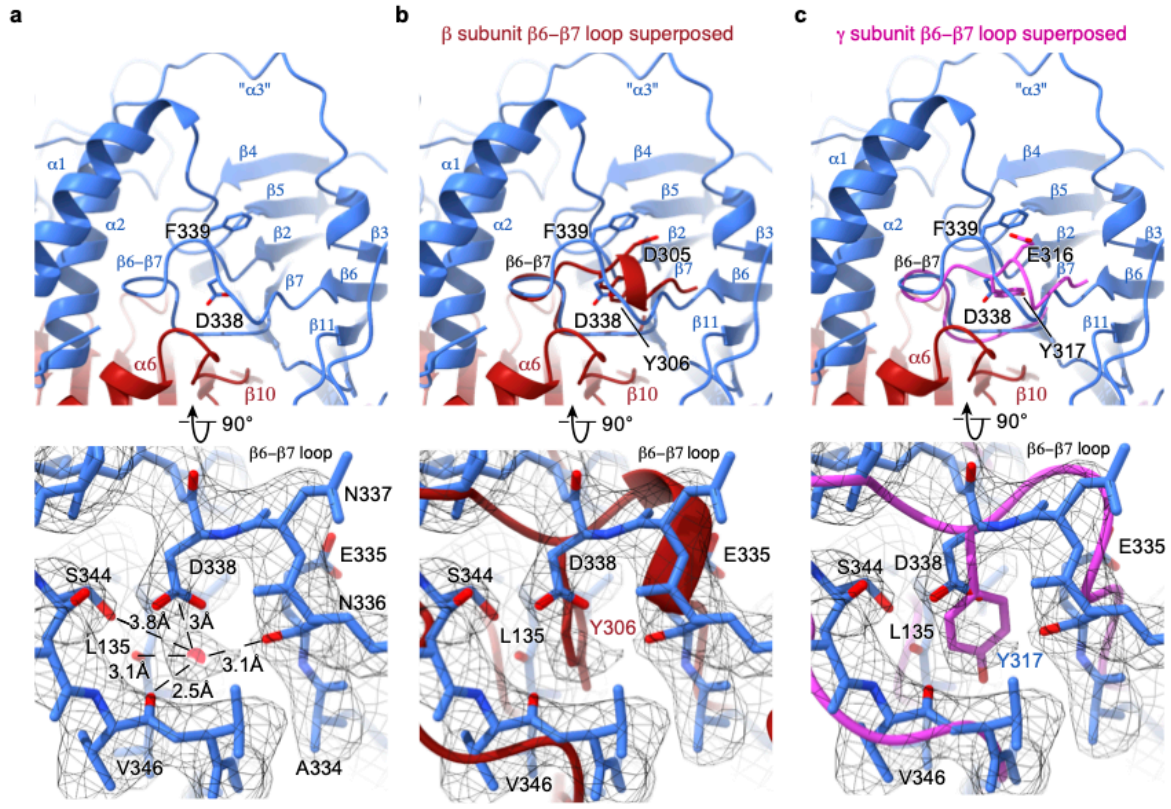

Figure 3.11. Putative Na^+ binding site found in the α-subunit. Subunits are colored the same as in **Figure 3.3. a,** D338 located in the β6-β7 loop of the α-subunit has been identified as a residue that is important for Na^+ self-inhibition. The cryo-EM map in this region reveal clear map features that potentially are caused by an Na^+ ion coordinated mainly by D338 and carbonyl groups of E335, L135, V346. Map is contoured at σ 9.1 **b,** Superposition of the β-subunit β6-β7 loop reveal that the corresponding acidic residue (D305) is flipped compared to D338 of α where Y306 is occupying the same pocket as D338. **c,** Superposition of β6-β7 loop of γ-subunit reveals that E316 in γ is similarly flipped as for D305 of β-subunit in **(b)** where Y317 is occupying the same pocket. This suggest that β and γ subunits do not bind Na^+ ions as α does.

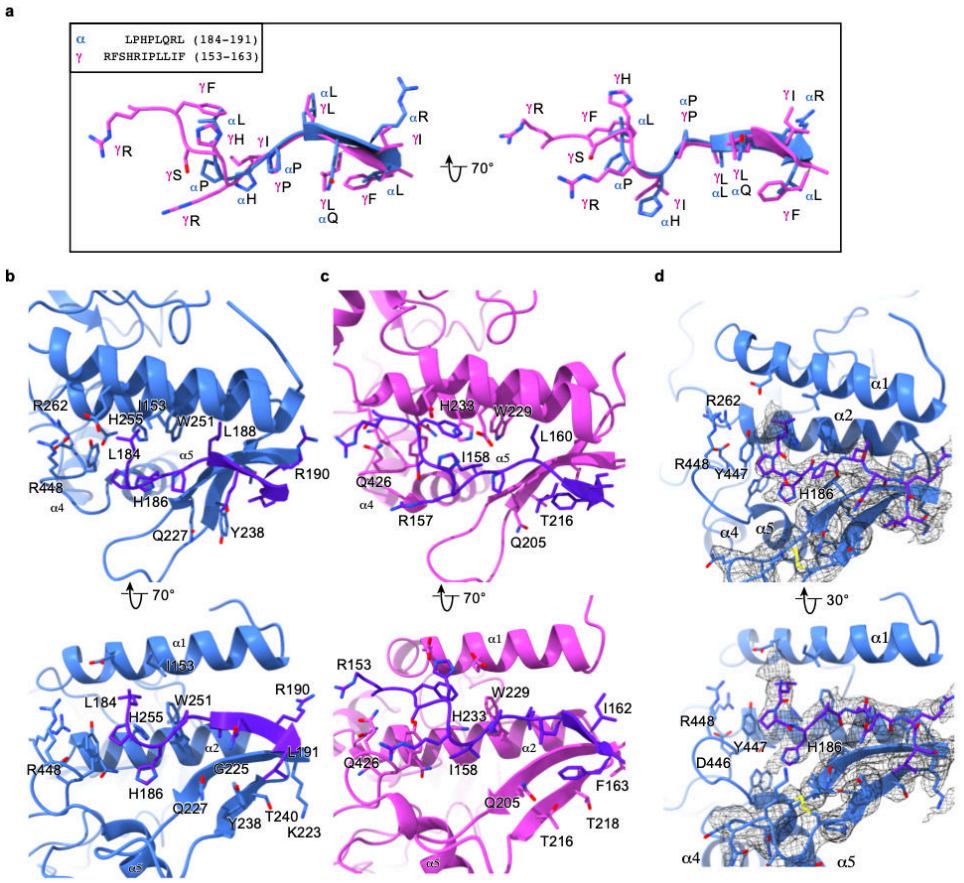

Figure 3.12. The inhibitory P1 peptides of α and γ. a, When superposing both α and γ subunits, the C-terminal end of α-P1 and γ-P1 peptide align and reveal that both peptides adopt a similar fold (C-terminal end highlighted in bold: αLPH**PLQRL**, γRFSHRI**PLLIF**). **b,c,** When comparing areas of interactions the C-terminal end of α and γ make similar interactions where αLeu191 and γPhe163 packs into a pocket formed by residues located within P3-P4 β-sheet. **d,** His186 of α-P1 appear to have additional density (that possibly is due to interaction with a water molecule), and is facing and area of interaction located at the top of the thumb domain and the N-terminal side α2 helix. Residues that make up this area of interaction (R448, Y447, D446 and R262) have all been shown to be important for the binding of α-P1 and has been related to the position of the His186 residue[227].

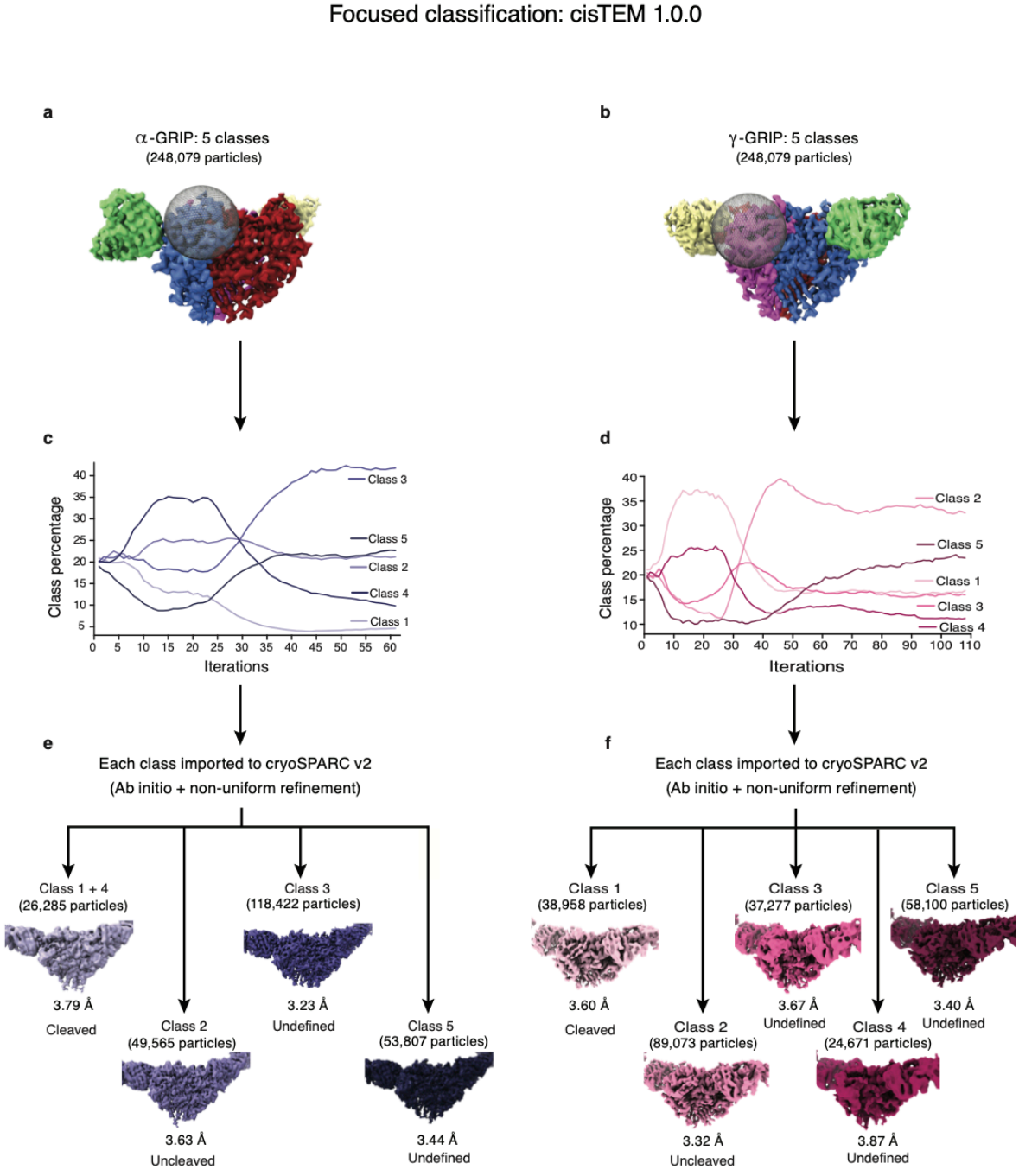

Figure 3.13. Workflow of focused classification. a,b, Cryo-EM map of FL-ENaC showing the circular "3D mask" that was specified for focused classification of α-GRIP **(a)** and γ-GRIP **(b)**. Subunits and Fabs are colored as in **Figure 3.3a,b. c,d,** Five classes were requested for focused

classification where all classes of α-GRIP **(c)** and γ-GRIP **(d)** reached a threshold after multiple iterations as illustrated. **e,f,** All the classes were imported to cryoSPARC for ab initio and 3D refinement to validate the results. Only four classes were refined of α-GRIP as two of the classes were combined because they looked similar upon inspection **(e)**. Five class were refined for γ-GRIP **(f)**.

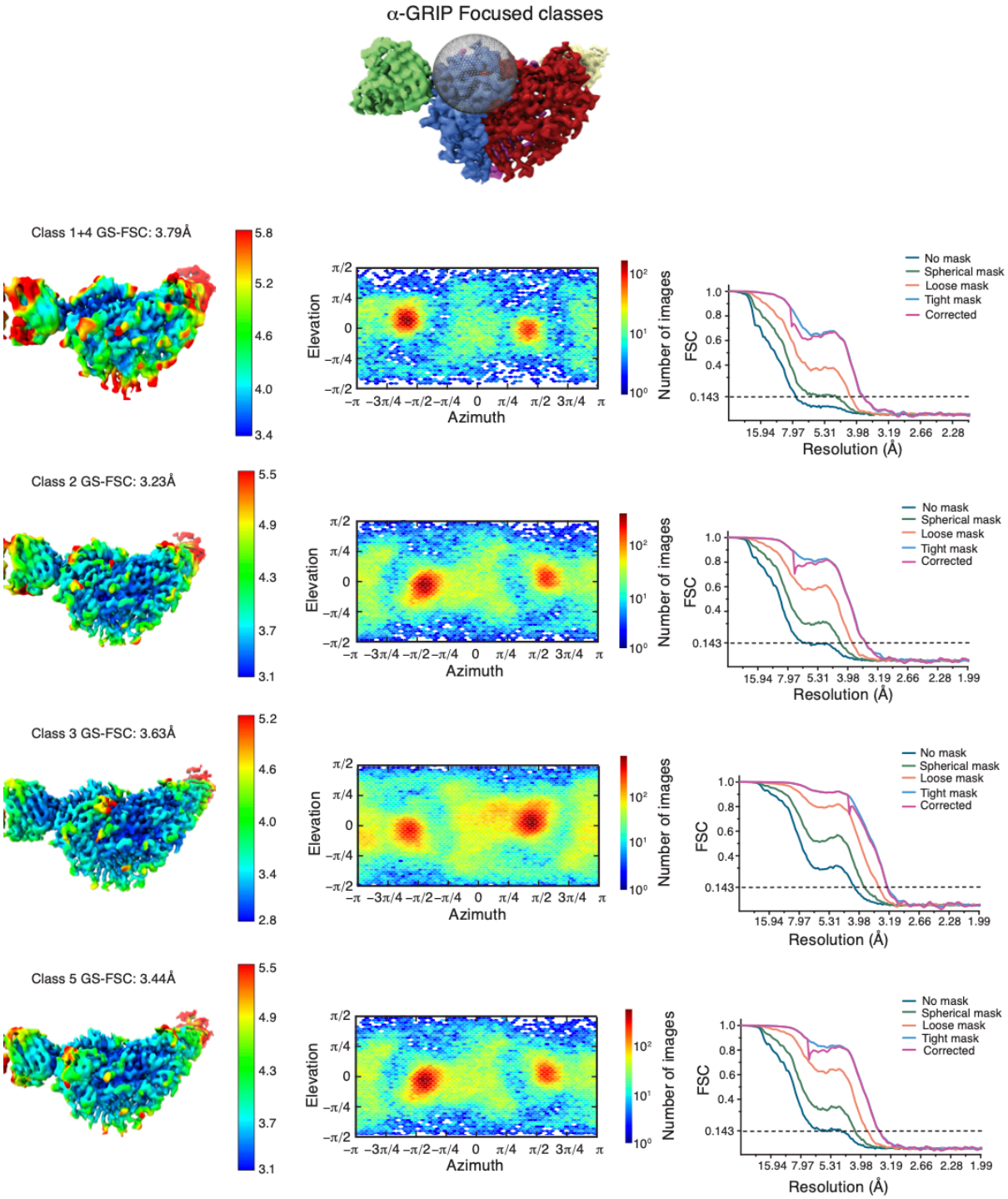

Figure 3.14. Cryo-EM data analysis of all α-GRIP classes in cryoSPARC. Local resolution estimate, angular distribution and gold standard FSC of the resulting four maps from focused

classification (as illustrated in **Figure 3.13e**) reveal that all classes have a similar overall particle distribution for the classification performed of the α-GRIP region.

γ-GRIP Focused classes

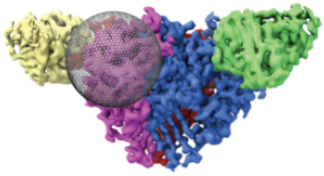

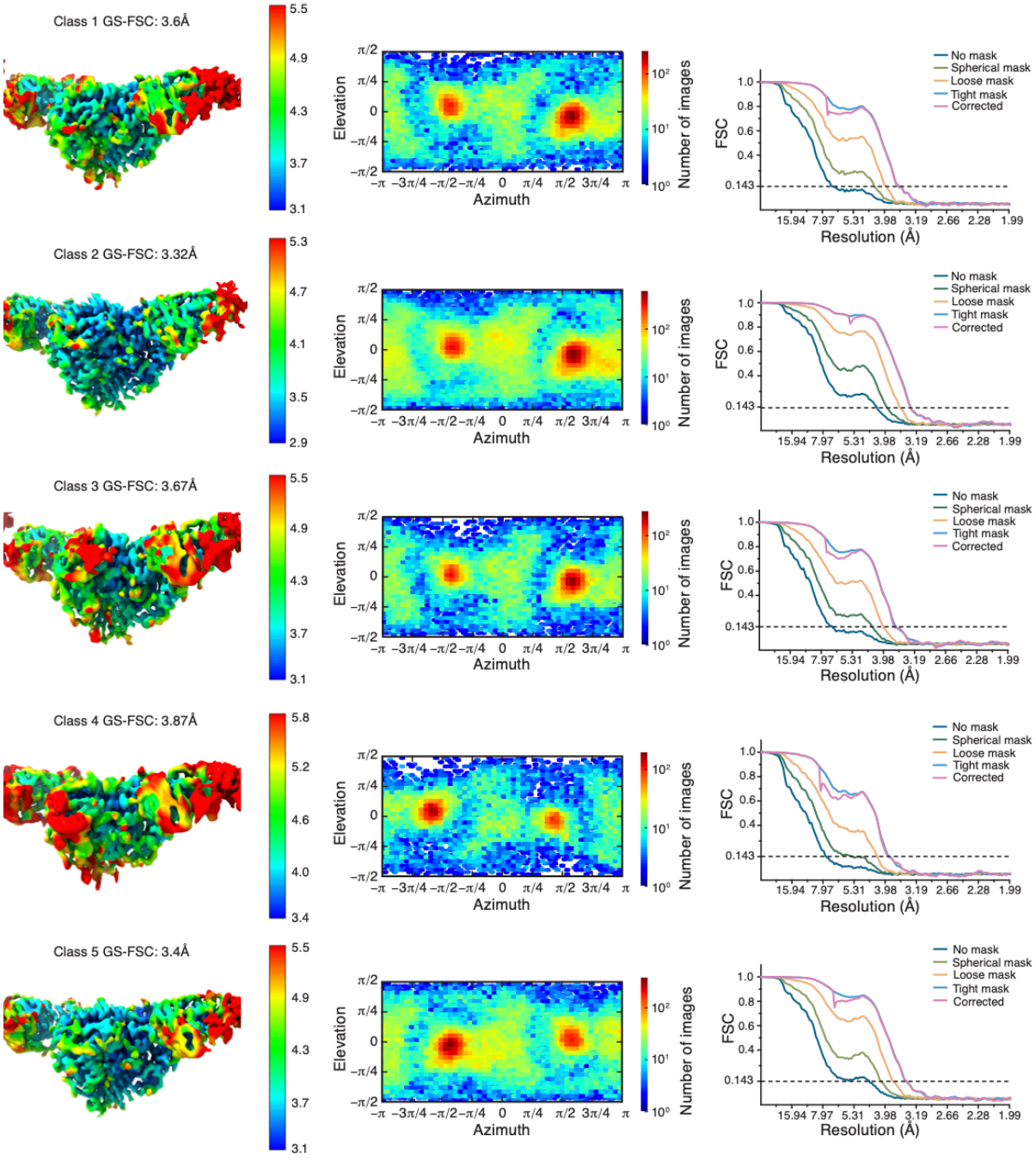

Figure 3.15. Cryo-EM data analysis of all γ-GRIP classes in cryoSPARC. Local resolution estimate, angular distribution and gold standard FSC of the resulting four maps from focused classification (as illustrated in **Figure 3.13f**) reveal that all classes have a similar overall particle distribution for the classification performed of the γ-GRIP region.

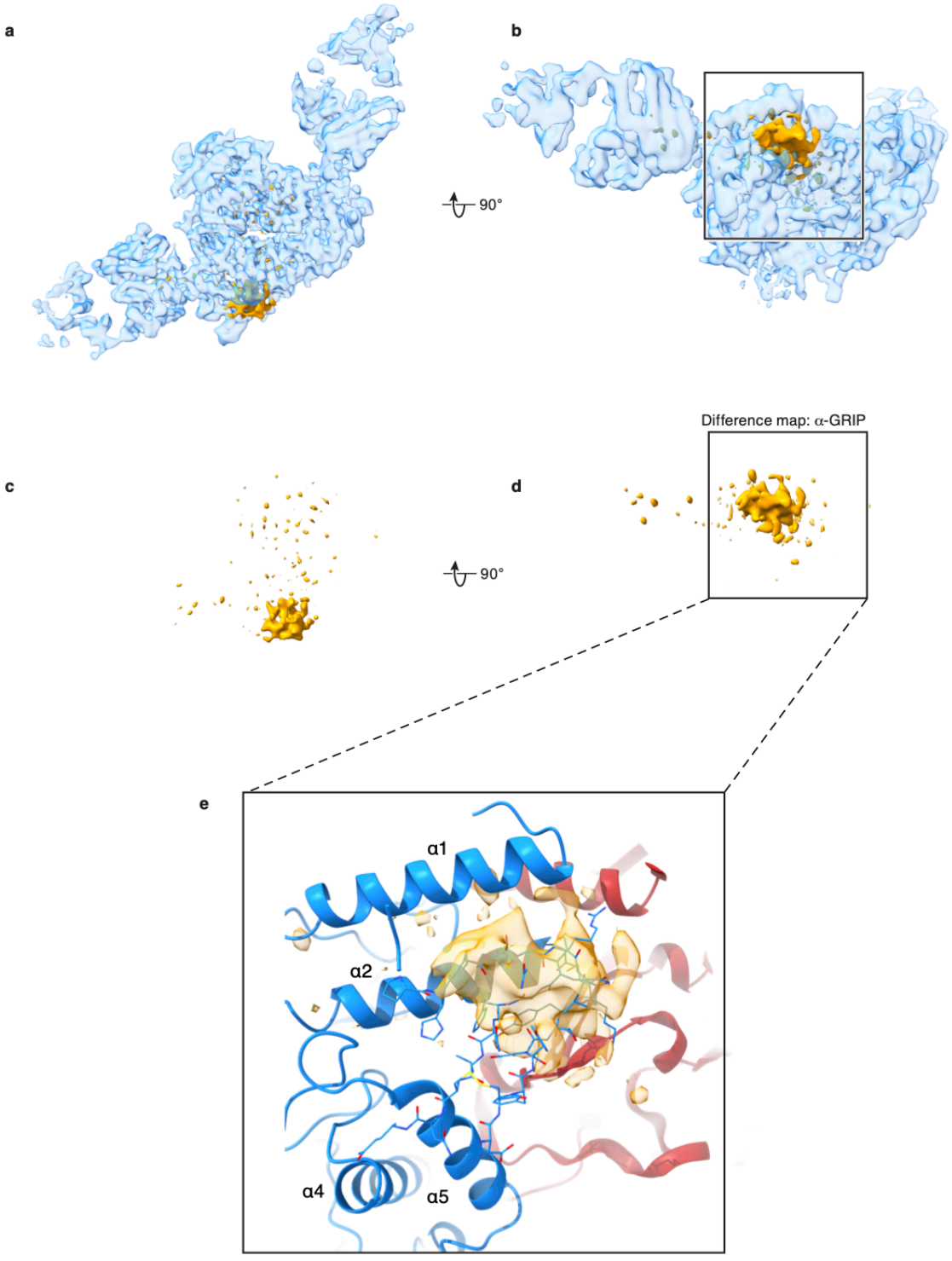
a
b
90°
c
d
90°
Difference map: α-GRIP
e
α1
α2
α4
α5

Figure 3.16. Difference map of α-GRIP cleaved and uncleaved maps. Difference map was generated by subtracting the cleaved α-GRIP map from the uncleaved map revealing a distinct density difference in the region of the GRIP domain. View of FL-ENaC-DiFab map perpendicular **(a)** and parallel to the membrane **(b)**. Map is colored in transparent blue to illustrate that this is from focused classification of α-GRIP, and the map presented is the α-GRIP cleaved map superposed with the difference map (gold). **c,d,** Difference map (gold) represented in the exact same view, perpendicular **(c)** as in **a**, and parallel **(d)** as in **b** to the membrane. **e,** Difference map, in transparent gold, is superposed with the model of FL-ENaC-DiFab map and reveal that the density difference between cleaved and uncleaved α-GRIP maps are in the area of the GRIP domain, which is located between the finger (α1 and α2 helices) and thumb domain (α4 and α5 helices). α-subunit model is colored in blue, and β-subunit model is colored in red.

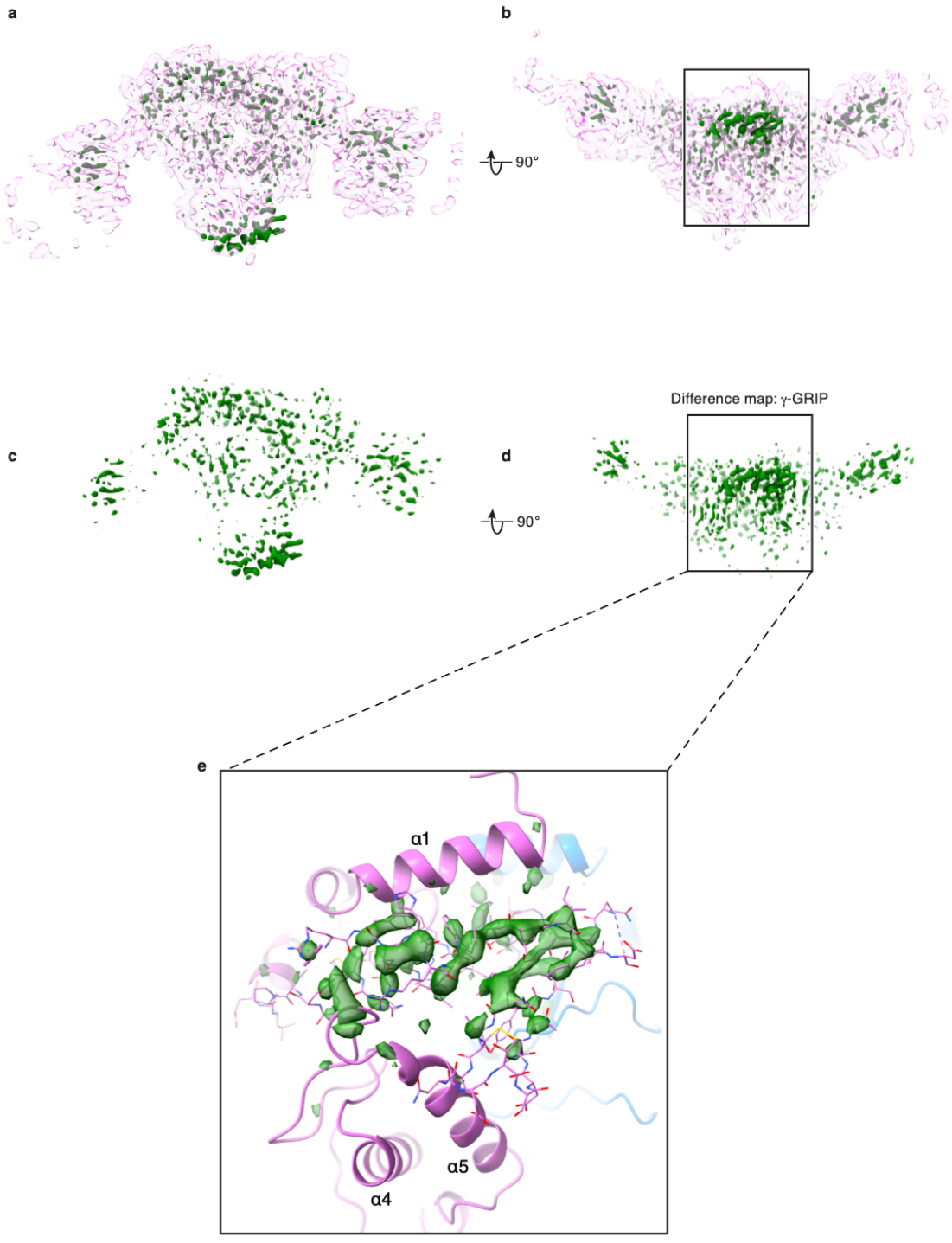
a
b
90°
c
d
90°
Difference map: γ-GRIP
e
α1
α5
α4

Figure 3.17. Difference map of γ-GRIP cleaved and uncleaved maps. Difference map was generated by subtracting the cleaved γ-GRIP map from the uncleaved map revealing a noisier map, however a larger density difference was seen in the region of the GRIP domain. View of FL-ENaC-DiFab map perpendicular **(a)** and parallel to the membrane **(b)**. Map is colored in transparent magenta to illustrate that this is from focused classification of γ-GRIP, and the map presented is the γ-GRIP cleaved map superposed with the difference map (green). **c,d,** Difference map (green) represented in the exact same view, perpendicular **(c)** as in **a**, and parallel **(d)** as in **b** to the membrane. **e,** Difference map, in transparent green, is superposed with the model of FL-ENaC-DiFab map and reveal that there is significant difference of density between cleaved and uncleaved γ-GRIP maps in the area of the GRIP domain, which is located between the finger (α1 and α2 helices) and thumb domain (α4 and α5 helices). γ-subunit model is colored in magenta, and α-subunit model is colored in blue.

a

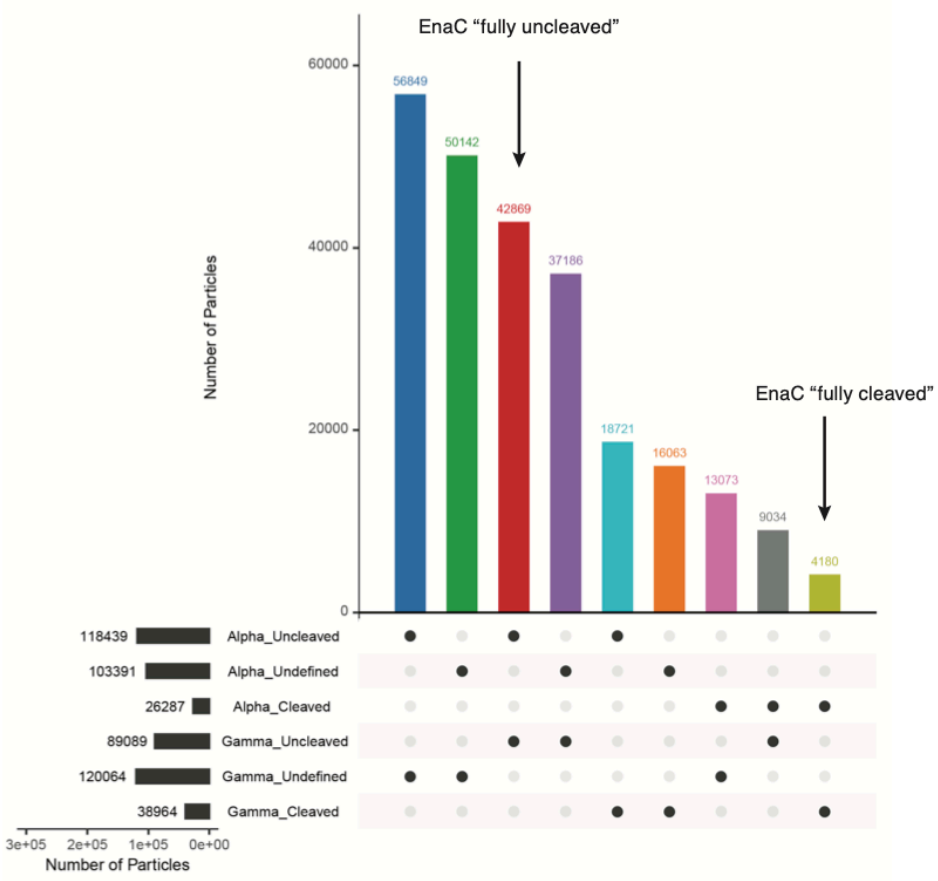
EnaC “fully uncleaved”
EnaC “fully cleaved”
Number of Particles
60000
40000
20000
0
56849
50142
42869
37186
18721
16063
13073
9034
4180
118439 Alpha_Uncleaved
103391 Alpha_Undefined
26287 Alpha_Cleaved
89089 Gamma_Uncleaved
120064 Gamma_Undefined
38964 Gamma_Cleaved
3e+05
2e+05
1e+05
0e+00
Number of Particles

b

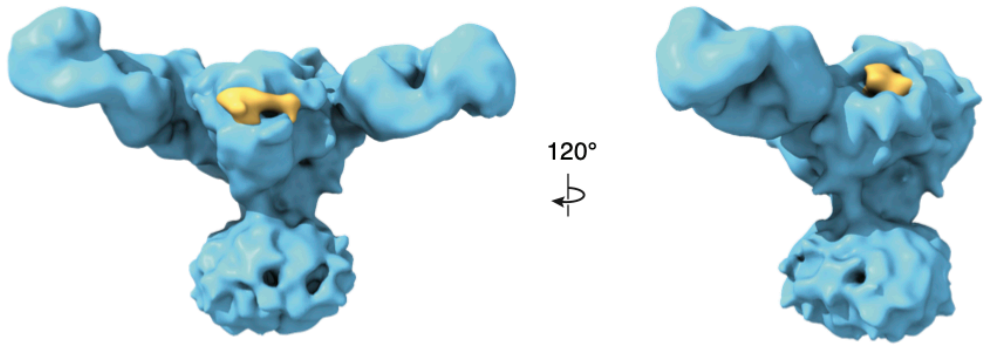
120°

Figure 3.18. A fraction of α-GRIP cleaved particles are also γ-GRIP cleaved particles. a, Analysis of all combinations of α-GRIP cleaved/uncleaved/undefined with γ-GRIP cleaved/uncleaved/undefined reveal that the smallest fraction of particles belongs to both α-GRIP and γ-GRIP cleaved classes, and is referred to as "fully cleaved". The third largest population of particles (red column) belongs to both α-GRIP uncleaved and γ-GRIP uncleaved and is referred to as "fully uncleaved". **b,** Difference map (gold) superposed with ENaC fully cleaved map (blue). The difference map reveal strong densitiy features only in the regions of α-GRIP and γ-GRIP doamins in ENaC.

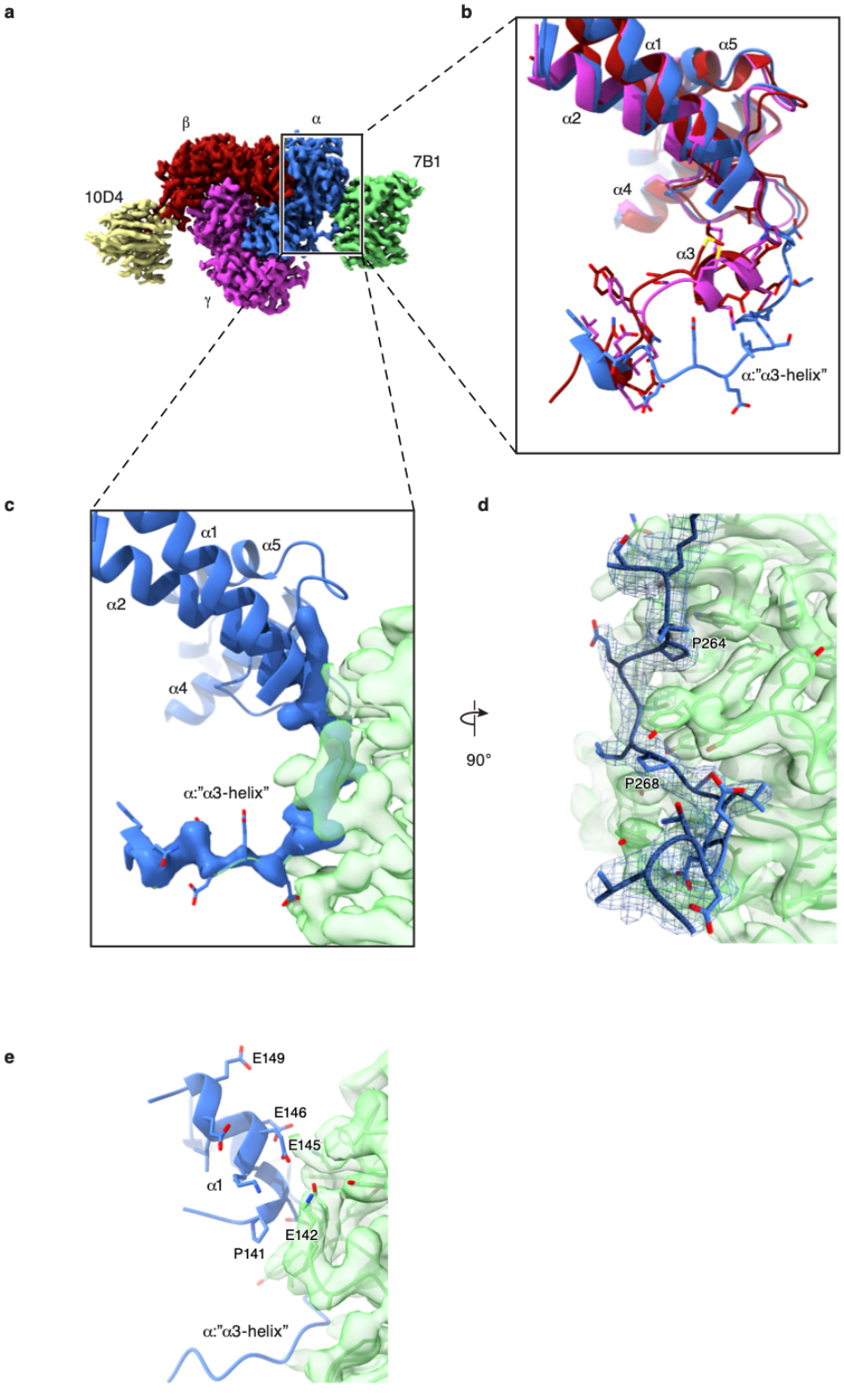
a
β
α
7B1
10D4
γ
b
α1
α5
α2
α4
α3
α:"α3-helix"
c
α1
α5
α2
α4
α:"α3-helix"
90°
d
P264
P268
e
E149
E146
E145
α1
E142
P141
α:"α3-helix"

Figure 3.19. Interactions between α-subunit and antibody 7B1. a, View of FL-ENaC-DiFab map as in **Figure 3.3** with the same color representation. The boxed region is highlighted in both **(b)** and **(c)**, where in **(b)**, the comparison of the α-subunit with β and γ subunits (all colored according to **Figure 3.3a**, reveal that the α-subunit sequence at the C-terminal side of α2 helix does not feature a two-turn helix which is seen for both β and γ subunits **(b)**, and is referred to as α3 helix. Instead α: "α3-helix" is pulled away from the channel core **(b)** making interactions with the antibody 7B1 (transparent green where 7B1 amino acids are represented in green sticks) **(c)**. Upon closer inspection, the α:"α3-helix" features two proline residues that contribute to the main area of contact **(d)**. **e,** The loop region preceding α1 helix of the α-subunit makes contact with 7B1. Altogether, regions of the α-subunit that interact with 7B1 are in close proximity to domains that presumably are involved in gating of ENaC.

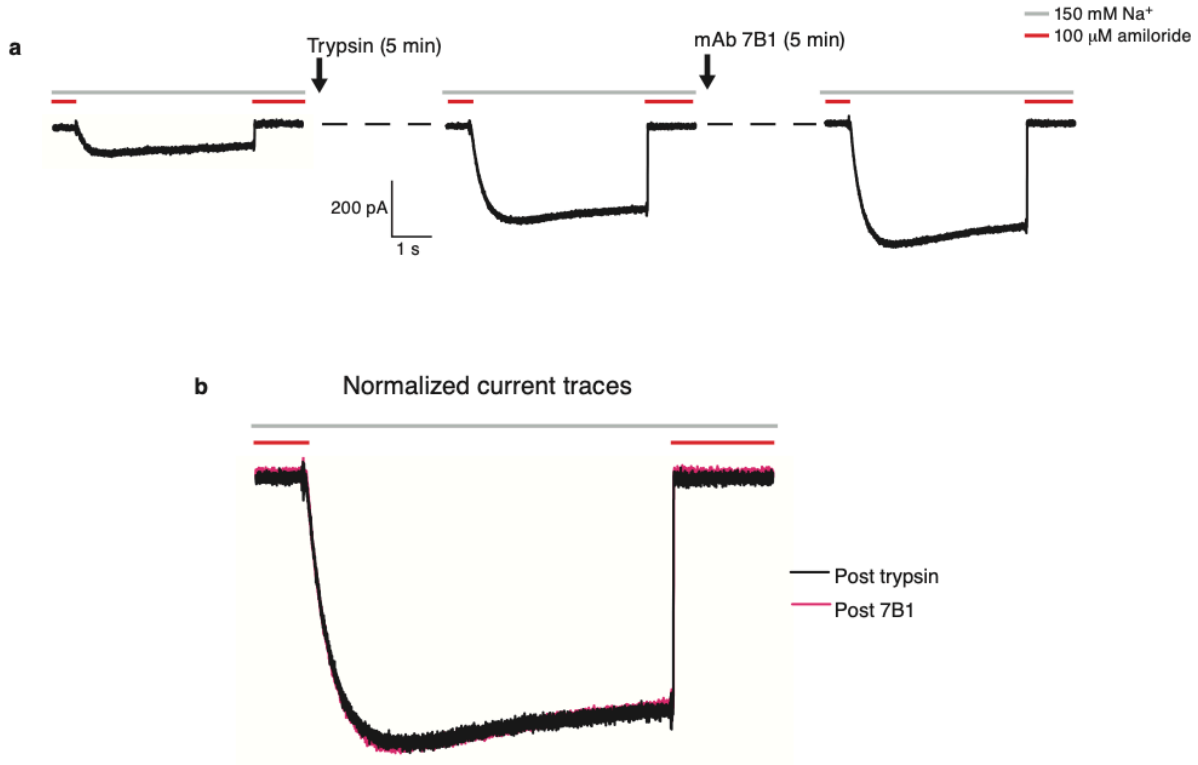

Figure 3.20: 7B1 does not alter ENaC gating kinetics upon binding. a, Representative whole cell patch clamp recording of FL-ENaC expressed in HEK293 cells at pre- and post trypsin treatment (5 µg/mL for 5min) showing an increase in steady state amiloride-sensitive Na^+-current upon treatment with trypsin. Further, monoclonal (mAb) 7B1 at 100 nM is incubated for 3 min before recording of amiloride-sensitive Na^+-current. **b,** Normalized Na^+-current traces pre- and post incubation of mAb 7B1 revealing identical traces. Experiments have been repeated individually more than 3 times.

Chapter 4

Concluding remarks

Summary

The epithelial sodium channel/degenerin (ENaC/DEG) superfamily represents a family of ion channels that serve a wide array of different functions in tissues ranging from epithelial transport of Na^+ ions to mechanosensation, neurodegeneration and nociception. ENaC is the founding member of this ion channel family and serves an important role in salt and water homeostasis. Its direct role in blood volume regulation is highlighted from disorders where ENaC dysregulation results in both hypertension and hypotension, making it an important target for development of novel therapeutics to modulate blood pressure.

The two-membrane model proposed by Koefoed-johnsson and Ussing in 1958 was the first description of transepithelial ion movement across a cell membrane[11]. Although the basic principles of the model were correct from the outset, it was not until much later that investigators discovered ENaCs as the molecular component facilitating Na^+ diffusion across the apical membrane of epithelial cells. Since the discovery of ENaCs, significant progress has been made into the physiology and cell biology of these receptors. However, detailing the molecular architecture and molecular mechanisms of activation, gating and ion transport for ENaC receptors has remained elusive for multiple reasons, as will be discussed below.

The discovery of amiloride in the late 1960s provided an important tool that advanced the studies of epithelial ion transport and thereby ultimately helped to identify ENaC. Shortly after the discovery of this small molecule, groups determined that amiloride blocks ion transport only from the apical side of the cell[23-25], and Lindeman and Van Driessche determined that amiloride blocked a Na^+-selective channel[26]. These discoveries set the stage for subsequent groups to functionally distinguish ENaC and determine its biophysical characteristics, including its unusually high Na^+-selectivity and low-conductance[45,48,49]. Other studies alluded to the

complexity of the receptor's gating properties, finding that ENaCs with different open probabilities (P_o) co-existed at the plasma membrane. The variation of ENaC P_o states, which were shown to dramatically vary from patch to patch in single-channel recordings, presumably reflected hormonal and feedback regulation of ENaC channels[55,56,242].

The molecular cloning of all ENaC subunits in the early 1990s identified the components that make up a functional ENaC channel (α/δ, β and γ subunits)[2,3,7]. This boosted the field and lead to discoveries of other ion channels that belong to the ENaC/DEG super family. Identification of the different ENaC subunits raised questions related to its underlying subunit composition, stoichiometry and molecular architecture. Additionally, the physiological role of ENaC in different tissues, as well as determining the gating and functional properties of ENaC in heterologous expression systems, became important research topics. Hints that proteases played a role in regulation of ENaC gating led to discoveries of multiple proteases that stimulated ENaC activity. While the majority of such protease could not be confirmed as *in vivo* regulators due to the complex nature of ENaC regulation, *in vitro* studies revealed that only two of the three subunits in ENaC (α and γ) harbor protease sensitive sites with inhibitory peptides within the primary sequence that must be released before the channel could open[98,99]. The release of the inhibitory peptides was shown to shift ENaC from a low to a high P_o, and studies suggested that both uncleaved and cleaved ENaCs co-existed at the membrane[113]. At present, the majority of proteases that stimulate ENaC activity have yet to be confirmed as physiologically relevant proteases and a complete picture of the number of cleaved and uncleaved states that exists, and in what ratios, remains unknown.

Alongside the work related to identifying the components of ENaC and its functional properties, the realization that mutations in ENaC that alter its function lead to Liddle syndrome

(causing chronic hypertension) and pseudohypoaldosteronism type 1 (PHA1, causing salt wasting and hypotension) emphasizes the importance of the receptor's role in regulating salt and water balance in the body[148,150]. Knockout studies also revealed the crucial role of ENaC in clearing airway surface liquid in the lungs[145]. Much work has been done to understand the different signaling pathways that regulate ENaC activation, especially in the kidney[125]. However, the complex nature of this regulation, mediated by multiple hormones as a response to low blood volume, is not fully understood. But, the regulation of ENaC activity by hormones control two main factors affecting ENaC function: the ENaC P_o and the number of ENaC receptors at the cell surface. Some of the pathways that modulate ENaC expression at the cell surface have been described[76,107,108,125], while the factors that regulate ENaC P_o are less well-known.

Although the low expression of ENaC combined with its functional heterogeneity have precluded structural analysis of ENaC by traditional methods like x-ray crystallography, the ENaC/DEG member acid sensing ion channel (ASIC) has been structurally well-characterized. Multiple structures of different functional states of ASIC have contributed to an improved understanding of the structural architecture of the ENaC/DEG family members and much can be learned about ENaC by comparing its sequence, structure, and function to that of ASIC[4,62,167-171]. Subunits that belong to ENaC/DEG resemble a hand holding a ball, and the hand comprises the large extracellular domain (ECD) that is divided into six domains, palm, knuckle, finger, thumb, wrist and β-ball (**Figure 1.5a**). Sequence comparison between ENaC and ASIC subunits confirms homology of all the domains mentioned above. However, an insertion of a larger sequence in the finger domain of each of the ENaC subunits, is not found in ASICSs. It is within this sequence that the protease sensitive sites and inhibitory peptides are located. Additionally, the pore lining transmembrane helix 2 (TM2) has been structurally well-characterized in ASICs,

and the sequence identity between ENaC and ASICs is very high in this region. However, the amino acids involved in Na^+ selectivity differ between ASICs and ENaCs[243], and these residue variations likely give rise to structural differences that causes ENaC to have a higher selectivity for Na^+ ions in comparison to ASIC. Elucidating these potential structural differences can provide tremendous insight into the molecular mechanism for ion selectivity.

At the onset of this work, the studies detailed above had outlined many of the functional properties and attempted to determine the stoichiometry and molecular architecture of ENaC to explain the unique characteristics of this ion channel. The available structures of ASIC provided insight into properties that are shared among members of ENaC/DEG family; however, the unique characteristics of ENaC that are not found in ASICs could not be explained, emphasizing the necessity for high-resolution structures of ENaC that reveal the molecular details needed to explain these characteristics. However, challenges related to expression and heterogeneity of ENaCs prevented the use of methods like x-ray crystallography. Crystallization of membrane proteins is challenging due to the nature of the hydrophobic transmembrane domains, in addition to heterogeneity and flexible domains often seen in ion channels. Additionally, milligrams quantities of purified protein is required for crystal packing, and therefore crystallography has been limited to highly expressing, homogeneous membrane proteins. Fortunately, cryo-electron microscopy (cryo-EM) has recently become an evolving technique in structural biology to overcome these exact limitations. Cryo-EM bypasses each of these problems, as proteins do not need to form a crystal for structural determination, and therefore significantly less protein is needed. Cryo-EM as a technique offered exciting opportunities to optimize conditions for ENaC expression and purification such that the first structure could be determined[234].

The work presented in this dissertation explains the biochemical approaches, combined with protein engineering, that were used to solve the first structure of ENaC. To reduce heterogeneity and capture ENaC in an uncleaved state, the construct ΔENaC was generated (truncations of the short N- and C- termini and knockout of putative protease sites). Biochemical analysis of ΔENaC confirmed its homogeneity, making it a promising candidate for structural determination. Early on, cryo-EM data of ΔENaC alone resulted in blurry 2D averages, likely due to the inherent threefold pseudosymmetry of ENaC, making it difficult to properly align particles. To break the pseudosymmetry, I took advantage of high-affinity monoclonal antibodies that were raised against the truncated ENaC construct. The monoclonal antibodies were found to target specific subunits to form a complex. By providing unique asymmetric features to the particles, using the antibodies greatly improved particle alignment, and subsequent 2D averages, leading to the first view of the ENaC architecture, and confirming the main domains as seen in ASICs. The work also elucidated ENaC's key gating components, the protease sensitive domains that are critical sites for ENaC inhibition. The unique protease sensitive domain was found in all three ENaC subunits, although the β-subunit does not actually undergo proteolysis. The domain is located between the finger and the thumb domain of ENaC, which in ASIC is the area where the proton sensing site is found[4]. To maintain consistency with the hand analogy that was first described in ASICs[4], the new protease sensitive domain was named: **G**ating **R**elief of **I**nhibition by **P**roteolysis (GRIP) domain.

One limitation of the findings was the poorly resolved transmembrane domain (TMD), preventing structural analysis of the Na^+ ion permeation pathway and ion selectivity. In an EM map, regions that are not resolved suggest an underlying unstructured region or a conformationally dynamic region or multiple, stable underlying conformations (heterogeneity).

To try to overcome this limitation and get a structure of the TMD, I solved the structure of wild type full-length (FL) ENaC in hopes that the initial truncations of ΔENaC were the main reason for an unstable and disordered TMD. However, working on FL ENaC brought me back to many of the initial challenges involving both low receptor expression and high receptor heterogeneity. I overcame these challenges by developing new protocols to improve yields and homogeneity of purified FL-ENaC. Unfortunately, structural analysis of FL-ENaC also revealed a disordered TMD, suggesting that the disordered TMD is not due to the N- and C-terminal truncations, but rather likely due to sensitivity of the TMD to the purification/reconstitution environment. I made numerous attempts to find conditions that would stabilize the TMD of FL-ENaC (different detergents and reconstitution of receptor into a lipid-like environment), in addition to using cryo-EM data processing strategies to try to separate different TMD states. However, all attempts thus far have not been able to produce a structure of the TMD.

From the optimized purification of FL-ENaC, however, I was able to greatly improve resolution of the cryo-EM map detailing significantly more information about the extracellular domain (ECD). Importantly, the improved map of FL-ENaC confirmed and validated the structure of ΔENaC. Further, it provided a basis to explore potential differences in structure between cleaved and uncleaved ENaC channels, as I knew that the final purified FL-ENaC sample also contained cleaved states of ENaC. The majority of purified FL-ENaCs are uncleaved, as confirmed biochemically by SDS PAGE and by visualization of the FL-ENaC cryo-EM map revealing the presence of the inhibitory peptides.

In an attempt to tease out structural differences related to cleaved and uncleaved states, I used focused classification, which is a classification method to separate structural variabilities within a region of interest in cryo-EM maps. By using focused classification in the GRIP domain

of either α-subunit or γ-subunit, I was able to separate cryo-EM maps based on whether density was present (uncleaved state) or missing (cleaved state) in the GRIP domain region. When comparing the different maps to each other, large conformational changes of the ECD, besides the areas of missing density, were not present. Although this was surprising, it makes sense that there were no large conformational changes as the cryo-EM map of all ENaC particles are at a fairly high resolution. Areas that would be flexible would be at lower resolution, and would have alluded to conformational heterogeneity of the particle. One potential explanation to there being no large conformations could be that the antibodies trap ENaC in a specific state upon binding. The Fab 7B1 that binds next to the α-subunit GRIP domain seemed like a potential candidate for this to occur, however, electrophysiology studies show that 7B1 does not change the gating mechanism of ENaCs (Chapter 3). All the results mentioned above raise multiple interesting questions as will be further discussed in the future direction section. Nevertheless, separating different ENaC cleaved and uncleaved states by focused classification of cryo-EM data offers an exciting strategy towards future structural studies on ENaC purified from native tissue.

Future directions

ENaC transmembrane domain

Although my structures have provided insight into this receptor's stoichiometry, molecular architecture and function[234], several important structural aspects of ENaC were missing, therefore limiting a complete understanding of the molecular mechanisms underlying ENaC gating and function. Among these involves defining the molecular architecture of the ENaC transmembrane domain (TMD). In my cryo-EM maps, density for the TMD was not resolved well; thus, structural determination of the ENaC TMD to elucidate the ion permeation

pathway and explain its unusual high Na^+ selectivity has proven to be challenging. Although we have not identified why our structures display weak density for the TMD, one possibility is simply that this domain's structural stability is dependent on its external environment. Recent discoveries of an N-terminal re-entrant loop that contribute to ion selectivity and permeation pathway in ASIC emphasizes the sensitivity of the TMD domain to its surrounding environment[172], and a similar stability issue might be the case for ENaC TMD. The N-terminal re-entrant loop in ASIC is visualized when ASIC remains in a lipid bilayer, while absent when ASIC is in a DDM/CHS environment, suggesting that this detergent combination does not provide the same environment necessary to stabilize the N-terminal re-entrant loop as the lipid environment.

Another potential possibility which may be a contributing factor to why we cannot visualize the ENaC TMD is heterogeneity in the TMD structure where ENaC might occupy multiple states. For example, the ENaC ECD may serve a role as a scaffold where small conformational changes of the ECD gives rise to large conformational changes within the TMD domain. In this situation, the resulting cryo-EM map, which would be an average of the multiple states, would not be resolved well. Cryo-EM softwares aligns 2D projections of proteins, where the consistency of the signal is important for successful alignment of the particle. Proteins harboring regions that undergo large movements will lead to a blurring of the signal as a result of the cryo-EM software aligning the constant domains of the protein. In the case of ENaC, the alignment of ENaC particles would solely be driven by alignment of the ECD due to large signal variation within the micelle region.

Unfortunately, multiple attempts to stabilize the ENaC TMD resulted in poorly resolved cryo-EM maps of both ΔENaC and FL-ENaC TMD. Additionally, data-processing strategies that

have tried to separate unique TMD conformations by classification and signal subtraction have not shown any promising results. All approaches, thus far, as explained in this dissertation, have provided inconclusive results, and so the most pressing remaining question related to ENaC structure is to elucidate the architecture of ENaC TMD.

Finally, although electrophysiological studies of FL-ENaC show that ENaCs are functional in the same expression system used to produce samples for structural studies, there is the possibility that only ENaCs at the plasma membrane harbor a functional TMD. All other ENaCs within the cell may lack an important co-factor for stabilization that perhaps only exists once fully mature at the plasma membrane. Because our purified sample would have a mixture of fully mature ENaC at the plasma membrane plus immature ENaC from the ER or Golgi, in this possibility, such a heterogeneous sample would result in a TMD that cannot be resolved. In addition, although less likely, the use of a heterologous expression system may give rise to misfolded ENaC TMD as a result of over-expression. Whether this is true remains to be established, and perhaps purification of native ENaC will solve this issue and elucidate the architecture of the TMD.

Regardless, the results so far are exciting, although more work is required to elucidate the molecular architecture of the ENaC TMD. Elucidation of the TMD of ENaC will have a major impact on our understanding of ENaC structure and function.

ENaC in native tissue

Other important and remaining questions in the field of ENaC are related to proteolytic processing and to what extent proteases regulate ENaC activity *in vivo*. Cryo-EM is an evolving technique in structural biology and because it does not require milligram amounts of protein in order to study structure, it offers a unique tool to study the multiple proteolytic states of ENaCs in native tissue. ENaCs are highly expressed in kidneys, and using our high-affinity monoclonal antibodies to extract and purify native ENaC, we are now uniquely positioned to address these questions using cryo-EM as a technique. As explained in this dissertation, structural differences found in the GRIP domains of the α and γ subunits can be separated by cryo-EM data processing strategies. Applying a similar strategy to natively purified ENaC will allow us to quantitate cleaved and uncleaved states of ENaC such that, in combination with mass-spectrometry methods, we will gain new insights into proteolytic ENaC regulation *in vivo*.

Functional and structural assessment of cleaved states of ENaC

Work presented in this dissertation have provided a foundation for extraction and purification of FL-ENaC from a heterologous expression system. Although native extraction and purification of ENaC for structural studies is more ideal, the use of recombinantly expressed ENaC remains crucial to further gain structural knowledge of ENaCs. The first structure of ENaC presented the molecular architecture of ENaC in an uncleaved state (chapter 2)[234], and the second structure of ENaC represented both cleaved and uncleaved states (chapter 3). Future studies should aim to understand the molecular architecture of ENaC in different cleaved states as this is an important regulation of ENaC P_o that will elucidate the gating mechanism of ENaCs. For example, knocking out specific protease sites and engineered protease sites combined with

functional assessment of these specific states will allow us to gain a deeper understanding behind ENaC structure and function. Additionally, the use of proteases that recognizes the specific sites within ENaC (for example, furin and prostasin) can be used to shift purified FL-ENaC protein population towards a more homogeneous population for structural determination. A similar approach can also be used for natively purified ENaC.

ENaC structure in high or low Na^+ environment

Studies have proposed that Na^+ ions bind to specific sites within the ENaC extracellular domain (ECD) and acts as an allosteric modulator to reduce ENaC P_o[64,71]. Our current structures have all captured ENaC in a high Na^+ environment (higher than 150 mM Na^+), and separation of cleaved and uncleaved states of ENaC reveal that there are no large conformational changes in this condition. This raises an interesting question related to whether Na^+ ions induces conformational changes within ENaC. Structural determination of ENaC purified in a low Na^+ environment (1mM) would evaluate the importance of Na^+ ions as an allosteric regulator of ENaC that perhaps may play a more direct and dominant role on regulation of ENaC P_o than proteolysis.

Concluding statement

The research outlined in this dissertation presents the first view of ENaC architecture and represents a substantial progress towards our understanding of the molecular mechanisms behind its gating and function. The work has detailed all the strategies used to identify a higher expressing and more homogenous ENaC sample, leading to elucidation of the important

protease-sensitive GRIP domains involved in ENaC gating. Additionally, the work has detailed a strategy towards separating cleaved and uncleaved states of ENaC, which creates a foundation for future studies that involve structural determination of native ENaC. Understanding the molecular mechanisms related to the physiological role behind the multiple states that ENaC occupies at the apical membrane in kidneys will potentially be important to facilitate development of therapeutics to treat hypertension.

Appendix 1

Biochemical approaches to stabilize the transmembrane domain of the epithelial sodium channel for structural studies

The contents of Appendix 1 will be part of a manuscript for future submission:

Noreng, S., Posert, R., Houser, A., Bharadwaj, A., and Baconguis, I. Biochemical approaches to stabilize the transmembrane domain of the epithelial sodium channel for structural studies

S.N., A.B., R.P. and I.B. expressed and purified ENaC. S.N., A.B., R.P. and I.B. reconstituted ENaC in lipid nanodiscs. S.N and R.P. prepared ENaC grids for cryo-EM data collection. S.N. and R.P collected and processed data of ENaC. A.H. expressed and purified ASIC. S.N. and A.H. prepared ASIC grids for cryo-EM data collection. S.N. and A.H. collected data for ASIC, and S.N. processed data of ASIC.

Overview

The work presented in this dissertation has described multiple novel discoveries related to the molecular architecture of the epithelial sodium channel (ENaC). However, one major challenge that remains unsolved is to elucidate the molecular architecture of the ENaC transmembrane domain (TMD). Resolving this challenge would reveal the cation permeation pathway and explain ENaC's unusually high Na^+ selectivity. The results presented in this appendix outlines the biochemical approaches that was used in order to stabilize ENaC TMD to elucidate the architecture of this domain.

Results

ENaC purified in DDM and CHS revealed poorly resolved cryo-EM maps in TMD region

The first structure of ENaC was solved using a truncated construct (ΔENaC, see chapter two)[234]. ΔENaC was extracted and purified in n-dodecyl-β-D-maltopyranoside (DDM) and cholesteryl hemisuccinate (CHS), and the cryo-EM map revealed poorly resolved map features in the ΔENaC TMD region. The initial conclusion from those results was that the truncation of the N- and C-termini of the ΔENaC subunits disrupted important cytosolic interactions, thereby reducing the stability of the TMD. To overcome this potential limitation found in the ΔENaC construct, I started working on wild type full-length (FL) ENaC. However, the cryo-EM maps of FL-ENaC revealed similarly poorly resolved TMD regions, suggesting that the truncations of the termini in the ΔENaC construct was not responsible for the unstable ENaC TMD. Because FL-ENaC was extracted and purified in DDM and CHS, the same conditions used for ΔENaC, we speculated that this offered an explanation as to why the FL-ENaC TMD remained unstable and

pursued studying the structure of ENaC in a more native, lipid-like environment by reconstitution into lipid nanodiscs.

Reconstitution of ENaC in lipid nanodiscs

Membrane scaffold proteins (Msps) are amphipathic helices that can form a belt around lipids to form a soluble complex called a nanodisc[244]. These nanodiscs can vary in size (8-16nm in diameter) and have become an emerging technique for reconstitution of membrane proteins to use for functional and structural studies in a more native-like environment. As the ENaC TMD was not stable in DDM and CHS, we started to explore the use of Msp nanodisc technology to reconstitute ENaC into lipid nanodiscs. Multiple variables were tested, which included different types of Msps (Msp1D1, Msp1E3D1, Msp2N2), as well as testing different types of lipids (BPL, POPC, POPE, POPG with and without cholesterol) to see if ENaC stability could be greatly improved by one or multiple nanodisc types. Additionally, we tested different ratios of ENaC, Msp and lipids to efficiently and properly reconstitute ENaC into lipid nanodiscs. However, after numerous attempts to optimize an ENaC-nanodisc complex, it became clear that our biochemical techniques have shortcomings when assessing the final soluble ENaC-nanodisc complex. Although purified ENaCs reconstituted into lipid nanodiscs appear biochemically stable as shown by fluorescence-size exclusion chromatography (FSEC), and SDS PAGE shows the presence of all the components that make up the ENaC-nanodisc complex, cryo-EM 2D averages still revealed a highly disordered TM domain region (**Appendix Figure 1.1**). In fact, the poorly resolved density features of the TMD region is more striking for the ENaC-nanodisc complexes than for ENaC purified in detergent - this puzzling finding is true for both ΔENaC and FL-ENaC. A contributing challenge, as revealed by 2D averages, is the strong preferred orientation of top

down views seen on grids prepared from purified ENaC-DiFab-nanodisc complexes. To overcome the preferred orientation problem, we tested different types of additives and coating of grids. However, the results so far, although somewhat promising, have not been conclusive.

Using different cryo-EM sample preparation methods to improve particle orientation and help establish conditions that might stabilize the ENaC TMD offers a large array of variables that can be tested and then optimized. Although the work on optimizing ENaC-nanodisc complexes appears to be promising, more effort is needed to identify the perfect conditions.

ASIC used as a template to test TMD stability by digitonin

The disappointing results revealing disordered cryo-EM maps of ENaC TMD in ENaC-DiFab-nanodisc complexes prompted us to explore other alternatives for extraction and purification of ENaC that did not involve reconstitution of ENaC into a lipid nanodisc. A recent discovery from the ENaC/degenerin family member, chicken acid sensing ion channel (cASIC), has provided some additional insight into this issue. A structure of cASIC, extracted by styrene maleic anhydride (SMA) to retain ASIC in a lipid bilayer, revealed that a DDM/CHS environment does not provide the same TMD stability as a lipid bilayer[172]. When ASIC remains in a lipid bilayer using SMA extraction, an additional ~ 25 amino acid N-terminal re-entrant loop located just prior to transmembrane helix 1 (TM1), can now be visualized in the map. The highly conserved His-Gly (HG) motif, known to reduce the open probability when mutated in ENaC subunits[157,158], is found within this re-entrant loop. The study revealed how the re-entrant loop interacts with both TM1 and TM2 in ASIC and contributes to the Na^+-selectivity and ion conduction pathway of ASICs. Given the high sequence similarity and importance of this motif within the ENaC/degenerin family, a similar architecture of this motif would be expected to

appear in ENaCs as well. Because this re-entrant loop in cASIC was only visualized when using SMA and not any other detergent combination, I speculate that a similar may be occurring with my ENaC samples. Thus, conditions that can stabilize the ENaC TMD need to be identified.

In a study from 1980, it was shown that digitonin can extract a benzamil-binding component from rat kidney cortex membranes[30]. The study noted that it was not clear whether digitonin solubilized the extracted macromolecule or if small membrane fragments were associated with the digitonin molecules[30]. Although the study utilizing radioactive benzamil has not confirmed that ENaC is the benzamil-binding component, the high-affinity of benzamil to this component combined with measuring binding for specific extraction conditions suggest that perhaps this is ENaC[29,30]. If this is ENaC, an interesting question is related to whether digitonin can stabilize the ENaC TMD when extracted from membranes.

Before working out conditions to purify ENaC in digitonin, we wanted to use ASIC as a model to test if digitonin could, like SMA, stabilize ASIC's re-entrance loop. If so, could digitonin then serve to stabilize a presumable re-entrance loop of ENaCs? Full-length (FL) cASIC, when purified in DDM and CHS does not show a presence of the N-terminal re-entrance loop, suggesting that the lower pore architecture in the TMD is highly sensitive to the external environment[170]. We extracted and purified FL-cASIC in digitonin (**Appendix Figure 1.2a, b**), and collected cryo-EM data that was processed in cryoSPARC v2 (**Appendix Figure 1.3, Appendix Table 1.1**). When extracted and purified in digitonin, the cASIC N-terminal re-entrance loop is present, supporting our hypothesis that digitonin stabilizes the transmembrane domain N-terminal re-entrance loop in ASICs (**Appendix Figure 1.2c**). Whether digitonin acts to stabilize cASIC TMD re-entrant loop directly or preserve important co-factors remains to be determined.

Conclusions

The promising results revealing that ASIC has improved TMD stability by digitonin, combined with past studies that extracted a benzamil-binding component from rat cortex kidney (assuming this is ENaC, which has not been established) suggest the hypothesis that ENaC TMD might be stabilized by digitonin as well. The results explained in this appendix is the reasoning as to why we used digitonin to extract and purify FL-ENaC which revealed a disordered TMD.

Materials and Methods

***Expression and purification of ENaC*:** See chapter three in this dissertation for description of expression and purification of FL-ENaC.

***Reconstitution of ENaC in lipid nanodiscs*:** Purified FL-ENaC was mixed with lipids, solubilized in 200mM NaCl, 20mM HEPES and 35mM n-dodecyl-β-D-maltoside (DM), and Msp at molar ratios 1:20:1000 (ENaC:Msp:lipid). The mix was incubated for 45 min at room temperature, before Bio-Beads were added to remove detergent (1:1 v/v). Fresh Bio-Beads was exchanged after two hours of incubation (1:1 v/v), and sample was left overnight. Final ENaC-nanodisc complex was purified by gel filtration using a Superose 6 Increase 10/300 GL column equilibrated in 200 mM NaCl and 20 mM HEPES pH 7.4.

***Expression and purification of ASIC*:** Human embryonic kidney cells lacking N-acetylglucosaminyltransferase I (HEK293S GnTI- cells) were grown in a suspension at a density of $3x10^6$ cells/mL and transduced via a baculovirus expression system containing one subunit of the chicken ASIC1a (cASIC) homotrimer with a N-terminal 8x His EGFP. The cells were infected at 37℃ with a multiplicity of infection (MOI) of 3 to account for the formation of the

trimer. Eight hours after infection sodium butyrate was added at a 10 mM concentration and the cells were moved to 30℃. They were allowed to grow for an additional 40 hrs. After 48 hrs from initial infection, the cells were spun at 5,000 rpm for 20 min. The supernatant was discarded, and the pellets were washed in 20 mM Tris pH 8 and 200 mM NaCl, combined and then spun at 3500 rpm for 20 min. The supernatant was discarded, and the pellet was flash frozen in liquid nitrogen, and then stored at -80℃. For purification, the cells were allowed to thaw on ice and then resuspended and homogenized using a dounce homogenizer in 1% digitonin (Millipore), 20 mM HEPES pH 7.4, 200 mM NaCl, 2 mM ATP, 2 mM $MgCl_2$, 25 U/mL of nuclease (Thermo Scientific), and 2 protease inhibitor tablets (Thermo Scientific). Following homogenization, the cells were allowed to solubilize for an hour while stirring at 4℃. The solubilized cells were then spun at 100,000 xg for 45 minutes. The supernatant was allowed to batch bind to TALON resin in the presence of 5 mM imidazole for 1 hr while nutating at 4℃. After batch binding, the TALON and solubilized material were centrifuged for 10 min at 800 rpm. The supernatant was discarded and the cASIC bound TALON was packed into an XK-16 column. The column was washed with two column volumes of 0.1% digitonin, 20 mM HEPES pH7.4, 200 mM NaCl. There were then four additional washes, each 2 column volumes, using the previously mentioned buffer containing the following; 2 mM ATP and 2 mM $MgCl_2$, 25 U/ml nuclease, 5 mM $CaCl_2$, and 10 mM imizadole. cASIC was eluted using 250mM imidazole. Eluted fractions were concentrated and a 1:50 molar ratio (cASIC:thrombin), and 5 mM $CaCl_2$ were added and allowed to nutate for 30 minutes at room temperature to cleave off the EGFP. The concentrated fractions were then injected onto a Superose 6 Increase 10/300 GL column equilibrated in 0.1% digitonin, 20 mM HEPES pH 7.4, 200 mM NaCl to isolate cASIC by size-exclusion chromatography. Monodispersed fractions were pooled and concentrated to 3.2 mg/mL.

***Image acquisition and data processing of ASIC*:** Purified GFP-cleaved cASIC at a concentration of 3.2 mg/mL was applied on holey-carbon cryo-EM grids which were prior glow discharged at 15mA for 60sec (Quantifoil Au 1.2/1.3 μm 300 mesh). Grids were prepared using a Vitrobot Mark III (FEI) at 100% humidity and 12 ºC, where 3.5 μL of purified cASIC was applied followed by a manual blot on the side of the grid. Then another 3.5 μL of purified cASIC was applied before a wait time of 10 s, 3.5 s blot time at blot force 1, and then plunge frozen in liquid ethane cooled by liquid nitrogen. 1,665 movies were collected in super resolution mode with a pixel size of 0.415Å. Total acquisition time was 3 s, and was dose-fractionated to 60 frames with a dose rate of 1 $e^-/Å^2$/frame and total dose of 60 $e^-/Å^2$. Multishot with image shift between four holes was performed to speed up data collection. The data set was binned 2 x 2 and motion corrected using motioncor2[204], before imported to cryoSPARCv2[208]. Defocus values were estimated using CTFFIND4[236], and cryoSPARCv2 blob picker was used for automated particle picking, initially resulting in 175,874 particles (**Appendix Table 1.1**). Multiple rounds of 2D classification removed false-positive classes, and the final data set consisted of 70,280 particles, and were processed using non-uniform refinement in cryoSPARCv2 with default settings and C3 symmetry for a final 3D reconstruction with a Gold standard Fourier Shell Correlation (GS FSC) resolution of 3.56 Å.

Tables

Table 1: Statistics of data collection, three-dimensional reconstruction, and model refinement.

Statistic	cASIC
Material Source	Whole cell
Detergent	Digitonin
Microscope	FEI Krios
Voltage (kV)	300
Detector	Gatan K2 Summit
Defocus range (μm)	-0.8 – -2.2
Exposure time (s)	3
Dose rate ($e^-/Å^2$/frame)	1.0
Frames per movie	60
Pixel size (Å)	0.415
Total dose ($e^-/Å^2$)	60
Motion correction	UCSF MotionCor2
CTF estimation	CTFFIND 4
Particle picking	cryoSPARC blob and template
2D/3D classification	cryoSPARC 2.11
3D classification and refinement	Relion 3.0, cryoSPARC 2.11, cisTEM 1.0
Symmetry	C3
Particles processed	175 874
Resolution masked (Å)	3.52
Map Sharpening B-factor ($Å^2$)	133.3
Protein residues	1 344
Resolution (FSC= 0.143, Å)	3.52
Molprobity score	3.27
C_β deviations	0
Ramachandran outliers	0
Ramachandran allowed	7.85%
Ramachandran favored	92.15%
Bond length rmsd (Å)	0.005
Bond angle rmsd (°)	1.046

Appendix Table 1.1. Cryo-EM data collection, refinement and validation statistics.

Figures and legends

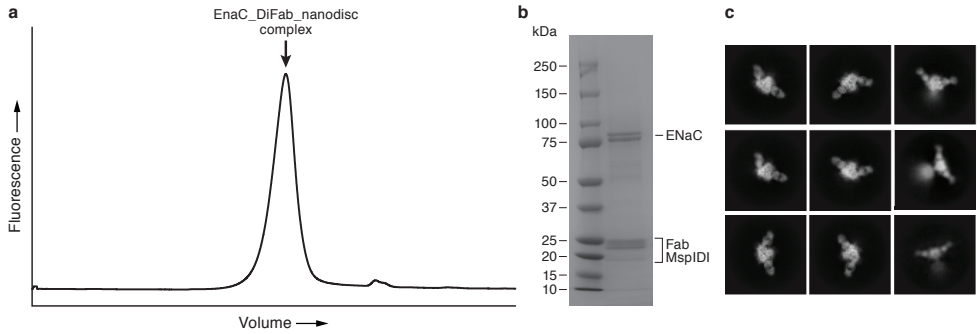

Appendix Figure 1.1. Biochemical assessments of FL-ENaC-DiFab-nanodisc complex. a,b, Fluorescence size-exclusion chromatography **(**FSEC) analysis **(a)** and SDS PAGE **(b)** reveal a soluble biochemical stable complex that contain all protein components to form a FL-ENaC-DiFab-nanodisc complex. **c,** 2D class averages of FL-ENaC-Difab-nanodisc complex show poorly resolved features in the transmembrane domain region of ENaC.

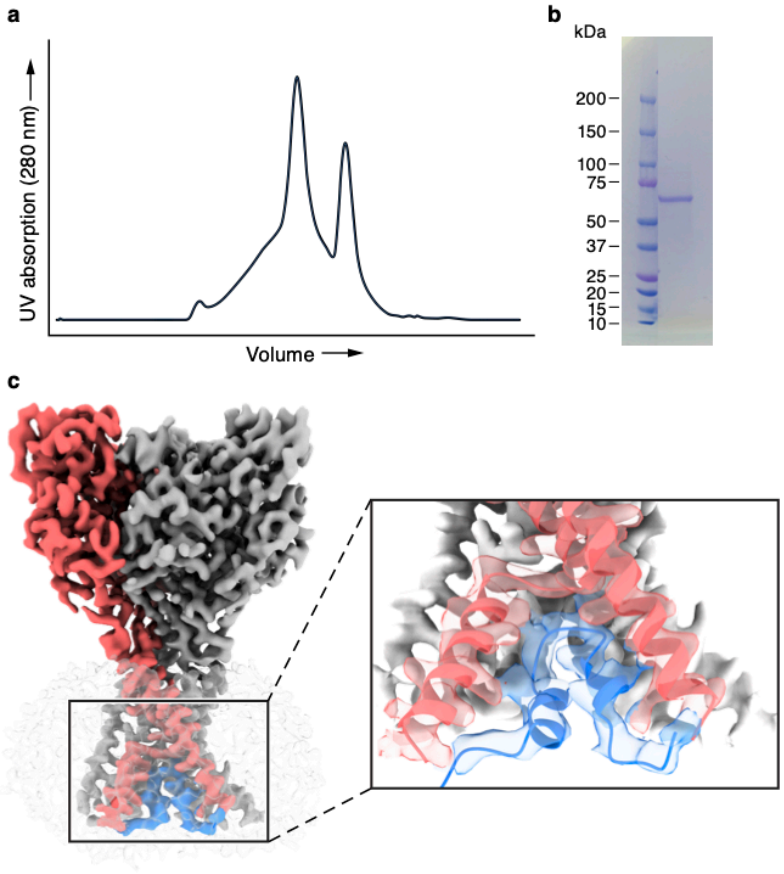

Appendix Figure 1.2. Purification of FL-cASIC at pH 7.4 in digitonin. Size-exclusion chromatography (SEC) trace **(a)** and SDS PAGE **(b)** analysis of cASIC at pH 7.4 in digitonin after SEC. **c,** cryo-EM potential map of cASIC in digitonin showing that the re-entrance loop is present. One subunit is colored red with the N-terminal re-entrant loop colored blue for illustration. The two other subunits are colored grey, and light grey transparent surface represent the digitonin micelle. In the zoomed in panel, the model of desensitized cASIC is shown in ribbon and superposed in the cryo-EM map.

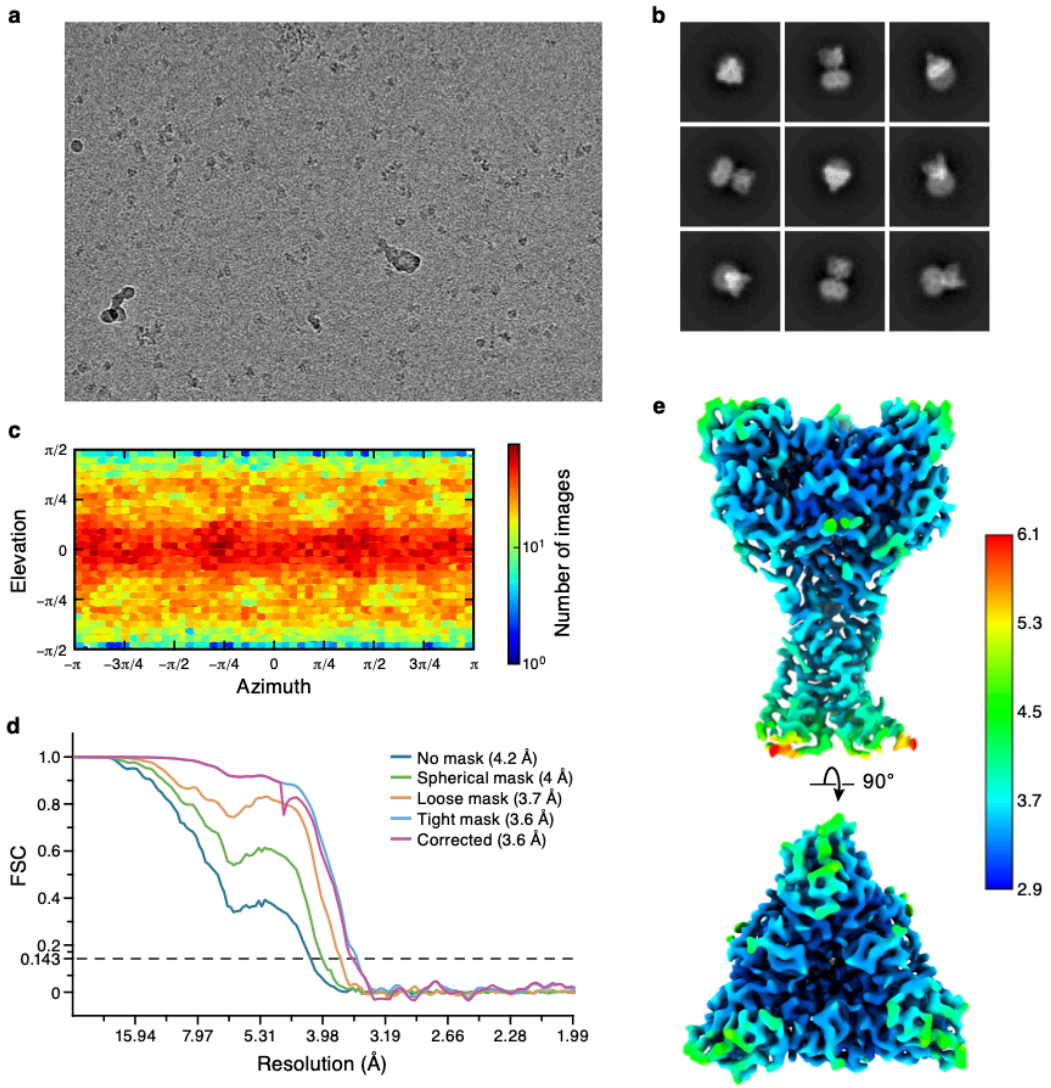

Appendix Figure 1.3. Cryo-EM of cASIC at pH 7.4. a-e, Representative micrograph **(a)** cryo-EM 2D classes **(b)**, angular particle distribution **(c)**, gold standard fourier shell correlation (GS-FSC) **(d)** and local resolution estimate **(e)** of cASIC at pH 7.4 in digitonin.

References

1 Driscoll, M. & Chalfie, M. The mec-4 gene is a member of a family of Caenorhabditis elegans genes that can mutate to induce neuronal degeneration. *Nature* **349**, 588-593, doi:10.1038/349588a0 (1991).

2 Canessa, C. M., Horisberger, J. D. & Rossier, B. C. Epithelial sodium channel related to proteins involved in neurodegeneration. *Nature* **361**, 467-470, doi:10.1038/361467a0 (1993).

3 Canessa, C. M. *et al.* Amiloride-sensitive epithelial Na+ channel is made of three homologous subunits. *Nature* **367**, 463-467, doi:10.1038/367463a0 (1994).

4 Jasti, J., Furukawa, H., Gonzales, E. B. & Gouaux, E. Structure of acid-sensing ion channel 1 at 1.9 A resolution and low pH. *Nature* **449**, 316-323, doi:10.1038/nature06163 (2007).

5 Eastwood, A. L. & Goodman, M. B. Insight into DEG/ENaC channel gating from genetics and structure. *Physiology (Bethesda)* **27**, 282-290, doi:10.1152/physiol.00006.2012 (2012).

6 Mano, I. & Driscoll, M. DEG/ENaC channels: a touchy superfamily that watches its salt. *Bioessays* **21**, 568-578, doi:10.1002/(SICI)1521-1878(199907)21:7<568::AID-BIES5>3.0.CO;2-L (1999).

7 Waldmann, R., Champigny, G., Bassilana, F., Voilley, N. & Lazdunski, M. Molecular cloning and functional expression of a novel amiloride-sensitive Na+ channel. *J Biol Chem* **270**, 27411-27414, doi:10.1074/jbc.270.46.27411 (1995).

8 Hanukoglu, I. & Hanukoglu, A. Epithelial sodium channel (ENaC) family: Phylogeny, structure-function, tissue distribution, and associated inherited diseases. *Gene* **579**, 95-132, doi:10.1016/j.gene.2015.12.061 (2016).

9 Ji, H. L. *et al.* delta ENaC: a novel divergent amiloride-inhibitable sodium channel. *Am J Physiol Lung Cell Mol Physiol* **303**, L1013-1026, doi:10.1152/ajplung.00206.2012 (2012).

10 Giraldez, T., Rojas, P., Jou, J., Flores, C. & Alvarez de la Rosa, D. The epithelial sodium channel delta-subunit: new notes for an old song. *Am J Physiol Renal Physiol* **303**, F328-338, doi:10.1152/ajprenal.00116.2012 (2012).

11 Koefoed-Johnsen, V. & Ussing, H. H. The nature of the frog skin potential. *Acta Physiol Scand* **42**, 298-308, doi:10.1111/j.1748-1716.1958.tb01563.x (1958).

12 Ussing, H. H. The active ion transport through the isolated frog skin in the light of tracer studies. *Acta Physiol Scand* **17**, 1-37, doi:10.1111/j.1748-1716.1949.tb00550.x (1949).

13 Ussing, H. H. Life with tracers. *Annu Rev Physiol* **42**, 1-16, doi:10.1146/annurev.ph.42.030180.000245 (1980).

14 Ussing, H. H. & Zerahn, K. Active transport of sodium as the source of electric current in the short-circuited isolated frog skin. *Acta Physiol Scand* **23**, 110-127, doi:10.1111/j.1748-1716.1951.tb00800.x (1951).

15 Larsen, E. H. Chloride transport by high-resistance heterocellular epithelia. *Physiol Rev* **71**, 235-283, doi:10.1152/physrev.1991.71.1.235 (1991).

16 Van Itallie, C. M. & Anderson, J. M. Claudins and epithelial paracellular transport. *Annu Rev Physiol* **68**, 403-429, doi:10.1146/annurev.physiol.68.040104.131404 (2006).

17 Palmer, L. G. & Andersen, O. S. The two-membrane model of epithelial transport: Koefoed-Johnsen and Ussing (1958). *J Gen Physiol* **132**, 607-612, doi:10.1085/jgp.200810149 (2008).

18 Wilson, J. D., Richmond, D. E., Simmonds, H. A. & North, J. D. MK 870: a new potassium-sparing diuretic. *N Z Med J* **65**, 505-511 (1966).

19 Cragoe, E. J., Jr., Woltersdorf, O. W., Jr., Bicking, J. B., Kwong, S. F. & Jones, J. H. Pyrazine diuretics. II. N-amidino-3-amino-5-substituted 6-halopyrazinecarboxamides. *J Med Chem* **10**, 66-75, doi:10.1021/jm00313a014 (1967).

20 Kleyman, T. R. & Cragoe, E. J., Jr. Amiloride and its analogs as tools in the study of ion transport. *J Membr Biol* **105**, 1-21, doi:10.1007/bf01871102 (1988).

21 Crabbe, J. Stimulation of active sodium transport by the isolated toad bladder with aldosterone in vitro. *J Clin Invest* **40**, 2103-2110, doi:10.1172/JCI104436 (1961).

22 Bentley, P. J. Amiloride: a potent inhibitor of sodium transport across the toad bladder. *J Physiol* **195**, 317-330, doi:10.1113/jphysiol.1968.sp008460 (1968).

23 Crabbe, J. & Ehrlich, E. N. Amiloride and the mode of action of aldosterone on sodium transport across toad bladder and skin. *Pflugers Arch* **304**, 284-296, doi:10.1007/bf00592131 (1968).

24 Baba, W. I., Lant, A. F., Smith, A. J., Townshend, M. M. & Wilson, G. M. Pharmacological effects in animals and normal human subjects of the diuretic amiloride hydrochloride (MK-870). *Clin Pharmacol Ther* **9**, 318-327, doi:10.1002/cpt196893318 (1968).

25 Salako, L. A. & Smith, A. J. Effects of amiloride on active sodium transport by the isolated frog skin: evidence concerning site of action. *Br J Pharmacol* **38**, 702-718, doi:10.1111/j.1476-5381.1970.tb09878.x (1970).

26 Lindemann, B. & Van Driessche, W. Sodium-specific membrane channels of frog skin are pores: current fluctuations reveal high turnover. *Science* **195**, 292-294, doi:10.1126/science.299785 (1977).

27 Cuthbert, A. W. Importance of guanidinium groups of blocking sodium channels in epithelia. *Mol Pharmacol* **12**, 945-957 (1976).

28 Benos, D. J., Simon, S. A., Mandel, L. J. & Cala, P. M. Effect of amiloride and some of its analogues of cation transport in isolated frog skin and thin lipid membranes. *J Gen Physiol* **68**, 43-63, doi:10.1085/jgp.68.1.43 (1976).

29 Cuthbert, A. W. & Edwardson, J. M. Benzamil binding to kidney cell membranes. *Biochem Pharmacol* **30**, 1175-1183, doi:10.1016/0006-2952(81)90294-x (1981).

30 Edwardson, J. M., Fanestil, D. D., Ellory, J. C. & Cuthbert, A. W. Extraction of a [3H]benzamil binding component from kidney cell membranes. *Biochem Pharmacol* **30**, 1185-1189, doi:10.1016/0006-2952(81)90295-1 (1981).

31 Kleyman, T. R. *et al.* Photoaffinity labeling of the epithelial sodium channel. *J Biol Chem* **261**, 2839-2843 (1986).

32 Barbry, P., Frelin, C., Vigne, P., Cragoe, E. J., Jr. & Lazdunski, M. [3H]phenamil, a radiolabelled diuretic for the analysis of the amiloride-sensitive Na+ channels in kidney membranes. *Biochem Biophys Res Commun* **135**, 25-32, doi:10.1016/0006-291x(86)90937-x (1986).

33 Barbry, P. *et al.* Purification and subunit structure of the [3H]phenamil receptor associated with the renal apical Na+ channel. *Proc Natl Acad Sci U S A* **84**, 4836-4840, doi:10.1073/pnas.84.14.4836 (1987).

34 Barbry, P. *et al.* Biochemical identification of two types of phenamil binding sites associated with amiloride-sensitive Na+ channels. *Biochemistry* **28**, 3744-3749, doi:10.1021/bi00435a018 (1989).

35 Barbry, P., Chassande, O., Marsault, R., Lazdunski, M. & Frelin, C. [3H]phenamil binding protein of the renal epithelium Na+ channel. Purification, affinity labeling, and functional reconstitution. *Biochemistry* **29**, 1039-1045, doi:10.1021/bi00456a028 (1990).

36 Barbry, P. *et al.* Human kidney amiloride-binding protein: cDNA structure and functional expression. *Proc Natl Acad Sci U S A* **87**, 7347-7351, doi:10.1073/pnas.87.19.7347 (1990).

37 Sariban-Sohraby, S. & Benos, D. J. Detergent solubilization, functional reconstitution, and partial purification of epithelial amiloride-binding protein. *Biochemistry* **25**, 4639-4646, doi:10.1021/bi00364a028 (1986).

38 Benos, D. J., Saccomani, G., Brenner, B. M. & Sariban-Sohraby, S. Purification and characterization of the amiloride-sensitive sodium channel from A6 cultured cells and bovine renal papilla. *Proc Natl Acad Sci U S A* **83**, 8525-8529, doi:10.1073/pnas.83.22.8525 (1986).

39 Benos, D. J., Saccomani, G. & Sariban-Sohraby, S. The epithelial sodium channel. Subunit number and location of the amiloride binding site. *J Biol Chem* **262**, 10613-10618 (1987).

40 Sariban-Sohraby, S., Sorscher, E. J., Brenner, B. M. & Benos, D. J. Phosphorylation of a single subunit of the epithelial Na+ channel protein following vasopressin treatment of A6 cells. *J Biol Chem* **263**, 13875-13879 (1988).

41 Garty, H. & Palmer, L. G. Epithelial sodium channels: function, structure, and regulation. *Physiol Rev* **77**, 359-396 (1997).

42 Sariban-Sohraby, S., Abramow, M. & Fisher, R. S. Single-channel behavior of a purified epithelial Na+ channel subunit that binds amiloride. *Am J Physiol* **263**, C1111-1117, doi:10.1152/ajpcell.1992.263.5.C1111 (1992).

43 Oh, Y. & Benos, D. J. Single-channel characteristics of a purified bovine renal amiloride-sensitive Na+ channel in planar lipid bilayers. *Am J Physiol* **264**, C1489-1499, doi:10.1152/ajpcell.1993.264.6.C1489 (1993).

44 Oh, Y., Smith, P. R., Bradford, A. L., Keeton, D. & Benos, D. J. Regulation by phosphorylation of purified epithelial Na+ channels in planar lipid bilayers. *Am J Physiol* **265**, C85-91, doi:10.1152/ajpcell.1993.265.1.C85 (1993).

45 Palmer, L. G. & Frindt, G. Amiloride-sensitive Na channels from the apical membrane of the rat cortical collecting tubule. *Proc Natl Acad Sci U S A* **83**, 2767-2770 (1986).

46 Kemendy, A. E., Kleyman, T. R. & Eaton, D. C. Aldosterone alters the open probability of amiloride-blockable sodium channels in A6 epithelia. *Am J Physiol* **263**, C825-837, doi:10.1152/ajpcell.1992.263.4.C825 (1992).

47 Novotny, W. F., Chassande, O., Baker, M., Lazdunski, M. & Barbry, P. Diamine oxidase is the amiloride-binding protein and is inhibited by amiloride analogues. *J Biol Chem* **269**, 9921-9925 (1994).

48 Palmer, L. G. Ion selectivity of the apical membrane Na channel in the toad urinary bladder. *J Membr Biol* **67**, 91-98, doi:10.1007/bf01868651 (1982).

49 Benos, D. J., Mandel, L. J. & Simon, S. A. Cationic selectivity and competition at the sodium entry site in frog skin. *J Gen Physiol* **76**, 233-247, doi:10.1085/jgp.76.2.233 (1980).

50 Sheng, S., Li, J., McNulty, K. A., Avery, D. & Kleyman, T. R. Characterization of the selectivity filter of the epithelial sodium channel. *J Biol Chem* **275**, 8572-8581, doi:10.1074/jbc.275.12.8572 (2000).

51 Kellenberger, S., Hoffmann-Pochon, N., Gautschi, I., Schneeberger, E. & Schild, L. On the molecular basis of ion permeation in the epithelial Na+ channel. *J Gen Physiol* **114**, 13-30, doi:10.1085/jgp.114.1.13 (1999).

52 Puoti, A. *et al.* The highly selective low-conductance epithelial Na channel of Xenopus laevis A6 kidney cells. *Am J Physiol* **269**, C188-197, doi:10.1152/ajpcell.1995.269.1.C188 (1995).

53 Ermishkin, L. N., Kasumov, K. M. & Potzeluyev, V. M. Single ionic channels induced in lipid bilayers by polyene antibiotics amphotericin B and nystatine. *Nature* **262**, 698-699, doi:10.1038/262698a0 (1976).

54 Imoto, K. *et al.* Rings of negatively charged amino acids determine the acetylcholine receptor channel conductance. *Nature* **335**, 645-648, doi:10.1038/335645a0 (1988).

55 Palmer, L. G. & Frindt, G. Conductance and gating of epithelial Na channels from rat cortical collecting tubule. Effects of luminal Na and Li. *J Gen Physiol* **92**, 121-138, doi:10.1085/jgp.92.1.121 (1988).

56 Palmer, L. G. & Frindt, G. Gating of Na channels in the rat cortical collecting tubule: effects of voltage and membrane stretch. *J Gen Physiol* **107**, 35-45, doi:10.1085/jgp.107.1.35 (1996).

57 Snyder, P. M. *et al.* Mechanism by which Liddle's syndrome mutations increase activity of a human epithelial Na+ channel. *Cell* **83**, 969-978 (1995).

58 Schild, L., Schneeberger, E., Gautschi, I. & Firsov, D. Identification of amino acid residues in the alpha, beta, and gamma subunits of the epithelial sodium channel (ENaC) involved in amiloride block and ion permeation. *J Gen Physiol* **109**, 15-26 (1997).

59 Adams, C. M., Snyder, P. M. & Welsh, M. J. Paradoxical stimulation of a DEG/ENaC channel by amiloride. *J Biol Chem* **274**, 15500-15504, doi:10.1074/jbc.274.22.15500 (1999).

60 Kieber-Emmons, T., Lin, C., Foster, M. H. & Kleyman, T. R. Antiidiotypic antibody recognizes an amiloride binding domain within the alpha subunit of the epithelial Na+ channel. *J Biol Chem* **274**, 9648-9655, doi:10.1074/jbc.274.14.9648 (1999).

61 Kelly, O. *et al.* Characterization of an amiloride binding region in the alpha-subunit of ENaC. *Am J Physiol Renal Physiol* **285**, F1279-1290, doi:10.1152/ajprenal.00094.2003 (2003).

62 Baconguis, I., Bohlen, C. J., Goehring, A., Julius, D. & Gouaux, E. X-ray structure of acid-sensing ion channel 1-snake toxin complex reveals open state of a Na(+)-selective channel. *Cell* **156**, 717-729, doi:10.1016/j.cell.2014.01.011 (2014).

63 Li, J. H., Cragoe, E. J., Jr. & Lindemann, B. Structure-activity relationship of amiloride analogs as blockers of epithelial Na channels: II. Side-chain modifications. *J Membr Biol* **95**, 171-185, doi:10.1007/bf01869162 (1987).

64 Bize, V. & Horisberger, J. D. Sodium self-inhibition of human epithelial sodium channel: selectivity and affinity of the extracellular sodium sensing site. *Am J Physiol Renal Physiol* **293**, F1137-1146, doi:10.1152/ajprenal.00100.2007 (2007).

65 Sheng, S., Bruns, J. B. & Kleyman, T. R. Extracellular histidine residues crucial for Na+ self-inhibition of epithelial Na+ channels. *J Biol Chem* **279**, 9743-9749, doi:10.1074/jbc.M311952200 (2004).

66 Sheng, S., Carattino, M. D., Bruns, J. B., Hughey, R. P. & Kleyman, T. R. Furin cleavage activates the epithelial Na+ channel by relieving Na+ self-inhibition. *Am J Physiol Renal Physiol* **290**, F1488-1496, doi:10.1152/ajprenal.00439.2005 (2006).

67 Kellenberger, S., Gautschi, I., Rossier, B. C. & Schild, L. Mutations causing Liddle syndrome reduce sodium-dependent downregulation of the epithelial sodium channel in the Xenopus oocyte expression system. *J Clin Invest* **101**, 2741-2750, doi:10.1172/JCI2837 (1998).

68 Anantharam, A., Tian, Y. & Palmer, L. G. Open probability of the epithelial sodium channel is regulated by intracellular sodium. *J Physiol* **574**, 333-347, doi:10.1113/jphysiol.2006.109173 (2006).

69 Fuchs, W., Larsen, E. H. & Lindemann, B. Current-voltage curve of sodium channels and concentration dependence of sodium permeability in frog skin. *J Physiol* **267**, 137-166, doi:10.1113/jphysiol.1977.sp011805 (1977).

70 Kleyman, T. R. & Eaton, D. C. Regulating ENaC's gate. *Am J Physiol Cell Physiol*, doi:10.1152/ajpcell.00418.2019 (2019).

71 Kashlan, O. B., Blobner, B. M., Zuzek, Z., Tolino, M. & Kleyman, T. R. Na+ inhibits the epithelial Na+ channel by binding to a site in an extracellular acidic cleft. *J Biol Chem* **290**, 568-576, doi:10.1074/jbc.M114.606152 (2015).

72 Macrobbie, E. A. & Ussing, H. H. Osmotic behaviour of the epithelial cells of frog skin. *Acta Physiol Scand* **53**, 348-365, doi:10.1111/j.1748-1716.1961.tb02293.x (1961).

73 Frindt, G., Silver, R. B., Windhager, E. E. & Palmer, L. G. Feedback regulation of Na channels in rat CCT. II. Effects of inhibition of Na entry. *Am J Physiol* **264**, F565-574, doi:10.1152/ajprenal.1993.264.3.F565 (1993).

74 Frindt, G., Silver, R. B., Windhager, E. E. & Palmer, L. G. Feedback regulation of Na channels in rat CCT. III. Response to cAMP. *Am J Physiol* **268**, F480-489, doi:10.1152/ajprenal.1995.268.3.F480 (1995).

75 Dinudom, A. *et al.* Nedd4 mediates control of an epithelial Na+ channel in salivary duct cells by cytosolic Na+. *Proc Natl Acad Sci U S A* **95**, 7169-7173, doi:10.1073/pnas.95.12.7169 (1998).

76 Knight, K. K., Wentzlaff, D. M. & Snyder, P. M. Intracellular sodium regulates proteolytic activation of the epithelial sodium channel. *J Biol Chem* **283**, 27477-27482, doi:10.1074/jbc.M804176200 (2008).

77 Sheng, S., Perry, C. J. & Kleyman, T. R. External nickel inhibits epithelial sodium channel by binding to histidine residues within the extracellular domains of alpha and gamma subunits and reducing channel open probability. *J Biol Chem* **277**, 50098-50111, doi:10.1074/jbc.M209975200 (2002).

78 Sheng, S., Perry, C. J. & Kleyman, T. R. Extracellular Zn2+ activates epithelial Na+ channels by eliminating Na+ self-inhibition. *J Biol Chem* **279**, 31687-31696, doi:10.1074/jbc.M405224200 (2004).

79 Collier, D. M. & Snyder, P. M. Extracellular protons regulate human ENaC by modulating Na+ self-inhibition. *J Biol Chem* **284**, 792-798, doi:10.1074/jbc.M806954200 (2009).

80 Collier, D. M. & Snyder, P. M. Extracellular chloride regulates the epithelial sodium channel. *J Biol Chem* **284**, 29320-29325, doi:10.1074/jbc.M109.046771 (2009).

81 Ma, H. P., Saxena, S. & Warnock, D. G. Anionic phospholipids regulate native and expressed epithelial sodium channel (ENaC). *J Biol Chem* **277**, 7641-7644, doi:10.1074/jbc.C100737200 (2002).

82 Yue, G., Malik, B., Yue, G. & Eaton, D. C. Phosphatidylinositol 4,5-bisphosphate (PIP2) stimulates epithelial sodium channel activity in A6 cells. *J Biol Chem* **277**, 11965-11969, doi:10.1074/jbc.M108951200 (2002).

83 Helms, M. N. *et al.* Phosphatidylinositol 3,4,5-trisphosphate mediates aldosterone stimulation of epithelial sodium channel (ENaC) and interacts with gamma-ENaC. *J Biol Chem* **280**, 40885-40891, doi:10.1074/jbc.M509646200 (2005).

84 Ma, H. P. & Eaton, D. C. Acute regulation of epithelial sodium channel by anionic phospholipids. *J Am Soc Nephrol* **16**, 3182-3187, doi:10.1681/ASN.2005040434 (2005).

85 Zhang, Z. R., Chou, C. F., Wang, J., Liang, Y. Y. & Ma, H. P. Anionic phospholipids differentially regulate the epithelial sodium channel (ENaC) by interacting with alpha, beta, and gamma ENaC subunits. *Pflugers Arch* **459**, 377-387, doi:10.1007/s00424-009-0733-4 (2010).

86 Ingolfsson, H. I. *et al.* Lipid organization of the plasma membrane. *J Am Chem Soc* **136**, 14554-14559, doi:10.1021/ja507832e (2014).

87 El Amri, M., Fitzgerald, U. & Schlosser, G. MARCKS and MARCKS-like proteins in development and regeneration. *J Biomed Sci* **25**, 43, doi:10.1186/s12929-018-0445-1 (2018).

88 Bao, H. F. *et al.* ENaC activity is increased in isolated, split-open cortical collecting ducts from protein kinase Calpha knockout mice. *Am J Physiol Renal Physiol* **306**, F309-320, doi:10.1152/ajprenal.00519.2013 (2014).

89 Carattino, M. D. *et al.* The epithelial Na+ channel is inhibited by a peptide derived from proteolytic processing of its alpha subunit. *J Biol Chem* **281**, 18901-18907, doi:10.1074/jbc.M604109200 (2006).

90 Bruns, J. B. *et al.* Epithelial Na+ channels are fully activated by furin- and prostasin-dependent release of an inhibitory peptide from the gamma-subunit. *J Biol Chem* **282**, 6153-6160, doi:10.1074/jbc.M610636200 (2007).

91 Chraibi, A., Vallet, V., Firsov, D., Hess, S. K. & Horisberger, J. D. Protease modulation of the activity of the epithelial sodium channel expressed in Xenopus oocytes. *J Gen Physiol* **111**, 127-138, doi:10.1085/jgp.111.1.127 (1998).

92 Caldwell, R. A., Boucher, R. C. & Stutts, M. J. Serine protease activation of near-silent epithelial Na+ channels. *Am J Physiol Cell Physiol* **286**, C190-194, doi:10.1152/ajpcell.00342.2003 (2004).

93 Orce, G. G., Castillo, G. A. & Margolius, H. S. Inhibition of short-circuit current in toad urinary bladder by inhibitors of glandular kallikrein. *Am J Physiol* **239**, F459-465, doi:10.1152/ajprenal.1980.239.5.F459 (1980).

94 Vallet, V., Chraibi, A., Gaeggeler, H. P., Horisberger, J. D. & Rossier, B. C. An epithelial serine protease activates the amiloride-sensitive sodium channel. *Nature* **389**, 607-610, doi:10.1038/39329 (1997).

95 Hughey, R. P. *et al.* Epithelial sodium channels are activated by furin-dependent proteolysis. *J Biol Chem* **279**, 18111-18114, doi:10.1074/jbc.C400080200 (2004).

96 Hughey, R. P. *et al.* Maturation of the epithelial Na+ channel involves proteolytic processing of the alpha- and gamma-subunits. *J Biol Chem* **278**, 37073-37082, doi:10.1074/jbc.M307003200 (2003).

97 Carattino, M. D., Hughey, R. P. & Kleyman, T. R. Proteolytic processing of the epithelial sodium channel gamma subunit has a dominant role in channel activation. *J Biol Chem* **283**, 25290-25295, doi:10.1074/jbc.M803931200 (2008).

98 Carattino, M. D. *et al.* Defining an inhibitory domain in the alpha-subunit of the epithelial sodium channel. *Am J Physiol Renal Physiol* **294**, F47-52, doi:10.1152/ajprenal.00399.2007 (2008).

99 Passero, C. J. *et al.* Defining an inhibitory domain in the gamma subunit of the epithelial sodium channel. *Am J Physiol Renal Physiol* **299**, F854-861, doi:10.1152/ajprenal.00316.2010 (2010).

100 Frateschi, S. *et al.* Mutations of the serine protease CAP1/Prss8 lead to reduced embryonic viability, skin defects, and decreased ENaC activity. *Am J Pathol* **181**, 605-615, doi:10.1016/j.ajpath.2012.05.007 (2012).

101 Hummler, E. & Planes, C. Importance of ENaC-mediated sodium transport in alveolar fluid clearance using genetically-engineered mice. *Cell Physiol Biochem* **25**, 63-70, doi:10.1159/000272051 (2010).

102 Andreasen, D., Vuagniaux, G., Fowler-Jaeger, N., Hummler, E. & Rossier, B. C. Activation of epithelial sodium channels by mouse channel activating proteases (mCAP) expressed in Xenopus oocytes requires catalytic activity of mCAP3 and mCAP2 but not mCAP1. *J Am Soc Nephrol* **17**, 968-976, doi:10.1681/ASN.2005060637 (2006).

103 Carattino, M. D. *et al.* Prostasin interacts with the epithelial Na+ channel and facilitates cleavage of the gamma-subunit by a second protease. *Am J Physiol Renal Physiol* **307**, F1080-1087, doi:10.1152/ajprenal.00157.2014 (2014).

104 Staub, O. *et al.* WW domains of Nedd4 bind to the proline-rich PY motifs in the epithelial Na+ channel deleted in Liddle's syndrome. *EMBO J* **15**, 2371-2380 (1996).

105 Zhou, R., Patel, S. V. & Snyder, P. M. Nedd4-2 catalyzes ubiquitination and degradation of cell surface ENaC. *J Biol Chem* **282**, 20207-20212, doi:10.1074/jbc.M611329200 (2007).

106 Staub, O. *et al.* Regulation of stability and function of the epithelial Na+ channel (ENaC) by ubiquitination. *EMBO J* **16**, 6325-6336, doi:10.1093/emboj/16.21.6325 (1997).

107 Hansson, J. H. *et al.* Hypertension caused by a truncated epithelial sodium channel gamma subunit: genetic heterogeneity of Liddle syndrome. *Nat Genet* **11**, 76-82, doi:10.1038/ng0995-76 (1995).

108 Hansson, J. H. *et al.* A de novo missense mutation of the beta subunit of the epithelial sodium channel causes hypertension and Liddle syndrome, identifying a proline-rich segment critical for regulation of channel activity. *Proc Natl Acad Sci U S A* **92**, 11495-11499 (1995).

109 Debonneville, C. *et al.* Phosphorylation of Nedd4-2 by Sgk1 regulates epithelial Na(+) channel cell surface expression. *EMBO J* **20**, 7052-7059, doi:10.1093/emboj/20.24.7052 (2001).

110 Renard, S., Lingueglia, E., Voilley, N., Lazdunski, M. & Barbry, P. Biochemical analysis of the membrane topology of the amiloride-sensitive Na+ channel. *J Biol Chem* **269**, 12981-12986 (1994).

111 Snyder, P. M., McDonald, F. J., Stokes, J. B. & Welsh, M. J. Membrane topology of the amiloride-sensitive epithelial sodium channel. *J Biol Chem* **269**, 24379-24383 (1994).

112 Adams, C. M., Snyder, P. M. & Welsh, M. J. Interactions between subunits of the human epithelial sodium channel. *J Biol Chem* **272**, 27295-27300, doi:10.1074/jbc.272.43.27295 (1997).

113 Hughey, R. P., Bruns, J. B., Kinlough, C. L. & Kleyman, T. R. Distinct pools of epithelial sodium channels are expressed at the plasma membrane. *J Biol Chem* **279**, 48491-48494, doi:10.1074/jbc.C400460200 (2004).

114 Mueller, G. M. *et al.* Cys palmitoylation of the beta subunit modulates gating of the epithelial sodium channel. *J Biol Chem* **285**, 30453-30462, doi:10.1074/jbc.M110.151845 (2010).

115 Mukherjee, A. *et al.* Cysteine palmitoylation of the gamma subunit has a dominant role in modulating activity of the epithelial sodium channel. *J Biol Chem* **289**, 14351-14359, doi:10.1074/jbc.M113.526020 (2014).

116 Mukherjee, A. *et al.* Specific Palmitoyltransferases Associate with and Activate the Epithelial Sodium Channel. *J Biol Chem* **292**, 4152-4163, doi:10.1074/jbc.M117.776146 (2017).

117 Shi, H. *et al.* Casein kinase 2 specifically binds to and phosphorylates the carboxy termini of ENaC subunits. *Eur J Biochem* **269**, 4551-4558, doi:10.1046/j.1432-1033.2002.03154.x (2002).

118 Shi, H. *et al.* Interactions of beta and gamma ENaC with Nedd4 can be facilitated by an ERK-mediated phosphorylation. *J Biol Chem* **277**, 13539-13547, doi:10.1074/jbc.M111717200 (2002).

119 Lee, I. H. *et al.* Regulation of the epithelial Na+ channel by the RH domain of G protein-coupled receptor kinase, GRK2, and Galphaq/11. *J Biol Chem* **286**, 19259-19269, doi:10.1074/jbc.M111.239772 (2011).

120 Dinudom, A. *et al.* The kinase Grk2 regulates Nedd4/Nedd4-2-dependent control of epithelial Na+ channels. *Proc Natl Acad Sci U S A* **101**, 11886-11890, doi:10.1073/pnas.0402178101 (2004).

121 Diakov, A. & Korbmacher, C. A novel pathway of epithelial sodium channel activation involves a serum- and glucocorticoid-inducible kinase consensus motif in the C terminus of the channel's alpha-subunit. *J Biol Chem* **279**, 38134-38142, doi:10.1074/jbc.M403260200 (2004).

122 Stockand, J. D. *et al.* Differential effects of protein kinase C on the levels of epithelial Na+ channel subunit proteins. *J Biol Chem* **275**, 25760-25765, doi:10.1074/jbc.M003615200 (2000).

123 Booth, R. E. & Stockand, J. D. Targeted degradation of ENaC in response to PKC activation of the ERK1/2 cascade. *Am J Physiol Renal Physiol* **284**, F938-947, doi:10.1152/ajprenal.00373.2002 (2003).

124 Kritz RW, K. B. *Structural organization of the mammalian kidney*. 595-691 (Academic Press, 2000).

125 Rossier, B. C. Epithelial sodium channel (ENaC) and the control of blood pressure. *Curr Opin Pharmacol* **15**, 33-46, doi:10.1016/j.coph.2013.11.010 (2014).

126 Palmer, L. G. Interactions of amiloride and other blocking cations with the apical Na channel in the toad urinary bladder. *J Membr Biol* **87**, 191-199 (1985).

127 Verouti, S. N., Boscardin, E., Hummler, E. & Frateschi, S. Regulation of blood pressure and renal function by NCC and ENaC: lessons from genetically engineered mice. *Curr Opin Pharmacol* **21**, 60-72, doi:10.1016/j.coph.2014.12.012 (2015).

128 Arroyo, J. P., Ronzaud, C., Lagnaz, D., Staub, O. & Gamba, G. Aldosterone paradox: differential regulation of ion transport in distal nephron. *Physiology (Bethesda)* **26**, 115-123, doi:10.1152/physiol.00049.2010 (2011).

129 Masilamani, S., Kim, G. H., Mitchell, C., Wade, J. B. & Knepper, M. A. Aldosterone-mediated regulation of ENaC alpha, beta, and gamma subunit proteins in rat kidney. *J Clin Invest* **104**, R19-23, doi:10.1172/JCI7840 (1999).

130 Frindt, G. & Palmer, L. G. Surface expression of sodium channels and transporters in rat kidney: effects of dietary sodium. *Am J Physiol Renal Physiol* **297**, F1249-1255, doi:10.1152/ajprenal.00401.2009 (2009).

131 Frindt, G., Ergonul, Z. & Palmer, L. G. Surface expression of epithelial Na channel protein in rat kidney. *J Gen Physiol* **131**, 617-627, doi:10.1085/jgp.200809989 (2008).

132 McCormick, J. A., Bhalla, V., Pao, A. C. & Pearce, D. SGK1: a rapid aldosterone-induced regulator of renal sodium reabsorption. *Physiology (Bethesda)* **20**, 134-139, doi:10.1152/physiol.00053.2004 (2005).

133 Nesterov, V. *et al.* Aldosterone-dependent and -independent regulation of the epithelial sodium channel (ENaC) in mouse distal nephron. *Am J Physiol Renal Physiol* **303**, F1289-1299, doi:10.1152/ajprenal.00247.2012 (2012).

134 Mamenko, M., Zaika, O., Ilatovskaya, D. V., Staruschenko, A. & Pochynyuk, O. Angiotensin II increases activity of the epithelial Na+ channel (ENaC) in distal nephron additively to aldosterone. *J Biol Chem* **287**, 660-671, doi:10.1074/jbc.M111.298919 (2012).

135 Sun, P., Yue, P. & Wang, W. H. Angiotensin II stimulates epithelial sodium channels in the cortical collecting duct of the rat kidney. *Am J Physiol Renal Physiol* **302**, F679-687, doi:10.1152/ajprenal.00368.2011 (2012).

136 Ring, A. M. *et al.* WNK4 regulates activity of the epithelial Na+ channel in vitro and in vivo. *Proc Natl Acad Sci U S A* **104**, 4020-4024, doi:10.1073/pnas.0611727104 (2007).

137 Yu, L. *et al.* WNK4 inhibition of ENaC is independent of Nedd4-2-mediated ENaC ubiquitination. *Am J Physiol Renal Physiol* **305**, F31-41, doi:10.1152/ajprenal.00652.2012 (2013).

138 Mironova, E., Bugaj, V., Roos, K. P., Kohan, D. E. & Stockand, J. D. Aldosterone-independent regulation of the epithelial Na+ channel (ENaC) by vasopressin in adrenalectomized mice. *Proc Natl Acad Sci U S A* **109**, 10095-10100, doi:10.1073/pnas.1201978109 (2012).

139 Snyder, P. M., Olson, D. R., Kabra, R., Zhou, R. & Steines, J. C. cAMP and serum and glucocorticoid-inducible kinase (SGK) regulate the epithelial Na(+) channel through convergent phosphorylation of Nedd4-2. *J Biol Chem* **279**, 45753-45758, doi:10.1074/jbc.M407858200 (2004).

140 Bankir, L., Bichet, D. G. & Bouby, N. Vasopressin V2 receptors, ENaC, and sodium reabsorption: a risk factor for hypertension? *Am J Physiol Renal Physiol* **299**, F917-928, doi:10.1152/ajprenal.00413.2010 (2010).

141 Marunaka, Y., Hagiwara, N. & Tohda, H. Insulin activates single amiloride-blockable Na channels in a distal nephron cell line (A6). *Am J Physiol* **263**, F392-400 (1992).

142 Blazer-Yost, B. L., Liu, X. & Helman, S. I. Hormonal regulation of ENaCs: insulin and aldosterone. *Am J Physiol* **274**, C1373-1379 (1998).

143 Gonzalez-Rodriguez, E., Gaeggeler, H. P. & Rossier, B. C. IGF-1 vs insulin: respective roles in modulating sodium transport via the PI-3 kinase/Sgk1 pathway in a cortical collecting duct cell line. *Kidney Int* **71**, 116-125, doi:10.1038/sj.ki.5002018 (2007).

144 Frindt, G. & Palmer, L. G. Effects of insulin on Na and K transporters in the rat CCD. *Am J Physiol Renal Physiol* **302**, F1227-1233, doi:10.1152/ajprenal.00675.2011 (2012).

145 Hummler, E. *et al.* Early death due to defective neonatal lung liquid clearance in alpha-ENaC-deficient mice. *Nat Genet* **12**, 325-328, doi:10.1038/ng0396-325 (1996).

146 Mall, M. A. *et al.* Airway surface liquid volume regulation determines different airway phenotypes in liddle compared with betaENaC-overexpressing mice. *J Biol Chem* **285**, 26945-26955, doi:10.1074/jbc.M110.151803 (2010).

147 Malsure, S. *et al.* Colon-specific deletion of epithelial sodium channel causes sodium loss and aldosterone resistance. *J Am Soc Nephrol* **25**, 1453-1464, doi:10.1681/ASN.2013090936 (2014).

148 Palmer, B. F. & Alpern, R. J. Liddle's syndrome. *Am J Med* **104**, 301-309, doi:10.1016/s0002-9343(98)00018-7 (1998).

149 Tetti, M. *et al.* Liddle Syndrome: Review of the Literature and Description of a New Case. *Int J Mol Sci* **19**, doi:10.3390/ijms19030812 (2018).

150 Cheek, D. B. & Perry, J. W. A salt wasting syndrome in infancy. *Arch Dis Child* **33**, 252-256, doi:10.1136/adc.33.169.252 (1958).

151 Hanukoglu, A. Type I pseudohypoaldosteronism includes two clinically and genetically distinct entities with either renal or multiple target organ defects. *J Clin Endocrinol Metab* **73**, 936-944, doi:10.1210/jcem-73-5-936 (1991).

152 Welzel, M. *et al.* Five novel mutations in the SCNN1A gene causing autosomal recessive pseudohypoaldosteronism type 1. *Eur J Endocrinol* **168**, 707-715, doi:10.1530/EJE-12-1000 (2013).

153 Wang, J. *et al.* Novel mutations in the SCNN1A gene causing Pseudohypoaldosteronism type 1. *PLoS One* **8**, e65676, doi:10.1371/journal.pone.0065676 (2013).

154 Strautnieks, S. S., Thompson, R. J., Gardiner, R. M. & Chung, E. A novel splice-site mutation in the gamma subunit of the epithelial sodium channel gene in three pseudohypoaldosteronism type 1 families. *Nat Genet* **13**, 248-250, doi:10.1038/ng0696-248 (1996).

155 Saxena, A. *et al.* Novel mutations responsible for autosomal recessive multisystem pseudohypoaldosteronism and sequence variants in epithelial sodium channel alpha-, beta-, and gamma-subunit genes. *J Clin Endocrinol Metab* **87**, 3344-3350, doi:10.1210/jcem.87.7.8674 (2002).

156 Edelheit, O. *et al.* Novel mutations in epithelial sodium channel (ENaC) subunit genes and phenotypic expression of multisystem pseudohypoaldosteronism. *Clin Endocrinol (Oxf)* **62**, 547-553, doi:10.1111/j.1365-2265.2005.02255.x (2005).

157 Grunder, S. *et al.* A mutation causing pseudohypoaldosteronism type 1 identifies a conserved glycine that is involved in the gating of the epithelial sodium channel. *EMBO J* **16**, 899-907, doi:10.1093/emboj/16.5.899 (1997).

158 Chang, S. S. *et al.* Mutations in subunits of the epithelial sodium channel cause salt wasting with hyperkalaemic acidosis, pseudohypoaldosteronism type 1. *Nat Genet* **12**, 248-253, doi:10.1038/ng0396-248 (1996).

159 Bonny, O., Knoers, N., Monnens, L. & Rossier, B. C. A novel mutation of the epithelial Na+ channel causes type 1 pseudohypoaldosteronism. *Pediatr Nephrol* **17**, 804-808, doi:10.1007/s00467-002-0945-8 (2002).

160 Belot, A. *et al.* Pseudohypoaldosteronisms, report on a 10-patient series. *Nephrol Dial Transplant* **23**, 1636-1641, doi:10.1093/ndt/gfm862 (2008).

161 Itani, O. A. *et al.* Human cystic fibrosis airway epithelia have reduced Cl- conductance but not increased Na+ conductance. *Proc Natl Acad Sci U S A* **108**, 10260-10265, doi:10.1073/pnas.1106695108 (2011).

162 Chen, J. H. *et al.* Loss of anion transport without increased sodium absorption characterizes newborn porcine cystic fibrosis airway epithelia. *Cell* **143**, 911-923, doi:10.1016/j.cell.2010.11.029 (2010).

163 Hobbs, C. A., Da Tan, C. & Tarran, R. Does epithelial sodium channel hyperactivity contribute to cystic fibrosis lung disease? *J Physiol* **591**, 4377-4387, doi:10.1113/jphysiol.2012.240861 (2013).

164 Rauh, R. *et al.* A mutation of the epithelial sodium channel associated with atypical cystic fibrosis increases channel open probability and reduces Na+ self inhibition. *J Physiol* **588**, 1211-1225, doi:10.1113/jphysiol.2009.180224 (2010).

165 Rauh, R. *et al.* A mutation in the beta-subunit of ENaC identified in a patient with cystic fibrosis-like symptoms has a gain-of-function effect. *Am J Physiol Lung Cell Mol Physiol* **304**, L43-55, doi:10.1152/ajplung.00093.2012 (2013).

166 Shobair, M. *et al.* Gain-of-Function Mutation W493R in the Epithelial Sodium Channel Allosterically Reconfigures Intersubunit Coupling. *J Biol Chem* **291**, 3682-3692, doi:10.1074/jbc.M115.678052 (2016).

167 Gonzales, E. B., Kawate, T. & Gouaux, E. Pore architecture and ion sites in acid-sensing ion channels and P2X receptors. *Nature* **460**, 599-604, doi:10.1038/nature08218 (2009).

168 Baconguis, I. & Gouaux, E. Structural plasticity and dynamic selectivity of acid-sensing ion channel-spider toxin complexes. *Nature* **489**, 400-405, doi:10.1038/nature11375 (2012).

169 Dawson, R. J. *et al.* Structure of the acid-sensing ion channel 1 in complex with the gating modifier Psalmotoxin 1. *Nat Commun* **3**, 936, doi:10.1038/ncomms1917 (2012).

170 Yoder, N., Yoshioka, C. & Gouaux, E. Gating mechanisms of acid-sensing ion channels. *Nature* **555**, 397-401, doi:10.1038/nature25782 (2018).

171 Yoder, N. & Gouaux, E. Divalent cation and chloride ion sites of chicken acid sensing ion channel 1a elucidated by x-ray crystallography. *PLoS One* **13**, e0202134, doi:10.1371/journal.pone.0202134 (2018).

172 Yoder, N. B. *Gating and modulation of acid-sensing ion channels* Doctor of Philosophy thesis, Oregon Health and Science University, (2019).

173 Franklin, S. S. & Wong, N. D. Hypertension and cardiovascular disease: contributions of the framingham heart study. *Glob Heart* **8**, 49-57, doi:10.1016/j.gheart.2012.12.004 (2013).

174 Neal, B., MacMahon, S., Chapman, N. & Blood Pressure Lowering Treatment Trialists, C. Effects of ACE inhibitors, calcium antagonists, and other blood-pressure-lowering drugs: results of prospectively designed overviews of randomised trials. Blood Pressure Lowering Treatment Trialists' Collaboration. *Lancet* **356**, 1955-1964 (2000).

175 Sanchis-Gomar, F., Perez-Quilis, C., Leischik, R. & Lucia, A. Epidemiology of coronary heart disease and acute coronary syndrome. *Ann Transl Med* **4**, 256, doi:10.21037/atm.2016.06.33 (2016).

176 Go, A. S. *et al.* Heart disease and stroke statistics--2013 update: a report from the American Heart Association. *Circulation* **127**, e6-e245, doi:10.1161/CIR.0b013e31828124ad (2013).

177 Pratt, J. H. Central role for ENaC in development of hypertension. *J Am Soc Nephrol* **16**, 3154-3159, doi:10.1681/ASN.2005050460 (2005).

178 Weber, M. A. The evolving clinical management of hypertension. *J Clin Hypertens (Greenwich)* **16**, 917-924, doi:10.1111/jch.12444 (2014).

179 Heran, B. S., Chen, J. M., Wang, J. J. & Wright, J. M. Blood pressure lowering efficacy of potassium-sparing diuretics (that block the epithelial sodium channel) for primary hypertension. *Cochrane Database Syst Rev* **11**, CD008167, doi:10.1002/14651858.CD008167.pub3 (2012).

180 Boscardin, E., Alijevic, O., Hummler, E., Frateschi, S. & Kellenberger, S. The function and regulation of acid-sensing ion channels (ASICs) and the epithelial Na(+) channel (ENaC): IUPHAR Review 19. *Br J Pharmacol* **173**, 2671-2701, doi:10.1111/bph.13533 (2016).

181 Chalfie, M. & Wolinsky, E. The identification and suppression of inherited neurodegeneration in Caenorhabditis elegans. *Nature* **345**, 410-416, doi:10.1038/345410a0 (1990).

182 Kellenberger, S. & Schild, L. Epithelial sodium channel/degenerin family of ion channels: a variety of functions for a shared structure. *Physiol Rev* **82**, 735-767, doi:10.1152/physrev.00007.2002 (2002).

183 Waldmann, R., Champigny, G., Bassilana, F., Heurteaux, C. & Lazdunski, M. A proton-gated cation channel involved in acid-sensing. *Nature* **386**, 173-177, doi:10.1038/386173a0 (1997).

184 Waldmann, R. *et al.* Molecular cloning of a non-inactivating proton-gated Na+ channel specific for sensory neurons. *J Biol Chem* **272**, 20975-20978, doi:10.1074/jbc.272.34.20975 (1997).

185 Krishtal, O. A. & Pidoplichko, V. I. A receptor for protons in the membrane of sensory neurons may participate in nociception. *Neuroscience* **6**, 2599-2601, doi:10.1016/0306-4522(81)90105-6 (1981).

186 Chelur, D. S. *et al.* The mechanosensory protein MEC-6 is a subunit of the C. elegans touch-cell degenerin channel. *Nature* **420**, 669-673, doi:10.1038/nature01205 (2002).

187 Cottrell, G. A., Green, K. A. & Davies, N. W. The neuropeptide Phe-Met-Arg-Phe-NH2 (FMRFamide) can activate a ligand-gated ion channel in Helix neurones. *Pflugers Arch* **416**, 612-614, doi:10.1007/bf00382698 (1990).

188 Lingueglia, E., Champigny, G., Lazdunski, M. & Barbry, P. Cloning of the amiloride-sensitive FMRFamide peptide-gated sodium channel. *Nature* **378**, 730-733, doi:10.1038/378730a0 (1995).

189 Busst, C. J. Blood pressure regulation via the epithelial sodium channel: from gene to kidney and beyond. *Clin Exp Pharmacol Physiol* **40**, 495-503, doi:10.1111/1440-1681.12124 (2013).

190 Ismailov, II *et al.* Regulation of epithelial sodium channels by the cystic fibrosis transmembrane conductance regulator. *J Biol Chem* **271**, 4725-4732, doi:10.1074/jbc.271.9.4725 (1996).

191 Rossier, B. C., Baker, M. E. & Studer, R. A. Epithelial sodium transport and its control by aldosterone: the story of our internal environment revisited. *Physiol Rev* **95**, 297-340, doi:10.1152/physrev.00011.2014 (2015).

192 McDonald, F. J., Snyder, P. M., McCray, P. B., Jr. & Welsh, M. J. Cloning, expression, and tissue distribution of a human amiloride-sensitive Na+ channel. *Am J Physiol* **266**, L728-734, doi:10.1152/ajplung.1994.266.6.L728 (1994).

193 Shimkets, R. A. *et al.* Liddle's syndrome: heritable human hypertension caused by mutations in the beta subunit of the epithelial sodium channel. *Cell* **79**, 407-414, doi:10.1016/0092-8674(94)90250-x (1994).

194 Kerem, E. *et al.* Pulmonary epithelial sodium-channel dysfunction and excess airway liquid in pseudohypoaldosteronism. *N Engl J Med* **341**, 156-162, doi:10.1056/NEJM199907153410304 (1999).

195 Soundararajan, R., Pearce, D., Hughey, R. P. & Kleyman, T. R. Role of epithelial sodium channels and their regulators in hypertension. *J Biol Chem* **285**, 30363-30369, doi:10.1074/jbc.R110.155341 (2010).

196 Hamm, L. L., Feng, Z. & Hering-Smith, K. S. Regulation of sodium transport by ENaC in the kidney. *Curr Opin Nephrol Hypertens* **19**, 98-105, doi:10.1097/MNH.0b013e328332bda4 (2010).

197 Zheng, H. *et al.* Urinary Proteolytic Activation of Renal Epithelial Na+ Channels in Chronic Heart Failure. *Hypertension* **67**, 197-205, doi:10.1161/HYPERTENSIONAHA.115.05838 (2016).

198 Vallet, V., Pfister, C., Loffing, J. & Rossier, B. C. Cell-surface expression of the channel activating protease xCAP-1 is required for activation of ENaC in the Xenopus oocyte. *J Am Soc Nephrol* **13**, 588-594 (2002).

199 Vuagniaux, G., Vallet, V., Jaeger, N. F., Hummler, E. & Rossier, B. C. Synergistic activation of ENaC by three membrane-bound channel-activating serine proteases (mCAP1, mCAP2, and mCAP3) and serum- and glucocorticoid-regulated kinase (Sgk1) in Xenopus Oocytes. *J Gen Physiol* **120**, 191-201, doi:10.1085/jgp.20028598 (2002).

200 Kleyman, T. R., Carattino, M. D. & Hughey, R. P. ENaC at the cutting edge: regulation of epithelial sodium channels by proteases. *J Biol Chem* **284**, 20447-20451, doi:10.1074/jbc.R800083200 (2009).

201 Rossier, B. C. & Stutts, M. J. Activation of the epithelial sodium channel (ENaC) by serine proteases. *Annu Rev Physiol* **71**, 361-379, doi:10.1146/annurev.physiol.010908.163108 (2009).

202 Goehring, A. *et al.* Screening and large-scale expression of membrane proteins in mammalian cells for structural studies. *Nat Protoc* **9**, 2574-2585, doi:10.1038/nprot.2014.173 (2014).

203 N., M. D. SerialEM: A Program for Automated Tilt Series Acquisition on Tecnai Microscopes Using Prediction of Specimen Position. *Microscopy and Microanalysis* **9**, doi:10.1017/S1431927603445911 (2003).

204 Zheng, S. Q. *et al.* MotionCor2: anisotropic correction of beam-induced motion for improved cryo-electron microscopy. *Nat Methods* **14**, 331-332, doi:10.1038/nmeth.4193 (2017).

205 Voss, N. R., Yoshioka, C. K., Radermacher, M., Potter, C. S. & Carragher, B. DoG Picker and TiltPicker: software tools to facilitate particle selection in single particle electron microscopy. *J Struct Biol* **166**, 205-213, doi:10.1016/j.jsb.2009.01.004 (2009).

206 Zhang, K. Gctf: Real-time CTF determination and correction. *J Struct Biol* **193**, 1-12, doi:10.1016/j.jsb.2015.11.003 (2016).

207 Scheres, S. H. RELION: implementation of a Bayesian approach to cryo-EM structure determination. *J Struct Biol* **180**, 519-530, doi:10.1016/j.jsb.2012.09.006 (2012).

208 Punjani, A., Rubinstein, J. L., Fleet, D. J. & Brubaker, M. A. cryoSPARC: algorithms for rapid unsupervised cryo-EM structure determination. *Nat Methods* **14**, 290-296, doi:10.1038/nmeth.4169 (2017).

209 Grant, T., Rohou, A. & Grigorieff, N. cisTEM, user-friendly software for single-particle image processing. *Elife* **7**, doi:10.7554/eLife.35383 (2018).

210 Arnold, K., Bordoli, L., Kopp, J. & Schwede, T. The SWISS-MODEL workspace: a web-based environment for protein structure homology modelling. *Bioinformatics* **22**, 195-201, doi:10.1093/bioinformatics/bti770 (2006).

211 Pettersen, E. F. *et al.* UCSF Chimera--a visualization system for exploratory research and analysis. *J Comput Chem* **25**, 1605-1612, doi:10.1002/jcc.20084 (2004).

212 Emsley, P. & Cowtan, K. Coot: model-building tools for molecular graphics. *Acta Crystallogr D Biol Crystallogr* **60**, 2126-2132, doi:10.1107/S0907444904019158 (2004).

213 DiMaio, F., Leaver-Fay, A., Bradley, P., Baker, D. & Andre, I. Modeling symmetric macromolecular structures in Rosetta3. *PLoS One* **6**, e20450, doi:10.1371/journal.pone.0020450 (2011).

214 Buchan, D. W., Minneci, F., Nugent, T. C., Bryson, K. & Jones, D. T. Scalable web services for the PSIPRED Protein Analysis Workbench. *Nucleic Acids Res* **41**, W349-357, doi:10.1093/nar/gkt381 (2013).

215 Xu, D. & Zhang, Y. Ab initio protein structure assembly using continuous structure fragments and optimized knowledge-based force field. *Proteins* **80**, 1715-1735, doi:10.1002/prot.24065 (2012).

216 Drozdetskiy, A., Cole, C., Procter, J. & Barton, G. J. JPred4: a protein secondary structure prediction server. *Nucleic Acids Res* **43**, W389-394, doi:10.1093/nar/gkv332 (2015).

217 Adams, P. D. *et al.* The Phenix software for automated determination of macromolecular structures. *Methods* **55**, 94-106, doi:10.1016/j.ymeth.2011.07.005 (2011).

218 Chen, V. B. *et al.* MolProbity: all-atom structure validation for macromolecular crystallography. *Acta Crystallogr D Biol Crystallogr* **66**, 12-21, doi:10.1107/S0907444909042073 (2010).

219 *https://pymol.org/2/*.

220 Kawate, T. & Gouaux, E. Fluorescence-detection size-exclusion chromatography for precrystallization screening of integral membrane proteins. *Structure* **14**, 673-681, doi:10.1016/j.str.2006.01.013 (2006).

221 Heymann, J. B. & Belnap, D. M. Bsoft: image processing and molecular modeling for electron microscopy. *J Struct Biol* **157**, 3-18, doi:10.1016/j.jsb.2006.06.006 (2007).

222 Collier, D. M. & Snyder, P. M. Identification of epithelial Na+ channel (ENaC) intersubunit Cl- inhibitory residues suggests a trimeric alpha gamma beta channel architecture. *J Biol Chem* **286**, 6027-6032, doi:10.1074/jbc.M110.198127 (2011).

223 Collier, D. M., Tomkovicz, V. R., Peterson, Z. J., Benson, C. J. & Snyder, P. M. Intersubunit conformational changes mediate epithelial sodium channel gating. *J Gen Physiol* **144**, 337-348, doi:10.1085/jgp.201411208 (2014).

224 Chen, J., Myerburg, M. M., Passero, C. J., Winarski, K. L. & Sheng, S. External Cu2+ inhibits human epithelial Na+ channels by binding at a subunit interface of extracellular domains. *J Biol Chem* **286**, 27436-27446, doi:10.1074/jbc.M111.232058 (2011).

225 Stockand, J. D., Staruschenko, A., Pochynyuk, O., Booth, R. E. & Silverthorn, D. U. Insight toward epithelial Na+ channel mechanism revealed by the acid-sensing ion channel 1 structure. *IUBMB Life* **60**, 620-628, doi:10.1002/iub.89 (2008).

226 Salih, M. *et al.* A Missense Mutation in the Extracellular Domain of alphaENaC Causes Liddle Syndrome. *J Am Soc Nephrol* **28**, 3291-3299, doi:10.1681/ASN.2016111163 (2017).

227 Kashlan, O. B. *et al.* Allosteric inhibition of the epithelial Na+ channel through peptide binding at peripheral finger and thumb domains. *J Biol Chem* **285**, 35216-35223, doi:10.1074/jbc.M110.167064 (2010).

228 Vullo, S. *et al.* Conformational dynamics and role of the acidic pocket in ASIC pH-dependent gating. *Proc Natl Acad Sci U S A* **114**, 3768-3773, doi:10.1073/pnas.1620560114 (2017).

229 Kashlan, O. B., Blobner, B. M., Zuzek, Z., Carattino, M. D. & Kleyman, T. R. Inhibitory tract traps the epithelial Na+ channel in a low activity conformation. *J Biol Chem* **287**, 20720-20726, doi:10.1074/jbc.M112.358218 (2012).

230 Rossier, B. C., Pradervand, S., Schild, L. & Hummler, E. Epithelial sodium channel and the control of sodium balance: interaction between genetic and environmental factors. *Annu Rev Physiol* **64**, 877-897, doi:10.1146/annurev.physiol.64.082101.143243 (2002).

231 Snyder, P. M. The epithelial Na+ channel: cell surface insertion and retrieval in Na+ homeostasis and hypertension. *Endocr Rev* **23**, 258-275, doi:10.1210/edrv.23.2.0458 (2002).

232 Schild, L. *et al.* A mutation in the epithelial sodium channel causing Liddle disease increases channel activity in the Xenopus laevis oocyte expression system. *Proc Natl Acad Sci U S A* **92**, 5699-5703 (1995).

233 Hummler, E. *et al.* A mouse model for the renal salt-wasting syndrome pseudohypoaldosteronism. *Proc Natl Acad Sci U S A* **94**, 11710-11715 (1997).

234 Noreng, S., Bharadwaj, A., Posert, R., Yoshioka, C. & Baconguis, I. Structure of the human epithelial sodium channel by cryo-electron microscopy. *Elife* **7**, doi:10.7554/eLife.39340 (2018).

235 Kashlan, O. B. & Kleyman, T. R. ENaC structure and function in the wake of a resolved structure of a family member. *Am J Physiol Renal Physiol* **301**, F684-696, doi:10.1152/ajprenal.00259.2011 (2011).

236 Rohou, A. & Grigorieff, N. CTFFIND4: Fast and accurate defocus estimation from electron micrographs. *J Struct Biol* **192**, 216-221, doi:10.1016/j.jsb.2015.08.008 (2015).

237 Asarnow, D., Palovcak, E., Cheng, Y. *UCSF pyem https://doi.org/10.5281/zenodo.3576630* 2019).

238 Afonine, P. V. *et al.* New tools for the analysis and validation of cryo-EM maps and atomic models. *Acta Crystallogr D Struct Biol* **74**, 814-840, doi:10.1107/S2059798318009324 (2018).

239 Hirsh, A. J. *et al.* Design, synthesis, and structure-activity relationships of novel 2-substituted pyrazinoylguanidine epithelial sodium channel blockers: drugs for cystic fibrosis and chronic bronchitis. *J Med Chem* **49**, 4098-4115, doi:10.1021/jm051134w (2006).

240 Haerteis, S. *et al.* Proteolytic activation of the human epithelial sodium channel by trypsin IV and trypsin I involves distinct cleavage sites. *J Biol Chem* **289**, 19067-19078, doi:10.1074/jbc.M113.538470 (2014).

241 Krishnamurthy, H. & Gouaux, E. X-ray structures of LeuT in substrate-free outward-open and apo inward-open states. *Nature* **481**, 469-474, doi:10.1038/nature10737 (2012).

242 Ling, B. N. & Eaton, D. C. Effects of luminal Na+ on single Na+ channels in A6 cells, a regulatory role for protein kinase C. *Am J Physiol* **256**, F1094-1103, doi:10.1152/ajprenal.1989.256.6.F1094 (1989).

243 Kellenberger, S. & Schild, L. International Union of Basic and Clinical Pharmacology. XCI. structure, function, and pharmacology of acid-sensing ion channels and the epithelial Na+ channel. *Pharmacol Rev* **67**, 1-35, doi:10.1124/pr.114.009225 (2015).

244 Denisov, I. G. & Sligar, S. G. Nanodiscs for structural and functional studies of membrane proteins. *Nat Struct Mol Biol* **23**, 481-486, doi:10.1038/nsmb.3195 (2016).